The Kiggavik Natural Analogue

By Ian Burron

A Thesis submitted to the Faculty of Graduate and Postdoctoral Studies of the University of Manitoba in partial fulfillment of the requirements of the degree of:

Doctor of Philosophy

Department of Earth Sciences

University of Manitoba

Winnipeg

Abstract

Nuclear energy produces large amounts of clean electricity, but also produces highly radioactive Used Nuclear Fuel (UNF). The most promising solution for long term disposal of UNF is burial in a Deep Geologic Repository (DGR); successfully implementing these plans, however, requires knowledge of how UNF will behave in the subsurface over ~1 Ma. The uranium (U) ore mineral uraninite is chemically similar to UNF, therefore the study of U deposits can yield valuable insights which are difficult to acquire by other means. In this thesis the history of U mobility in the Kiggavik U deposits in central Nunavut are developed as such a natural analogue for a DGR.

The Kiggavik U deposits are hosted with metasedimentary and lesser granitic host rocks and formed in five stages. The first stage consists of albitization and U-enrichment, which is consistent with development of an albitite-hosted U deposit within a Metasomatic Iron Alkali Calcic (MIAC) system. This stage is Ar-Ar dated to ~1830 Ma, and muscovite formed at this time has δ^2H values up to +128.9 ‰, indicating it was precipitated from an extremely fractionated fluid produced through multiple cycles of boiling and condensation. The second stage consists of hematization and development of quartz breccias. The third stage consists of bleaching and primary (U1) U mineralization. This U1 mineralization is U-Pb dated to 1553 ± 16 Ma and comprises front-style (U1a), disseminated (U1b) and vein-hosted (U1c) uraninite, coffinite, and brannerite. Stable O and H isotopic compositions of illite associated with U1 indicates the presence of fractionated and basinal fluids at this time, suggesting Kiggavik has aspects of both MIAC and unconformity related U deposits. Stages one to three are associated with significant increases in the porosity of host rocks, which reaches ~12% in bleached granitic rocks, which may explain the deposits long history of continuing fluid infiltration and U

mobility. The fourth stage consists of U alteration and resetting/remobilization (U2) events isotopically linked to the infiltration of basinal fluids at 1440 ± 21, 1417 ± 17 Ma, 1276.4 ± 8.7 Ma, 1249 ± 33 Ma, 937 ± 24 Ma, and 274 ± 69 Ma. The fifth stage consists of geologically recent (< 1 Ma) remobilization and alteration of U minerals (U3).

This U3 alteration occurred in distinct pulses dated to 36.5 ± 1.9 Ka, 55.7 ± 4.8 Ka, 153.3 ± 3.7 Ka, 258.6 ± 11.6 Ka, and 471.3 ± 6.3 Ka via U-Th disequilibrium geochronology. It is isotopically linked to the infiltration of subglacial fluids along fractures systems and, to a much lesser extent, through the porous host rock matrix. This infiltration caused relatively minor degrees of short-range (~<5 cm) U mobility, but more widespread disruption to U decay chains through selective leaching of vulnerable isotopes. Probable factors restricting U mobility include reduction and reprecipitation of dissolved U by preexisting U minerals and Ti-oxides, adsorption onto clay mineral surfaces, and fracture sealing and pore filling, which reduces the porosity of affected rocks by ~50%, by precipitation of secondary calcite, Fe-oxides, U-minerals and vanadinite precipitated by infiltrating fluids.

The results of this thesis indicate Kiggavik has a long and complex history of U deposition, mobility, and reprecipitation, and suggests the region may be prospective for both unconformity related and MIAC affiliated deposits. Glaciation may impact UNF within a DGR if subglacial fluids are able to penetrate deeply into the subsurface along fractures and bypass safety barriers. Interactions with host rocks and precipitation of fracture-sealing secondary minerals, however, greatly restricts the rate and overall distance of radionuclide mobility, suggesting natural host rock barriers are capable of providing significant containment even in non-ideal circumstances.

Acknowledgments

First and foremost, I would like to thank my supervisor, Dr. Mostafa Fayek. His guidance and support, maintained for many years, has made this these possible. I am particularly grateful for the freedom he has granted me in conducting my research, and the considerable patience he has shown for my many mistakes and delays. Under his supervision I have been able to develop my own research interests, scientific process, and expertise; these gifts will last a lifetime and have made me the scientist I am today. I also thank my co-supervisor Julie Brown, who's encyclopedic knowledge of geologic disposal has made this thesis possible, and who's warmth and gentle encouragement has motivated me to continue during times of uncertainty and doubt.

I would also like to thank my fellow students and alumni at the Department of Earth Science. The spirit of support and comradery they have shown is truly inspirational, and has made the experience of grad school infinitely more rewarding and enjoyable than would otherwise be the case. I would also be remised if I didn't extend my heartfelt thanks to the staff of the Clayton H Riddel faculty. Over my (too) many years as a student I have seen a great deal of change in the faculty, but the commitment to the highest standards of science and education has remained consistent. I especially thank the technicians in the department's many labs, Ryan Sharpe and Panseok Yang in particular. The tireless and all-too-often unsung efforts of these experts has made my research possible.

Last but certainly not least I deeply and sincerely thank my friends and family. Academics have a long tradition of leaving their hometowns behind to seek greener pastures around the world, and Winnipeg is widely and rightly known as a fridged, windswept, pothole-

blighted, and mosquito infested backwater, but yet I feel no desire to leave. The warmth, love, friendship, and support I feel here is worth more to me than the rest of the world combined.

Table of Contents

Contribution of Authors

Chapter 2. Remnants of a 1.55 Ga Metasomatic Iron-Alkali-Calcic (MIAC) system in the Kiggavik Region, Nunavut, Canada

This chapter is an article published in Economic Geology with coauthors Mostafa Fayek, Julie Brown, and David Quirt. Samples analyzed were taken from the Mostafa Fayek's library of samples, which were gathered with the assistance of David Quirt and Orano Canada. I was responsible for sample preparation, gathering and interpretation of data, writing of the manuscript, and drafting/modification of all figures. All coauthors provided edits and revisions to help improve the manuscript.

Chapter 3. Glaciation-induced radionuclide release: implications for geological disposal of nuclear waste

This chapter is an article published in Geology with coauthors Mostafa Fayek and Julie Brown. Samples analyzed were taken from the Mostafa Fayek's library of samples. I was responsible for sample preparation, gathering and interpretation of data, writing of the manuscript, and drafting/modification of all figures. Mostafa Fayek and I interpreted the U-Th-Pb data together. All coauthors provided edits and revisions to help improve the manuscript.

Chapter 4. Extreme H isotope fractionation of phyllosilicates from the Kiggavik Uranium deposits

This chapter is an article published in the Journal of Geochemical Exploration with coauthors Mostafa Fayek, Julie Brown, and Alfredo Camacho. Samples analyzed were taken from the Mostafa Fayek's library of samples. I was responsible for sample preparation, gathering

and interpretation of data, writing of the manuscript, and drafting/modification of all figures. Alfredo Camacho and I gathered the Ar-Ar data together. All coauthors provided edits and revisions to help improve the manuscript.

Chapter 5. The Evolution of Porosity and its Impacts on Radionuclide Mobility in the Kiggavik Analogue

This chapter is currently in preparation for journal submission with coauthors Mostafa Fayek, Julie Brown, Larry Anovitz, and Jan Ilavsky. Samples analyzed were taken from the Mostafa Fayek's library of samples. I was responsible for sample preparation, gathering and interpretation of data, writing of the manuscript, and drafting/modification of all figures. Jan Ilavsky and I gathered the (U)SAXS data together. Jan Ilavsky and Larry Anovitz assisted me in interpreting the (U)SAXS data. All coauthors provided edits and revisions to help improve the manuscript.

List of Figures and Tables

Chapter 1: Introduction

Chapter 2: Remnants of a 1.55 Ga Metasomatic Iron-Alkali-Calcic (MIAC) system in the Kiggavik Region, Nunavut, Canada

Chapter 4: Extreme H isotope fractionation of phyllosilicates from the Kiggavik Uranium deposits

List of copyrighted material for which permission was obtained

Chapter 1: Introduction

Figure 1. From Brook (2011).

Figure 3. From Noronha (2016).

Figure 3. From Shabaga, et al. (2017).

Chapter 2: Remnants of a 1.55 Ga Metasomatic Iron-Alkali-Calcic (MIAC) system in the Kiggavik Region, Nunavut, Canada

Burron, I., Fayek, M., Brown, J., and Quirt, D., 2024, Remnants of a 1.55 Ga Hybrid Between Metasomatic Iron-Alkali-Calcic and Unconformity-Related Uranium Environments in the Kiggavik Region, Nunavut, Canada: Economic Geology, v. 119, p. 1861–1888.

Figure. 1. From Chi et al. (2016).

Chapter 3: Glaciation-induced radionuclide release: implications for geological disposal of nuclear waste

Burron, I., Fayek, M., and Brown, J., 2025, Glaciation-induced radionuclide release: implications for geological disposal of nuclear waste: Geology, https://doi-org.uml.idm.oclc.org/10.1130/G53021.1.

Figure. 3. Modified from Jouzel et al. (2007).

Chapter 4: Extreme H isotope fractionation of phyllosilicates from the Kiggavik Uranium deposits

Figure 1. From Chi et al. (2016).

Figure 2. Modified from Burron et al. (2024).

Chapter 5: The Evolution of Porosity and its Impacts on Radionuclide Mobility in the Kiggavik Analogue

Figure 1. Modified from Shabaga et al. (2017; 2020).

Figure 2. From Burron et al. (2025).

Chapter 1: Introduction

Geologic Disposal of Used Nuclear Fuel

Nuclear power is the second largest source of clean energy after hydroelectricity (World Nuclear Association, 2025) and a key asset in combating climate change. Nuclear energy produced 2602 TWh of zero-carbon electricity in 2023 (World Nuclear Association, 2025). Canada has a long history of nuclear energy production, both as the world's second largest uranium producer and as center for design and production of reactors (CNSC, 2020; Government of Canada, 2020). CANadian Deuterium-Uranium (CANDU) reactors use a heavy-water (D_2O) moderator to fission natural, unenriched uranium oxide fuel. Although this design is a major departure from the light-water designs used by most western nations it has proven extremely successful both domestically and internationally: approximately 10% of all reactors operating in the world today are derived from the original CANDU design. Canada is among the first nations to begin construction of the next generation of Small Modular Reactors (SMRs).

One issue that continues to restrict the widespread use of nuclear energy is the production of nuclear waste in the form of used nuclear fuel (UNF). Used nuclear fuel is extremely radioactive due to the accumulation of fission fragments and heavy actinides created by fission and neutron capture events occurring inside reactors. Most fission fragments have relatively short half-lives and therefore their radiotoxicity will decline to low levels within a few hundred years. Actinides are much longer-lived; their persistence means UNF will require 100's of Ka to return to levels of radiotoxicity similar to natural uranium (U) ores (Fig. 1; CNSC, 2020). For this reason UNF is generally considered to require management and isolation from the biosphere

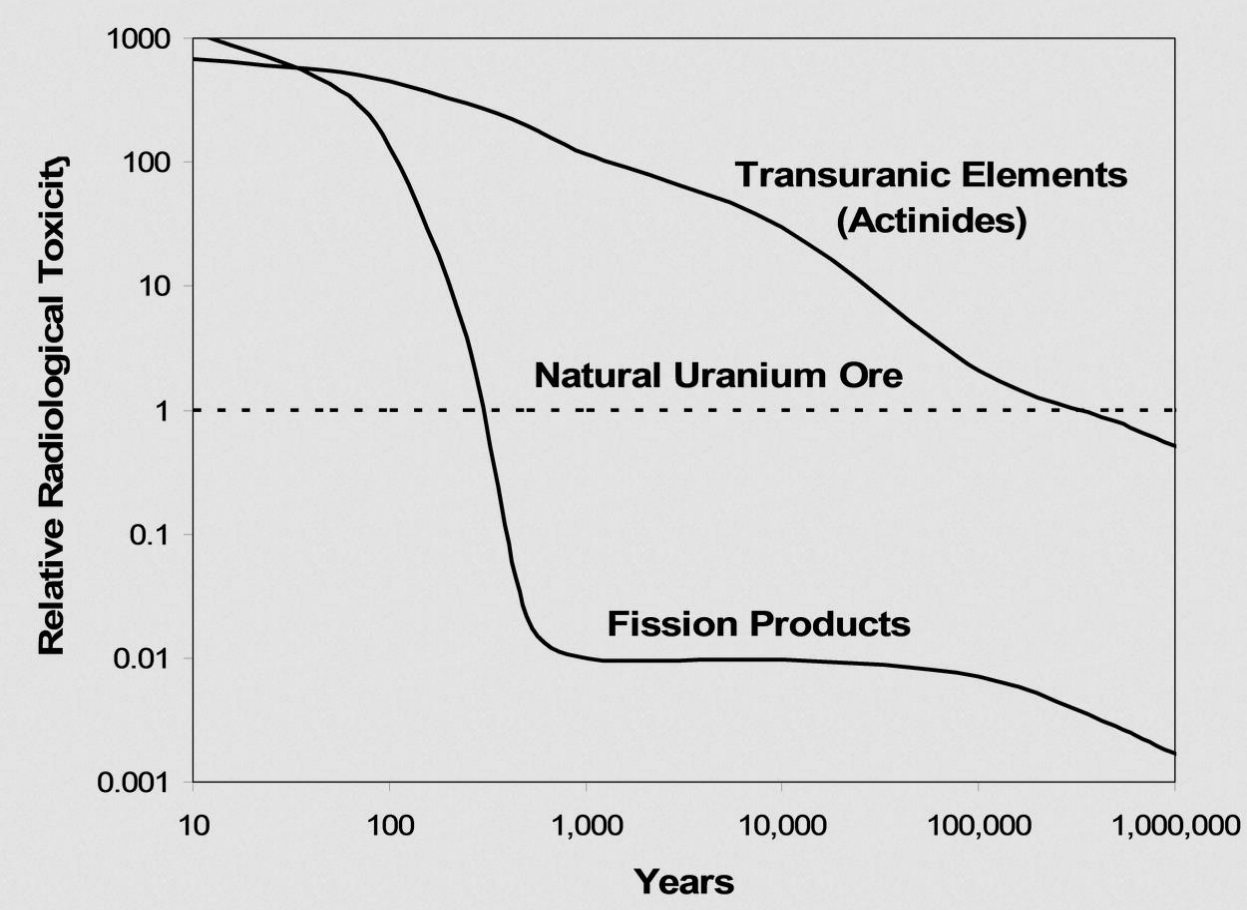

Figure 1. Diagram illustrating the evolution of UNF radiotoxicity over 1 Ma. From Brook, 2011.

for as long as one million years (IAEA, 1999; CNSC 2006; SKB, 2010; NWMO, 2021a). Ensuring the isolation of UNF over a time period that is more than three times the age of *Homo sapiens* and 200 times the age of the pyramids presents considerable technical and societal challenges.

Although all reactors produce UNF, CANDU reactors use unenriched fuel, which has a relatively low energy density, and therefore require higher volumes of fuel, and produce corresponding larger volumes of UNF, per unit of electricity produced than other designs. This is part of the reason Canada has accumulated one of the world's largest inventories of UNF, with a steadily growing stockpile of over 60 000 metric tons (CNSC, 2020). This UNF is currently stored in large steel or concreate casks for above-ground interim storage (CNSC, 2020). While these casks are designed to last well over 100 years, this is only ~0.01% of the total timeframe over which UNF must be managed, and a more permanent solution for UNF disposal is required (CNSC, 2020).

Many methods of permanent UNF disposal have been proposed over the decades, however most concepts, including disposal at sea, in ocean trenches, in outer space, in near-surface repositories, and reprocessing and 'burning' in specialized reactors, are not considered viable with modern technology due to environmental concerns, weapons proliferation risks, and/or economic considerations (Pusch, 2008; Noronha, 2016; CNSC, 2020). Canada, as well as most nations with nuclear waste inventories, considers disposal in a Deep Geological Repository (DGR) to be the most promising and viable method of UNF disposal (CNSC, 2006; 2020; IAEA 2020, NEA 2020; NWMO, 2021a). The DGR concept would entomb UNF within a system of tunnels constructed at depths of at least several hundred meters underground, with a series of engineered (reinforced canister, bentonite clay sealant and backfill) and natural (host rock)

barriers working together in a defense-in-depth system to provide long-term isolation of UNF from the biosphere (CNSC, 2020; IAEA 2020, NEA 2020; NWMO, 2021b; Fig. 2). This concept offers the advantages of very long-term stability, relatively manageable risks, economic feasibility with existing technology, and potential reversibility should the need arise (Noronha, 2016; CNSC, 2020; NWMO, 2021b).

In Canada, the construction, operation, and decommissioning of a DGR is the responsibility of the Nuclear Waste Management Organization (WNMO), an industry-funded non-profit organization (CNSC, 2020; NWMO, 2021a; b). The NWMO has selected a DGR site near the town of Ignace, Ontario, where UNF is to be entombed approximately 500 m below ground in a unit of tectonically stable, impermeable granitic host rock (NWMO, 2024). Plans call for UNF to be sealed inside copper-clad steel vessels, which would then be packed within a block of highly compacted bentonite, before being emplaced within specially constructed tunnels at which point any remaining space in the tunnel would be backfilled with more bentonite (Fig. 2; Noronha, 2016; NWMO, 2021b). After the end of its operational life and an extended monitoring period the DGR would be sealed, all surface facilities demolished, and the land returned to its natural state (Noronha, 2016; CNSC, 2020; NWMO, 2021b). Regulatory approval and construction of this DGR is expected to span several decades (CNSC, 2020; NWMO, 2021b), with operations anticipated to begin sometime between 2040-2045 (NWMO, 2021b).

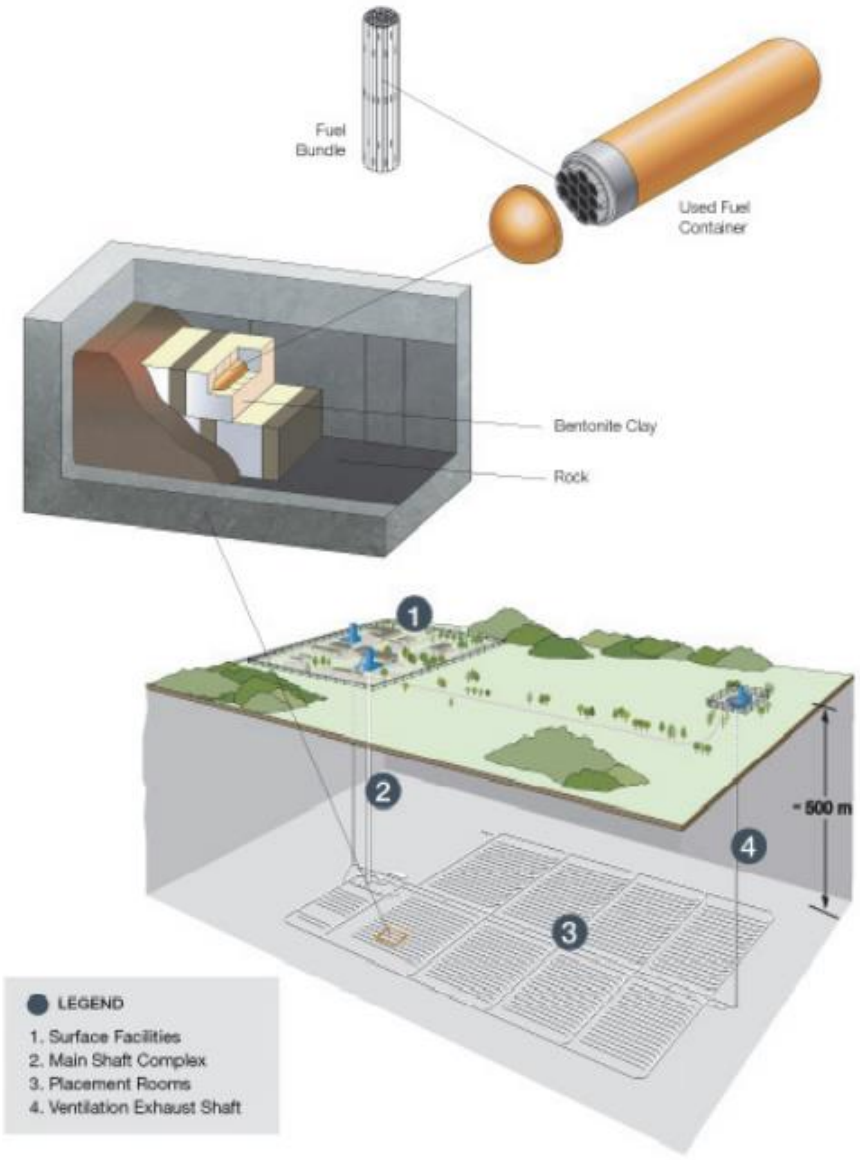

Figure 2. Diagram of a generalized Canadian DGR design employing multiple layers of protection to isolate UNF from the environment. From Noronha, 2016.

Natural Analogues

While DGR's are widely considered to offer a safe and effective solution for the disposal of UNF (CNSC, 2006; 2020; IAEA 2020; NEA 2020: NWMO, 2021a), investigating DGR performance over ~1 Ma timespans poses significant challenges. The results of laboratory experiments lasting at most a few years must be extrapolated over six or more orders of magnitude (Janeczek, *et al*., 1996; Fayek and Brown, 2021). These experiments indicate the rate of U redeposition exceeds the rate of U transport in the subsurface, limiting U mobility over relatively short timescales (Wronkiewicz and Buck, 1999), but they cannot guarantee this will hold true over geologic timescales (Murphy, 1992; Ildefonse, *et al*., 1990; Murphy, 2000). In principal mathematical modelling and computer simulations can readily probe these timescales; in practice, however, they are only as reliable as the available data on which they are based and often rely on simplifying assumptions which may not be applicable to real world systems (IAEA, 1999; CNSC, 2006; Martin et al., 2023).

The study of geologic materials, which have been subject to subsurface processes over periods of Ka to many Ma, provides a more direct and robust method of gathering real-world data (IAEA, 1999; CNSC, 2006; Fayek and Brown, 2021). Geologic studies also play a vital role in the site selection process, as host rock properties such as mechanical strength, thermal conductivity, permeability, pH, and redox state control overall repository conditions and very long-term performance (IAEA, 1999; CNSC, 2006). Furthermore, geologic studies are invaluable for illustrating the DGR concept and demonstrating safety and effectiveness to the general public in a direct, common sense, and non-technical manner (IAEA, 1999; Fayek and Brown, 2021). Community engagement and public acceptance are core principles of Canada's DGR program, without which construction and operations cannot proceed (CNSC, 2020;

NWMO, 2021a; b). Indeed, gaining the necessary public trust and acceptance has often proven to be a greater challenge than gaining the required scientific knowledge (Diaz-Maurin and Ewing, 2018).

While a variety of geologic materials such as native copper, volcanic glasses, bitumen, and natural cements can act as natural analogues for repository materials (Fayek and Brown, 2021) the study of natural U deposits is particularly informative. The most common U ore mineral, uraninite (UO_{2-x}), is chemically similar to the UO_2 that makes up the bulk of UNF, (Janeczek, *et al*., 1996*,* Ewing, 1999; Fayek and Brown, 2021). Uranium ore bodies at Oklo, Gabon, sustained fission chain reactions 1.95 billion years ago, functioning as natural nuclear reactors that produced natural UNF (Gauthier-Lafaye, et al., 1986; Nagy et al., 1991; Janeczek and Ewing, 1995; Evins et al., 2005). The study of how and why uraninite is corroded, transported, and redeposited in the subsurface over geologic timescales may therefore yield valuable insight into the fate of UNF in a DGR over repository timescales and beyond (IAEA, 1999; CNSC, 2006; Fayek and Brown, 2021).

Studies of uranium deposit analogues such as Oklo (Gauthier-Lafaye, et al., 1986; Nagy et al., 1991; Janeczek and Ewing, 1995; Evins et al., 2005) and Cigar Lake, Canada (Cramer, J. and Smellie, 1994; Smellie, J. and Karllson, 1996; Fayek and Brown, 2021), indicate that U oxides are likely to remain stable underground for greater than one billion years (Gauthier-Lafaye, et al., 1986; Nagy et al., 1991; Cramer, J. and Smellie, 1994; Janeczek and Ewing, 1995; Smellie, J. and Karllson, 1996; Evins et al., 2005; Fayek and Brown, 2021), and have informed the DGR concept.

Most natural analogue studies have focused on locations where U remained isolated and contained for geologically long timeframes. As such they provide useful analogues for studying

overall DGR performance in an ideal setting, but do not address certain knowledge gaps. Analogue studies have generally not investigated conditions under which radionuclide migration and remobilization could occur and may not encapsulate worst-case scenarios. Many analogue studies such as Oklo have also been conducted in warm climates and as such may not reflect the process which will impact a Canadian DGR. Glaciation is of particular concern for Canadian DGR plans, as the ~1 Ma repository timeframe is long enough for multiple glacial cycles to elapse, covering virtually the entire landmass of Canada in icesheets >1 km thick (Cummings, 2020).

Thesis Objectives

The overall objective of this thesis is to develop the Kiggavik U deposits in central Nunavut, Canada (Fig. 3) as a natural analogue for a DGR. This location is well suited for informing Canadian DGR development for a number of reasons: 1) the host rocks comprise both metasedimentary and granitic rocks (Pehrsson et al., 2013; Jefferson et al., 2015; Scott et al., 2015; Johnstone et al., 2017) which are generally similar to proposed Canadian DGR host rocks 2) the northerly location has been subject to intense, prolonged, and dynamic glaciation over the last ~2.6 Ma (McMartin et al., 2020) 3) previous studies indicate a long, complex, and possibly ongoing history of U mobility in the area (Sharpe et al., 2015; Shabaga et al., 2017; Ashcroft, 2020; Grare et al., 2020). Specific research questions include: 1) what processes have contributed to U mobility or lack thereof? 2) Over what timeframes and distances does U mobility occur? 3) How has the nature (i.e. lithology, porosity) of host rocks affected U mobility?

The Kiggavik region contains a series of U deposits and prospects, with the Kiggavik, Bong, End, and Andrew Lake deposits containing the bulk of the region's known mineralization (Sharpe et al., 2015; Shabaga et al., 2017; Grare et al., 2020; Ashcroft, 2020) and being the

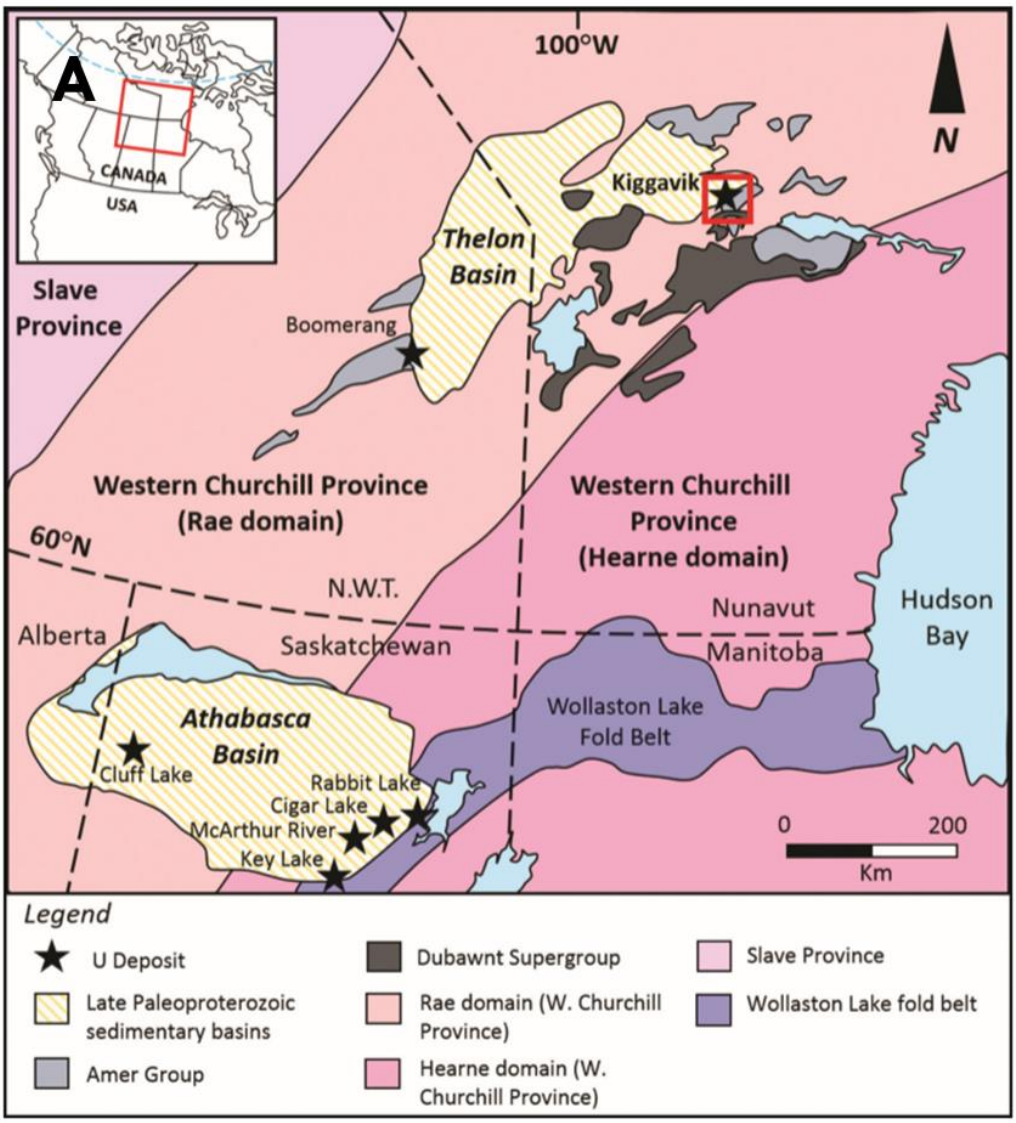
A
CANADA
USA
100°W
N
Kiggavik
Thelon Basin
Slave Province
Boomerang
Western Churchill Province (Rae domain)
Western Churchill Province (Hearne domain)
60°N
N.W.T.
Nunavut
Hudson Bay
Alberta
Saskatchewan
Manitoba
Athabasca Basin
Wollaston Lake Fold Belt
Cluff Lake
Rabbit Lake
Cigar Lake
McArthur River
Key Lake
0
200
Km
Legend
U Deposit
Late Paleoproterozoic sedimentary basins
Amer Group
Dubawnt Supergroup
Rae domain (W. Churchill Province)
Hearne domain (W. Churchill Province)
Slave Province
Wollaston Lake fold belt

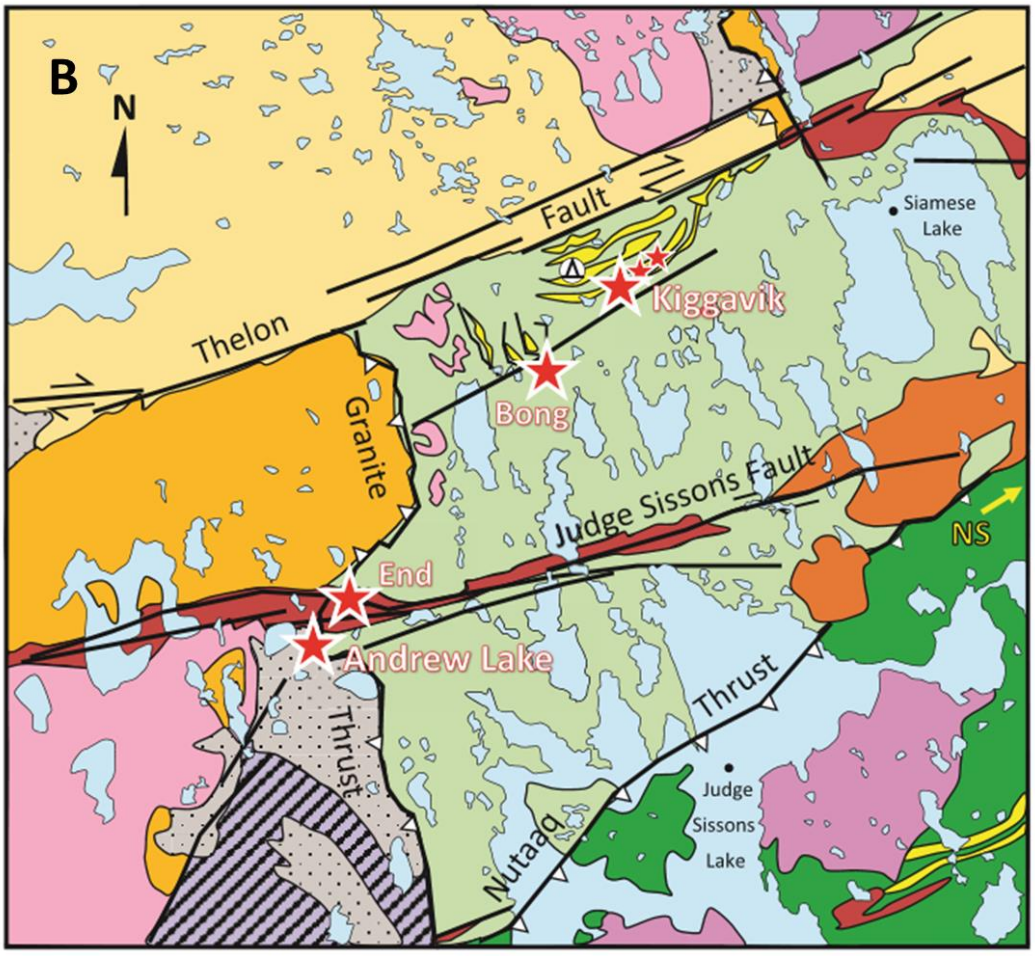

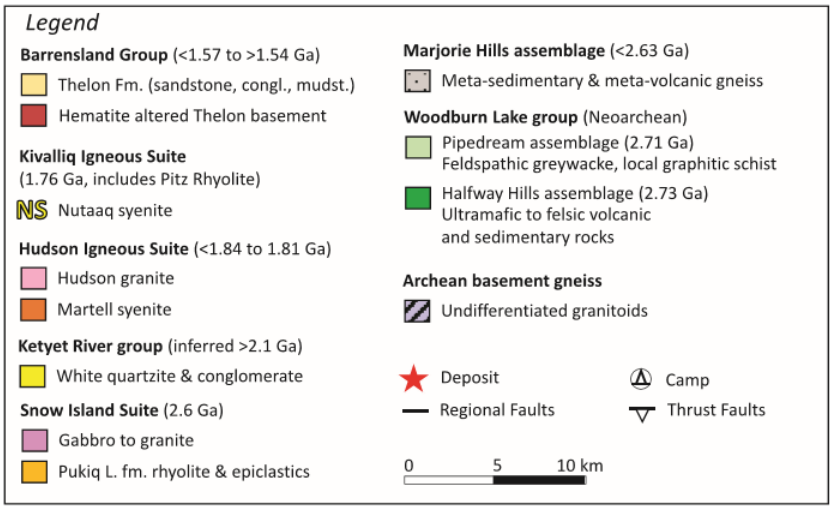

Figure 3. A) Location of the Kiggavik region within Canada, B) Simplified geologic map of the Kiggavik uranium deposits. From Shabaga, *et al*. (2017).

subject of this study. Mineralization is dominantly hosted in Archean metasedimentary rocks, with subordinate mineralization in Proterozoic granitic rocks (Scott et al., 2015; Johnstone et al., 2017; Grare et al., 2020). Uranium deposits are hosted from surface to ~500 m depth along a series of major faults which are the site of brittle deformation and intense hydrothermal alteration consisting of mainly of illitization, chloritization, and hematization of the host rocks (Grare et al., 2020). The main U mineral is uraninite/pitchblende with lesser coffinite (Sharpe et al., 2015; Shabaga et al., 2017; Ashcroft, 2020). These U deposits are often considered to be unconformity-style deposits similar to the deposits in the Athabasca Basin, however the fluid history of these deposits is complex, with many generations of U mobility spanning > 1 Ga (Sharpe et al., 2015; Shabaga et al., 2017; Grare et al., 2020). Most studies of the area have focused on U mineralization within metasedimentary rocks, leaving the granitic host rocks understudied.

Understanding patterns of U mobility requires a detailed understanding of the starting point of U, i.e. the distribution and mineralogy of primary U mineralization as well as how this has been modified by subsequent geological processes. The mineralogy, genesis, and geologically ancient (> 1 Ma) history of U in the Kiggavik deposits is investigated in Chapter 2 of this thesis. This was accomplished by optical and scanning electron microscopy, electron probe micro-analysis, and U-Pb geochronology conducted via Secondary Ion Mass Spectroscopy (SIMS). In addition to insights into the genesis and history of these deposits, this study provides the first comprehensive description of U mineralization within Kiggavik granitic host rocks.

Understanding how radionuclides become mobilized in the subsurface, and the spatial and temporal scales over which mobility occurs, is crucial to understanding potential hazards to the integrity of a DGR. The most likely processes by which radionuclides may escape a DGR and reach the surface are through dissolution and transport by subsurface fluids (IAEA, 1999).

Uranium in the Kiggavik deposits is locally concentrated along interfaces between oxidized and reduced host rocks, which has been interpreted as evidence of U mobilization by redox processes occurring at 982 ± 19 Ma (Sharpe et al., 2015), 750 ± 74 Ma (Ashcroft, 2020), and ~550 and ~345 Ma (Grare et al., 2020) or via acid-base processes within the last ~1 Ma (Shabaga et al., 2017). Determining the timing and nature of this U mobility has proven challenging due to the complexity of the deposit's history and the fact that while conventional U-Pb Concordia geochronology techniques are effective at dating U minerals which are ~>1 Ma (see Chapter two), they cannot determine the age of geologically young minerals as insufficient time has elapsed for radiogenic Pb to accumulate.

Chapter three investigates the timing of geologically recent U mobility via U-Th-Pb geochronology, which is capable of dating much younger U minerals by measuring disturbance to the U decay chain. While the decay of U to Pb via a series of intermediate isotopes allows U minerals to be dated, the isotopic composition of clay minerals contains information about the source of geologic fluids (Suzuoki and Epstein, 1976; Capuano, 1992; Sheppard and Gilg, 1996; Fayek and Kyser, 1999; Chacko et al., 2001; Sharp, 2017). The nature of the fluids involved in U mobility was investigated by measuring the stable oxygen (O) and hydrogen (H) composition of clay minerals affected by these fluids. U-Th-Pb geochronology and stable isotope measurements were conducted via SIMS.

The second chapter of this thesis investigates the history of Kiggavik U minerals via mineralogy and U-Pb Concordia geochronology; Chapter four builds off this work by studying the nature and origin of the clay minerals associated with these U minerals. This was accomplished through the use of SIMS stable O and H isotope analysis and in-situ Ar-Ar geochronology. This study places temporal and genetic constraints on the complex overall

mineralization paragenesis described in Chapter Two. This chapter also describes the heaviest H isotope composition ever observed in a natural terrestrial mineral and suggests a novel mechanism of extreme H isotope fractionation. This mechanism is significant to nuclear waste disposal as radiolysis could produce significant amounts of H_2 gas (Smellie and Karlsson, 1996), and exchange with H_2 may also significantly fractionate H isotopes (Galley et al., 1972). Establishing an alternate, non-radiogenic mechanism ensures such a process is not mistaken for evidence of leakage of radiogenic H_2.

As discussed in Chapter three, the infiltration of fluids into the subsurface is a potential threat to DGR integrity (IAEA, 1999) and has affected U in the Kiggavik deposits (Sharpe et al., 2015; Shabaga et al., 2017; Grare et al., 2020). While faults and fractures provide the main conduits for fluid migration in the subsurface, the porosity of rock formations is a major control on how fluids interact with the bulk rock matrix, which in turn influences the transport of radionuclides in the subsurface (IAEA, 1999; Boers, 2017). The infiltration of fluids can also modify the primary porosity and permeability of a DGR host rock by creating and/or infilling pores and vugs and sealing fractures through mineral dissolution/precipitation (Steefel and Lichtner, 1998; Sonnenthal and Spycher, 2001; Simmons and Stuckless, 2010; Martin et al., 2016; Fayek and Brown, 2021; Martin et al., 2023). Despite the potential significance of these processes on host rock properties, the effects of specific geologic fluids on specific host rocks have received only limited study (i.e. Sandström et al., 2010; Martin et al., 2016).

Chapter five of this thesis investigates the porosity of Kiggavik host rocks which have been affected by various generations of fluid alteration described in the first three studies (chapters 2-4). Porosity measurements were conducted via (Ultra) Small Angle X-ray Scattering, a powerful technique which allows total porosity, pore size distribution, and specific surface area

of pores to be evaluated. These measurements are cross referenced with the mineralogy and mineral textures observed via optical and electron microscopy to elucidate the effects of the various geological fluids identified in chapters 2-4 on host rock porosity, and how this has shaped patterns of radionuclide mobility in the Kiggavik deposits.

Associated Abstracts and Publications

During the course of this research, I published chapters 2 and 3, as well as presenting preliminary findings of chapters 2-5 at a number of conferences. These publications are listed below.

Journal publications:

Burron, I., Fayek, M., Brown, J., and Quirt, D., 2024, Remnants of a 1.55 Ga Hybrid Between Metasomatic Iron-Alkali-Calcic and Unconformity-Related Uranium Environments in the Kiggavik Region, Nunavut, Canada: Economic Geology, v. 119, p. 1861–1888.

Burron, I., Fayek, M., and Brown, J., 2025, Glaciation-induced radionuclide release: implications for geological disposal of nuclear waste: Geology, https://doi-org.uml.idm.oclc.org/10.1130/G53021.1.

Conference Abstracts:

Burron, I., Fayek, M., Brown, J., and Quirt, D., 2022, Evidence for an IOAA-U system in the Kiggavik Region, Nunavut, Canada (Accepted presentation); GAC-MAC Conference, May 15-18, 2022, Halifax, NB, Canada.

Burron, I, Fayek, M., and Brown, J., 2022, Recent Uranium Mobility in the Kiggavik Region, Nunavut, Canada: Implications for the Effects of Glaciation on a DGR (Accepted poster); Goldschmidt Conference, July 10-15, Honolulu, Hawaii, USA.

Burron, I, Fayek, M., and Brown, J., 2025, Glaciation-induced radionuclide mobility from the Kiggavik uranium deposits: natural analogues for geological disposal of nuclear waste (Accepted

presentation); European Geological Society Annual General Meeting, April 28 – May 2, 2025, Vienna, Austria.

Burron, I., Fayek, M., Brown, J., and Quirt, D., 2023, Evidence for an MIAC-U system in the Kiggavik Region, Nunavut, Canada (Accepted presentation); Central Canada Mineral Exploration Convention, November 4-5, 2023, Winnipeg, MB, Canada.

References

Ashcroft, G., 2020, The geochemistry and geochronology of the End Deposit, NE Thelon region, Nunavut, Canada: Insight into the Athabasca Basin's closest relative. MSc thesis, University of Manitoba, 217 pages.

Boers, C., 2017, Investigation of pore evolution in concrete by spin-echo small angle neutron scattering. B.Sc Thesis, Delft University of Technology, NL.

Brook, B., 2011, Critique of MIT future of nuclear fuel cycle study. Retrieved from: https://bravenewclimate.com/2011/05/31/critique-mit-fnfc-2011/.

Capuano, R.M., 1992, The temperature dependence of hydrogen isotope fractionation between clay minerals and water: evidence from a geopressured system. Geochimica et Cosmochimica Acta, **56**, 2547–2554.

Chacko, T., Cole, D. R., and Horita, J., 2001, Equilibrium Oxygen, Hydrogen and Carbon Isotope Fractionation Factors Applicable to Geologic Systems. Reviews in Mineralogy and Geochemistry; **43**, 1–81.

CNSC (Canadian Nuclear Safety Commission), 2006, Assessing the long-term safety of radioactive waste management/Regulatory Guide G–320.

CNSC, 2020, Radioactive waste. Retrieved From: https://www.cnscccsn.gc.ca/eng/waste/index.cfm.

Cramer, J. and Smellie, J., 1994, Final report of the AECL/SKB Cigar Lake Analog Study. SKB Technical Report 94-04.

Cummings, D. I., 2020, The bedrock surface in Canada: Glacial erosion rates, patterns and processes, past and future. CNSC report; 39 pages.

Diaz-Maurin, F., and Ewing, R. C., 2018, Mission Impossible? Socio-Technical Integration of Nuclear Waste Geological Disposal Systems. Sustainability; **10**, 4390, doi:10.3390/su10124390.

Evins, L. A., Jensen, K. A., and Ewing, R. C., 2005, Uraninite recrystallization and Pb loss in the Oklo and Bangombé natural fission reactors, Gabon. Geochimica et Cosmochimica Acta; **69**, 6, 1589 –1606.

Ewing, R.C., 1999, Less geology in the geological disposal of nuclear waste. Science; **286**, 415–416.

Fayek, M., and Kyser, K., 1999, Stable Isotope Geochemistry of Uranium Deposits, In Burns, P. C. and Finch, R. (eds) Uranium: Mineralogy, Geochemistry, and the Environment, Reviews in Mineralogy, De Gruyter, **38**, 181–220.

Fayek, M., and Brown, J., 2021, Natural and anthropogenic analogues for high-level nuclear waste disposal repositories: A review. The Canadian Mineralogist, **59**, 287–317.

Galley, M. R., Miller, A. I., Atherly, J. F., and Mohn, M., 1972, GS Physical Process- Physical properties, Chalk River, Ontario, Canada, Atomic Energy of Canada Limited, AECL-4255.

Gauthier-Lafaye F., Weber F., and Ohmoto H., 1989, Natural fission reactors of Oklo. Economic Geology; **84**, 2286 –2295.

Government of Canada, 2020, Energy and the Economy: Retrieved from: https://www.nrcan.gc.ca/science-data/data-analysis/energy-data-analysis/energy-facts/energy-and-economy/20062.

Grare, A., Benedicto, A., Mercadier, J., Lacombe, O., Trave, A., Guilcher, M., Richard, A., Ledru, P., Blain, M., Robbins, J., and Lach, P., 2020, Structural controls and metallogenic model of polyphase uranium mineralization in the Kiggavik area (Nunavut, Canada). Mineralium Deposita; https://doi.org/10.1007/s00126-020-00957-x.

IAEA, 2020, Design Principals and Approaches for Radioactive Waste Repositories: IAEA Nuclear Energy Series No. NW-T-1.27, 89 pages.

International Atomic Energy Agency (IAEA), 1999, Use of natural analogues to support radionuclide transport models for deep geological repositories for long lived radioactive wastes. IAEA-TECDOC-1109, 45 pages.

Ildefonse, P., Agrinier, P., Muller, J. P., 1990, Crystal-chemistry and isotope geochemistry of alteration associated with the U Nopal I deposit, Chihuahua, Mexico. Chem Geol; **84**, 371–372.

Janeczek, J. and Ewing, R. C., 1995, Mechanisms of lead release from uraninite in the natural fission reactors in Gabon. Geochimica et Cosmochimica Acta; **59**, 10, 1917–1931.

Janeczek, J., Ewing, R.C., Oversby, V.M., Werme, L.O., 1996, Uraninite and UO2 in spent nuclear fuel: a comparison. J. Nucl. Mater; **238**, 121–130.

Jefferson, C.W., Pehrsson, S., Peterson, T., Tschirhart, V., Anand, A., Wollenberg, P., LeCheminant, A.N., Riegler, T., McEwan, B., Bethune, K., Chorlton, L.B., Tschirhart, P., Scott, J.M.J., Davis, W., McNicholl, V., Riemer, W., White, J.C., Patterson, J., Morris, W.A., Keating, P., and Stieber, C., 2015, Bedrock geology of the western Marjorie-Tehek supracrustal belt and Aberdeen Sub-basin margin in parts of NTS 66A and 66B, Nunavut – context of the Kiggavik uranium camp: *Geological Survey of Canada*, Open File #7241.

Johnstone, D., Nethune, K., Quirt, D., Benedicto, A., Ledru, P., 2017, Lithostructural controls of U mineralization in the Kiggavik Main and Centre zones, north-central Rae craton: A record of long-lived tectonism and ground preparation for U ore systems. In: *Abstracts volume, GAC– MAC joint annual meeting*, Kingston 2017, May 2017, p 190.

Martin, L. H. J., Leemann, A., Milodowski, A. E., Mäder, U. K., Münch, B., Giroud, N., 2016, A natural cement analogue study to understand the long-term behaviour of cements in nuclear waste repositories: Maqarin (Jordan). Applied Geochemistry; **17**, 20-34.

Martin, L., Kosakowski, G., Papafotiou, A., and Smith, P. A., 2023, Evolution of the Sealing System Porosity and its Impact on Performance. nagra working report NAB 23-21, 127 pages.

McMartin, I., Godbout, P.-M., Campbell, J. E., Tremblay, T. and Behnia, P., 2020, A new map of glaciogenic features and glacial landsystems in central mainland Nunavut, Canada. Boreas; https://doi.org/10.1111/bor.12479. ISSN 0300- 9483.

Murphy, W. M., 1992, Source–term constraints for the proposed repository at Yucca Mountain, Nevada, derived from the natural analog at Peña Blanca, Mexico. Mat Res Symp Proc; **257**, 521–527.

Murphy, W. M., 2000, Natural analogues and performance assessment for geologic disposal of nuclear waste. Mat Res Symp Proc; **608**, 533–544.

Nagy, B., Gauthier-Lafayet, F., Holliger, P., Davis, D. W., Mossmanll, D. J., Leventhal, J.S., Rigali, M. J., and Parnel, J., 1991, Organic matter and containment of uranium and fissiogenic isotopes at the Oklo natural reactors. Nature; **354.**

Nuclear Energy Agency (NEA), 2020, Two decades of Safety Case Development: An IGSC 20th Anniversary Brochure, 52 pages.

Noronha, J., 2016, Deep Geological Repository Conceptual Design Report Crystalline / Sedimentary Rock Environment. Nuclear Waste Management Organization; APM-REP-00440-0015 R001, 191 pages.

NWMO (Nuclear Waste Management Organization), 2021a, Canada's Plan. Retrieved from: https://www.nwmo.ca/en/Canadas-Plan/What-Other-Countries-Are-Doing/Monitoring-Alternate-Fuel-Cycles.

NWMO, 2021b, Implementing Adaptive Phased Management 2021 to 2025; 51 pages.

NWMO, 2024, The Nuclear Waste Management Organization selects site for Canada's deep geological repository. NWMO press release; Retrieved from: https://www.nwmo.ca/News/The-Nuclear-Waste-Management-Organization-selects-site-for-Canadas-deep-geological-repository.

Pehrsson, S.J., Berman, R., Davis, W.J., 2013, Paleoproterozoic orogenesis during Nuna aggregation: A case study of reworking of the Rae craton, Woodburn Lake, Nunavut. Precamb Res; **232**, 167-188.

Pusch, R., 2008, Geological Storage of Highly Radioactive Waste. Springer-Verlag, Berlin, 9-11.

Sandström, B., Annersten, H., and Tullborg, E.-L., 2010, Fracture-related hydrothermal alteration of metagranitic rock and associated changes in mineralogy, geochemistry and degree of oxidation: a case study at Forsmark, central Sweden. Int J Earth Sci (Geol Rundsch); **99**, 1–25, DOI 10.1007/s00531-008-0369-1.

Scott, J.M.J., Peterson, T.D., Davis, W.J., Jefferson, C.W., Cousens, B.L., 2015, Petrology and geochronology of Paleoproterozoic intrusive rocks, Kiggavik uranium camp, Nunavut. Can J Earth Sci; **52**, 495–518.

Simmons, A.M., and Stuckless, J.S., 2010, Analogues to features and processes of a high-level radioactive waste repository proposed for Yucca Mountain, Nevada. U.S. Geological Survey Professional Paper 1779, 195 p.

Shabaga, B., Fayek, M., Quirt, D., Jefferson, C., and Camacho, A., 2017, Mineralogy, geochronology, and ghttps://ourworldindata.org/safest-sources-of-energyenesis of the Andrew Lake uranium deposit, Thelon Basin, Nunavut, Canada. Can. J. Earth Sci; **54**, 850–868.

Sharp, Z. D., 2017, Principles of Stable Isotope Geochemistry, 2nd edition. doi: https://doi.org/10.25844/h9q1-0p82.

Sharpe, R., Fayek, M., Quirt, D., and Jefferson, C., 2015, Geochronology and Genesis of the Bong Uranium Deposit, Thelon Basin, Nunavut, Canada. Economic Geology; **110**, 1759–1777.

Sheppard, S. M. F., and Gilg, H. A., 1996, Stable isotope geochemistry of clay minerals. Clay Minerals; **31**, 1–24.

SKB, 2010, Spent nuclear fuel for disposal in the KBS-3 repository. Technical Report TR-10-13.

Smellie, J. and Karllson, F., 1996, A reappraisal of some Cigar Lake issues of importance to performance assessment. SKB Technical Report 96-08.

Sonnenthal, E.L., and Spycher, N., 2001, Drift-scale coupled processes (DST and THC seepage) models: Las Vegas, Nevada, Bechtel SAIC Company, Report MDL-NBS-HS-000001 REV01, variously paginated.

Steefel, C.I. and Lichtner, P. C., 1998, Multicomponent reactive transport in discrete fractures II: Infiltration of hyperalkaline groundwater at Maqarin, Jordan, a natural analogue site. Journal of Hydrology; **209**, 200–224.

Suzuoki, T., and Epstein, S., 1976, Hydrogen isotope fractionation between OH-bearing minerals and water. Geochimica et Comochim Acta; **40**, 1229–1240.

World Nuclear Association, 2025, https://world-nuclear.org/information-library/current-and-future-generation/nuclear-power-in-the-world-today#key-statistics

Wronkiewicz, D.J. and Buck, E.C., 1999, Uranium mineralogy and the geologic disposal of spent nuclear fuel. In: Uranium: Mineralogy, Geochemistry, and the Environment, (Burns, P.C. and Finch, R., Eds.). Min Soc Proc*;* **38**, 475-497.

Chapter 2: Remnants of a 1.55 Ga Metasomatic Iron-Alkali-Calcic (MIAC) system in the Kiggavik Region, Nunavut, Canada

Ian Burron[1], Mostafa Fayek[1], Julie Brown[2], and David Quirt[3]

1: Department of Earth Sciences, University of Manitoba, Winnipeg, MB R3T 2N2, Canada

2: Canadian Nuclear Safety Commission, 280 Slater Street, Ottawa, Ontario K1P 5S9, Canada

3: Orano Canada, 817 45th Street W., Saskatoon, SK S7K 3X5, Canada

Corresponding author: Ian Burron ianmburron@gmail.com

Abstract

A series of U deposits in the Thelon region, Nunavut, including the Kiggavik, Bong, End, and Andrew Lake deposits host uranium mineralization preceded by albitization, brecciation, silicification, and hematization of the host rocks. Uranium mineralization comprises three stages, with the first stage having three substages: (1) front-style (U1a; 1594 ± 95 Ma), (2) euhedral disseminated (U1b; 1553 ± 16 Ma), and (3) polymetallic and monometallic vein-hosted (U1c; 1553 ± 16 Ma). The uraninite, coffinite, and local brannerite mineralization is associated with bleaching (dehematization), which overprints earlier styles of alteration.

Some U1 minerals, as well as U2 minerals (fractured and texturally-altered U-minerals), record multiple isotopic resetting/U remobilization events at 1440 ± 21, 1417 ± 17 Ma, 1276.4 ± 8.7 Ma, 1249 ± 33 Ma, 937 ± 24 Ma, and 274 ± 69 Ma. Paragenetically late uranium minerals associated with orange goethite-bearing alteration (U3) have very low lead contents, indicating recent (<1 Ma) formation or isotopic resetting.

Albitization is associated with corrosion of zircon, transport of HFSE, and precipitation of hydrothermal zircon and uranothorite in equilibrium with fluorite, suggesting the presence of a F-rich fluid during albitization.

Although the geochronology, structural controls, and some aspects of the alteration and mineralization mineralogy are generally consistent with those of basement-hosted unconformity-related uranium deposits, they are also largely consistent with a Metasomatic Iron-Alkali-Calcic-Uranium (MIAC-U)-style metallogenetic model. The presence of early albitization, evidence for a F-rich fluid chemistry, polymetallic nature of U mineralization, presence of hydrothermal zircon, and brannerite, absence of dravitic tourmaline and fault graphite, and spatial and temporal

links to magmatic-hydrothermal processes, fit the MIAC model. This raises the prospect of a previously unrecognized MIAC district in central Nunavut.

Introduction

The Kiggavik area of the Northeast Thelon Basin region contains U deposits and prospects including the Kiggavik, Bong, End, and Andrew Lake deposits. These U deposits are hosted by Archean basement lithologies and are located between 2 and 25 km south of the margin of the Mesoproterozoic Thelon Basin. The Thelon Basin shares many geological similarities with the economically important Athabasca Basin in northern Saskatchewan (Orrell et al., 1999; Ramaekers, 2004; Rainbird and Davis, 2007), and the Kiggavik deposits have often been interpreted as basement-hosted unconformity-related U (URU) deposits, similar to those in the Athabasca (Fuchs et al., 1986; Weyer et al., 1987; Riegler et al., 2014; 2016; Chi et al., 2016; Grare et al., 2020; Ashcroft, 2020).

A definitive link to unconformity-related processes, however, has proved difficult to establish, primarily due to the lack of a preserved unconformity and overlying strata in the Kiggavik region. Recent studies indicate the Kiggavik deposits have had a complex and protracted fluid history, with multiple generations of clay alteration and U deposition and remobilization (Riegler, 2014; 2016; Sharpe et al., 2015; Chi et al., 2016; Shabaga et al., 2017; Ashcroft, 2020; Grare et al., 2018; 2020; Shabaga et al., 2020). The timing of the original mineralization period is not well constrained. The oldest reported age for U minerals is 1520 ± 79 Ma from uraninite in the Bong deposit (Sharpe et al., 2015), however the overall range of U-Pb, Pb-Pb, and Ar-Ar ages obtained is very large; ~1850 Ma to <1 Ma (Table A1). While most publications have been generally supportive of an URU model, some have described mineralogical, isotopic, and structural data that is not consistent with the URU models (Flotté, 2009; Sharpe et al., 2015; Chi et al., 2016; Grare et al., 2020). Despite these observations, an

alternative model has not been developed and the URU model has continued to dominate interpretations of U mineralization in the area.

In this paper, we are proposing a new metallogenetic model for Kiggavik, Bong, End, and Andrew Lake U deposits that is inclusive of all their features. This model is based on a reassessment of the mechanisms of host rock alteration and U deposition and remobilization stemming from detailed sample characterization, new petrographic observations, and U-Pb geochronology of the various generations of U minerals identified.

Geological Setting

Regional Geology

The Thelon Basin is a large (>10000 km^2), Paleoproterozoic to Mesoproterozoic intracratonic basin located in the Rae Domain of the Churchill Province in the northwestern Canadian Shield (Fig. 1). The Archean-Paleoproterozoic Rae Domain, dominated by Meso- to Neoarchean orthogneisses and 2.9-2.68 Ga volcano-sedimentary rocks of the Mary River, Prince Albert and Woodburn Lake group (Pehrsson et al., 2013), is bordered to the west by the ~1.9 Ga Taltson-Thelon tectonomagmatic zone, which was formed by the ~2.0-1.9 Ga collision of the western Churchill and Slave provinces (Hoffman, 1988; Rainbird et al., 2003). The Rae Domain is separated from the Hearne Domain to the East by the Snowbird Tectonic Zone (Hoffman, 1988; Regan et al., 2022). The ~1.8 Ga Trans-Hudson Orogen forms the eastern margin of the Churchill Province and the Hearne Domain, separating them from the Superior Province (Rainbird et al., 2003). The ~1850-1700 Ma timing and intracratonic setting of the formation of

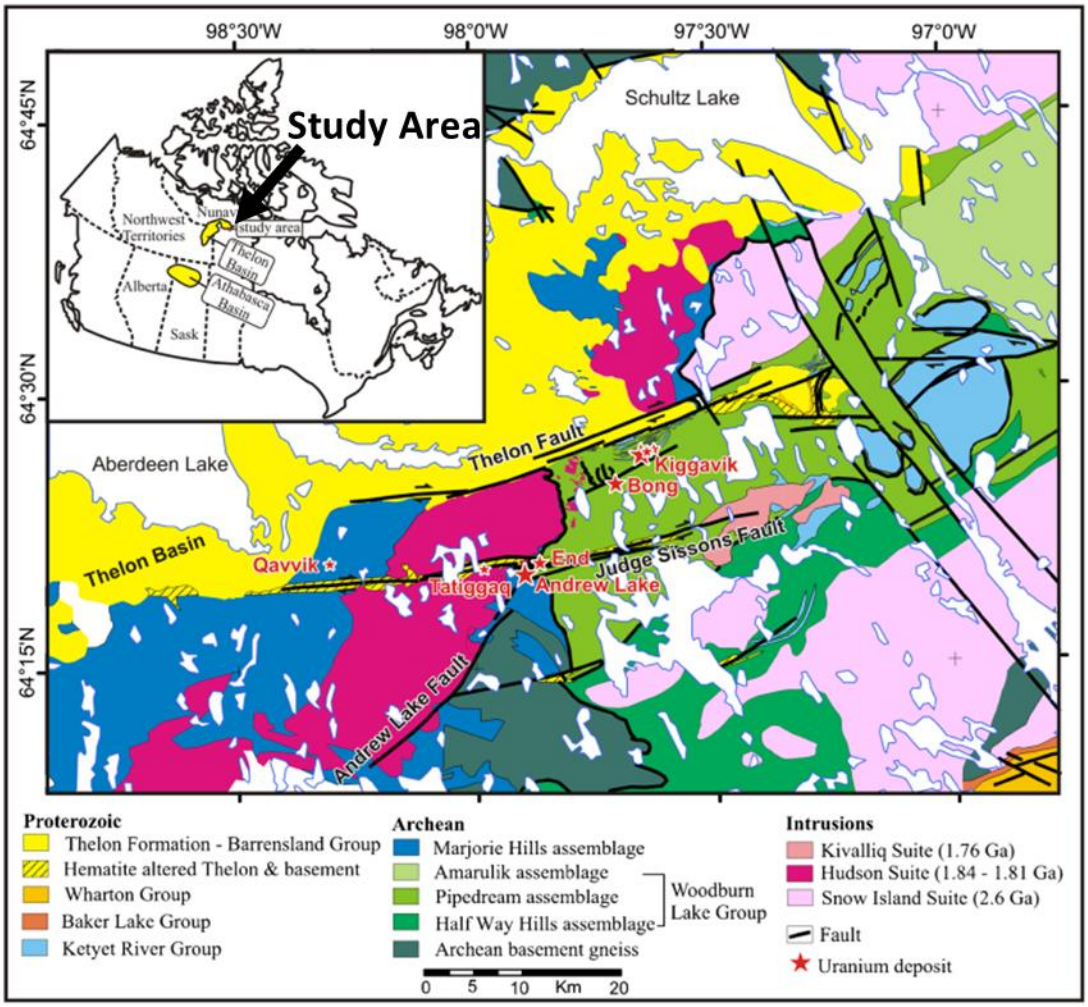

Fig. 1. Simplified geological map of the Kiggavik project area (Chi et al., 2016).

the Thelon Basin is similar to that of the economically important Athabasca Basin (Orrell et al., 1999; Ramaekers 2004; Rainbird and Davis, 2007).

The crystalline basement below the Thelon and Baker Lake basins consists of Archean granitoid gneiss, ~2.7 Ga supracrustal rocks of the Woodburn Lake group (WLg) (Pehrsson et al., 2013), ~2.6 Ga felsic volcanic and related intrusive rocks of the Snow Island Suite (Jefferson et al., 2011; Peterson et al., 2015a; Johnsone, 2017), and orthoquartzite of the Paleoproterozoic Keyet River Group (Rainbird et al., 2010). The 2.74-2.68 Ga WLg comprises five assemblages, with the first four being dominantly felsic-ultramafic volcanics and the fifth, youngest assemblage consisting of quartz-feldspar-feldspathic wacke with subordinate to minor semipelite, conglomerate, iron formation, dolostone, quartz arenite, and mafic to ultramafic sills (Pehrsson et al., 2013). The Pipedream assemblage of the WLg, which hosts most of the mineralization in the Kiggavik area, consists of felsic, intermediate, and ultramafic volcanic rocks, and subordinate greywacke-mudstone turbidites and iron-formation (Pehrsson et al., 2013). This assemblage is proposed to have formed in an intra-continental back-arc to marginal basin setting (Zaleski et al. 2001; Pehrsson et al., 2013).

These basement rocks are overlain by undeformed volcano-sedimentary rocks of the 1845-1540 Ma Dubawnt Supergroup which fills the Baker Lake Basin and overlying Thelon Basin (Rainbird et al., 2003; Peterson, 2006; Chamberlain et al., 2010). The Dubawnt Supergroup is composed of three stratigraphic groups (sequences): the 1845-1785 Ma Baker Lake, ~1756 Ma Wharton, and <1720 Ma Barrensland sequences (Rainbird et al., 2003). Deposition of the Baker Lake and Wharton sequences, which fill the Baker Lake Basin, was followed by a period of erosion and intense chemical weathering and subsequent unconformable deposition of the flat-lying fluvial-alluvial conglomerate and sandstone of the Thelon Formation

(Barrensland Sequence) that forms the major fill of the smaller Thelon Basin (Hiatt et al., 2010). The Thelon Basin is capped by the uppermost formations of the Barrensland Sequence; the 1540 ± 30 Ma Kunngmi shoshonitic basalts (Chamberlain et al., 2010) and the Lookout Point Formation dolomite (Gall et al., 1992). These units are synchronous with the capping of the Athabasca Basin by the 1541 ± 13 Ma Douglas Formation shales (Creaser and Stasiuk, 2007) and overlying Carswell Formation dolomite (Hendry and Wheatley, 1985).

The sub-Thelon basement lithologies in the Kiggavik region are intruded by two widespread igneous suites: the 1.84-1.79 Ga Hudson Granites and the 1.76-1.73 Ga Nueltin Granites, which together comprise the Schultz Lake Intrusive Complex (SLIC; Peterson et al., 2002; Peterson, 2006; Scott et al., 2012; Scott et al., 2015) in this area. The Hudson Granites are late syn-orogenic, medium-grained monzonite, granodiorite, and granite that were emplaced along pre-syn magmatic structures close to their source region at mid-crustal levels (Peterson et al., 2002; Scott et al., 2015). These rocks are contemporaneous with the ultrapotassic lamprophyres and minettes (bostonites) of the Baker Lake sequence of the Dubawnt Supergroup (Peterson et al., 2002). They contain alkali feldspar and plagioclase (~An_{10-20}), quartz, and biotite, with accessory magnetite and zircon (Peterson et al., 2002). The Neultin Granites are anorogenic rapakivi-granite predominately comprised of megacrystic K-feldspar with interstitial quartz, plagioclase (An_{10-70}), and biotite, with minor amphibole and titanite, and accessory fluorite, zircon, apatite, allanite, magnetite, and ilmenite (Peterson et al., 2002; Peterson, 2006; Scott et al., 2012). The Nueltin intrusive rocks are contemporaneous with the equivalent extrusive Pitz Formation rhyolite of the Wharton Group, and represent the felsic component of the bimodal 1770-1730 Ma Kivalliq Igneous Suite (KIS), which also comprises basalt, gabbro/anorthosite, and diabase dykes (Scott et al., 2015). Although the Thelon Basin is capped

by the Kuungmi basalt, no intrusive or bimodal equivalents or feeder dykes have been discovered.

The 1267 ± 2 Ma intrusion of the Mackenzie diabase dykes (LeCheminant and Heaman, 1989) mark the last phase of igneous activity in the Kiggavik area.

Significant (10's km long by 100's-1000's m wide) corridors of hematite alteration associated with major E-W trending faults have been documented in the region (Scott et al., 2015; Chi et al., 2016; Shabaga et al., 2017). Although some U deposits are hosted within these corridors, others are not and the relationship between hematization and mineralization in the area has not been systematically investigated.

Deposit Geology

The Kiggavik project area, owned by Orano Canada (66.2%), Denison Mines (16.9%), and UEX Corp (16.9%), is located approximately 3-10 km southeast of the faulted contact between the Aberdeen (Northeast Thelon) sub-basin of the Thelon Basin and the Archean basement. The Kiggavik project area contains an estimated 51 million kg U at an average grade of 0.46% U across the main deposits of Kiggavik, Bong, End, and Andrew Lake (AREVA, 2011). Uranium deposits are located at the intersections of faults which trend roughly ESE-WNW and NNE-SSW and have been the sites of brittle deformation and intense hydrothermal alteration consisting mainly of clay and hematite alteration and bleaching of host rocks (Fuchs et al., 1987; Sharpe et al., 2015; Grare et al., 2018; 2020). Hematite alteration consists mainly of very fine-grained earthy hematite with lesser specular hematite, while bleaching is characterized by Fe-removal, giving bleached rocks a pale yellow-white colour. Several U deposits and showings, including the Kiggavik, Bong, End, Andrew Lake, and Contact deposits, form a NE-

SW trending feature informally termed the Kiggavik-Andrew Lake structural trend (Riegler et al., 2014; Sharpe et al., 2015).

The bulk of U mineralization in the Kiggavik region is hosted within metagraywackes of the Woodburn Lake group, with subordinate mineralization in the Lone Gull granite at the Kiggavik Main Zone and Kiggavik North deposits. The Lone Gull granitic stock is considered to be a hybrid between the Hudson and Nueltin granites, with the younger Nueltin magma infiltrating into and altering the older Hudson pluton (Scott et al., 2015). It was described by Scott et al. (2015) as a peraluminous granite consisting of quartz, rounded alkali and plagioclase feldspar, and sericite, in a felsic groundmass with variable amounts of chloritized biotite, and accessory zircon, titanite, and apatite. Epiclastic rocks are also significant in the area, and locally host mineralization, although these rocks have often not been recognized and have instead been mapped as metasedimentary or other rocks (Johnstone, 2017).

One of the more enigmatic aspects of mineralization in the area is the quartz breccia (QB) <30 m thick sheet-like bodies consisting of clasts of hematized breccia in a matrix comprising multiple stages of quartz and hematite (Grare et al., 2018). Oxygen isotope and trace element data indicate it was formed by mixing of igneous and meteoric/basinal fluids in an overall epithermal system (Grare et al., 2018). Although it has been considered to be of Nueltin age (Grare et al., 2018; 2020) and thus predate U mineralization, it has not been directly dated, being loosely bracketed between 1.83 Ga Hudson intrusives and the >1.54 Ga deposition of the Thelon Basin (Grare et al., 2018). The QB is found in the core of most Kiggavik U deposits, and is associated with pervasive hematization of the host rock, and is believed to have controlled the flow of U-mineralizing fluids by acting as a barrier to fluid flow (Grare et al., 2018). The QB

itself is considered to be barren, and is locally crosscut by later U-bearing veins and replaced by illite (Grare et al., 2018).

Uranium mineralization itself has been historically described as pitchblende (UO_{2-x}), with partial replacement by coffinite ($U(SiO4) \cdot nH_2O$), surrounded by a halo of illite ± hematite ± sudoite alteration (Fuchs et al., 1987). More recent studies have revealed a more complex sequence of mineralization (Sharpe et al., 2015; Shabaga et al., 2017; Grare et al., 2020), with early polymetallic, vein-type mineralization potentially predating the main stage of monometallic U (Grare et al., 2020).

Methods

Samples were selected from the University of Manitoba's library of core samples and polished thin sections from the Kiggavik region, obtained for thesis studies (Sharpe et al., 2015; Shabaga et al., 2017; 2020; Ashcroft, 2020). The over 350 drill-core samples and corresponding thin sections examined in this study represent the various types of U mineralization, associated alteration, and unaltered host rocks from the Kiggavik, Bong, End, and Andrew Lake deposit areas. New polished thin sections were made where previous polished sections were unavailable or inadequate. The mineralogy and textures of sections were characterized through optical petrography and scanning electron microscopy in order to develop a mineral paragenesis.

The chemical compositions of minerals were determined using a CAMECA SX100 Universal Electron Probe MicroAnalyser (EMPA), equipped with five wavelength-dispersive spectrometers and a Princeton Gamma-Tech (PGT) energy-dispersive spectrometer, at the University of Manitoba. A 1 μm electron beam with a beam current of 20 nA, and an accelerating voltage of 15 kV was used. Elemental detection limits were below 1000 ppm for all elements

except for U, Th, Pb, Zr, and Hf, which had detection limits of ~3000, 3000, 2500, 2000, and 2500 ppm, respectively.

Uranium and lead isotope ratios in uraninite and other U-bearing minerals were measured using a CAMECA 7f Secondary Ion Mass Spectrometer (SIMS) instrument at the University of Manitoba, using methods similar to those described in Sharpe and Fayek (2016). Prior to analysis, samples were cleaned by immersion in an ultrasonic cleaner in four ten-minute stages: a dilute soap solution was followed by water, distilled water and finally ethanol. A conductive surface was established by sputter-coating the cleaned samples with a ~200Å-thick layer of gold.

SIMS analysis of uraninite was carried out using a ~9 nA, O^- primary beam accelerated at 12.5 kV. The beam was focused to a spot size of 15 x 30 μm by a 750 μm aperture in the primary column. An energy bandpass of ± 25 eV and a 150 μm image field were used in concert with the largest contrast (400 μm) and field (1800 μm) apertures in order to maximize sensitivity. A sample accelerating voltage of + 7.95 kV was used, with the electrostatic analyzer in the secondary column set to +8.00 kV, thus creating a 50 V offset to minimize hydride interferences. Entrance slits were set to 36.9 μm, and a mass resolving power of 1300 was used to produce flat-topped peaks. Uranium and Pb isotopes, specifically $^{204}Pb^+$, $^{206}Pb^+$, $^{207}Pb^+$, $^{235}U^+$, and $^{238}U^+$ were measured. Analyses comprised 40 cycles and required ~7 minutes to complete. Common Pb was detected, with $^{206}Pb/^{204}Pb$ ratios ≥150 for the majority of samples used in the study. Fine-grained, texturally altered U minerals in a few samples had lower and more variable $^{206}Pb/^{204}Pb$ ratios (~1000-50).

The fractionation of U-Pb ratios is known to vary as a function of PbO (Fayek et al., 2002a; b). This fractionation was accounted for via a calibration curve using the methodology and reference materials of Sharpe and Fayek (2016). U-Pb isotopic ages were determined by

plotting corrected data points on Concordia diagrams using the ISOPLOT software (Ludwig, 1993). A correlation coefficient of 0.9 was used, with uncertainties reported at the 1σ level. Overall errors for U/Pb ratios were ~2%. Where a number of data points yielded overlapping data, these data were grouped and averaged by their $^{206}Pb/^{238}U$ ratios.

Lead isotope ratios were measured in the same analytical session as the U isotope ratios. The $^{206}Pb/^{207}Pb$-$^{206}Pb/^{204}Pb$ isochron ages of U minerals were calculated using ISOPLOT software (Ludwig, 1993). A correlation coefficient of 0.9 was used, with uncertainties reported at the 1σ level.

Whole Rock Geochemistry

Nineteen samples of drill core were sent for analysis at Actlabs, Ancaster, Ontario. Samples were crushed and pulverized using a mild steel mill. Major and trace elements were determined from a 0.5 g split by lithium metaborate/tetraborate fusion. The resulting bead was rapidly digested in a nitic acid solution, which was analyzed via inductively coupled plasma-optical emission spectrometry (ICP-OES) and inductively coupled plasma mass spectrometry (ICP-MS). Fluorine was determined by KOH fusion analyzed via ion selective electrode (ISE). Gold was analyzed by instrumental neutron activation analysis (INAA). A total of nine standards were used.

Results

Petrography

With the exception of mineralization hosted within granites in the Kiggavik Deposit, sample mineralogies and textures are broadly similar between all four studied deposits, and they

will hereafter be considered together, except where noted. Generalized parageneses for the granitic and metasedimentary rocks are presented in Fig. 2.

*Metasedimentary Rocks*The stages of host rock alteration have been divided into groups on the basis of timing. These groups include “Fresh” (prograde metamorphic, but variably-retrograded, metagraywacke), pre-mineralization alteration (cryptic albitization), pre-syn-mineralization alteration (brecciation, silicification, hematization, clay mineral alteration), syn-mineralization alteration (bleaching associated with U1), and late alteration (ferric iron minerals associated with U3).

Most U mineralization in the Kiggavik camp is hosted within Neoarchean Woodburn Lake group metagraywacke. Fresh metagraywacke is grey-green, fine-grained, and is strongly foliated with primary bedding transposed parallel to the subhorizontal D_1 foliation (Pehrsson et al., 2013). The mineralogy is dominated by quartz (~60%) and feldspar (~25%), mainly K-feldspar with lesser plagioclase, with ~10-15% metamorphic muscovite and biotite, and accessory zircon, pyrite, fluorapatite, rutile, and trace garnet. Quartz and feldspars are sub-rounded to rounded and 0.1-0.5 mm in size, while muscovite and biotite are tabular and 0.1-0.3 mm in size, although laths up to 1 cm long are locally present. Biotite is strongly altered to Fe-Mg chlorite, and the feldspars are commonly partially to strongly altered to sericite. Accessory minerals, with the exception of garnet, are <0.2 mm. Zircon is zoned and fractured.

The earliest phase of host rock alteration is characterized by mineralogically complex alteration, with prominent albitization of plagioclase (Fig. 3). This pseudomorphic albite is texturally highly porous, containing numerous <5 μm pores, which are often partially infilled by paragenetically later minerals (Fig. 3). The resulting rocks are composed of ~20-40% albite. Although true albitites were not observed, their existence in the area cannot be ruled out, as most

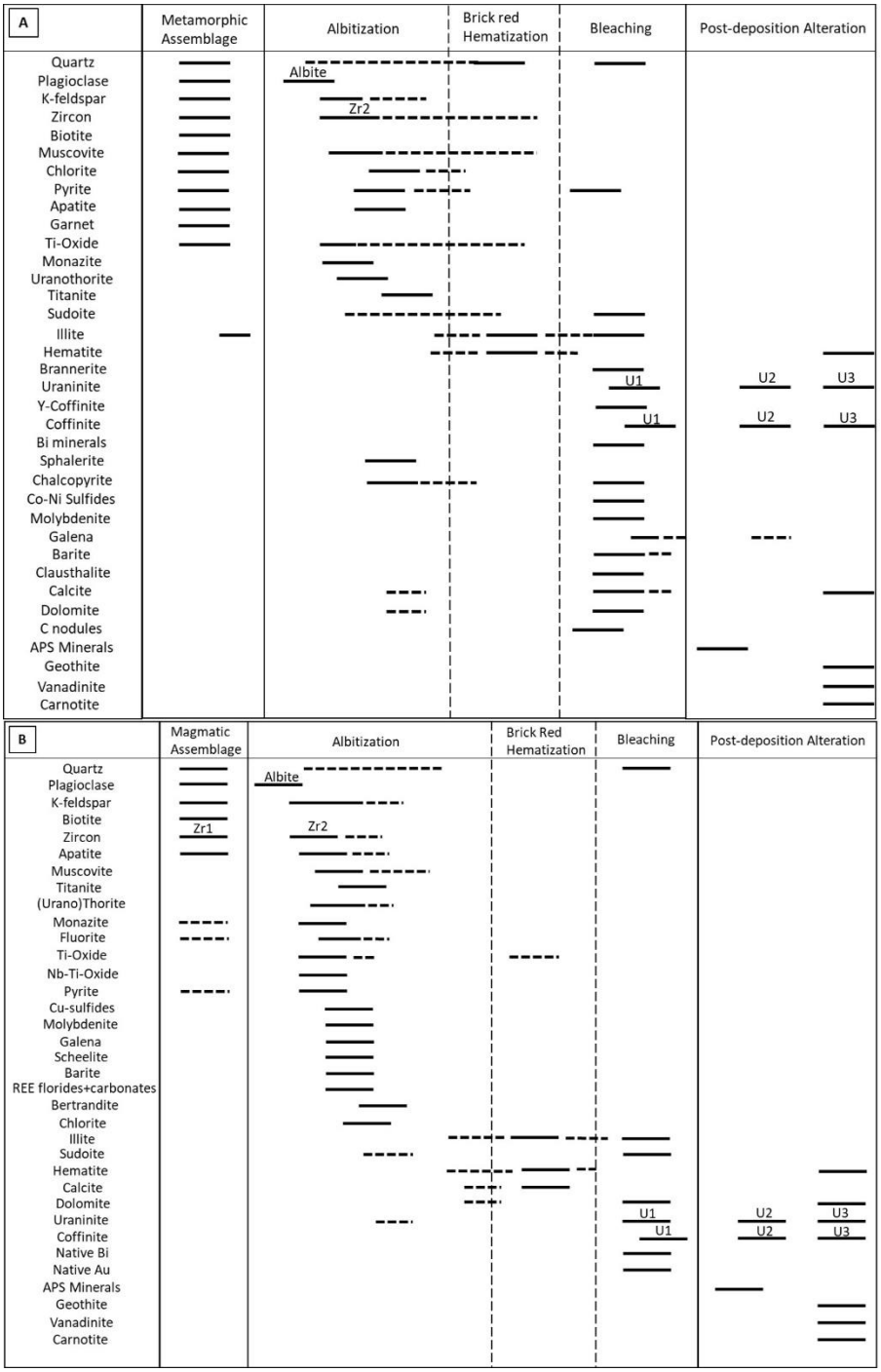

Fig. 2. Simplified, generalized parageneses for A) granitic rocks, and B) Metasedimentary rocks in the Kiggavik deposits. Dashed lines indicate uncertainty in the timing of events.

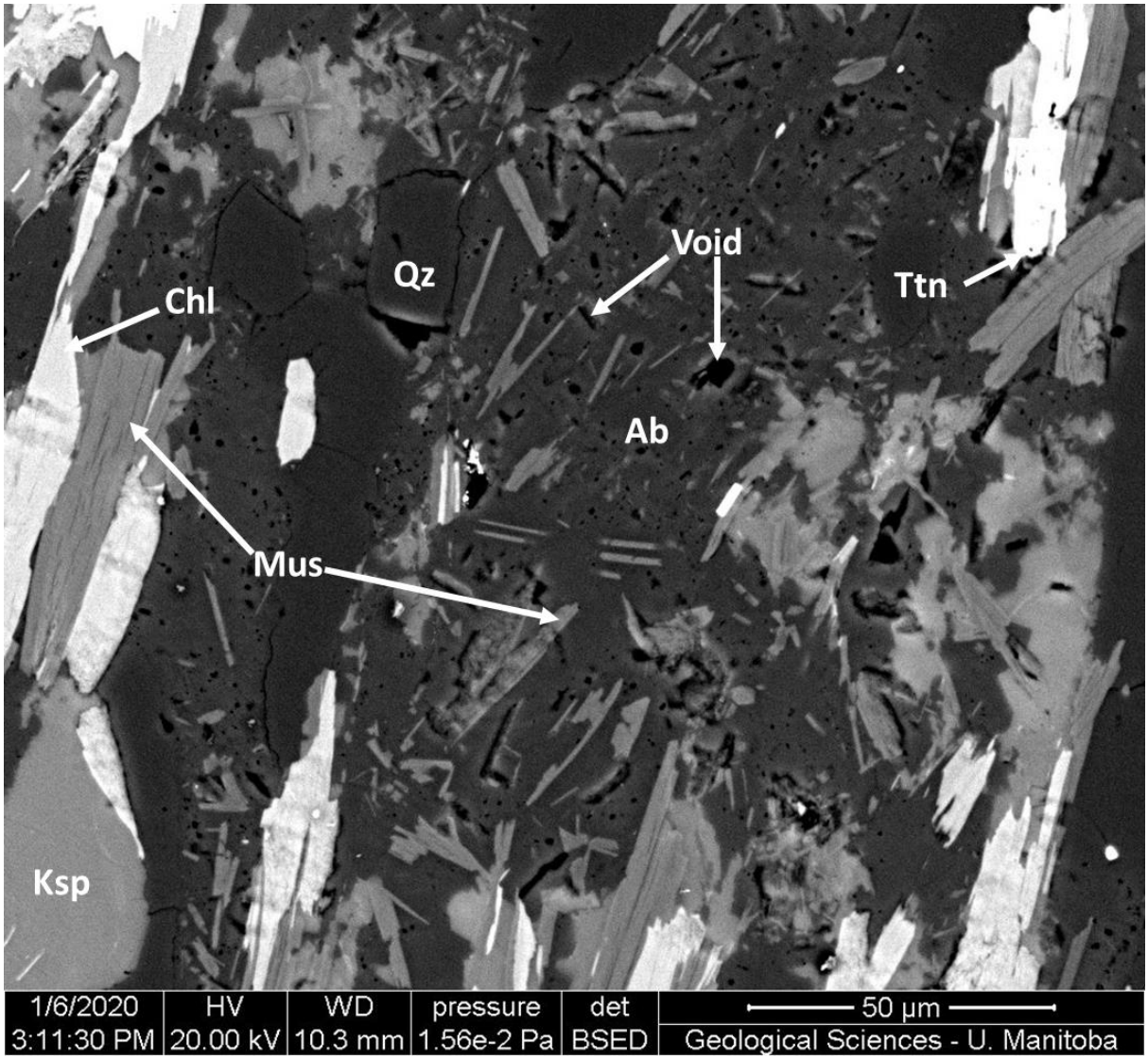

Fig. 3. Backscattered electron image of early albite-sericite-K-feldspar-titanite alteration and micro-porosity developed in metagraywackes at the Bong deposit. Abbreviations: Qz = quartz, Ab = albite, Ksp = K-feldspar, Ttn = titanite, Chl = chlorite, Mus = muscovite, Void = open microporosity.

of the studied rocks, including all of the U-mineralized rocks in the core of the Kiggavik deposits, have been subject to extremely intense overprinting illite-hematite alteration, which leaves little to no trace of pre-existing mineralogy and textures.

Albite is the most common and earliest mineral formed by albitization, and is commonly crosscut or rimmed by porous K-feldspar, which also pseudomorphically replaces earlier K-feldspar, as well as muscovite. These potassic minerals are associated with apatite, which is locally surrounded by muscovite, sporadic sulfides (pyrite, chalcopyrite, and sphalerite), Ti-oxides, and zircon, with rare uranothorite, monazite, and titanite. Titanite locally replaces chlorite. The poor preservation of albitization in metasedimentary rocks makes determining the precise timing relationships difficult, although they are likely similar to the paragenesis of albitized granitic rocks (see below).

Anhedral, weakly-zoned to unzoned Ca-Al±Th-U-Fe-P-S-bearing and Si-Zr-depleted zircon (Zr2), uranothorite, and sulfides are anhedral, <0.2 mm in size, and commonly fill fractures and void/pore space. Monazite and titanite tend to be slightly larger (<0.3 mm) and are subhedral equant-tabular in habit. This style of alteration is highly cryptic as the original textures are largely preserved with only slight changes to bulk mineralogy, and affected rocks appear much like fresh metasedimentary rocks to the naked eye and in thin section. The very small size of the individual pores and muscovite intergrowths makes this alteration very difficult to detect without the use of high magnification electron microscopy. Furthermore, early albite alteration has been heavily overprinted by subsequent generations of alteration and is only preserved on the outermost fringes of the alteration envelope.

Paragenetically later pre-syn-mineralization alteration is structurally-related and is characterized by brecciation along pre-existing faults, with silicification and hematization.

Although breccia zones can be large (10's of m) (Grare et al., 2018; 2020), many breccia zones observed are small (typically <20 cm) and consist of clasts of host rock cemented by quartz (Fig. 4a), with subordinate amounts of carbonate (calcite with minor dolomite and trace ankerite) and small, locally present, pods of semi-massive sulfides (overwhelmingly pyrite (Fig. 4b). The brecciation is commonly associated with brick-red hematization of the host rocks. Quartz is commonly weakly-moderately replaced by illite, and the breccia is uncommonly completely infilled by illite (Fig. 4c). Although the QB is considered to be barren (Grare et al., 2018; 2020), small amounts of uraniferous zircon, locally associated with muscovite, were observed filling pore space in a texture very similar to that found in albitized rocks (Fig. 4d). This pore-filling zircon is closely associated with vuggy, locally brecciated veins of course specular hematite ± drusy quartz crosscutting an earlier phase of the QB (Fig. 4e).

The hematization is characterized by fine-grained, locally Ti-bearing, hematite and specular hematite, with subordinate amounts of Ti-oxides and apatite, and minor zircon, disseminated in a groundmass of massive illite. Corroded quartz grains and relict laths of heavily altered muscovite and chlorite are commonly present. Hematite comprises ~10-15% of the hematized rocks and is typically anhedral and <0.1 mm in size. Specular hematite, where present, comprises ~5-15% of the hematized rocks typically forms 0.1-0.3 mm acicular laths, although it may reach 5 mm in veins crosscutting the QB (Fig. 4e), and gives affected rocks a purplish-red color. The distribution of specular hematite is patchy and affects only a fraction of hematized rocks although it is more common in proximity to the QB. Relatively sparse sampling density through much of the intensely hematized areas makes assessing the overall proportions and distribution of specular hematite difficult.

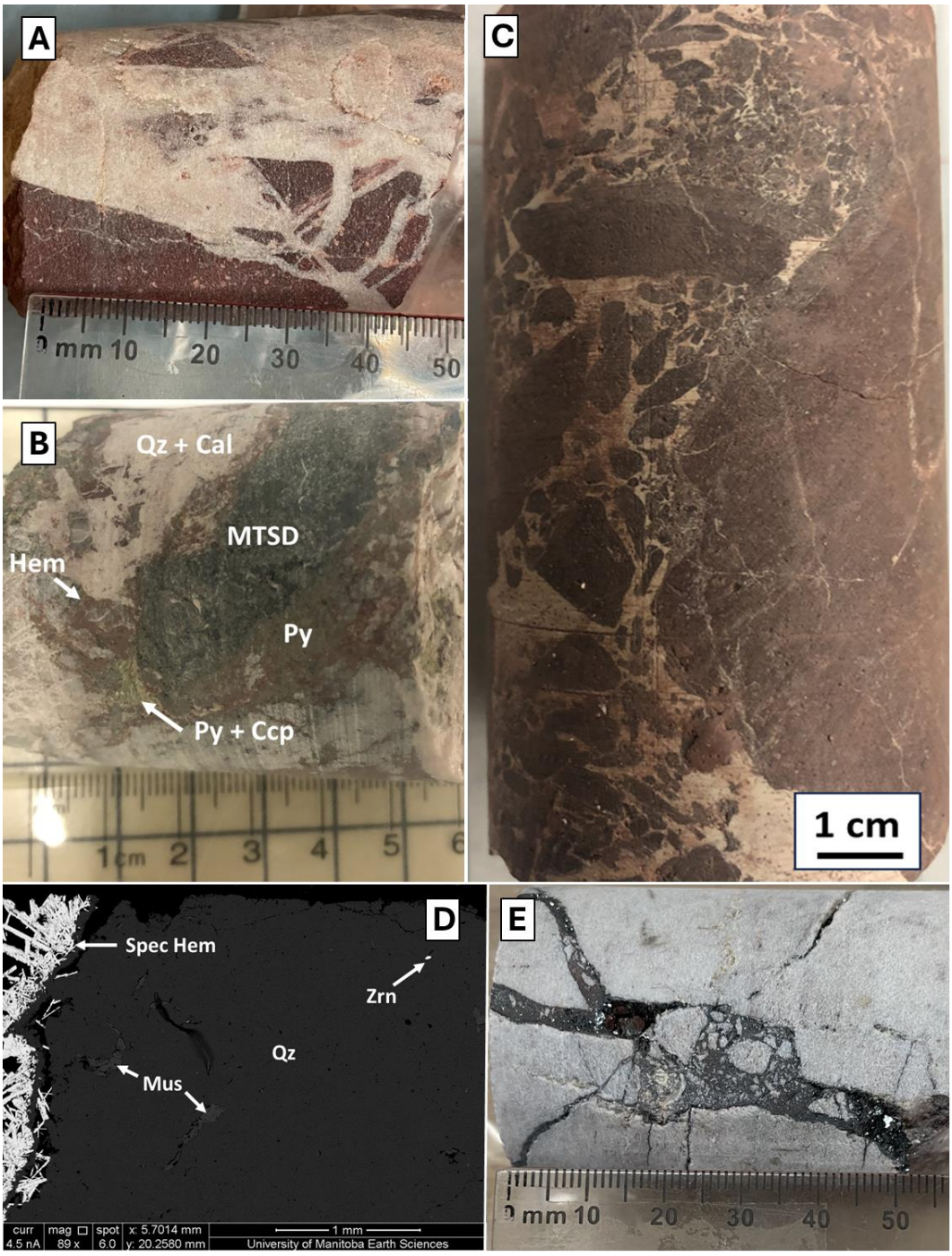
A
mm 10
20
30
40
50
B
Qz + Cal
MTSD
Hem
Py
Py + Ccp
1cm
2
3
4
5
C
1 cm
D
Spec Hem
Zrn
Qz
Mus
curr
4.5 nA
mag
89 x
spot
6.0
x: 5.7014 mm
y: 20.2580 mm
1 mm
University of Manitoba Earth Sciences
E
mm 10
20
30
40
50

Fig. 4. Textures and mineralogy of the QB. A. Typical QB texture with strongly hematite altered clasts cemented by quartz (END-10-03-42.4). B. More unusual, sulfide-bearing QB phase with negligible hematite-illite alteration of clasts cemented by quartz and calcite (END-10-02A-334.7). C. Intensely hematite-illite altered clasts cemented by illite (END-10-04-203.65). D. Backscattered electron image of muscovite and U-Ca-Al-Fe-bearing zircon associated with a specular hematite vein crosscutting an earlier phase of the QB (Bong-49-121.75). E. The same specular hematite vein in drill core. Abbreviations: Qz = quartz, Cal = calcite, MTSD = unaltered metasedimentary host rock clast, Hem = hematite, Py = pyrite, Ccp = chalcopyrite, Zrn = zircon, Spec Hem = specular hematite, Mus = muscovite.

Apatite and zircon occur in hematized rocks as <0.2 mm, anhedral, unzoned grains disseminated in a matrix of extremely fine grained (<15 μm) massive illite, which pervasively replaces feldspars and quartz and forms 70-90% of strongly hematized rocks. This illite is differentiated from muscovite, which is locally fine grained and chemically similar to illite, by its finer grain size, massive texture, and appearance later in the paragenesis. Sulfide pods are absent in the hematitic material, and carbonate is much less common. Although the exact timing of the brick-red hematization and of the brecciation and silicification could not be definitively established, the strong spatial association between these features suggest they are generally synchronous.

The dominant U-mineral comprising the first stage of U mineralization (U1) is uraninite [UO_2], with lesser amounts of coffinite commonly being present. Variable amounts (0-20% of U-minerals) of brannerite [UTi_2O_6] are commonly associated with uraninite and coffinite in the End Deposit. Brannerite is rare to absent in the other deposits. U1 mineralization is present in three forms: chemical fronts (U1a), disseminated (U1b), and vein hosted (U1c).

U1a mineralization occurs as mineral dissolution-precipitation (chemical) fronts with fine-grained uraninite and coffinite grains intergrown with illite and rimming/filling fractures in quartz, Ti-oxides, and sulfide grains. While this mineralization typically follows the distinct redox boundaries between bleached and hematized host rocks, it also occurs in bleached zones that show only trace amounts of relict hematite/goethite and the geometry of some occurrences are partially controlled by the presence of Qz (±U) veins (Fig. 5). These mineral dissolution-precipitation fronts have micro-textures that are very similar to those of the U-minerals that fringe U1c veins.

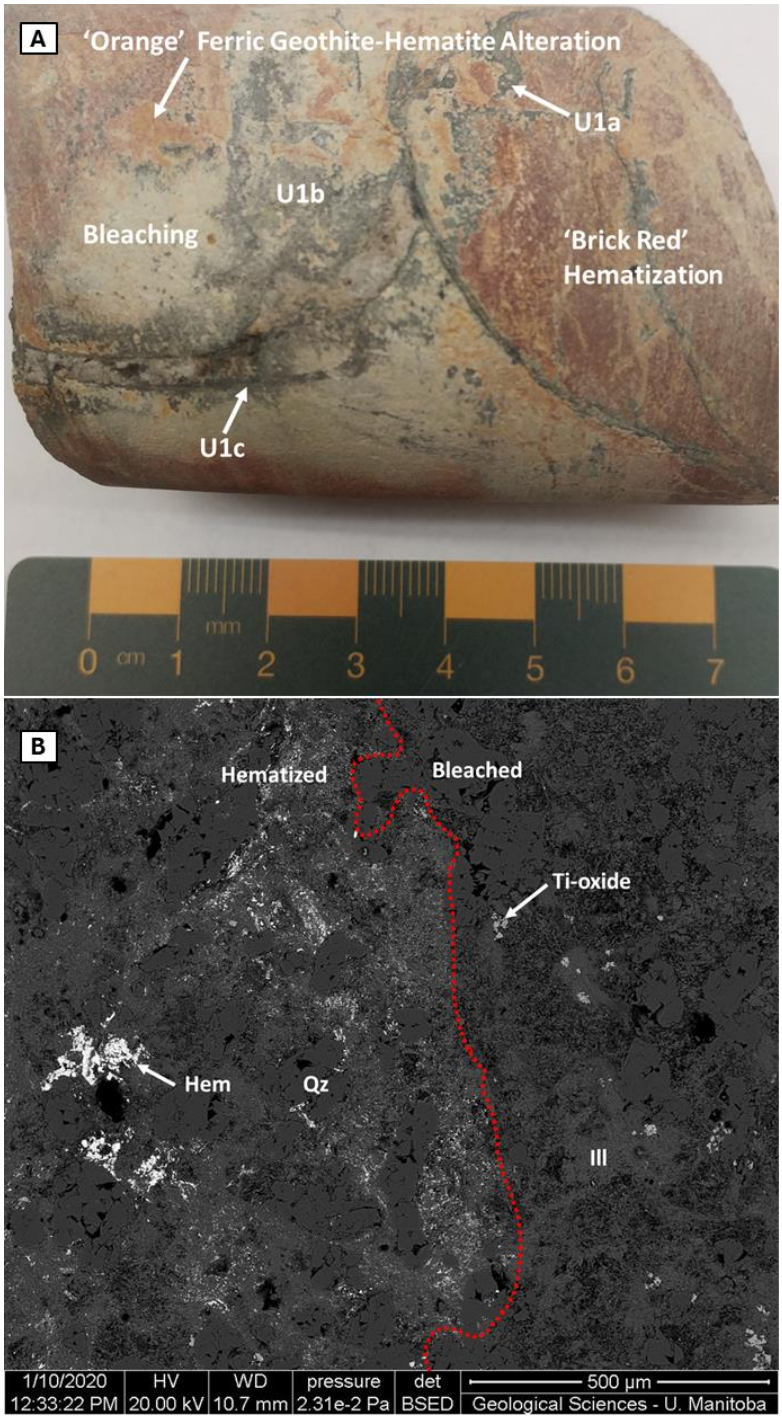

Fig. 5. U1a, b, and c and associated bleaching crosscutting brick red hematization in drill core (END-11-02-327.8). Patches of incipient orange geothite-hematite alteration, associated with U3, is also beginning to form near hematization/bleaching interfaces and vein margins.

U1b is present in the End and Bong deposits and comprises euhedral to subhedral, <1 mm uraninite grains. Brannerite and uraninite/coffinite show complex rimming relationships, each locally rimming the other; in some cases brannerite appears to replace Ti-oxides (Fig. 6a). Brannerite also occurs as disseminated anhedral grains. U1b uraninite, and to a lesser extent brannerite, in the End Deposit infrequently occurs intergrown with highly chemically variable Bi ± Pb, Pt, Pd, As, Se, Te, U minerals. Clausthalite (PbSe) is uncommonly intergrown with U1b uraninite in the End and Bong deposits. Although U1b minerals may occur independently of veins, they are often concentrated near vein margins, and are larger and more euhedral within a few centimeters of U-bearing quartz-carbonate veins. U1b grains may also be weakly aligned, forming semi-continuous bands in the matrix surrounding, and perpendicular to, U1c veins. Both U1b and U1c are ubiquitously fringed by very fine-grained uraninite and coffinite intimately intergrown with the illite matrix clay.

Stage U1c comprises the majority of the U mineralization and consists of stringers, colloform bands, and disseminated subhedral grains within <1 cm quartz-carbonate veins (Fig. 6b-f). These grains are often strongly zoned, with lesser coffinite commonly rimming or replacing uraninite along zone contacts (Fig. 6c). While many of these veins are essentially monometallic, hosting only U-bearing minerals ± pyrite, other veins are polymetallic and host diverse mineral assemblages such as uraninite-molybdenite-chalcopyrite-pyrite-(Ni-Co sulfides), uraninite-galena±barite, and uraninite-coffinite-native Bi. A particularly unusual Y-rich coffinite-pyrite-Bi±Cu sulfides/selenides/tellurides-chalcopyrite assemblage was observed in one sample from the End Deposit. Uraninite in veins is typically concentrated along the vein margins, where it often rims or replaces pyrite. It is locally rimmed by galena and uncommonly by other Mo-Cu-Ni-Co sulfides. The U-bearing veins themselves are vuggy, with some veins displaying comb

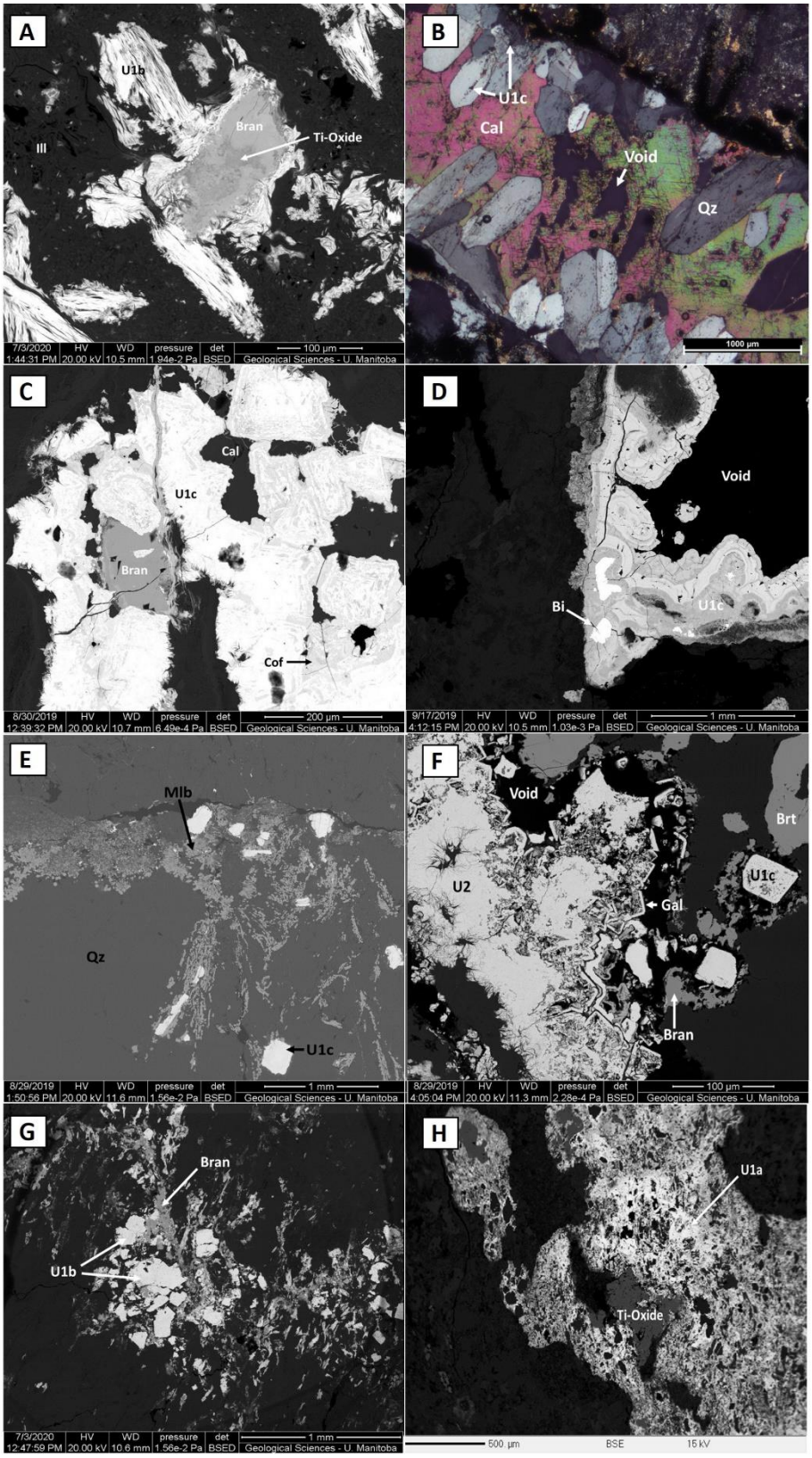
A
U1b
Bran
Ill
Ti-Oxide
7/3/2020 1:44:31 PM HV 20.00 kV WD 10.5 mm pressure 1.94e-2 Pa det BSED 100 µm Geological Sciences - U. Manitoba
B
U1c
Cal
Void
Qz
1000 µm
C
Cal
U1c
Bran
Cof
8/30/2019 12:39:32 PM HV 20.00 kV WD 10.7 mm pressure 6.49e-4 Pa det BSED 200 µm Geological Sciences - U. Manitoba
D
Void
Bi
U1c
9/17/2019 4:12:15 PM HV 20.00 kV WD 10.5 mm pressure 1.03e-3 Pa det BSED 1 mm Geological Sciences - U. Manitoba
E
Mlb
Qz
U1c
8/29/2019 1:50:56 PM HV 20.00 kV WD 11.6 mm pressure 1.56e-2 Pa det BSED 1 mm Geological Sciences - U. Manitoba
F
Void
Brt
U2
U1c
Gal
Bran
8/29/2019 4:05:04 PM HV 20.00 kV WD 11.3 mm pressure 2.28e-4 Pa det BSED 100 µm Geological Sciences - U. Manitoba
G
Bran
U1b
7/3/2020 12:47:59 PM HV 20.00 kV WD 10.6 mm pressure 1.56e-2 Pa det BSED 1 mm Geological Sciences - U. Manitoba
H
U1a
Ti-Oxide
500 µm BSE 15 kV

Fig. 6. U1 textures. A. Ti-oxides being replaced by brannerite and rimmed by U1b uraninite (END-09-04-322.3). B. Comb-texture quartz and vuggy calcite in a polymetallic U1a vein (END-34-1026). C. BSE image of zoned U1a uraninite intergrown with coffinite and crosscut by brannerite in a monometallic U1a vein (END-09-04-339.1). D. Colloform U1a with inclusions of native Bi partially cementing breccia (LG86-158.5). E. U1a uraninite and molybdenite in a quartz-carbonate vein (END-34-1026). F. U1a uraninite, partially altered to U2 along vein margin, associated with barite and partially rimmed by galena and brannerite (END-40-902). G. U1b uraninite and brannerite aligned with former foliation planes in intensely bleached metasedimentary rocks (END-09-02-341.2). H. U1c uraninite rimming Ti-oxides and intergrown with illite (Bong-50-292.2). Abbreviations: Qz = quartz, Cal = calcite, Ill = illite, Cof = coffinite, Bran = brannerite, Gal = galena, Mlb = molybdenite, Brt = barite, Bi = native Bi, Void = open vug/pore space.

texture (Fig. 6b). In some cases, quartz and carbonate have been extensively replaced by illite and they are locally found as inclusions preserved within uraninite.

Host rock alteration associated with U1 is characterized by bleaching, which crosscuts brick-red hematization of the earlier alteration stage. This bleaching, which has historically been used to describe the whitening of the host rocks, is characterized by the visible color change caused by the removal of Fe-oxides. Gangue mineralogy in the bleached areas is dominated by illite, with variable, but lesser, quantities of calcite, sudoite (Mg-Al chlorite), and remnant quartz, Ti-oxides, Fe-Mg chlorite, apatite, and muscovite. Where bleaching is weak remnant hematite is locally preserved in cleavage planes in muscovite and chlorite laths. Bleaching typically removes hematite without causing other major changes to mineralogy; where bleaching is intense, however, other minerals such as quartz and muscovite may also be variably corroded. Where muscovite and chlorite are present, these phyllosilicates show degradation and uraninite is commonly observed along cleavage planes within them or they are completely pseudomorphed by uraninite. Variable amounts of carbonate (calcite and rare dolomite) are commonly present in the matrix surrounding the U1c veins, and carbon nodules similar to those reported from the Bong Deposit (Sharpe et al*.,* 2015) and commonly observed in Athabasca U deposits (Hoeve and Quirt, 1987; Jefferson et al., 2007a; Alexandre et al., 2009), are rarely present in the End Deposit associated with polymetallic U1c veins. The alteration front between bleaching and brick-red oxidation, marked by the abrupt disappearance of hematite, is locally mineralized with U1a. U1a does not occur on the hematite-bearing side of the alteration front.

U1 textures and mineralogy, polymetallic veins in particular, are more common and display lower degrees of textural and chemical alteration in the End Deposit relative to other deposits.

A secondary generation of U minerals, U2, comprises altered uraninite and coffinite. U2 uraninite is subhedral to anhedral and slightly to heavily fractured. Texturally, it strongly resembles an altered version of U1b and U1c mineralization, with the exception being an absence of polymetallic veins. Disseminated U2 uraninite in the Andrew Lake deposit, and locally in the End deposit may exhibit a distinctive 'worm-rock' texture, where uraninite grains are rimmed by a <1 mm halo of bleached zone within an overall hematite-rich illite matrix (Fig. A1a). U2 comprises the majority of U-minerals in the Andrew Lake and Bong deposits, while U1 and U2 comprise subequal proportions of U minerals in the End and Kiggavik deposits.

A third stage of U mineralization (U3) consists of very fine-grained uraninite and coffinite, with traces of a U mineral tentatively identified as carnotite [$K_2(UO_2)_2(VO_4)_2 \cdot 3H_2O$]. U3 is intergrown with the illite matrix and is concentrated along chemical fronts and fills fractures within quartz veins. U3 forms a relatively minor proportion of U-mineralization in all deposits.

U3 is associated with distinctive ferric iron ("orange") alteration that is characterized by very fine-grained ("dusty"), anhedral hematite and goethite. U3 is locally associated with calcite and, in U mineralized areas, vanadinite [$Pb_5(VO_4)_3Cl$] (Fig. A1d). Orange hematite-geothite alteration overprints the earlier brick-red oxidation and bleaching features, and locally appears to overprint and remobilize U1 and U2 into U3. Chemical fronts developed between hematite-geothite alteration and hematite-free, previously bleached areas are occasionally U-bearing, however, this mineralization is much finer-grained and less substantive than the U1a mineralization found between brick-red hematitic and bleached areas. Hematite-geothite alteration is spatially strongly associated with open fractures and vuggy quartz veins, some of which are U1c mineralized.

Uranium minerals display substantial variations in chemical composition (Table 1). U1 uraninite contains high amounts of UO_2 (74.2-89 wt%), a broad and highly variable range in PbO (0.0-17.1 wt%), 0.0-5.5% SiO_2, 0.9-4.3% CaO, and 0.0-0.5% ThO_2. U1c and U1b uraninite are chemically very similar, while U1a uraninite is slightly less variable in composition, with a lower maximum PbO content (12.7 wt%). U2 uraninite is less pure, containing slightly lower amounts of UO_2 (62.4-86.0 wt%), a lower maximum PbO content (14.1 wt%), and generally higher amounts of SiO_2 (maximum 12.0 wt%) and CaO (up to 8.0 wt%), and similar ThO_2. U3 uraninite is chemically similar to U2 uraninite, but contains occasionally lower UO_2 (57.5-87.5 wt%) and has lower PbO content (maximum 5.7 wt%).

Coffinite, associated with all generations of uraninite, does not show mineralization-stage chemical variation, containing lower amounts of UO_2 than the uraninite (46.9-76.9 wt%), lower amounts of PbO (maximum 3.0 wt%), and greater amounts of SiO_2 (12.0-20.4 wt%).

Brannerite shows a restricted compositional range, containing around 50 wt% UO_2, 33 wt% TiO_2, 1.4 wt% PbO, 3.5 wt% SiO_2, and 1.7 wt% CaO. Carnotite grains were too fine-grained for their mineral chemistry to be reliably measured, however U, V, and K were detected.

Igneous Rocks Although a portion of the Kiggavik deposit is known to be hosted within granitic rocks of the Lone Gull stock, mineralization within these rocks has not been well studied or documented. The only dedicated study of the Lone Gull stock is by Scott et al. (2015), who did not study the altered rocks that host U mineralization. There are a few available descriptions of U mineralization within the altered granitic rocks (Weyer et al., 1987; Farkas, 1984; Shabaga et al., 2020) that briefly report the presence of disseminated uraninite within a granitic host comprising quartz, partially-illitized feldspar, muscovite, and partially-chloritized biotite, and accessory

Table 1. Chemical compositions of U-minerals in the Kiggavik, Bong, End, and Andrew Lake deposits. Average compositions in brackets. All values reported in wt % and measured via EMPA.

Mineral	**Points (n)**	**UO_2**	**ThO_2**	**PbO**	**SiO_2**	**CaO**	**TiO_2**
Uraninite (U1a)	17	79.0-87.9 (**84.1**)	0.0-0.1 (**0.0**)	0.2-12.7 (**1.6**)	0.2-3.0 (**1.8**)	1.3-3.8 (**3.2**)	0.1-0.8 (**0.3**)
Uraninite (U1b)	35	75.0-89.0 (**81.6**)	0.0-0.4 (**0.1**)	0.2-16.4 (**11.8**)	0.0-4.3 (**0.7**)	0.8-4.2 (**1.6**)	0.1-1.4 (**0.5**)
Uraninite (U1c)	58	74.2-87.7 (**81.9**)	0.0-0.5 (**0.1**)	0.0-17.1 (**10.5**)	0.0-5.5 (**1.1**)	0.9-4.3 (**2.0**)	0.0-1.4 (**0.3**)
Uraninite (U2)	110	62.4-86.0 (**78.6**)	0.0-0.2 (**0.0**)	0.0-14.1 (**0.9**)	0.9-12.0 (**6.1**)	0.9-8.0 (**3.3**)	0.0-3.2 (**0.2**)
Uraninite (U3)	66	57.5-87.5 (**77.3**)	0.0-0.5 (**0.1**)	0.0-5.7 (**0.4**)	1.6-11.8 (**5.8**)	1.9-5.4 (**3.6**)	0.0-1.6 (**0.1**)
Coffinite	48	46.9-76.9 (**66.1**)	0.0-0.3 (**0.1**)	0.0-3.0 (**0.3**)	12.0-20.4 (**15.0**)	1.0-5.3 (**2.2**)	0.0-1.6 (**0.2**)
Brannerite	7	45.9-51.3 (**49.5**)	0.0-0.1 (**0.1**)	1.3-1.7 (**1.4**)	3.1-3.7 (**3.5**)	1.4-2.4 (**1.7**)	32.2-34.4 (**33.5**)

zircon. However, the observations made during this study differ substantially from the previously published descriptions.

The altered Lone Gull granitic rocks described here come from the Kiggavik Main Zone and Kiggavik North mineralized areas and are similar in most respects. Granitic rocks have been affected by albitization, brick red hematization, bleaching, and orange hematite-goethite alteration similar to that observed in the altered metasedimentary rocks. Albitization is more intense and pervasive in the granite than in the metasedimentary rocks; although igneous textures are largely preserved, no non-albitized plagioclase was observed. Primary textures are not observed where hematization and/or bleaching alteration is most intense, and several samples initially identified as altered metasedimentary rocks were revealed to be altered granitic rocks after careful examination of thin sections. Granitic rocks and the overlying country rocks are commonly micro-fractured and locally brecciated. Breccia zones are generally <5 cm wide and are composed of <1 cm clasts cemented by illite ± quartz and uraninite.

Two granitic dykes which are texturally and mineralogically similar to the granitic rocks observed at the Kiggavik Deposit were observed in the End Deposit. One of these dykes has been albitized while the other has been hematized and subsequently bleached. The albitized dyke contains carbonate pods and trace amounts of uraninite.

Albitized granitic rocks consist of feldspar (albite (An_{1-7}, avg. ~An_3) and K-feldspar), quartz, biotite, and muscovite, with accessory zircon, fluorapatite, uranothorite, rutile, pyrite, chalcopyrite, molybendite, galena, biotite, fluorite, Fe-oxides, and Alumino-Phosphate-Sulfate (APS) minerals, and trace amounts of ilmenite, monazite, REE-(F)-carbonates, scheelite, and native Au (Fig. 7a-h; A2a-d). With the exception of strongly zoned zircons (Zr1) and potentially the cores of some large, partially altered quartz, K-feldspar, and biotite grains, all these minerals

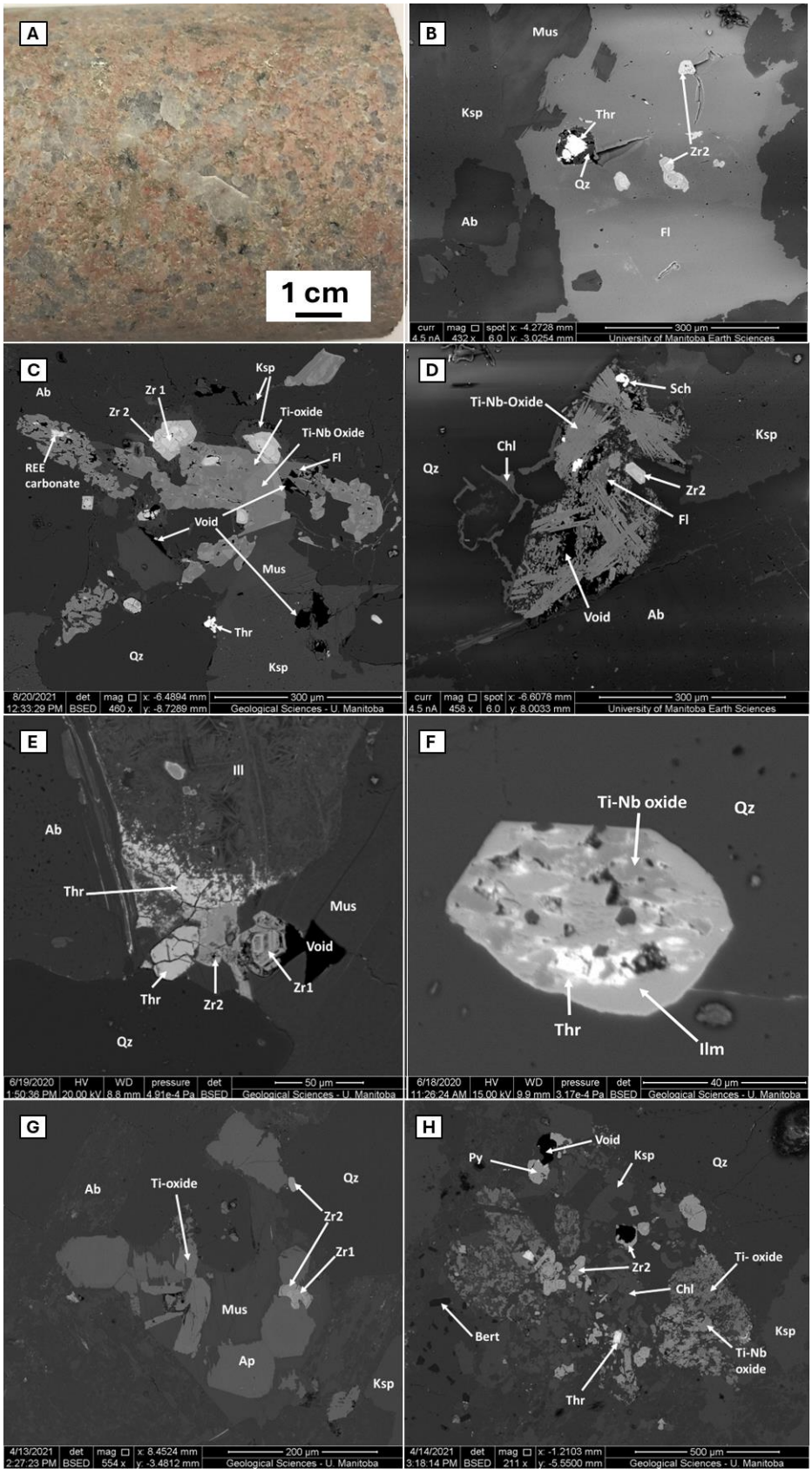
A
1 cm
B
Mus
Ksp
Thr
Zr2
Qz
Ab
Fl
curr mag spot x: -4.2728 mm 300 µm
4.5 nA 432 x 6.0 y: -3.0254 mm University of Manitoba Earth Sciences
C
Ab
Zr 1
Ksp
Zr 2
Ti-oxide
Ti-Nb Oxide
Fl
REE carbonate
Void
Mus
Thr
Qz
Ksp
8/20/2021 12:33:29 PM det BSED mag 460 x x: -6.4894 mm y: -8.7289 mm 300 µm Geological Sciences - U. Manitoba
D
Ti-Nb-Oxide
Sch
Ksp
Chl
Qz
Zr2
Fl
Void
Ab
curr mag spot x: -6.6078 mm 300 µm
4.5 nA 458 x 6.0 y: 8.0033 mm University of Manitoba Earth Sciences
E
Ill
Ab
Thr
Mus
Void
Zr1
Thr
Zr2
Qz
6/19/2020 HV WD pressure det 50 µm
1:50:36 PM 20.00 kV 8.8 mm 4.91e-4 Pa BSED Geological Sciences - U. Manitoba
F
Ti-Nb oxide
Qz
Thr
Ilm
6/18/2020 HV WD pressure det 40 µm
11:26:24 AM 15.00 kV 9.9 mm 3.17e-4 Pa BSED Geological Sciences - U. Manitoba
G
Ab
Ti-oxide
Qz
Zr2
Zr1
Mus
Ap
Ksp
4/13/2021 2:27:23 PM det BSED mag 554 x x: 8.4524 mm y: -3.4812 mm 200 µm Geological Sciences - U. Manitoba
H
Void
Py
Ksp
Qz
Zr2
Ti- oxide
Chl
Bert
Ksp
Ti-Nb oxide
Thr
4/14/2021 3:18:14 PM det BSED mag 211 x x: -1.2103 mm y: -5.5500 mm 500 µm Geological Sciences - U. Manitoba

Fig. 7. Textures of albitized granitic rocks. A. Least altered granite in drill core (KN02-245.6). B. BSE image of hydrothermal zircon (Zr2) and uranothorite encased with fluorite (KN04-126). C. A typical accessory mineral pocket in least-altered granite (KN04-126). D. Pocket partially filled by acicular Ti-Nb oxides and other minerals in least-altered granite (KN04-126). E. Partially dissolved magmatic zircon (Zr1) rimmed and associated with hydrothermal zircon (Zr2), uranothorite, and a Zr-Si-U-Ca phase filling pore space within a sericitized feldspar phenocryst in bleached granite (MZ-10-130). F. Zr-Si-U-Ca phase filling pore space within ilmenite which has been partially altered to sieve-textured Ti-Nb oxide in bleached granite (MZ-10-130). G. Zr1 embayed by apatite and overgrown by Zr2 enclosed with a muscovite lath (KN04-126). H. Pyrite and chlorite rich accory mineral pocket bordered by a bertrandite-quartz vein (MZ-01-237.3). Abbreviations: Qz = quartz, Ab = albite, Ksp = K-feldspar, Chl = chlorite, Mus = muscovite, Ill = illite, Zr1 = zoned magmatic zircon, Zr2 = unzoned, Ca-Al-Fe-bearing hydrothermal zircon, Thr = (urano)thorite, Zr-Si-U-Ca = Zr-Si-U-Ca phase, Fl = fluorite, Ilm = ilmenite, Sch = scheelite, Bert = bertrandite, Void = open cavity/pore space.

are interpreted as the products of (pseudomorphic) replacement of igneous minerals by metasomatic fluids. Major rock-forming minerals are generally euhedral to subhedral in habit, and <5 mm in size, however, anhedral quartz grains may exceed 1 cm. Graphic texture is locally present. Muscovite exhibits a wide range of textures, from <5 mm euhedral laths and radial aggregates developed interstitial to quartz and feldspar grains, to small (<50 μm) acicular to anhedral grains intergrown with albite. Apatite displays a variety of textures, from <500 μm euhedral grains to <100 μm sub-anhedral grains which commonly occur along cleavage planes within muscovite and chlorite laths, as well as uncommonly embaying zircons. Feldspars ubiquitously contain microporosity in the form of <5 um dissolution pits. Some larger pits are filled by sulfides (mainly galena), barite, fluorite, zircon, and thorite. Muscovite and biotite have been variably chloritized, with the latter present only as heavily altered relicts.

Paragenetic relationships between minerals are complex and indicate a large degree of overlap (Fig. 2). Albite is the earliest phase, followed by K-feldspar, muscovite, apatite, Ti-oxides, and locally pyrite; these are commonly partially replaced by a later assemblage of chlorite, Nb-bearing Ti-oxides, uranothorite, fluorite, and anhedral, Zr2, and local Fe-oxides (Fig.7 b-h). Zr2 commonly rims Zr1, and less commonly pyrite, and occurs together with uranothorite. These minerals fill cavities, fractures, and other pore space. Zirconium-rich uranothorite also occurs along cleavage planes in muscovite and chlorite (Fig. 7e). Molybdenite also rarely occurs along such cleavage planes.

Lone Gull granitic rocks ubiquitously contain <1 mm pockets, interpreted as dissolution pits, which are partially to completely infilled with a diverse assortment of accessory minerals, including muscovite, zircon, apatite, uranothorite, Ti-oxides, Fe-oxides, pyrite, chalcopyrite, fluorite, monazite, and REE-(F)-carbonates (Fig. 7b-h; A2a-d)). Where void space is present,

minerals such as monazite, Ti-oxides, and Fe-oxides may exhibit skeletal textures. Ti-oxides commonly occur as sieve-textured laths containing substantial microporosity, which is locally partially filled by Zr2 and uranothorite (Fig. 7f).

Uranothorite, thorite and uraniferous Zr2 zircon (<3.1 wt% UO_2) are major hosts for U in the granitic rocks. These minerals contain a wide range of impurities such as Ca, Al, Fe, Ti, P, S, and Cl, and have low microprobe totals (~70-90%), suggesting hydration and metamictization (Table A2). Uranothorite and Zr2 display an almost complete solid solution between zircon and uranothorite (Fig. 8a.). Uraninite, where present, is hosted in quartz veins similar to those observed in the metasedimentary rocks, and is ascribed to U1c mineralization. Mineral assemblages in the U1 veins include monometallic uraninite ± coffinite, as well as polymetallic uraninite-coffinite-native Bi (Fig. 4d). As in the metasedimentary rocks, these veins are associated with bleaching. In some samples, bertrandite [$Be_4(Si_2O_7)(OH)$] and trace amounts of uraninite are hosted in a zone of silicification comprising at least 5 generations of quartz overgrowths. Trace amounts of native Au are associated with quartz veins that are texturally similar to U1c-bearing veins in brecciated areas.

Orange hematite-geothite (U3) alteration is rare in the granitic rocks and it occurs in association with strongly altered U1c veins and with U3 uraninite and coffinite. Vanadinite and trace carnotite were observed filling fractures in one sample from the Kiggavik Main Zone.

Regardless of the type of alteration present, albite, K-feldspar, and muscovite have been pervasively, moderately, and weakly altered to illite, respectively. Albite, fluorite, and ilmenite have been extensively corroded and replaced by illite and/or Fe-oxides, with fluorite and ilmenite preserved in only the least altered samples. Ilmenite has been partially altered to sieve-textured

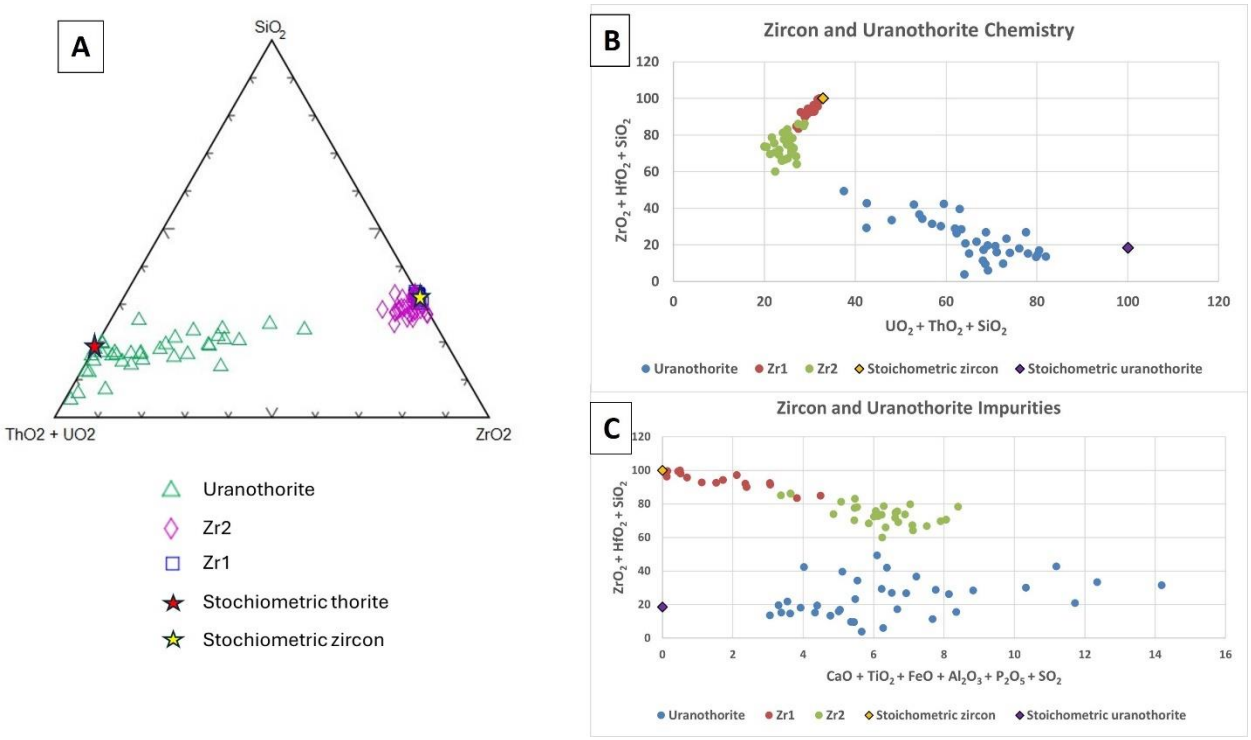

Figure 8. A-C. Chemistry of zircon and uranothorite in the Kiggavik Deposit granitic rocks. All data is in wt.% oxides.

Ti-rich laths, suggesting the sieve-textured Ti-oxides formed by corrosion and removal of Fe and Mn from primary ilmenite.

Epiclastic Rocks Epiclastic rocks were only observed in the upper ~50 m of drill core samples from the Kiggavik Deposit and consist mainly of quartz and muscovite with lesser amounts of K-feldspar and plagioclase. Rounded quartz clasts up to 3 mm were observed; these comprise up to 30% of the rock and are the principle means of distinguishing epiclastic from other rock types. Quartz clasts have been heavily recrystallized into a fine-grained, mosaic texture. Foliation, defined by muscovite, wraps around these clasts. Epiclastic rocks appear to have been subject to hematization and bleaching similar to metasedimentary rocks in the area, although the limited number of epiclastic rocks observed prevents more though characterization of alteration to these rocks. No mineralized epiclastic rocks were observed.

Geochemistry

Two suites of samples of Kiggavik granitic rocks, one from the Main Zone and one from Kiggavik North, were analyzed in order to define chemical changes related to the various stages of host rock alteration (Table A3). As all of the examined samples of granitic rocks were affected by some degree of albitization, hematization, and/or bleaching, a sample of monzogranite, KMZ-MG, sampled from an outcrop above the Kiggavik Main Zone by Scott, et al. (2015) was used to represent fresh, unaltered host rock compositions.

Samples affected by albitization show a marked depletion in CaO, and enrichment in SiO_2 versus fresh monzogranite (Fig. 9a, b). The behavior of Na and K is more variable, where some samples are strongly enriched and some are strongly depleted in these elements, although they are generally depleted in Na_2O and slightly enriched in K_2O (Fig. 9d, f). The trace element

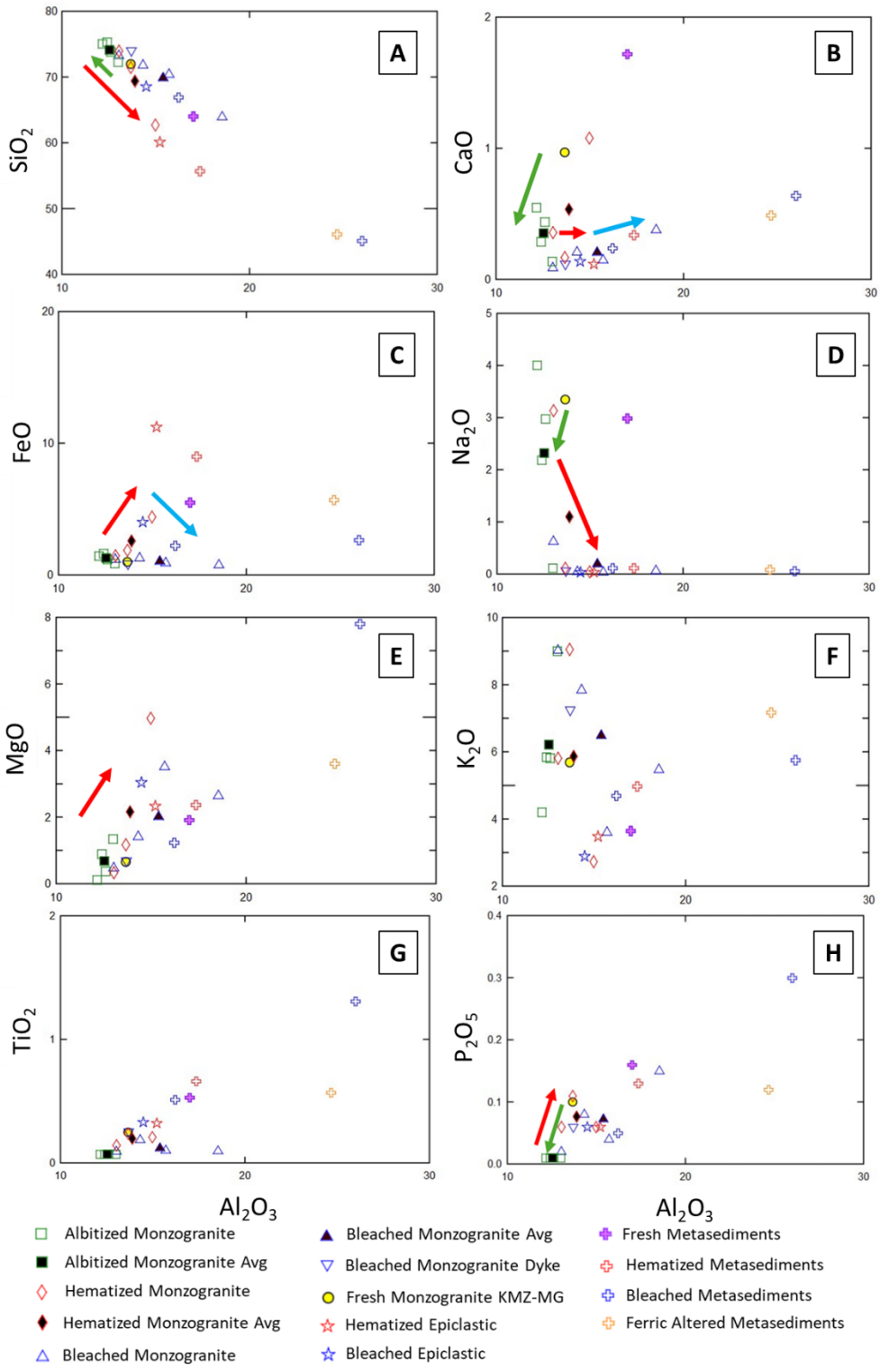
A
B
C
D
E
F
G
H
SiO2
CaO
FeO
Na2O
MgO
K2O
TiO2
P2O5
Al2O3
Al2O3
Albitized Monzogranite
Albitized Monzogranite Avg
Hematized Monzogranite
Hematized Monzogranite Avg
Bleached Monzogranite
Bleached Monzogranite Avg
Bleached Monzogranite Dyke
Fresh Monzogranite KMZ-MG
Hematized Epiclastic
Bleached Epiclastic
Fresh Metasediments
Hematized Metasediments
Bleached Metasediments
Ferric Altered Metasediments

Figure 9. Plots of whole rock geochemical data. A-H, major and trace element oxides vs Al_2O_3. General trends of alteration indicated by arrows. Green arrow = albitization, red arrow = hematization, blue arrow = bleaching.

and REE plots were normalized relative to KMZ-MG (Fig. 10). Changes in minor elements are more consistent, where the albitized monzogranite is moderately to strongly depleted in P_2O_5, TiO_2, Y, Zr, Th, REEs, Cs, Ba and Sr, strongly enriched in U and Pb, and weakly enriched in Ta (Fig. 9g, h; 10a). The REE patterns show a bowl-shaped pattern where the LREEs are more depleted relative to the HREE (Fig. 10b).

Samples affected by brick-red hematization show more variable, but generally larger compositional changes, where more variable chemical alteration is ascribed to variations in the intensity of hematization. Sample KN04-106 displays only incipient hematization, with limited development of Fe-oxides and preservation of albitized textures, whereas KN04-66.5 and MZ-10-01-79.4 are strongly hematized with extensive corrosion of quartz and textural modification. The magnitude of changes to bulk chemistry were observed to correlate with the visually apparent intensity of hematization.

All hematized monzogranites are significantly enriched in FeO, MgO, TiO_2, P_2O_5, Ba, and REEs, weakly-strongly enriched in Pb and Zr, and strongly depleted in SiO_2 and Na_2O relative to the albitized monzogranites they overprint (Fig. 9c, e, g, h; 10c). K_2O and U content is variable, where some samples are strongly enriched, strongly depleted, and some showing little change (Fig. 9f; 10c). KMZ-normalized REE patterns have a gently-sloping peak centered on Ho, with a slight negative Eu anomaly (Fig. 10d).

Bleached monzogranite is strongly depleted in FeO, TiO_2, and REEs, moderately enriched in K_2O and very strongly enriched in U relative to the hematized monzogranite they overprint (Fig. 9c, f, g; 10e). Abundances of other major and minor elements are generally similar to those of hematized samples. KMZ-normalized REE patterns have a slight trough centered on Nd, and a strong positive Eu anomaly (Fig. 10f).

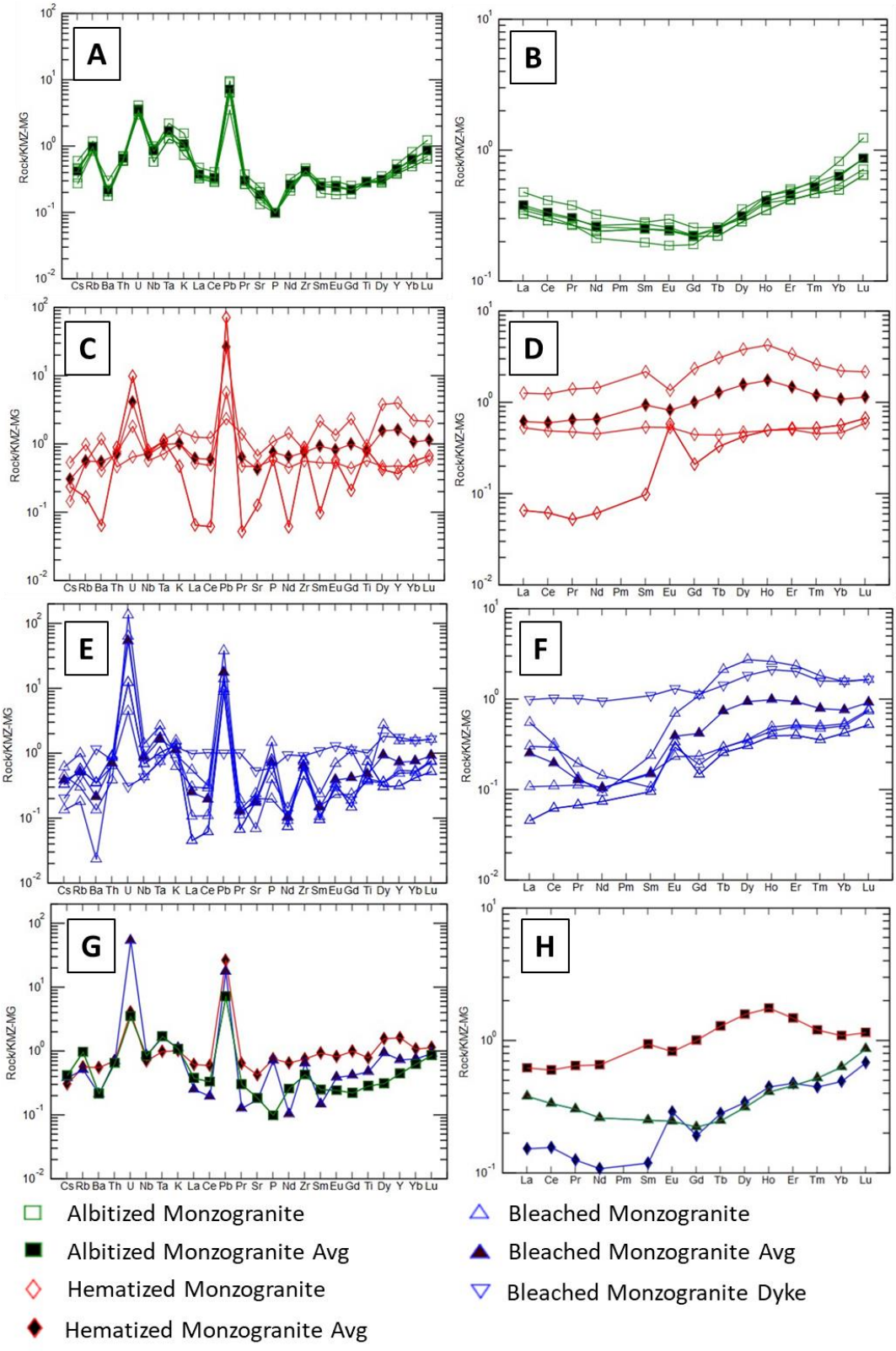
A
B
C
D
E
F
G
H
Rock/KMZ-MG
Cs Rb Ba Th U Nb Ta K La Ce Pb Pr Sr P Nd Zr Sm Eu Gd Ti Dy Y Yb Lu
La Ce Pr Nd Pm Sm Eu Gd Tb Dy Ho Er Tm Yb Lu
Albitized Monzogranite
Albitized Monzogranite Avg
Hematized Monzogranite
Hematized Monzogranite Avg
Bleached Monzogranite
Bleached Monzogranite Avg
Bleached Monzogranite Dyke

Fig. 10. Fresh monzogranite (KMZ-MG) normalized trace element and REE spider diagrams. A, B. Albitized monzogranite. C, D. Hematized Monzogranite. E, F. Bleached Monzogranite. G, H. Averages of albitized, hematized, and beached monzogranite.

A bleached granitic dyke from the End Deposit was also analyzed, yielding data which is very similar to unaltered Main Zone monzogranite, except that it is strongly depleted in CaO, Na_2O, P_2O_5, and U, and moderately enriched in K_2O, and a flat REE pattern from Ce to Gd and a humped pattern similar to bleached monzogranite from Gd to Lu (Fig. 9b, d, f, h; 10e, f).

A more limited suite of samples was selected from metasedimentary and epiclastic rocks. Five samples of metasedimentary host rocks were analyzed. One, END-10-02A-400 is unaltered, two represent hematized and bleached sides of a U1a-mineralized front in the End Deposit, with the remaining two representing bleached and geothite-bearing sides of a U3 mineralized front in the Kiggavik Deposit. Two samples of epiclastic rocks, one from each side of a sharply defined, U-barren brick-red/bleached alteration front from the Kiggavik North area were analyzed. No albitized samples of these rocks were analyzed.

Hematized metasedimentary rocks are strongly enriched in FeO, moderately enriched in MgO, K_2O, TiO_2, U, and Pb, and strongly depleted in SiO_2, CaO, Na_2O, Sr, REEs, and Th relative to unaltered metasedimentary rocks (Fig. 9a-g; 11a). REE patterns, normalized to unaltered metasedimentary rock END-10-02A-400, form an arc-like pattern, with a positive Ce anomaly (Fig. 11b).

Bleached metasedimentary rocks are enriched is SiO_2, REEs, U, Pb, and are strongly depleted in FeO and moderately depleted in MgO and TiO_2 relative to the hematized metasedimentary rocks they overprint (Fig. 9a, c, e, g; 11a). Elemental abundances in bleached metasedimentary rocks are otherwise similar to hematized metasedimentary rocks. REE are similar to the REE of hematized samples except they do not have a positive Ce anomaly (Fig. 11b).

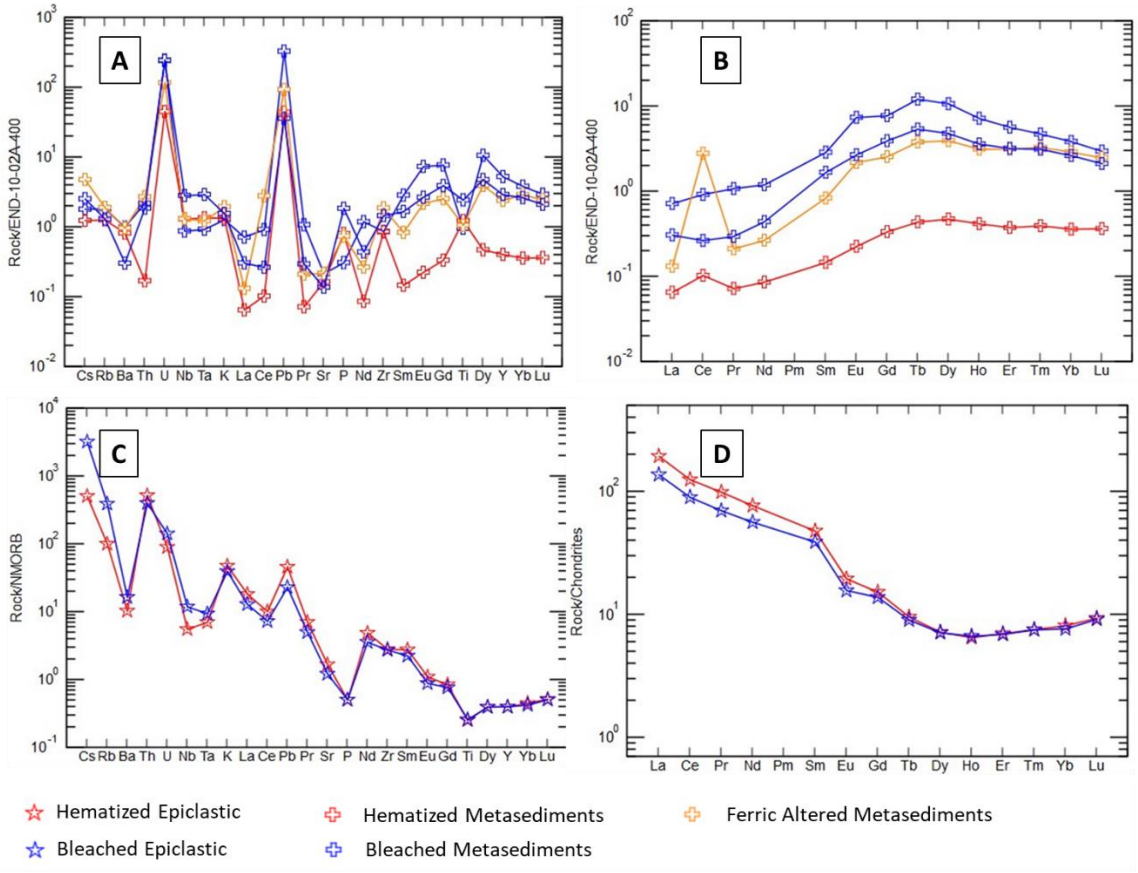

Fig. 11. Trace and REE spider diagrams for epiclastic and metasedimentary rocks. A, B. MORB normalized trace element and REE spider diagrams comparing hematized and bleached epiclastic rocks. C, D. Unaltered metasediment (END-10-02A-400) normalized trace element and REE spider diagrams for hematized, bleached, and ferric altered metasedimentary rocks.

Ferric-altered metasedimentary rocks are enriched in FeO, and K_2O, but are otherwise similar to the bleached metasedimentary rocks they overprint and have very similar REE patterns to the bleached metasedimentary rocks (Fig. 9c, f; 11b).

Bleached epiclastic rocks are depleted in FeO, and enriched in SiO_2, K_2O, and MgO relative to the hematized epiclastics they overprint, but otherwise have very similar elemental abundances (Fig. 9a, c, e, f). NMORB-normalized spider diagrams shows prominent Ba, Nb-Ta, P, and Ti troughs (Fig. 11c), and slight negative Eu anomaly REE patterns (Fig. 11d).

U-Pb and Pb-Pb Geochronology

U-Pb and Pb-Pb isotopic ages were calculated for all U-mineralization generations where the U-minerals were of sufficient size for *in situ* isotopic analysis by SIMS. The corrected isotopic data are presented in Appendix Table A4. These data were plotted to generate U-Pb Concordia ages.

U1a uraninite from a chemical front in the Bong Deposit yielded an extremely discordant U-Pb age of 1594 ± 95 Ma, with an MSWD of 2.3 (Fig. 12a). U1b and U1c uraninite, hosted in both polymetallic and monometallic veins, in the End Deposit yielded a U-Pb age of 1553 ± 16 Ma, with an MSWD of 0.64 (Fig. 12b).

U1b and U1c brannerite mineralization in the End Deposit yielded an age of 1440 ± 21, MSWD 0.9 (Fig. A3a). Some U1b and U1c uraninites in the End Deposit, which are texturally identical to grains with a 1553 ± 16 Ma age, yielded U-Pb ages of either 1417 ± 17 Ma, MSWD 0.82, or less commonly 1249 ± 33, MSWD 3.5 (Fig. A3b, c). Altered U2 from the Kiggavik deposit, altered from a polymetallic U1c vein and associated U1b uraninite, yielded a highly discordant age of 1276 ± 8.7, MSWD 3.4 (Fig. A3d). ‘Worm-rock’ texture U2 disseminated

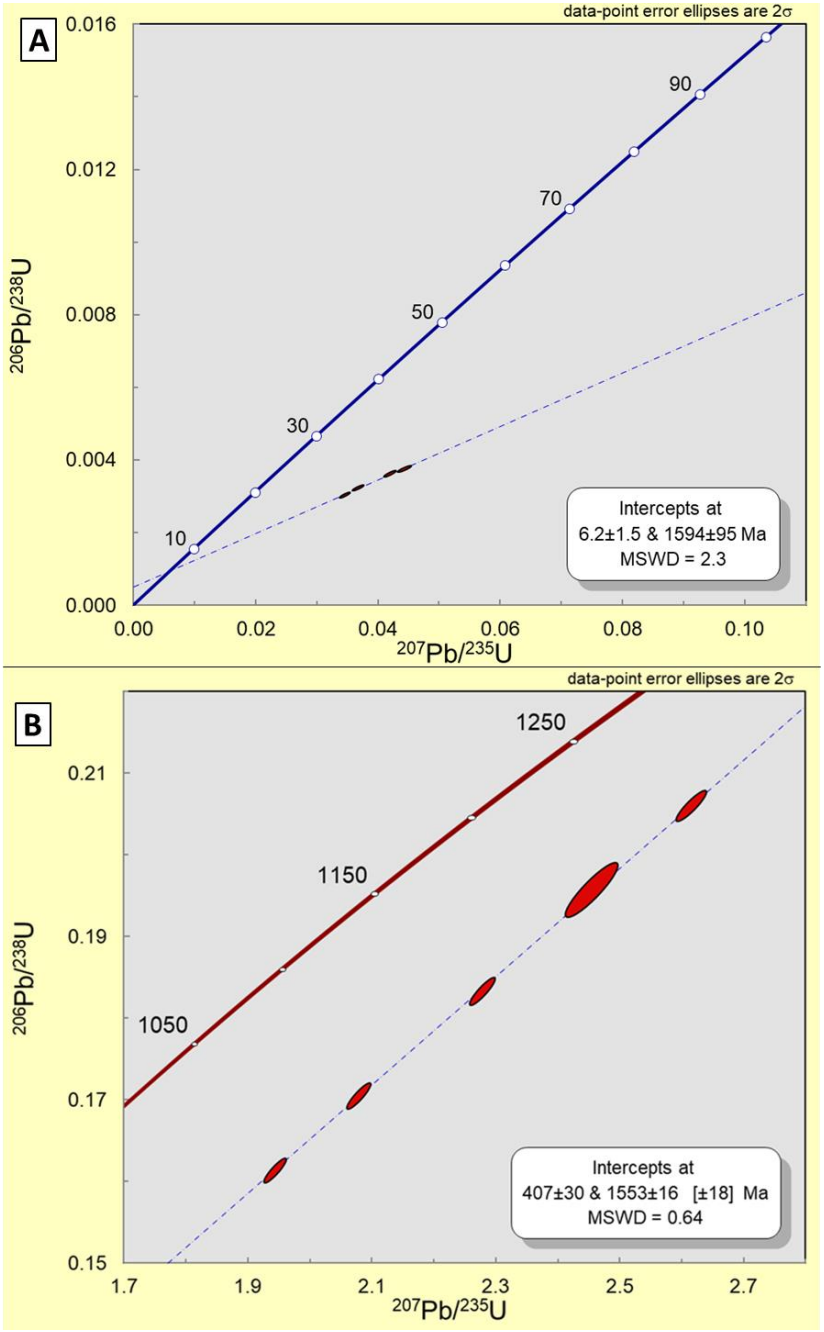

Fig. 12. U-Pb Concordia plots of SIMS data from U1a, b, and c uraninite. A. U1a uraninite from the Bong Deposit. B. U1b and c uraninite from the End Deposit.

uraninite from Andrew Lake yielded a U-Pb age of 937 ± 24, MSWD 14 (Fig. A3e). Anhedral disseminated brannerite from the End Deposit yielded a near-concordant age of 274 ± 69 Ma, with an MSWD of 1.6 (Fig. A3f).

Discussion

Summary of Deposit Models

The Kiggavik U deposits have most often been classified as basement-hosted URU deposits, showing similarities to those deposits in the Athabasca Basin (Jefferson et al., 2007a; b; Riegler et al., 2014; Chi et al., 2016; Shabaga et al., 2017; Ashcroft, 2020; Grare et al., 2020). Some studies, however, have cited evidence, such as polymetallic veining and associations with igneous processes, that show similarities to other types of U mineralization (Weyer et al., 1987; Flotté, 2009; Grare et al., 2020). Some aspects of the Kiggavik deposits, such as albite and K-feldspar alteration, polymetallic veining and presence of brannerite, are potentially consistent with multiple types of U deposits such as metamorphite, metasomatite, granite-related or volcanic-related,. These deposit types, however, do not typically involve the type of widespread, pervasive illite-hematite alteration observed in the Kiggavik deposits, and in the case of metasomatite U, may be linked to MIAC systems (Potter et al., 2019). The lack of shearing or known volcanic centers in the Kiggavik area further argue against volcanic-related or metamorphite models. Most other types of U deposit (sandstone, paleo-quartz-pebble conglomerate etc.) can be ruled out based on Kiggavik's metamorphic and granitic host rocks and clearly hydrothermal alteration and ore textures.

Using the new information obtained in this study, two hypotheses for the origin of the Kiggavik U mineralization will be considered: the unconformity-related U (URU) model and a Metasomatite Iron-Alkali-Calcic-Uranium (MIAC-U) model.

URU deposits are hydrothermal U deposits defined by a spatial and genetic link to an unconformity between a sedimentary basin and the underlying basement. Most known URU deposits are Proterozoic in age and are found in the Athabasca Basin of northern Saskatchewan, and the McArther River Basin of Northern Australia. The diagenetic-hydrothermal metallogenetic model for the URU deposits, in particular the Athabasca deposits, describes the lithostructural framework that controlled the locations and characteristics of the U mineralization (Hoeve and Sibbald, 1978; Hoeve and Quirt, 1984; Jefferson et al., 2007a,b; IAEA, 2018). Components of this model include locations of brittle faulting, movement of basinal brine, focused discharge of reduced basement fluids at sites of dilational fault structures, fluid mixing, basement-sandstone fluid interaction, transport of U, and redox-controlled U mineralization at or near the unconformity. The deposits are structurally-controlled by faults which are generally graphitic (Hoeve and Sibbald, 1978; Hoeve and Quirt, 1984; Wallis et al., 1985; Quirt, 2003; Jefferson et al., 2007a; b; Cloutier et al., 2009; Shehan et al., 2016).

There are three main types of URU deposits that are characterized by the form of fluid interaction and deposit location relative to the unconformity (Jefferson et al., 2007a): (1) basin-hosted deposits involving fluid mixing of oxidized basinal brine with relatively reduced fluids issuing from the basement, (2) basement-hosted deposits involving fluid-rock reactions between wall rock and oxidized basinal brine entering basement fault zones, and (3) unconformity-hosted deposits straddling the unconformity, which may combine elements of basin and basement hosted deposits. For the basin-hosted deposits, fluid-fluid interactions best explain the presence

of massive and fracture polymetallic mineralization, while for the basement-hosted deposits, fluid-rock interactions best explain the presence of monometallic fracture-filling mineralization. All types of mineralization and associated host rock alteration occurred near the unconformity (10's-100's m) at sites of basement/sandstone fluid interaction where a spatially stable redox gradient/front was present (Hoeve and Quirt, 1987). The prevailing hydrological conditions controlled the location of fluid interaction relative to the unconformity. In some deposits mineralization plunges from basin-hosted pods to basement-hosted pods within deposit-scale strike lengths.

Coupled redox and acid-base reactions resulted in precipitation of massive pitchblende/uraninite and minor coffinite with associated hematite and varying amounts of base/precious metals at sites of fluid-fluid and fluid-rock interaction (Hoeve and Quirt, 1984; Quirt, 2003; Jefferson et al., 2007a,b; IAEA, 2018; Alexandre, 2020). However, the geochemical signatures of the individual URU deposits vary significantly. Uranium grades range from <0.1 % to >10% U. Basin-hosted deposits are typically polymetallic containing U plus base metal sulfides and arsenides, and varying amounts of other elements (eg., HREE, Bi, Au, etc.); however, they range from being strongly U-dominant, with very minor accessory elements (eg., Pb, Cu, Ni, Co, S, As, HREE; McArthur River) to sub-equal U+Ni+Co+As mineralization (Key Lake). The basement-hosted deposits tend to be less geochemically diverse, but may still show significant variations in geochemistry, ranging from near-monomineralic U (eg. Rabbit Lake, Millenium) to U with Cu (Eagle Point, McArthur River), V (Sue C), or Au (Cluff Lake).

Concurrent with URU mineralization, pH-, pK-, and pMg-controlled reactions resulted in the formation of host rock alteration haloes made up of several broad zones of differing mineralogy that are dominated by clay minerals (illite), chlorite, tourmaline, hematite, and

desilicification and bleaching (Hoeve and Quirt, 1984; Quirt, 2003; Jefferson et al., 2007a; b; Cloutier et al., 2009; Shehan et al., 2016). Some deposits, like McArthur River, are hosted by sandstone affected by pre-mineralization silicification and display restricted clay mineral alteration haloes. Around basin-hosted deposits, the clay mineral alteration mineralogy is dominantly illitic with sudoite generally being restricted more tightly to the mineralization, with both developed at the expense of kaolinite (eg. Cigar Lake, Midwest, McClean Lake, Collins Bay, Shea Creek). However, around some deposits, chlorite dominates (eg. Spring Point, Maurice Bay). Locally, dravitic tourmaline (alkali-deficient dravite) is an important alteration mineral (McArthur River, Key Lake).

Around the basement-hosted deposits, the dominant host rock alteration is similar to that of the basin-hosted deposits and comprises desilicification, hematization and bleaching, and chloritic clay mineral alteration, with typically lesser amounts of illite, at the expense of metamorphic biotite, cordierite, and garnet (eg., Eagle Point, Rabbit Lake, Sue C). The host rock alteration zone is controlled by, and tightly restricted to, the fault and fracture zones that host the mineralization, with only rare expressions of alteration in the basin above basement deposits. Chloritization (sudoite) is the dominant host rock alteration at basement-hosted deposits (eg. Eagle Point; Sopuck et al., 1983; Quirt, 1989). Illite alteration is characteristic of the core of the altered and mineralized zones, while sudoite occurs immediately peripheral to this zone. The sudoitic alteration grades outward, through an intermediate Mg(-Fe) chlorite, into trioctahedral Fe-Mg chlorite-bearing rock and then biotite-bearing unaltered rock. Minor amounts of dravitic tourmaline are also present in the alteration zone, while bleaching and desilicification (loss of rock coherence) are ubiquitous.

Metasomatic Iron Alkali-Calcic Uranium (MIAC-U) systems, sometimes termed Iron-Oxide-Alkali-Altered Uranium (IOAA-U) systems, are complex metasomatic systems capable of forming a range of diverse hydrothermal deposits including Iron-Oxide-Copper-Gold ± Uranium (IOCG and IOCG-U), Iron-Oxide-Apatite (IOA), and albite-hosted U (Corriveau et al., 2022a; b; Skirrow, 2022). Based on the IAEA deposit classification scheme (Fayek, 2013; IAEA 2014) these deposits are metasomatite type uranium deposits. Some of these deposits, such as IOCGs, are rich in Fe, whereas others, such as most albite-hosted U deposits, are Fe poor (Corriveau et al., 2022a; b). The MIAC concept was proposed relatively recently to explain the observed temporal and spatial associations between these apparently disparate deposit types, although the precise nature of the links between these deposit families is a subject of debate (Groves et al., 2010; Wilde, 2013; Barton, 2014; Montreuil et al., 2015; Corriveau et al., 2016; Potter et al., 2019; Skirrow, 2022).

The tectonic settings of MIACs are variable; magmatically-active extensional continental arc and rift settings are most common for IOCGs and iron-rich Cu deposits, although this may not necessarily be the case for all the possible deposit types developed from these systems (Barton, 2014; Corriveau et al., 2022a; b; Skirrow, 2022). Deposits age from the Archean to the Cenozoic, however albitite-hosted deposits, which comprise the majority of primary U deposits developed in MIAC systems, are concentrated between 1900-1500 Ma (ie the 1851-1800 Ma Michelin Deposit, Central Mineral Belt (CMB), Canada (Sparkes et al., 2017), the 1870-1840 Ma Great Bear Magmatic Zone (GBMZ), Canada (Montreuil et al., 2015), and the 1555 Ma Valhalla Deposit, Mt Isa District, Asutralia (Polito et al., 2009). They are also commonly hosted within Proterozoic metamorphic terrains, especially those that are 2000-1800 Ma (Wilde, 2013; Sparkes et al., 2017) and within and/or immediately beneath volcano-sedimentary basins,

typically of continental to shallow marine character, affected by syn-mineralization igneous activity (ie. deposits of the GBMZ, CMB, Mt Isa). Deposits developed in MIAC systems characteristically display a strong temporal, but weak spatial, association with regional igneous events (Groves et al., 2010; Barton, 2014; Skirrow, 2022).

Mineralization in most known deposits formed in MIAC systems is linked to magmatic-hydrothermal fluids mixing with meteoric/basinal fluids as well as reacting with country rocks (Groves et al., 2010; Barton, 2014; Corriveau et al., 2022b; Skirrow, 2022). These deposits are characterized mainly by the presence of extensive, often overprinting facies of Fe-Na-K-Ca alteration, with one or several of these facies developed in individual deposits. Other common, although not universal, features include an evolution from early sodic/calcic to later potassic and Fe alteration, brecciation, quartz-carbonate veining, and extensive (specular) hematite-sericite-chlorite alteration. Iron-oxides are typically the dominant Fe-minerals, although Fe alteration can sometimes take the form of Fe-sulfides, silicates, and carbonates.

The main economic elements in deposits formed in MIAC systems include Cu, Au, Fe, U, Co, Bi, REE, Ni, Mo, W, and Ni. Primary U deposits developed in MIAC systems tend to be relatively low-grade (<0.2% U_3O_8), large tonnage deposits (Cuney and Kyser, 2008). Notable U-rich deposits developed in MIAC systems include Valhalla, Mt Isa District, Queensland, Australia (Polito et al., 2009; Wilde et al., 2013); Michelin, Central Mineral Belt, Labrador, Canada (Sparkes, 2017; Duffet et al., 2020); Aricheng South, Guyana (Alexandre, 2010); and the Southern Breccia Zone showings and Sue Dianne deposit, GBMZ; Northwest Territories, Canada (Montreuil et al., 2015; 2016a; b; Corriveau et al., 2016; Potter et al., 2019). The GBMZ is the nearest well-studied MIAC system to the Kiggavik area, although U-rich MIAC mineralization has been reported from MacInnis Lake Area, Nonacho Basin, Northwest Territories (Landry et

al., 2022). Many other deposits developed in MIAC systems, such as the Olympic Dam deposit (South Australia), a Fe-Cu hematite group IOCG, host low-grade (<0.1% U_3O_8) but potentially large-tonnage U resources.

MIAC systems are known to form a suite of deposits linked to spectrum of alteration facies (Montreuil et al., 2015; 2016; Corriveau et al., 2016; 2022a-d; Potter et al., 2019). MIAC systems typically evolve from early, deep, high-T facies to later, shallower, low-T facies (Montreuil et al., 2015; 2016; Corriveau et al., 2016; Potter et al., 2019). This general relationship is complicated by the fact that later-formed facies are often superimposed on, and may pervasively replace, earlier-formed facies, and that one or more facies may not be developed in an area or may go unrecognized due to the cryptic or unexpected nature of the alteration (Montreuil et al., 2015; 2016; Corriveau et al., 2016; Potter et al., 2019; Skirrow, 2022).

The early, high-T endmember of the MIAC spectrum consists of albitization corridors, in which albitites can be formed over 100's – 1000's of m, which tend to be developed above subvolcanic intrusions and along fault systems, and are dominated by secondary albite, with lesser quartz, titanite, zircon, Ti-oxides, and Fe-oxides (Montreuil et al., 2015; Corriveau et al., 2016; Potter et al., 2019). This albitization is the result of <600° C Na ± Ca metasomatism and serves as ground preparation for later facies (Montreuil et al., 2015; 2016; Corriveau et al., 2016; Potter et al., 2019). This albitization destabilizes most minerals within the protolith, potentially liberating large amounts of metals which may participate later alteration facies and mineralization (Corriveau et al., 2016; 2022b; Acosta-Gongora et al., 2022a). Albitization also creates porosity and permeability through mineral dissolution and brecciation of host rocks, making albitized areas favorable sites for continued alteration and mineralization (Corriveau et al., 2016; 2022b; Potter et al., 2019).

In MIAC districts such as the GBMZ early albitization may be followed by higher-T (<800° C) Ca-Fe ± Na, Mg metasomatism, which is characterized by extensive replacement of host rocks by amphiboles, magnetite, and apatite, and sometimes by formation of IOA deposits (Corriveau et al., 2016; 2022a; b). High-T Ca-Fe metasomatism may then be followed by high-T K-Fe alteration, where biotite and Fe-oxides form at the expense of earlier-formed amphibole, or K-feldspar and Fe-oxides replace less altered or albitized host rocks (Corriveau et al., 2016). This type of alteration is associated with magnetite-facies IOCG deposits (Corriveau et al., 2016; Skirrow, 2022), and, in some U deposits such as the Southern Breccia Zone in the GBMZ, primary U mineralization (Montreuil, et al., 2015). The magnetite-hematite facies transition is marked by the development of more aerially restricted K-feldspar-rich breccias and, in carbonate-rich hosts, skarns (Corriveau et al., 2016; 2022). This transitional facies, as well as earlier albitization, is sometimes marked by development of albitite-hosted U deposits, low-grade U deposits where U may be hosted in a range of minerals such as uraninite, coffinite, brannerite, and silicates such as zircon and uranothorite in a matrix dominated by porous albite, within early-formed albitite-corridors (Alexandre, 2010; Wilde, 2013; Montreuil et al., 2015; 2016; Potter et al., 2019; Duffet et al., 2020).

High-T Fe-K metasomatism may be followed by low-T Fe-K alteration assemblages defined by K-feldspar and hematite, or a more hydrolytic assemblage dominated by carbonate-chlorite-hematite-muscovite/illite (Corriveau et al., 2016). This low-T Fe-K alteration tends to form at shallow depths (<1 km) and is associated with hematite-group IOCG-U mineralization at very large Australian deposits such as Olympic Dam and Prominent Hill (Skirrow, 2010; Corriveau et al., 2016). In the GBMZ, the latest alteration facies is characterized by epithermal fluids, leading to development of quartz and barite veins as well as phyllic, argillic and advanced

argillic alteration assemblages in areas such as Port Radium, Terra, and the NICO deposit (Mumin et al., 2010; Corriveau et al., 2015; Corriveau et al., 2016). This late epithermal alteration also altered primary uraninite to coffinite in many GBMZ systems (Corriveau et al., 2016).

Many deposits formed in MIAC systems have U contents ranging from <10 to a few 100 ppm, but primary U deposits such as Valhalla and deposits in the CMB may exceed 1000 ppm U (Hitzman and Valenta, 2005; Wilde et al., 2013; Duffet et al., 2020). The reason for such variable U grades is uncertain, but may be tied to the U content of host rocks, as acidic, relatively oxidized ore-forming fluids in MIAC systems are believed to be capable of leaching substantial amounts of U from host rocks (Hitzman and Valenta, 2005; Schlegel et al., 2018; 2020). Relatively oxidized, sulfide-poor deposits developed in MIAC systems formed in post-orogenic extensional settings (ie Olympic Dam) tend to be the most U-rich (Skirrow, 2022).

Uranium is prone to becoming remobilized in some deposits formed in MIAC systems, likely because hexavalent U could be quite mobile in the relatively low-T, oxidized fluids which prevail in later stages of MIAC systems, allowing U to become decoupled from its original host alteration and metal association (Potter et al., 2019). Such a process likely formed late, U-mineralized 5-element veins in the GBMZ (Gandhi et al., 2018; Potter et al., 2019; Acosta-Gongora et al., 2022a).

Uranium mineralogy in MIACs is variable and often complex, although an assemblage dominated by uraninite, often with minor coffinite and brannerite, is most common (Hitzman and Valenta, 2005; Skirrow, 2022). Uranium mineralization in GBMZ deposits comprises uraninite, coffinite, and brannerite, with U-bearing thorite, zircon, hydrothermal Zr ± U-Th-Ca-Al silicates, Ti-oxides, Fe-oxides, and many other minerals being commonly present (Montreuil, et al., 2015;

Potter, et al., 2019). Uranium in the GBMZ is hosted in albitites, as well as late, polymetallic U-Ag-Cu-Ni-Co-Bi veins, alteration fronts, and disseminations (Montreuil et al., 2015; 2016; Potter et al., 2019). Uranium in the CMB deposits is associated with albitites and is hosted primarily in uraninite, with some alteration to coffinite, and more rarely brannerite, (urano)thorite, and zircon (Acosta-Góngora, et al., 2022a; b; Duffet, et al., 2022). In the Valhalla deposit, U-rich minerals include uraninite, brannerite, and uraniferous zircon within albitized sedimentary rocks (Polito, et al., 2009; Wilde, et al., 2013).

Geochemistry and Mineralogy

Pre-ore Alteration Interpretation of whole rock geochemistry is based largely on granitic rocks. Although trends of element mobility are generally similar between host rock types, the absence of a whole-rock geochemistry data from albitized metasedimentary rocks and both unaltered and albitized epiclastics, limits interpretation of the alteration of these rocks.

The observed removal of Ca and addition of Si in albitizied monzogranite is consistent with a more calcic magmatic plagioclase being replaced by albite and quartz. The variable contents of Na_2O and K_2O suggests these were mobile, but obscures whether or not these were systematically transported into or out of the system.

Pseudomorphic alteration is accompanied by a strong depletion in HFSE such as P_2O_5, Zr, Th, REE, and TiO_2 which are normally considered to be immobile in hydrothermal fluids. This is consistent with the observation of corroded magmatic zircon (Zr1), monazite, and Fe-Ti oxides (Fig. 7e-g). The precipitation of Zr-rich uranothorite and hydrothermal zircon (Zr2) in equilibrium with fluorite within dissolution pits (Fig. A2b) and the presence of up to 0.62 wt% Cl in Zr2 indicates the albitizing fluids contained both F and Cl. The transport of ‘insoluble’ HFSE

by F and Cl rich fluids has been described in U-Cu-Fe showings of the Fab magnetite IOCG system in the GBMZ (Montreuil et al., 2016b). The observation of S and P impurities in Zr2 and uranothorite also suggests these fluids contained these elements as well.

This fluid introduced U, increasing U content in the affected monzogranites by a factor of approximately 4. The presence of pyrite, galena, and other sulfides indicates these fluids were reduced, suggesting U was transported in its U^{4+} state, which is soluble in acidic F-bearing fluids (Hazen et al., 2009; Xing et al., 2019). The magnitude of Pb enrichment, which is significantly greater than that of U, suggests this fluid also introduced Pb independent of the radiogenic Pb created by the decay of U and Th. The unusual mineral assemblage infilling dissolution pits, rich in apatite, muscovite, Zr-Th-U silicates, Ti(Nb) oxides, and more locally REE minerals, sulfides, and fluorite, likely formed from fluids which became trapped as dissolution features filled in.

Similar mineral assemblages have been reported from the Southern Breccia and Fab U showings (Montreuil et al., 2015; 2016b) as well as granites and rhyolites in the Olympic Dam Province (ODP) (Agani et al., 2010; Domnick et al., 2017; 2020a; b). In the ODP, these minerals often occur in pockets similar to those observed in Kiggavik (Agani et al., 2010; Domnick et al., 2017; 2020a; b) and are interpreted to have been formed from late-stage magmatic fluid that was rich in F, CO_2, P, and S (Agani et al., 2010).

Another common observation concerning the Lone Gull granitic rocks is corrosion of magmatic zircon (Zr1) and precipitation of hydrothermal zircon (Zr2) that is enriched in Ca and Al (±Fe, Th, U) and depleted in Si and Zr. Hydrothermal, often U-bearing, zircon is a common feature of albitite hosted U deposits (Alexandre, 2010; Wilde et al., 2013; Montreuil et al., 2015). Hydrothermal zircon formed in these systems is typically enriched in U, Al, Fe, Ca, and other non-formula elements, depleted in Zr and Si, and often has low microprobe totals (Alexandre,

2010; Wilde et al., 2013; Courtney-Davis et al., 2019), which is consistent with the Zr2 observed at Kiggavik. Courtney-Davis et al. (2019) concluded that an enrichment of non-formula elements in zircon, particularly Fe, Al, Ca and Mn, as well as depletion in Si and Zr, was diagnostic of the metasomatic overprint associated with the development of a MIAC system in the Roxby Downs granite surrounding the Olympic Dam IOCG deposit. While hydrothermal (urano)thorite has been observed in the Southern Breccia deposits and showing (Montreuil et al., 2015), the solid solution between uranothorite and Zr2 observed in Kiggavik is highly unusual. Such solid solutions between Zr, U, and Th silicates is only possible when these minerals are hydrated and likely requires F-bearing fluids rich in Zr, U, and Th (Förster, 2005). This solid solution may be analogous to the unusual solid solution developed between hydrothermal zircon and a U-silicate described by Wilde et al. (2013) in the Valhalla albite U deposit.

Pervasive albitization corridors are diagnostic features of primary U deposits developed in MIAC systems (Groves et al., 2010; Barton, 2014; Corriveau et al., 2016; Kontonikas-Charos et al., 2017; Corriveau et al., 2022a; b). This Na metasomatism typically produces dramatic changes to the host rock's mineralogy and chemistry to produce nearly pure albitites associated with primary U deposits developed in MIAC systems (Corriveau et al., 2022a; b). Feldspars in the Kiggavik deposits have been ubiquitously altered, as shown by their substantial microporosity, intergrowth with muscovite/sericite ± K-feldspar and rarely fluorite, near end-member albite plagioclase compositions, and late K-feldspar overgrowths; true albitites, however, were not observed at the Kiggavik deposits. The original extent of albitization is difficult to fully access due to pervasive, texturally destructive overprinting illitization and hematization, it is highly likely that much of the albitized rocks have been preferentially altered by subsequent fluid events, as albitites tend to be porous and brittle leading to preferential

alteration, replacement, and mineralization during later fluid events (Putnis and Austrheim, 2010; Putnis, 2015; Corriveau et al., 2022a; c; d). While the original extent of albitization has been obscured, the presence of albitization at all four studied deposits, which span a >20 km trend, indicates it is widespread in the project area. In the Kiggavik Deposit this alteration is particularly pervasive, with no unaltered feldspar surviving in any of the studied granitic rocks throughout 100's of m of drill core. This alteration is spatially associated with U mineralization (10-100's m from ore zones) and has not been observed regionally in areas more distal from U deposits, consistent with the localization of U deposits within zones of albitization observed in many U-rich MIAC systems globally (Polito et al., 2009; Alexandre, 2010; Wilde, 2013; Duffet et al., 2020; Corriveau et al., 2022a-d).

Although albitized rocks show mobility of many of the HFSE, which is not unusual in albitite U deposits and U-rich MIAC systems (Alexandre, 2010; Wilde et al., 2013; Corriveau et al., 2022b), Kiggavik is unusual in that HFSE are depleted rather than enriched, with an enrichment in Si rather than Na. The remnant albitization in Kiggavik may represent a zone of net HSFE leaching and U-bearing silicification developed on the periphery of the system. Kiggavik is also unusual in that it contains no mafic minerals such as amphiboles which are commonly a major constituent of albitites developed in many U-rich MIAC systems (Corriveau et al., 2022a; b). It is possible that Kiggavik formed in an unusually shallow, low temperature environment which did not favor the formation of higher temperature mafic minerals, or that subsequent intense alteration completely altered these high temperature minerals.

The enrichment of FeO in hematized monzogranite is due to the formation of hematite, and indicates oxidizing fluids transported Fe rather than merely oxidizing preexisting Fe-bearing minerals. The hematizing fluid also introduced Mg, hosted in chlorite and illite, and HFSE such

as Ti, P, Zr, and REE. The detection of Ti, P, and Zr by EDS in specular hematite suggests that HFSE may be hosted as substitutions in hematite. The depletion of SiO_2 and Na_2O correlates with observed quartz corrosion and the complete absence of albite/plagioclase in hematized rocks. The variable K_2O and U enrichment/depletion indicates these elements were mobile but prevents confident identification of systematic trends.

Where protoliths of hematized rocks are identifiable, these protoliths have been albitized, with distinctive mineral assemblages such as aggregates of Zr2, Ti-oxides, apatite, and muscovite being preserved, while quartz and feldspars have undergone varying degrees of corrosion and sericitization, respectively. In more intensely hematized rocks, protolith textures and mineralogy are not preserved; the observed uniform distribution of massive illite and hematite with only traces of remnant quartz, muscovite, apatite, zircon, and Ti-oxides, however, would be consistent with a hematized and sericitized albitite.

Hematization is spatially, and likely temporally, associated with the QB (Grare et al., 2018). Based on studies of fluid inclusions, oxygen isotopes, cathodoluminescence and trace elements, Grare et al. (2018) concluded the QB formed via mixing of a >350° magmatic fluid, and a lower temperature meteoric fluid in an epithermal setting, with many pulses of brecciation, quartz-magnetite/hematite precipitation, and influxes of fresh magmatic fluids. These fluids may be similar to the magmatic-hydrothermal fluids responsible for albitization and subsequent brecciation and high-temperature Fe alteration in the Southern Breccia U deposits and showings (Montreuil et al., 2015).

The observation of uraniferous zircon (Zr2) and muscovite in dissolution pits, a texture common in Kiggavik albitized rocks, associated with a late specular hematite veins crosscutting the QB, suggests a spatial and temporal link between albitization and hematization. It is

intriguing that hematized rocks are enriched in many of the same HFSE that are depleted in albitized rocks, raising the possibility that elements leached during albitization became concentrated in later hematizing fluids, similar to the recharging and metal enrichment of fluid plumes in MIAC systems (Corriveau et al., 2022b; e).

The possibility of a link between albitization and hematization raises a further possibility: that the regional hematite altered corridors developed along regional faults in the Kiggavik/Theon Basin area may represent the altered remains of albitization corridors, which would be analogous to the albitization corridors which are commonly developed along major faults in MAIC systems (Montreuil et al., 2015; Corriveau et al., 2016; 2022a-e; Potter et al., 2019). Unfortunately these corridors of hematite alteration are severely understudied and their origin and link to mineralization, if any, is unclear.

Mineralization and Associated Bleaching Bleached monzogranite is strongly depleted in FeO, consistent with the observation that removal of hematite is the main mineralogical difference from hematized rocks. The depletion of TiO_2 and REE may also be a result of de-hematization if these were hosted mainly in hematite. Potassium content is once again variable, although on average there appears to be an enrichment in K_2O associated with bleaching. Bleaching introduced significant amounts of U, with the most significant U enrichment, and the presence of uraninite, coffinite, and brannerite, being associated with vuggy quartz ± calcite veins.

Uranium mineralization in the Kiggavik area is mineralogically diverse. While uraninite is the dominant U-mineral, coffinite and brannerite are also present. Brannerite is particularly common in the End Deposit. All of these minerals occur intergrown, and commonly yield statistically identical U-Pb ages, indicating this assemblage is primary, rather than the result of

subsequent alteration. The close spatial and temporal association between these minerals suggests contents of Si and Ti in mineralizing fluids fluctuated. Although much U-mineralization occurs as monometallic veins and disseminations, polymetallic veins are common, and are texturally and geochronologicaly cogenetic with monometallic mineralization.

The suite of minerals associated with polymetallic U-bearing veins and disseminations is even more diverse, with various combinations of Fe-Cu-Mo-Pb-Ni sulfides, native Bi and Bi ± Pb, Cu, PGE sulfides/selenides/tellurides, barite, bertrandite, and trace native Au observed. While pyrite generally predates the U minerals, other minerals in polymetallic veins are contemporaneous with uranium mineral formation. The observation of U-minerals rimming and replacing Fe-sulfides and surrounding Ti-oxides in U1 mineralization indicates these early-formed minerals also acted to facilitate U deposition in a manner very similar to what is observed in the MacInnis Lake MIAC related U occurrences (Landry et al., 2022).

The uraninite observed in the Kiggavik deposits is low in Th, indicating it formed under low temperature conditions (Mercadier et al., 2011; Frimmel et al., 2014). Uraninite formed in U-rich deposits developed in MIAC systems can form at either high or low temperatures, with generations of both high and low temperature uraninite sometimes occurring together in the same deposit (Duffet et al., 2020). Much of the uraninite in the GBMZ formed at high temperatures (Montreuil et al., 2015), whereas all uraninite formed at low temperatures in occurrences such as MacInnis Lake in the Nonacho Basin, Northwest Territories (Landry et al., 2022). Uraninite also forms at low temperatures in unconformity related deposits (Wilson and Kyser 1987; Alexandre et al., 2005; Jefferson et al., 2007b).

Many of the alteration minerals observed in the Kiggavik deposits, such as illite, sudoite, Fe-Mg chlorite, and hematite, are part of the alteration suite typical of basement-hosted

unconformity deposits (Jefferson et al., 2007a; b). The clay alteration in the Kiggavik deposits is, however, dominated by illite, with only relatively minor sudoite and no systematic gradation or zonation between these minerals, which is not typical of basement-hosted URUs. Dravitic tourmaline, which is ubiquitous in basement-hosted URUs, is absent in the Kiggavik deposits. Specular hematite, which is commonly present in the Kiggavik deposits, is typical of IOCG deposits (Barton, 2014), but uncommon in URU deposits. The pargenetically early porous albite + sericite alteration of feldspars has not been observed in unconformity deposits. Although quartz corrosion is common and zircon corrosion has been described locally in some sandstone-hosted unconformity deposits in the Athabasca Basin (Quirt et al., 1991; Jefferson et al., 2007a; b), the precipitation of hydrothermal Zr-Th±U minerals has not been documented.

Mineralizing fluids in the Athabasca Basin are interpreted as basinal brines originating from seawater, as indicated by both fluid-inclusion and isotopic studies, notably B isotopes in dravite (Sheahan et al., 2016; Martz et al., 2019; Alexandre, 2020). In contrast, dravite is not present in the Kiggavik area, and isotopic studies have failed to find unambiguous evidence of basinal fluids (Sharpe et al., 2015; Ashcroft, 2020; Shabaga et al., 2020). There is little evidence to suggest that F played a major role in fluid chemistry or deposit formation.

The polymineralic and polymetallic nature of U mineralization in the Kiggavik area is not consistent with a basement-hosted URU deposit. While base metal sulfides and arsenides are not uncommon in sandstone-hosted unconformity deposits, basement-hosted deposits are typically far more monometallic (Jefferson et al., 2007a; b; IAEA, 2018; Alexandre, 2020). The presence of brannerite, bertrandite, barite, and Bi-minerals is particularly unusual, as these minerals have not been reported from Athabasca Basin URU deposits. Furthermore, the Fe-oxides and sulfide minerals that are present in URUs are typically paragenetically later than U minerals (Fayek and

Kyser, 1997; Alexandre et al., 2009), which is the opposite of what is observed in the Kiggavik deposits.

Unlike basement-hosted URU deposits, U mineralization developed in MIAC systems commonly contains a very diverse suite of minerals. All of the U-bearing minerals identified in the Kiggavik deposits are present in the U-rich MIAC districts such as the ODP, GBMZ, CBM, and Mt Isa (Wilde et al., 2013; Montreuil et al., 2015; Gandhi et al., 2018; Duffet et al., 2020; Ehrig et al., 2021). In addition to U, polymetallic veins in the GBMZ are commonly mineralized with a diverse suite of metals, including Ag, Au, Cu-Ni-Co-Pb-Zn-Mo sulfides, and native Bi, among others (Montreuil et al., 2015; 2016; Corriveau et al., 2016; Gandhi et al., 2018; Potter et al., 2019). Although bertrandite is not typical of MIAC or URU deposits it is sometimes present in volcanogenic U deposits and other F-rich, U-bearing epithermal systems (Ayuso et al., 2020; Bonnetti et al., 2021).

Structural Controls

By definition, URU deposits have a strong spatial and genetic link to an unconformity, specifically between sedimentary basin strata and underlying metamorphic lithologies. Faults, which acted as major conduits for fluid flow between the basement and basin lithologies, are the major local structural control for unconformity deposits (Jefferson et al., 2007a; b; IAEA, 2018). The graphitic nature of these basement faults has been interpreted to have also contributed to the mineralization process by acting as a redox trap for oxidized, U-bearing fluids (Hoeve and Sibbald, 1978; Hoeve and Quirt, 1984; Alexandre et al., 2005; 2009; Cloutier et al., 2009; Jefferson et al., 2007a; b; Martz et al., 2019).

Although the Kiggavik deposits almost certainly formed beneath an unconformity, its role, if any, is difficult to access because the unconformity itself has been eroded away in the project area (Sharpe et al., 2015; Grare et al., 2020). The Kiggavik deposits are hosted within and controlled by basement fault systems (Riegler et al., 2014; Chi et al., 2016; Shabaga et al., 2017; Grare et al., 2018; 2020; Ashcroft, 2020), however, these faults are notably lacking in graphite (Riegler et al., 2014; Sharpe et al., 2015; Grare et al., 2020). While the overall setting of the Kiggavik deposits around and in the Thelon Basin shares some similarities with URU deposits in the Athabasca Basin, these similarities do not necessarily establish a similar genesis for mineralization.

While many studies have emphasized the potential role of basinal fluids in the Kiggavik deposits and similarities between the Athabasca and Thelon basins (Jefferson et al., 2007a; b; Shabaga et al., 2017; Grare et al., 2020), the area also has a complex history of tectonic and igneous activity. The Thelon and Judge Sissons fault, major regional fault systems which host the End deposit, are long-lived features which have a complex history of reactivation and hydrothermal activity (Grare et al., 2020; Hunter et al., 2021). Initial faulting occurred at ~1830-1760 Ma (Hunter et al., 2021), with early faulting events likely related to the end stages of the Hudsonian orogeny (Grare et al., 2020). This was followed by an epithermal faulting and silicification event, which formed the QB, attributed to ~1750 Ma (Grare et al., 2020; Hunter et al., 2021). These early 1830-1760 and ~1750 Ma faulting events are similar in age to the ~1830 Ma Hudson and ~1750 Ma Nueltin intrusions. Late (~1600-1300 Ma) reactivation events may be related to U mineralization (Grare et al., 2020; Hunter et al., 2021).

Many Kiggavik deposits and prospects share a spatial association with igneous intrusions (Fig. A4a), with some hosted partially within or immediately overlying igneous bodies.

Albitization is more pervasively developed, or at least more systematically preserved, in Kiggavik granitic rocks, including at least one dyke observed in the End Deposit, suggesting an association between albitization and igneous processes. Albitization has been linked to igneous activity in the GBMZ (Montreuil et al. 2015; Corriveau et al, 2016). An association to igneous processes is also shown by the Quartz Breccia (QB), which is closely spatially associated with U mineralization in all of the Kiggavik deposits and is present even in deposits which lack an obvious association with intrusions themselves (Flotte, 2009; Chi et al., 2016; Grare et al., 2018; 2020; Fig. A4b).

Many deposits developed in MIACs systems are associated with extensive breccia complexes. As well as the spatial association with the QB, a number of U1c veins exhibit small-scale brecciation of host rocks, and ~cm scale brecciation and micro-fracturing is commonly observed in the Kiggavik Deposit granitic rocks. It is possible that the ore zone formed in rocks that underwent more extensive pre-syn ore brecciation, as the heavily-illite altered rocks making up most of the ore zone do not preserve host rock textures.

Evidence from fluid inclusions indicates the End Deposit formed at a depth of ≤2 km (Chi et al., 2016). A shallow depth of formation is also supported by the common observation of epithermal textures such as colloform banding, open vugs, and comb-texture quartz. Such a shallow depth would be at odds with most URU deposits, which typically form at a depth of ≥5 km (Kotzer and Kyser, 1995; Jefferson et al., 2007b; Richard et al., 2016; IAEA, 2018). In contrast, MIAC deposits are known to form over a range of depths, which may be as shallow as ≤2 km in the ODP (Oreskes and Einaudi, 1992; Courtney-Davis et al., 2020; Schlegel et al., 2020).

Geochronology

Despite relatively few studies reporting isotopic ages from the Kiggavik region, these ages vary considerably (App. Table A1). The new 1594 ± 95 Ma U-Pb Concordia age from U1a in the Bong Deposit and 1553 ± 16 Ma U-Pb age from U1b and U1c in the End Deposit are the oldest and second oldest ages reported from U-minerals in the Kiggavik region, respectively. Both of these ages agree with the previous oldest age, 1520 ± 79 Ma, which was obtained from disseminated uraninite from the Bong Deposit by Sharpe et al. (2015). The 1594 ± 95 Ma age is in good agreement with the 1589 ± 39 Ma Pb-Pb age obtained from galena in the Kiggavik deposit (Fayek et al., 2019), as well as muscovite Ar-Ar ages of 1604 ± 4 Ma from the End Deposit (Ashcroft, 2020) and 1599 ± 20 Ma from the Andrew Lake deposit (Shabaga et al., 2017). These muscovites are not spatially associated with U mineralization (Shabaga et al., 2017; Ashcroft, 2020), and while they may correspond to metamorphic muscovite affected by an early alteration event (Ashcroft, 2020), the significance of these ages in the context of mineralization is not clear.

Although it is conceivable that the 1594 ± 95 Ma age obtained from Bong U1a accurately represents the age of primary mineralization, this interpretation is complicated by the fact that uraninite is known to be readily affected by Pb-loss and isotopic resetting to younger ages. The high degree of discordance in the U-Pb data which gave the ~1594 Ma age produced a large error (± 95 Ma) and indicates these minerals have experienced significant alteration and Pb-loss.

A second, more likely, possibility is that the 1594 ± 95 Ma age represents a low-precision replication of the 1553 ± 16 Ma age obtained from U1b and U1c uraninite in the End Deposit. These U1b and U1c minerals often occurred within a few cm of paragenetically coeval U1a minerals. 1553 ± 16 Ma is considered likely to represent the primary age of mineralization rather than a resetting event because uraninites yielding this age comprise relatively large, euhedral

grains which preserve primary zoning and contain only small amounts of CaO and SiO_2 impurities. They are the most texturally and chemically pristine U-minerals observed. Furthermore, the U-Pb isotopic data obtained from these uraninites are statistically robust, comprising 31 highly consistent data points. Despite being sourced from four separate drillholes, analyses of these uraninites frequently yield $^{207}Pb/^{235}U$ and $^{206}Pb/^{238}U$ ratios which are identical within error. The relatively low degree of discordance of these data supports a low degree of isotopic resetting.

A 1553 ± 16 Ma primary mineralization age is the same, within error, as the 1540 ± 30 Ma U-Pb baddeleyite age obtained by Chamberlain et al. (2010) for the formation of the Kuungmi Formation shoshonitic basalts which cap the Thelon Basin (Hiatt et al., 2003; Chamberlain et al., 2010; Jefferson et al., 2013). While very little material has been published on the Kuungmi basalts, it is postulated that their location was controlled by major faults (Hiatt et al., 2003; Chamberlain et al., 2010). Furthermore, Chamberlain et al. (2010) noted the presence of vesicle-rich, diapir-like pipes within the Kuungmi basalts suggests the presence of volatile-rich, late-stage melts rising through earlier flows.

Although the Kuungmi basalts are not observed in the Kiggavik area, igneous activity in the region, including the Hudson and Nueltin granites and the QB, was controlled by fault systems showing evidence of repeated reactivation and/or fluid activity (Scott et al., 2015; Grare et al., 2018; 2020), much like the fault systems controlling U mineralization in the region. If Kuungmi age ultrapotassic igneous activity were accompanied by fluids, it is plausible that such fluids could have exploited the same faults as previous igneous activity in the Kiggavik area. This would be consistent with the observation that while MIACs display a strong temporal link to intrusions, they often form at considerable distance from their causative intrusion, and

frequently do not display a clear spatial association with them (Groves et al., 2010; Barton, 2014; Skirrow, 2022).

At the time of Kiggavik U1 mineralization, ~1.6-1.55 Ga, what is now northwestern Canada was in contact with what now are parts of Australia (Thorkelson et al., 2001; Nordsvan et al., 2018; Verbaas et al., 2018). It has been proposed that both areas were part of the same U-mineralized MIAC province (Thorkelson et al., 2001; Verbaas et al., 2018), which would include 1595 ± 5 Ma (Thorkelson et al., 2001) U-bearing IOCG mineralization in the Wernecke Breccia, Yukon (Laughton et al., 2005), as well as the ODP and potentially Mount Isa albitite-hosted U deposits.

The ages obtained from U1, 1594 ± 95 Ma for U1a and 1553 ± 16 Ma for U1b and U1c, are consistent with the ages U-rich MIAC systems in Australia such as the ODP, including the 1591 ± 1 Ma (Courtney-Davies et al., 2020) Olympic Dam IOCG deposit, as well as smaller IOCG deposits and prospects dated to as late as 1567 ± 10 Ma (Skirrow et al., 2007; Reid et al., 2013), and the 1.56-1.51 Ga Mount Isa albitite-hosted U deposits and associated IOCG deposits (Oliver et al., 2004; Wilde, 2013). Overlap in age is particularly strong between 1553 ± 16 Ma U1b and U1c mineralization at Kiggavik and the 1551±7 Ma Valhalla albitite-hosted U deposit (Polito et al., 2009).

Deposits of the GBMZ are much older than the Kiggavik deposits, having been dated to ~1875-1855 Ma (Corriveau et al., 2016; Gandhi et al., 2018). The GBMZ deposits are linked to igneous activity, with deposition peaking at the time of high-K calc-alkaline to shoshonitic magmatism in the GBMZ (Gandhi et al., 2001; Azar, 2007; Hildebrand et al., 2010; Montreuil et al., 2016a). The GBMZ deposits formed beneath and within a Mesoproterozoic sedimentary basin, the Treasure Lake Group, and are temporally associated with the sedimentary basin being

capped by shoshonitic volcanics (Gandhi et al., 2014; Montreuil et al., 2016a). This setting is analogous to the setting of the Kiggavik deposits: beneath the Proterozoic Theon Basin, which is capped by shoshonitic volcanics which are temporally associated with U mineralization. In some deposits U and other metals were subsequently remobilized into polymetallic epithermal veins by hydrothermal fluids related to intrusions (Gandhi et al., 2000; Montreuil et al., 2015).

The 1594 ± 95 Ma Kiggavik U1a age overlaps with the 1644 ± 13 Ma (U-Pb) zircon age for the Athabasca Wolverine Point Formation tuffs (Rainbird and Davis, 2007), and is similar to the ~1590 Ma ages reported from the McArthur River, Rabbit Lake, Dawn Lake, Virgin River, Millenium, and Southwest deposits, which are the oldest U-minerals known in the Athabasca deposits (Alexandre et al., 2005; Alexandre et al., 2009; Cloutier et al., 2009). Ages similar to the ~1.55 Ga age have been reported from the McArthur River and Sue C Zone Athabasca Basin U deposits (Alexandre and Kyser, 2003; Alexandre et al., 2005; Alexandre et al., 2009). These ages most likely represent Pb-loss events, rather than primary mineralization ages (Alexandre et al., 2009).

The 1440 ± 21 Ma U-Pb age obtained from U1b and U1c brannerite in the End Deposit overlaps with Sharpe et al (2015) 1520 ± 79 Ma U-Pb uraninite age from the Bong Deposit, as well as Ashcroft (2020) U-Pb uraninite age of 1459 ± 55 Ma from the End Deposit. This age also agrees with Sm-Nd ages of 1434 ± 23 Ma and 1434 ± 60 Ma reported by Turner (2003) from fluorite in the Mallory Lake epithermal Au-Ag deposit ~70 km to the south of Kiggavik. The Mallory Lake deposit is strongly associated with Nueltin intrusions despite being much younger than these granites (Turner, 2003). Although the Mallery Lake deposit is not U-mineralized, the nearby Spec showing contains more diverse U-Pb-Cu-Ag-fluorite mineralization (Jefferson et al.,

2013). The 1440 ± 21 Ma age agrees with the 1417 ± 17 Ma U-Pb age recorded by U1b and U1c in the End Deposit.

This 1417 ± 17 Ma age is present as an overprinting age in vein and disseminated uraninite which also yield the 1553 ± 16 Ma age. This 1417 ± 17 Ma age overlaps with the 1459 ± 55 Ma U-Pb age reported from uraninite by Ashcroft (2020) and is similar to the 1403 ± 10 Ma and 1418 (no error reported) ages obtained from uraninite and galena from the Kiggavik deposit by Farkas (1984). This 1417 ± 17 Ma age also agrees with the Turner's (2003) Sm-Nd ages of 1434 ± 23 Ma and 1434 ± 60 Ma from Mallory Lake.

U-Pb and Pb-Pb uraninite ages of ~1400 Ma have been reported from Athabasca Basin U deposits (Fayek et al., 2002a; Alexandre et al., 2009; Cloutier et al., 2009; Fayek et al., 2010). These ages have been interpreted as the age of primary mineralization (Fayek et al., 2002a; Fayek et al., 2010) or as resetting of ~1590 Ma mineralization (Alexandre et al., 2009; Cloutier et al., 2009). Uraninite from the GBMZ deposits also underwent multiple isotopic resetting events, including one at 1453 ± 18 Ma (Montreuil et al., 2015; Gandhi et al., 2018). While the tectonic significance of this age is unclear, it may be linked with a period of A-type magmatism which affected large areas of North America at this time (Jefferson et al., 2013) or the Berthoud Orogeny in the southwestern United States (Alexandre et al., 2009; Cloutier et al., 2009). Whatever the root cause, this ~1400 Ma event also isotopically reset much of the primary U-mineralization in the Kiggavik area.

The 1249 ± 33 and 1276 ± 8.7 Ma ages obtained from vein-hosted uraninite in the End and Kiggavik deposits, respectively, are similar to the 1277 ± 10 Ma and 1257 ± 58 Ma ages reported from the End Deposit by Grare et al. (2020), as well as Chi et al.'s (2016) 1295 ± 12 Ma age from the End Deposit and Shabbaga et al.'s (2020) 1284 ± 53 age from the Kiggavik

Deposit. These ~1260 Ma ages are almost certainly related to isotopic resetting by the 1267 ± 2 Ma (LeCheminant and Heaman, 1989) intrusion of the Mackenzie diabase dykes. Overprinted ages similar to the Mackenzie Dykes have also commonly been reported from the Athabasca Basin (Cuney et al., 2002; Alexandre et al., 2009; Cloutier et al., 2009; Sheahan et al., 2016).

The 937 ± 24 Ma U-Pb age from "worm-rock"-textured disseminated uraninite in the Andrew Lake deposit agrees with a 941 ± 31 Ma Ar-Ar age obtained from illite in the same deposit by Shabaga et al. (2017) as well as K-Ar ages of 930.4 ± 18.4 Ma, 930.0 ± 19.9 Ma, and 912.8 ± 16.7 Ma obtained by Weyer (1992) from illite in the Kiggavik deposit and a 937 ± 35 Ma U-Pb age obtained from infill uraninite in the End deposit by Ashcroft (2020). While this 937 ± 24 Ma is similar to previously reported ages from the Kiggavik area, its high MSWD suggests its reliability is less than ideal and caution should be used in its interpretation. Ages of circa 1000-900 Ma have been reported from uraninite in the Athabasca Basin (Fayek et al., 2002a; Alexandre et al., 2009; Cloutier et al., 2009), and is broadly consistent with the age of the Grenville Orogeny and assembly of Rodinia (Fayek et al., 2002a; Alexandre et al., 2009; Cloutier et al., 2009), suggesting it may be linked to far-field effects of this event.

The 274 ± 69 Ma age obtained from disseminated brannerite in the End Deposit overlaps with the 284 ± 19 Ma age reported by Shabbaga et al. (2020) for vein-hosted uraninite in the Kiggavik Deposit as well as the 347 ± 58 Ma, and 344 ± 19 Ma ages reported from Andrew Lake by Grare et al. (2020). These relatively young ages are similar to younger ages reported from the Athabasca (e.g., Fayek and Kyser, 1997; Fayek et al., 2002a), and may potentially be related to the Appalachian Orogeny and the assembly of Pangea (Grare et al., 2020).

Many uranium minerals of all textures and from all four studied deposits were found to have Pb contents too low to yield a U-Pb Concordia age (<~1% PbO), indicating geologically

recent (~<1 Ma) resetting or remobilization. This is a similar result to the <1 Ma alteration of U-minerals reported from Andrew Lake by Shabaga et al. (2017) and is also consistent with recent alteration of the Kiggavik deposits by high-latitude meteoric fluids (Sharpe et al., 2015; Ashcroft, 2020; Shabaga et al., 2020).

Taken as a whole, the geochronology indicates primary mineralization in the Kiggavik region occurred at 1600-1550 Ma, with numerous resetting and alteration events over the last 1.6 Ga (Table 2). Although later alteration events have clearly caused significant isotopic resetting, especially in the Andrew Lake and Kiggavik deposits where the age of primary mineralization is not preserved, a ~1550 Ma age has now been obtained from (polymetallic) vein-hosted, disseminated, and front-style uraninite from the End and Bong deposits. This indicates that primary mineralization was regional in extent, and diverse in both texture and mineralogy. Additionally, texturally identical U-minerals, often only 10's of micrometres apart, commonly yielded different U-Pb ages, suggesting (in)complete isotopic resetting has affected these U-minerals multiple times.

Although previous studies have generally ascribed different U-minerals and textures to different events many millions of years apart (Sharpe et al., 2015; Shabaga et al., 2017; 2020; Ashcroft, 2020; Grare et al., 2020), these new data suggests that most of these apparently disparate textural features in fact formed at or soon after the time of primary mineralization, with differing U-Pb ages due mainly to differing degrees of overprinting alteration.

Genetic Model

Based on data presented in this study, a MIAC system model explains the Kiggavik deposits' temporal link to alkaline magmatism (the Kuungmi basalts) and mineralogy including

Table 2. Selected U-Pb ages from the literature from the Kiggavik, Athabasca Basin, Mount Isa, and Great Bear Magmatic Zone areas, sorted by age, compared to ages from this study (Burron, et al., this study).

Reference	Type	Deposit	Technique	Mineral	Age
Corriveau et al., 2016	Intrusions bracketing mineralization	GBMZ district	U-Pb	Zircon	~1875-1855 Ma
Rainbird et al. (2007)	Host Rock	Athabasca Region	U-Pb	Zircon	1644 ± 13 Ma
Ashcroft (2020)	Host Rock	End (Metasedimentary Rocks)	Ar-Ar	Muscovite	1603 ± 4 Ma
Shabaga et al. (2017)	Host Rock	Andrew Lake (Metasedimentary Rocks)	Ar-Ar	Muscovite	1599 ± 20 Ma
Thorkelson et al. (2001)	Alteration	Wernecke Breccia (Yukon)	U-Pb	Titanite	1595 ± 5 Ma
Burron et al. (this study)	**Mineralization (U1a)**	**Bong**	**U-Pb**	**Uraninite**	**1594 ± 95 Ma**
Alexandre et al. (2009)	Mineralization	Southwest (Athabasca)	U-Pb	Uraniferous bitumen	1594 ± 64 Ma
Alexandre et al. (2009)	Mineralization	Virgin River (Athabasca)	U-Pb	Uraninite	1593 ± 47 Ma
Cloutier et al. (2009)	Mineralization	Millennium (Athabasca)	U-Pb (chemical)	Uraninite	1590 (no errors reported)
Fayek et al. (2019)	Alteration	Kiggavik (Main)	Pb-Pb	Galena	1589 ± 39 Ma
Oliver et al. (2004)	Alteration	Knobby Quarry (Mt Isa)	U-Pb	Titanite	1555 ± 9 Ma
Burron et al. (this study)	**Mineralization (U1b+c)**	**End**	**U-Pb**	**Uraninite**	**1553 ± 16 Ma**
Polito et al., 2009	Alteration	Valhalla	Ar-Ar	Reibeckite	1551 ± 7 Ma
Polito et al., 2009	Mineralization	Valhalla (Mt Isa)	Pb-Pb	Brannerite	1543 ± 15 Ma
Alexandre and Kyser (2003)	Mineralization	McArthur River (Athabasca)	U-Pb	Uraninite	1540 ± 38 Ma
Chamberlain et al. (2010)	Volcanic	Kuungmi ultrapotassic Lavas	U-Pb	Baddeleyite	1540 ± 30 Ma
Alexandre et al. (2009)	Mineralization	McArthur River (Athabasca)	U-Pb	Uraninite	1540 ± 19 Ma
Oliver et al. (2004)	Alteration	Knobby Quarry (Mt Isa)	U-Pb	Titanite	1527 ± 7 Ma
Sharpe et al. (2015)	Mineralization	Bong	U-Pb	Uraninite	1520 ± 79 Ma
Alexandre et al. (2009)	Mineralization	Virgin River (Athabasca)	U-Pb	Uraninite	1471 ± 37 Ma
Fayek et al. (2002a)	Mineralization	Cigar Lake (Athabasca)	U-Pb	Uraninite	1461 ± 47 Ma
Ashcroft (2020)	Mineralization	End	U-Pb	Uraninite	1459 ± 55 Ma
Gandhi et al. (2018)	Mineralization	Eldorado (GBMZ)	U-Pb	Uraninite	1453 ± 18 Ma
Burron, et al. (this study)	**Mineralization (U1 + U2)**	**End**	**U-Pb**	**Brannerite**	**1440 ± 21 Ma**
Turner (2003)	Alteration	Mallory Lake	Sm-Nd	Fluorite	1434 ± 23 Ma; 1434 ± 60 Ma
Cloutier et al. (2009)	Mineralization	Millennium (Athabasca)	Pb-Pb	Uraninite	1421 ± 7 Ma

Farkas (1984)	Alteration	Various Lone Gull	Pb-Pb	Galena	1418 Ma (no errors reported)
Burron et al. (this study)	**Mineralization (U1+U2)**	**End**	**U-Pb**	**Uraninite**	**1417 ± 17 Ma**
Farkas (1984)	Mineralization	Various Lone Gull	U-Pb	Uraninite	1403 ± 10 Ma
Chi et al. (2017)	Mineralization	End	U-Pb	Uraninite	1295 ± 12 Ma
Weyer (1992)	Alteration	Lone Gull granite (Kiggavik Main/Centre)	K-Ar	Illite	1291 ± 23 Ma
Weyer (1992)	Alteration	Lone Gull granite (Kiggavik Main/Centre)	K-Ar	Illite	1287 ± 18 Ma
Shabaga et al. (2020)	Mineralization	Kiggavik (Main)	U-Pb	Uraninite	1284 ± 53 Ma
Ashcroft (2020)	Mineralization	End	U-Pb	Uraninite	1280 ± 32 Ma
Sheahan et al., (2016)	Mineralization	Shea Creek (Athabasca)	U-Pb	Uraninite	1280 ± 30 Ma
Cloutier et al., 2009	Mineralization	Millennium (Athabasca)	U-Pb	Uraninite	1278 ± 200 Ma
Grare et al. (2020)	Mineralization	End	U-Pb	Uraninite	1277 ± 10 Ma
Burron et al. (this study)	**Mineralization (U1+U2)**	**Kiggavik (Main)**	**U-Pb**	**Uraninite**	**1276 ± 8.7 Ma**
LeCheminant and Heaman (1989)	Intrusion	Mackenzie diabase dykes	U-Pb	Baddeleyite and Zircon	1267 ± 2 Ma
Grare et al. (2020)	Mineralization	End	U-Pb	Uraninite	1257 ± 58 Ma
Burron et al. (this study)	**Mineralization (U1+U2)**	**End**	**U-Pb**	**Uraninite**	**1249 ± 33**
Alexandre et al., (2009)	Mineralization	McArthur River (Athabasca)	U-Pb	Uraninite	1247±19 Ma
Weyer (1992)	Alteration	Lone Gull granite (Kiggavik Main/Centre)	K-Ar	Illite	1229 ± 18 Ma
Alexandre et al., (2009)	Mineralization	McArthur River (Athabasca)	U-Pb	Uraninite	971 ± 27 Ma
Shabaga et al. (2017)	Alteration	Andrew Lake	Ar-Ar	Illite	941 ± 31 Ma
Burron et al. (This study)	**Mineralization (U2)**	**Andrew Lake**	**U-Pb**	**Uraninite**	**937 ± 24 Ma**
Weyer (1992)	Alteration	Lone Gull granite (Kiggavik Main/Centre)	K-Ar	Illite	930.4 ± 18.4 Ma; 930.0 ± 19.9 Ma; 912.8 ± 16.7 Ma
Grare et al. (2020)	Mineralization	Andrew Lake	U-Pb	Uraninite	347 ± 58 Ma; 344 ± 19 Ma
Shabaga et al. (2020)	Mineralization	Kiggavik (Main)	U-Pb	Uraninite	284 ± 19 Ma
Burron et al. (this study)	**Mineralization (U2)**	**End**	**U-Pb**	**Brannerite**	**274 ± 69 Ma**
Burron et al. (this study)	**Mineralization (U3)**	**Bong, End, Kiggavik (Main), Andrew Lake**	**U-Pb**	**Uraninite**	**<1 Ma**

Shabaga et al. (2017)	Mineralization	Andrew Lake	U-Pb	Uraninite	<1 Ma

* only plateau age from Riegler (2014) where >50% ^{39}Ar released

brannerite, hydrothermal zircon and uranothorite, secondary feldspar, Bi minerals, and lacking in graphite and dravite. These features are consistent with MIAC provinces such as the GBMZ, CMB, and Mount Isa, and inconsistent with URU deposits in the Athabasca Basin (Table 3).

The albitization observed in Kiggavik bears many similarities to that observed in MIAC-U systems. The albite-rich, U-Th-Zr silicate-bearing mineralogy with development of (micro)porosity is common in many albite U deposits and other U-rich MIAC systems (Alexandre, 2010; Wilde, 2013; Corriveau et al., 2022b). The mobility of HFSE, especially Zr, and presence of chemically aggressive, F-bearing fluids is also observed in many such systems (Polito et al., 2009; Agani et al., 2010; Wilde, 2013; Wilde et al., 2013; Montreuil et al., 2016b). These attributes are uncommon generally and are not observed in unconformity systems and other types of U deposits.

The hematization observed in Kiggavik bears a resemblance to Fe-rich alteration facies developed in some MIAC systems. Hematization in the Kiggavik deposits is marked by the influx of Fe, and to a lesser extent Mg and K, and the development of Fe-oxide-rich breccias in the core areas of many of the deposits, features which are similar to those observed in MIAC systems such as the Southern Breccia Zone of the GBMZ. The resulting mineral assemblage, dominated by hematite and white mica (illite) with local quartz and carbonate associated with the QB is most similar to the low temperature K-Fe facies of Corriveau (2022a). In deposits and showings such as the Southern Breccia Zone, U mineralization is associated with high-temperature K-Fe alteration (Montreuil et al., 2015), however Fe-K alteration in the Kiggavik deposits contains only trace amounts of hydrothermal zircon, and most hematized rocks are depleted in U, suggesting this alteration may have acted mainly as a U redistribution event. The observation of hydrothermal zircon, muscovite, and specular hematite infilling pores in the QB,

Table 3. Comparison of key features of URU, U-rich deposits in MIAC systems, and Kiggavik deposits.

	Basement-hosted URU	**U-rich deposits in MIAC systems**	**This study**
Location	Athabasca Basin	Great Bear Magmatic Zone	Kiggavik
Association with alkaline magmatism	None	Spatial and temporal	Spatial and temporal
Albitization overprinted by Fe alteration and brecciation	No	Yes	Yes
Non-U mineralogy	Ill, Hem (± specular), Sud, Chl, dravite, Qz, polymetallic sulfides, native Cu, local carnotite, APS minerals	Ab, Kfs, Ill, (specular) Hem, Mag, Chl, Amp, Ap, Qz, Cb sulfides, ± fluorite, Bi-minerals, Bar, Sch, REE minerals	Ab, Kfs, Ill, (specular) Hem, Chl, Sud, Ap, Qz, Cb, sulfides, ± fluorite, Bi-minerals, Bar, Sch, REE (F)-carbonates, APS minerals
U mineralogy	Urn, Coff	Urn, Coff, Brn, U-Zr-Th silicates	Urn, Coff, Brn, U-Zr-Th silicates

which is spatially and temporally linked to hematization (Grare et al., 2018) suggests a close temporal and, and possibly genetic, link between albitization and hematization.

The bleaching and associated epithermal veining which hosts the majority of U in Kiggavik is more enigmatic. It may be equivalent to the late U-bearing epithermal veins found in some of the GBMZ deposits, or represent a fluid of a completely different origin. Although the age of the hematization is uncertain, the work of Grare et al. 2018 suggests a ~200 Ma time gap between the QB and the age obtained for U1. This is certainly enough time for a completely different hydrothermal system to develop in the area, although the timing and overall setting of U1 would be consistent with a second pulse of MIAC activity. This possibility and the nature of the relationship between albitization and U1 will be more fully evaluated with Ar-Ar geochronology and stable isotope data in Burron et al. (in prep).

MIAC-U systems are typically developed within large corridors of very pervasive albitization (Wilde, 2013; Montreuil et al., 2015; Corriveau et al., 2022a; b). The albitization observed in the Kiggavik deposits is weaker than typical MIAC-U deposits; this albitization, however, is only preserved on the fringes of the Kiggavik deposits, indicating the core of the albitized zones has been completely overprinted by intense, texturally-destructive hematization and bleaching. The porosity developed during albitization focuses subsequent fluid flow through these areas, potentially leading to preferential overprinting of albite-hosted U deposits (Corriveau et al., 2016; 2022b; Potter et al., 2019), a process which seems to have been particularly pervasive in the Kiggavik deposits. The combination of hematization and bleaching has resulted in remobilization of nearly all of the elements which were enriched or depleted by albitization.

Although the U-Pb ages obtained for the Kiggavik deposits are largely similar to those of the Athabasca Basin U deposits many of these similarities appear to be the result of the areas

sharing a common history of post-depositional resetting events, rather than necessarily sharing a common origin. ~1.6-1.55 Ga Primary mineralization in the Kiggavik region was also synchronous with a protracted period of widespread development of MIAC systems which formed IOCG-U and albitite-hosted U mineralization across much of Australia and the Yukon Territory.

Uranium grades at Kiggavik are substantially higher (0.47 vs <0.2 %) than those of most U deposits developed in MIAC systems. This may be the result of particularly fertile source rocks in the region. Granites of the Hudson and Nueltin suites, collected from areas 10's-100's of km south of Kiggavik, have U contents as high as 42 and 106 ppm U, respectively (Peterson et al., 2015b). Uranium-rich pegmatites have been described from both the Hudson (Jefferson et al., 2007a; b; Mercadier et al., 2013) and Nueltin (Scott et al., 2012) suites, and Nueltin-aged, U-rich (~800 ppm U) (Peterson et al., 2011) bostonite dykes have been observed near the Kiggavik Main Zone (Anand and Jefferson 2017; Grare et al., 2020). The bleaching event associated with U1 mineralization, which has a more ambiguous relationship with the MIAC system, also increased grades by introducing and/or reconcentrating U.

The prevalence of brecciation, epithermal textures, association with brittle structures, presence of open pores/vugs, and lack of definitively high temperature minerals indicates a relatively shallow depth of formation prevailed throughout the various stages of alteration and mineralization. A relatively shallow depth of formation is also consistent with the fluid inclusion data of Chi et al. (2016) and the Grare et al. (2018)'s investigation of the QB. A shallow and low temperature environment and unusually high degree of subsequent hydrothermal overprinting may explain many of Kiggavik's unusual features, such as lack of preserved albitites, lack of

hydrothermal mafic minerals and high temperature alteration facies, high U grade, and abundance of epithermal features.

Based on the pargenesis, mineralogy, structure, and geochronology, a 4-stage genetic model for the formation of the Kiggavik deposits is proposed:

Stage 1a: Albitization The earliest observed alteration in both the metasedimentary rocks and Lone Gull rocks consists of albitization which replaced host rocks with highly porous quartz, porous albite and K-feldspar, muscovite, chlorite, apatite, with minor to trace hydrothermal zircon and uranothorite, Ti-oxides, sulfides, REE-minerals, scheelite, and calc-silicates. This left the depleted in most HFSE but enriched in U, and prepared the ground for subsequent stages of alteration and mineralization by creating porous, brittle rocks through which fluid flow was focused, and by introducing U.

Stage 1b: Fe-K Alteration This stage is dominated by hematite, some of which is specular, which gives this alteration its characteristic brick-red color, and illite, along with trace quantities of zircon, apatite, and Ti-oxides. This hematization and illitization pervasively replaced the albitites, leaving only traces of albitized rocks on the periphery of the deposits. Although hematization systematically crosscuts and overprints albitization, the observation of hydrothermal zircon associated with specular hematite veins crosscutting the QB suggests a degree of overlap in timing. Hematized rocks are enriched in Fe, Mg, and K, but also enriched in the same HFSE which are depleted in the albitized rocks, raising the prospect of elements leached during albitization becoming concentrated in later hematizing fluids. While U was likely redistributed by hematization, only trace amounts of U-bearing hydrothermal zircon were formed by this alteration.

As noted by Grare et al. (2018), this brick-red hematization is spatially associated with the QB, which supports the hypothesis that these events were broadly synchronous, although their exact timing is uncertain. The presence of brecciated and slightly hematized semi-massive sulfide blebs in areas of the QB largely unaffected by brick-red hematization indicates the early stages of QB emplacement may have occurred under more reducing conditions and precipitated at least some sulfides. Grare et al. (2018) also suggested redox conditions may have fluctuated during QB emplacement based on the observation of magnetite being replaced by hematite. The observation of specular hematite veins locally crosscutting the QB suggests emplacement in multiple stages over a protracted time period.

Stage 2: bleaching and U-mineralization The temporal association between U1 and volatile-rich shoshonitic volcanism and spatial association with structures which have previously exploited by magmatic-hydrothermal fluids (i.e. the QB) suggests the possibility of magmatic-hydrothermal fluids being involved. Contributions from basinal or meteoric fluids are common in MIAC systems and likely played a role in the Kiggavik deposits. Mixing of magmatic-derived fluids with such brines could have contributed to the fluid associated with bleaching and U mineralization, as well as contributing U from the overlying basin. Such mixing of U-bearing post-magmatic fluids with fresh magmatic fluids and basinal brines would be analogous to the process which led to U mineralization in the ODP.

If an influx of hot, basement-derived fluids into or beneath a basin induced circulation of basinal brines into the basement, as suggested by fluid inclusion studies in the End deposit (Chi et al., 2016), it could also explain some the Kiggavik deposit's URU-like features, such as widespread illite alteration and high U grades. If basinal fluids (±U) played a significant role in

U mineralization, the Kiggavik deposits could be interpreted as a hybrid between MIAC and URU systems.

Bleaching fluids may be equivalent to the late hydrothermal fluids which remobilized uranium and other metals out of MIAC deposits and into polymetallic epithermal veins in the GBMZ (Gandhi et al., 2000; Montreuil et al., 2015; Potter et al., 2019). The observation of uraninite rimming and replacing sulfides suggests that sulfides deposited during earlier stages may have acted as redox traps, further facilitating U deposition.

Although U1 mineralization is texturally diverse, petrography and geochronology indicate U1a, b, and c share a similar genesis, with ore-forming fluids precipitating U in veins as well as infiltrating the surrounding matrix to precipitate U in the vugs and finer-scale porosity created by the dissolution of the vein and matrix minerals. Some samples show a gradation between all three of these textures (Fig. A5).

While the timing relationships between Stages 1a and b, and Stage 2 are broadly supported by paragenetic relationships, a full paragenesis likely includes many distinct fluid events, as proposed by Grare et al. (2018) for the origin of the QB.

Stage 3: Post-mineralization Resetting Events U-Pb geochronology records major isotopic resetting events at 1417 ± 17 Ma, ~1267 Ma, 937 ± 24 Ma, and 274 ± 69 Ma. These ages are broadly consistent with U-Pb ages previously reported from both the Kiggavik and Athabasca Basin U deposits and reflect periods of igneous activity and/or distant orogenic events. Although the 1417 ± 17, ~1267, and 937 ± 24 Ma ages are the oldest measured in some samples, the similarity in textures and proximity of U minerals yielding this age and the circa 1550 Ma

primary mineralization age suggests these younger ages are primarily the result of isotopic resetting of circa 1550 Ma U minerals.

Fluids infiltrating the deposit subsequent to the main stage of MIAC activity could have overprinted and perhaps remobilized and reconcentrated MIAC U mineralization. Such a process likely increased U grades in the Olympic Dam Deposit (Ehrig et al., 2021), and offers another potential explanation for the Kiggavik deposit's high U grade. Any late, downward-flowing fluids affecting the Kiggavik deposits would likely be channelized and directed into the deposit core by their network of porous veins, where preexisting sulfides would form redox traps to precipitate any dissolved U.

Stage 4: Recent U Mobility Many U minerals yielded isotopic data which was too discordant to calculate a Concordia age, suggesting these minerals formed or suffered near-total Pb-loss within the last ~1 Ma. These circa <1 Ma U minerals are strongly, although not universally, associated with orange hematite-geothite and carbonate alteration, with traces of vanadinite and carnotite in U-mineralized areas. The observation of small U-rich fronts developed along boundaries between orange hematite-geothite and other types of alteration suggests this alteration was accompanied by some degree of U mobility. The hematite, geothite, and locally carnotite-bearing mineralogy suggests late mobilizing fluids were low temperature and oxidized.

The observation of geologically recent U mobility suggests the Kiggavik deposits may represent a useful natural analogue for deep geologic repositories for used nuclear fuel.

Conclusions

The Kiggavik, Bong, End, and Andrew Lake deposits contain the U minerals uraninite, coffinite, and brannerite, which formed and evolved over four main stages.

In Stage 1, prior to significant U mineralization, the host rocks underwent high temperature albite-sericite alteration, leaching of HFSE, silicification, brecciation, illitization, and hematization. Although uraniferous zircon, uranothorite, and trace uraninite were deposited during albitization, this alteration is associated with only minor U enrichment.

Stage 2 uraninite and coffinite comprises three styles: chemical front U (U1a), disseminated U (U1b), and vein-hosted U (U1c). U1c mineralization is hosted by small, vuggy quartz-carbonate veins, and is commonly associated with a diverse suite of minerals, including base metal sulfides, Bi minerals, and barite. U1b and U1c mineralization is dated using SIMS U-Pb geochronology at 1553 ± 16 Ma, while U1a mineralization yielded a broad, but overlapping, age of 1594 ± 95 Ma. This mineralization timing overlaps with the 1540 Ma age of the Kuungmi basalt.

Stage 3 mineralization consists of multiple resetting and remobilization events occurring at 1440 ± 21 Ma, 1417 ± 17 Ma, ~1267 Ma, 937 ± 24 Ma, and 274 ± 69 Ma. These events are related to igneous activity and far-field effects of distant tectonic events.

Stage 4 comprises resetting and U remobilization that occurred within the last ~1 Ma, resulting in U minerals containing essentially no radiogenic Pb. The geologically recent timing and associated low-temperature, oxidized goethite-calcite ± vanadinite alteration assemblage suggests that this remobilization is the result of the infiltration of high-latitude meteoric and/or glacial fluids, which is consistent with the observations of previous studies.

Many of the observations of this study, such as polymetallic mineralization, a strong spatial and temporal association with igneous processes, and alteration indicative of a F-rich fluid chemistry, are inconsistent with the mineralization being solely the result of basement-

hosted, URU metallogenesis, but are consistent with genetic model involving early MIAC alteration and possible primary mineralization, potentially followed by overprinting URU mineralization. Basinal fluids may have contributed to mineralization, but if so, likely played a supporting role by mixing with late epithermal fluids, or acting as a late overprinting and/or U remobilizing event.

Acknowledgements

We would like to thank the NSERC Alliance grant program (grant #549904) and the Canadian Nuclear Safety Commission (contract #3000069567) for funding this project. Electron Probe Micro-Analysis and Secondary Ion Mass Spectrometry was carried out with the assistance of Panseok Yang and Ryan Sharpe.

References

Acosta-Góngora, P., Potter, E.G., Lawley, C.J.M., Corriveau, L., and Sparkes, G., 2022a, Geochemical characterization of the Central Mineral Belt U ± Cu ± Mo ± V mineralization, Labrador, Canada: Application of unsupervised machine-learning for evaluation of IOCG and affiliated mineral potential: Journal of Geochemical Exploration, v. 237, doi:10.1016/j.gexplo.2022.106995.

Acosta-Góngora, P., Potter, E.G., Lawley, C.J.M, Petts, D., Sparkes, G., 2022b, Uraninite chemistry of the Central Mineral Belt, Labrador, Canada: Application of grain-scale unsupervised machine-learning: Journal of Geochemical Exploration, v. 233, doi:10.1016/j.gexplo.2021.106910.

Agani, A., Kamenetsky, V.S., and McPhie, J., 2010, The role of fluorine in the concentration and transport of lithophile trace elements in felsic magmas: Insights from the Gawler Range Volcanics, South Australia: Chemical Geology, v. 273, p. 314–325.

Alexandre, P., and Kyser, T.K., 2003, Geochronology of the Paleoproterozoic basement-hosted unconformity-type uranium deposits in northern Saskatchewan, Canada: Uranium Geochemistry 2003, International Conference, Université Henri Poincaré, Nancy, France, April 13–16, 2003, Proceedings, p. 37–40.

Alexandre, P., Kyser, K., Polito, P., and Thomas, D., 2005, Alteration mineralogy and stable isotope geochemistry of paleoproterozoic basement-hosted unconformity-type uranium deposits in the Athabasca Basin, Canada: Economic Geology, v. 100, p. 1547–1563.

Alexandre, P., Kyser, K., Thomas, D., Polito, P., and Marlat, J., 2009, Geochronology of unconformity-related uranium deposits in the Athabasca Basin, Saskatchewan, Canada and their integration in the evolution of the basin: Mineralium Deposita v. 44, p. 41–59.

Alexandre, P., 2010, Mineralogy and geochemistry of the sodium metasomatism-related uranium occurrence of Aricheng South, Guyana: Miner Deposita, v. 45, p. 351–367.

Alexandre, P., 2020, Geochemistry of the Athabasca Basin, Saskatchewan, Canada, and the unconformity-related uranium deposits hosted by it: The Canadian Mineralogist, v. 58, p. 1-22.

Anand, A., and Jefferson, C.W., 2017, Reactivated fault systems and their effects on outcrop patterns of thin-skinned early thrust imbrications in the Kiggavik uranium camp, Nunavut. Geological Survey of Canada Open File 7895, doi:10.4095/30277.

AREVA Resources Canada Inc., 2011, Kiggavik Project EIS: Popular Summary; Tier 1, v. 1: p. 51.

Ashcroft, G., 2020, The geochemistry and geochronology of the End Deposit, NE Thelon region, Nunavut, Canada: insight into the Athabasca Basin's closest relative: MSc thesis, Winnipeg, Canada, University of Manitoba, 217 pages.

Ayuso, R.A., Foley, N.K., Vazquez, J.A., and Jackson, J.C., 2020, SHRIMP U-Pb zircon geochronology of volcanic rocks hosting world class Be-U mineralization at Spor Mountain, Utah, U.S.A.: Journal of Geochemical Exploration, v. 209, doi:10.1016/j.gexplo.2019.106401.

Azar, B., 2007, The lithogeochemistry of volcanic and subvolcanic rocks of the Fab Lake area, Great Bear magmatic zone, Northwest Territories, Canada: B.Sc. thesis, Toronto, Canada, University of Toronto, 96 p.

Barton, M., 2014, Iron oxide (–Cu–Au–REE–P–Ag–U–Co) systems: Treatise on Geochemistry, second edition, Amsterdam, Elsevier, v. 13, p. 515–541.

Bonnetti, C., Liu, X., Mercadier, J., Cuney, M., Wu, B., Li, G., 2021, Genesis of the volcanic-related Be-U-Mo Baiyanghe deposit, West Junggar (NW China), constrained by mineralogical, trace element and U-Pb isotope signatures of the primary U mineralization: Ore Geology Reviews, v. 128, doi:10.1016/j.oregeorev.2020.103921.

Chamberlain, K.R., Schmitt, A.K, Swapp, S.M., Harrison, T.M., Swoboda-Colberg, N., Bleeker, W., Peterson, T.D., Jefferson, C.W., and Khudoley, A.K., 2010, In situ U–Pb SIMS (IN-SIMS) micro-baddeleyite dating of mafic rocks: Method with examples: Precambrian Research, v. 183, p. 379–387.

Chi, G., Haid, T., Quirt, D., Fayek, M., Blamey, N., and Chu, H., 2016, Petrography, fluid inclusion analysis, and geochronology of the End uranium deposit, Kiggavik, Nunavut, Canada: Mineralium Deposita, v. 52, p. 211–232.

Cloutier, J., Kyser, K., Olivo, G.R., Alexandre, P., and Halaburda, J., 2009, The Millennium uranium deposit, Athabasca Basin, Saskatchewan, Canada: An atypical basement-hosted unconformity-related uranium deposit: Economic Geology, v. 104, p. 815–840.

Corriveau, L., Lauzière, K., Montreuil, J.-F., Potter, E., Prémont, S., and Hanes, R., 2015, Dataset of new lithogeochemical analysis in the Great Bear magmatic zone, Northwest Territories, Canada: Geological Survey of Canada Open File 7643, 19 p.

Corriveau, L., Montreuil, J-F., and Potter, E.G., 2016, Alteration Facies Linkages Among Iron Oxide Copper-Gold, Iron Oxide-Apatite, and Affiliated Deposits in the Great Bear Magmatic Zone, Northwest Territories, Canada: Economic Geology, v. 111, p. 2045–2072.

Corriveau, L., Mumin, A.H., and Potter, E.G., 2022a, Mineral systems with iron oxide copper-gold (Ag-Bi-Co-U-REE) and affiliated deposits: introduction and overview, in Corriveau, L., Potter, E.G. and Mumin, A.H., eds., Mineral systems with iron oxide copper-gold (IOCG) and affiliated deposits: Geological Association of Canada, Special Paper 52, p. 1-26.

Corriveau, L., Montreuil, J.-F., Potter, E.G., Blein, O., and De Toni, A.F., 2022b, Mineral systems with IOCG and affiliated deposits: Part 3 - metal pathways and ore deposit model, *In* Corriveau, L., Potter, E.G., and Mumin, A.H., Eds., Mineral Systems with Iron Oxide-Copper-Gold (IOCG) and Affiliated Deposits, Special Paper 52: Geological Association of Canada, Ottawa, Canada, p. 89–121.

Corriveau, L., Montreuil, J.-F., De Toni, A.F., Potter, E.G., and Percival, J.B., 2022c, Mapping mineral systems with IOCG and affiliated deposits: a facies approach, in Corriveau, L., Potter, E.G. and Mumin, A.H., eds., Mineral systems with iron oxide copper-gold (IOCG) and affiliated deposits: Geological Association of Canada, Special Paper 52, p. 69-111.

Corriveau, L., Montreuil, J.-F., Potter, E.G., Ehrig, K., Clark, J., Mumin, A.H., and Williams, P.J., 2022d, Mineral systems with IOCG and affiliated deposits: part 1–metasomatic footprints of alteration facies, in Corriveau, L., Potter, E.G. and Mumin, A.H., eds.,

Mineral systems with iron oxide copper-gold (IOCG) and affiliated deposits: Geological Association of Canada, Special Paper 52, p. 113-158.

Corriveau, L., Montreuil, J.-F., Blein, O., Ehrig, K., Potter, E.G., Fabris. A., and Clark, J., 2022e, Mineral systems with IOCG and affiliated deposits: part 2 – geochemical footprints, in Corriveau, L., Potter, E.G. and Mumin, A.H., eds., Mineral systems with iron oxide copper-gold (IOCG) and affiliated deposits: Geological Association of Canada, Special Paper 52, p. 159-204.

Creaser, R.A., and Stasiuk, L.D., 2007, Depositional age of the Douglas Formation, northern Saskatchewan, determined by Re-Os geochronology: Geological Survey of Canada Bulletin, no. 588, 341–346.

Cuney, M.L., Chabiron, A., Kister, P., Golubev, V., and Deloule, E., 2002, Chemical versus ion microprobe isotopic dating (CAMECA IMS 3F) of the Shea Creek unconformity type uranium deposit (West Athabasca, Saskatchewan, Canada): Geological Association of Canada, Mineralogical Association of Canada Joint Annual Meeting, Program with Abstracts, v. 27, p. 25.

Cuney, M. and Kyser, K., 2008, Deposits related to Na-metasomatism and high-grade metamorphism, In, Recent and Not-so-recent Developments in Uranium Deposits and Implications for Exploration. Edited by M. Cuney and K. Kyser. Mineralogical Association of Canada, Short Course Series 39, p. 97–116.

Courtney-Davies, L., Ciobanu, C.L., Verdugo-Ihl, M.R., Slattery, A., Cook, N.J., Dmitrijeva, M., Keyser, W., Wade, B.P., Dominick, U.I., Ehrig, K., Xu, J., and Kontonikas-Charos, A.,

2019, Zircon at the nanoscale records metasomatic processes leading to large magmatic-hydrothermal ore deposits: Minerals, v. 9, doi:10.3390/min9060364.

Courtney-Davies, L., Ciobanu, C.L., Tapster, S.R., Cook, N.J., Ehrig, K., Crowley, J.L., Verdugo-Ihl, M.R., Wade, B.P., and Condon, D.J., 2020, Opening the magmatic-hydrothermal window: high-precision U-Pb geochronology of the Mesoproterozoic Olympic Dam Cu-U-Au-Ag deposit, South Australia: Economic Geology, v. 115, p. 1855–1870.

Domnick, U.; Cook, N.J.; Bluck, R.; Brown, C.; Ciobanu, C.L., 2017, Petrography of granitoids from the Samphire Pluton, South Australia: Implications for uranium mineralization in overlying sediments: Lithos, v. 300–301, p. 1–19.

Domnick, U., Cook, N.J., Ciobanu, C.L., Wade, B.P., Courtney-Davies, L, and Bluck, R, 2020a, A Mineralization Age for the Sediment-Hosted Blackbush Uranium Prospect, North-Eastern Eyre Peninsula, South Australia: Minerals v. 10, doi:10.3390/min10020191.

Domnick, U., Cook, N.J., Ciobanu, C.L., Courtney-Davies, L., Dmitrijeva, M., Verdugo-Ihl, M.R., Xua, J., Keyser, W., Slattery, A., Kennedy, A.K., and Bluck, R., 2020b, Micron- to nanoscale characterization and U-Pb geochronology of zircon from granites of the Samphire Pluton, South Australia: Precambrian Research, v. 350, doi:10.1016/j.precamres.2020.105924.

Duffett, C.L., Potter, E.G., Petts, D.C., Acosta-Gongóra, P., Cousens, B.L., and Sparkes, G.W., 2020, The evolution of metasomatic uranium ore systems in the Kitts-Post Hill belt of the Central Mineral Belt, Labrador, Canada: Ore Geology Reviews, v. 126, doi:10.1016/j.oregeorev.2020.103720.

Ehrig, K., Kamenetsky, V.S., McPhie, J., Macmillan, E., Thompson, J., Kamenetsky, M., and Maas, R., 2021, Staged formation of the supergiant Olympic Dam uranium deposit, Australia: Geology, v. 49, doi:10.1130/G48930.1.

Farkas, A., 1984, Mineralogy and host rock alteration of the Lone Gull deposit: Urangesellschaft Internal report.

Fayek, M., and Kyser, T.K., 1997, Characterization of multiple fluid events and rare-earth-element mobility associated with formation of unconformity-type uranium deposits in the Athabasca Basin, Saskatchewan: Canadian Mineralogist v. 35, p. 627–658.

Fayek, M., Harrison, T.M., Ewing, R.C., Grove, M., Coath, C.D., 2002a, O and Pb isotope analyses of uranium minerals by ion microprobe and U-Pb ages from the Cigar Lake deposit: Chemical Geology, v. 185, p. 205–225.

Fayek, M., Kyser, T.K., and Riciputi, L.R., 2002b, U and Pb isotope analysis of uranium minerals by ion microprobe and the geochronology of the McArthur River and Sue Zone uranium deposits, Saskatchewan, Canada: Canadian Mineralogist, v. 40, p. 1553–1569.

Fayek, M., Camacho, A., Beshears, C., Jiricka, D., and Halaburda, J., 2010, Two Sources of Uranium at the Millennium Uranium Deposit, Athabasca Basin, Saskatchewan, Canada, AAPG Search and Discovery Article #90172: GeoConvention, Calgary, Canada, 2010.

Fayek, M., Shabaga, B.M., Share, R., and Quirt, D., 2019, U-Pb and Pb-Pb geochronology of U-ore minerals by SIMS, *In* T.K. Kyser, M. Fayek, B. Eglington, and F. Longstaffe, eds., Applied Isotope Geochemistry: Mineralogical Association of Canada, v. 48, p. 59–76.

Flotté, N., 2009, AREVA Resources Canada Inc. Kiggavik and Sissions project END-Grid Geological Observations and interpretation and 3D modelling in GoCad, 46p.

Forster, H-J., 2005, Composition and origin of intermediate solid solutions in the system thorite–xenotime–zircon–coffinite. Lithos, v. 88, p. 35–55.

Frimmel, H., Schedel, S., and Brätz, H., 2014, Uraninite chemistry as forensic tool for provenance analysis: Applied Geochemistry, v. 48, p. 104-121.

Fuchs H.D., Hilger W, and Prosser E., 1986, Geology and exploration history of the Lone Gull property: Canadian Institute of Mining and Metallurgy Special Publication 33, p. 286–292.

Gall, Q., Peterson, T.D., and Donaldson, J.A., 1992, Early Proterozoic stratigraphy of the Thelon and Baker Lake basins, District of Keewatin: a proposed revision, In, Current Research, Part C, Geological Survey of Canada Paper 92-1C, p. 129–137.

Gandhi, S.S., Carrière, J.J., and Prasad, N., 2000, Implications of a preliminary fluid inclusion study of giant quartz veins of the southern Great Bear magmatic zone, Northwest Territories: Geological Survey of Canada, Paper 2000-1C, 13p.

Gandhi, S.S., Mortensen, J.K., Prasad, N., and van Breemen, O., 2001, Magmatic evolution of the southern Great Bear continental arc, northwestern Canadian Shield: Geochronological constraints: Canadian Journal of Earth Sciences, v. 38, p. 767–785.

Gandhi, S.S., Montreuil, J.-F., and Corriveau, L., 2014, Geology of the Mazenod area: Geological Survey of Canada, Canadian Geoscience Map Series, CGM 148P.

Gandhi, S.S., Potter, E.G., and Fayek, M., 2018, New constraints on genesis of the polymetallic veins at Port Radium, Great Bear Lake, Northwest Canadian Shield: Ore Geology Reviews, v. 96, p. 28-47.

Grare, A., 2016, The Kiggavik Uranium Project (Nunavut, Canada) structural model. Characterization and relationships between fractures, alteration, and uranium mineralization. Based on the Contact and 85W recent discoveries: Ph.D thesis, Paris, France, University of Paris, 114 p.

Grare, A., Lacombe, O., Mercadier, J., Benedicto, A., Marie Guilcher, M., Trave, A., Ledru, P., and Robbins, J., 2018, Fault zone evolution and development of a structural and hydrological barrier: the quartz breccia in the Kiggavik area (Nunavut, Canada) and its control on uranium mineralization: Minerals*,* v. 8, doi:10.3390/min8080319.

Grare, A., Benedicto, A., Mercadier, J., Lacombe, O., Trave, A., Guilcher, M., Richard, A., Ledru, P., Blain, M., Robbins, J., and Lach, P., 2020, Structural controls and metallogenic model of polyphase uranium mineralization in the Kiggavik area (Nunavut, Canada): Mineralium Deposita*,* doi:10.1007/s00126-020-00957-x.

Groves, D.I.; Bierlein, F.P.; Meinert, L.D.; Hitzman, M.W., 2010, Iron oxide copper-gold (IOCG) deposits through Earth history: Implications for origin, lithospheric setting, and distinction from other epigenetic iron oxide deposits: Economic Geology, v. 105, p. 641–654.

Hazen, R.M., Ewing, R.C., and Sverjensky, D.A., 2009, Evolution of uranium and thorium minerals: American Mineralogist, v. 94, p. 1293–1311.

Hendry, H.E. and Wheatley, K.L., 1985, The Carswell Formation, Northern Saskatchewan: Stratigraphy, sedimentology, and structure, *in*, Laine, R., Alonso, D., and Svab, M., eds., The Carswell Structure Uranium Deposits, Saskatchewan: Geological Association of Canada Special Paper 29, p. 87–103.

Hiatt, E.E., Kyser, T.K., and Dalrymple, R.W., 2003, Relationships among sedimentology, stratigraphy and diagenesis in the Proterozoic Thelon basin, Nunavut, Canada: Implications for paleo-aquifers and sedimentary-hosted mineral deposits: Journal of Geochemical Exploration, v. 80, p. 221–240.

Hiatt, E.E., Palmer, S.E., Kyser, T.K., and O'Connor, T.K., 2010, Basin evolution, diagenesis and uranium mineralization in the Paleoproterozoic Thelon basin, Nunavut, Canada: Basin Research, v. 22, p. 302–323.

Hitzman, M.W., and Valenta, R.K., 2005, Uranium in Iron-Oxide-Copper-Gold (IOCG) systems: Economic Geology, v. 100, p. 1657–1661.

Hildebrand, R.S., Hoffman, P.F., Housh, T., and Bowring, S.A., 2010, The nature of volcano-plutonic relations and shapes of epizonal plutons of continental arcs as revealed in the Great Bear magmatic zone, northwestern Canada: Geosphere, v. 6, p. 812–839.

Hoeve, J., and Quirt D.H., 1984, Mineralization and host rock alteration in relation to clay mineral diagenesis and evolution of the Middle Proterozoic Athabasca Basin, northern Saskatchewan, Canada: Saskatchewan Research Council Technical Report 187, 187 p.

Hoeve, J. and Quirt D., 1987, A stationary redox front as a critical factor in the formation of high-grade, unconformity-type uranium ores in the Athabasca basin, Saskatchewan, Canada: Bulletin de Minéralogie, v. 110, p. 157–171.

Hoeve, J. and Sibbald, T.I.I., 1978, On the genesis of Rabbit Lake and other unconformity-type uranium deposits in northern Saskatchewan, Canada: Economic Geology, v. 73, p. 1450–1473.

Hoffman, P.F., 1988, United plates of America, the birth of a craton: Early Proterozoic assembly and growth of Laurentia: Annual Review of Earth and Planetary Sciences, v. 16, p. 543–603.

Hunter, R.C., Lafrance, B., Heaman, L.M., and Thomas, D., 2021, Long-lived deformation history recorded along the Precambrian Thelon and Judge Sissons faults, northeastern Thelon Basin, Nunavut: Canadian Journal of Earth Sciences, v. 58, p. 433–457.

International Atomic Energy Agency (IAEA), 2018, Unconformity-related Uranium Deposits: IAEA-TECDOC-1857, 310 p.

Jefferson, C. J., Thomas, D., Quirt, D.H., Mwenifumbo, C.J., and Brisbin, D. , 2007a, Empirical models for unconformity-associated uranium deposits, *in*, Milkereit, B., ed., Proceedings of Exploration 07: Fifth Decennial International Conference on Mineral Exploration, p. 741–769.

Jefferson, C.W., Thomas, D.J., Gandhi, S.S., Ramaekers, P., Delaney, G., Brisbin, D., Cutts, C., Quirt, D., Portella, P., and Olson, R.A., 2007b, Unconformity-associated uranium deposits of the Athabasca Basin, Saskatchewan and Alberta, *in*, Goodfellow, W.D., ed., Mineral Deposits of Canada: A Synthesis of Major Deposit-Types, District Metallogeny, the Evolution of Geological Provinces, and Exploration Methods: Geological Association of Canada, Mineral Deposits Division, Special Publication 5, p. 273–305.

Jefferson, C.W., Pehrsson, S., Peterson, T., Chorlton, L., Davis, W., Keating, P. et al., 2011, Northeast Thelon region geoscience framework—new maps and data for uranium in Nunavut: Geological Survey of Canada Open File 6949, 1 sheet, doi:10.4095/288791.

Jefferson, C.W., Peterson, T.D., Tschirhart, V., Davis, W., Scott, J.M.J., Reid, K., Ramaekers, P., Gandhi, S.S., Bleeker, W., Pehrsson, S., Morris, W.A., Fayek, M., Potter, E., Bridge, N., Grunsky, E., Keating, P., Ansdell, K., and Banerjee, N., 2013, LIPs and Proterozoic Uranium (U) deposits of the Canadian Shield: Geological Survey of Canada Open File 7352, 56 p., doi:10.4095/292377.

Johnstone, D., 2017, Lithostratigraphic and structural controls of uranium mineralization in the Kiggavik East Zone, Centre Zone, and Main Zone deposits, Thelon Basin, Nunavut: unpublished MSc. Thesis, University of Regina, 193 p.

Kontonikas-Charos, A., Ciobanu, C.L., Cook, N.J., Ehrig, K., Krneta, S., and Kamenetsky, V.S., 2017, Feldspar evolution in the Roxby Downs Granite, host to Fe-oxide Cu-Au-(U) mineralization at Olympic Dam, South Australia. Ore Geology Reviews, v. 80, p. 838–859.

Kotzer, T.G. and Kyser, T.K., 1995, Petrogenesis of the Proterozoic Athabasca Basin, northern Saskatchewan, Canada, and its relation to diagenesis, hydrothermal uranium mineralization and paleohydrogeology: Chemical Geology, v. 120, p. 45–89.

Landry, K., Adlakha, E., Roy-Garand, A., Terekhova, A., Hanley, J., Falck, H., and Martel, E., 2022, Uranium Mineralization in the MacInnis Lake Area, Nonacho Basin, Northwest Territories: Potential Linkages to Metasomatic Iron Alkali-Calcic Systems: Minerals, doi: 0.3390/min12121609.

Laughton, J.R., Thorkelson, D.J., Brideau, M-A., Hunt, J.A., and Marshall, D.D., 2005, Early Proterozoic orogeny and exhumation of Wernecke Supergroup revealed by vent facies of Wernecke Breccia, Yukon, Canada: Canadian Journal of Earth Sciences, v. 42, p. 1033–1044.

LeCheminant, A.N., and Heaman, L.M., 1989, Mackenzie igneous events, Canada: Middle Proterozoic hotspot magmatism associated with ocean opening: Earth and Planetary Science Letters, v. 96, p. 38–48.

Ludwig, K., 1993, ISOPLOT, excel based program for plotting radiogenic isotopes: USGS Open File Rep 91-445, p. 1–42.

Martz, P., Mercadier, J., Cathelineau, M., Boiron, M-C., Quirt, D., Doney, A., Olivier Gerbeaud, O., Wally, E.D., and Ledru, P., 2019, Formation of U-rich mineralizing fluids through basinal brine migration within basement-hosted shear zones: A large-scale study of the fluid chemistry around the unconformity-related Cigar Lake U deposit (Saskatchewan, Canada): Chemical Geology, v. 508, p. 116–143.

Mercadier, J., Cuney, M., Lach, P., Boiron, M-C., Bonhoure, J., Richard, A., Leisen, M., and Kister, P., 2011, Origin of uranium deposits revealed by their rare earth element signature: Terra Nova, v. 23, p. 264–269.

Montreuil, J.-F., Corriveau, L., and Potter, E.G., 2015, Formation of albitite-hosted uranium within IOCG systems: the Southern Breccia, Great Bear magmatic zone, Northwest Territories, Canada: Miner Deposita, v. 50, p., 293–325.

Montreuil, J.-F., Corriveau, L., Potter, E.G., and De Toni, A.F., 2016a, On the Relationship Between Alteration Facies and Metal Endowment of Iron Oxide-Alkali-Altered Systems,

Southern Great Bear Magmatic Zone (Canada): Economic Geology, v. 111, p. 2139–2168.

Montreuil, J.-F., Potter, E.G., Corriveau, L., and Davis, W.J. 2016b, Element mobility patterns in magnetite-group IOCG systems: The Fab IOCG system, Northwest Territories, Canada: Ore Geology Reviews, v. 72, p. 562-584.

Mumin, A.H., Somarin, A.K., Jones, B., Corriveau, L., Ootes, L., and Camier, J., 2010, The IOCG-porphyry-epithermal continuum of deposits types in the Great Bear magmatic zone, Northwest Territories, Canada: Geological Association of Canada, Short Course Notes 20, p. 59–78.

Nordsvan, A.R., Collins, W.J., Li, Z-X., Spencer, C.J., Pourteau, A., Withnall, I.W., Betts, P.G., and Volante, S., 2018, Laurentian crust in northeast Australia: Implications for the assembly of the supercontinent Nuna: Geology, v. 46, p., 251–254.

Oliver, N.H.; Cleverley, J.S.; Mark, G.; Pollard, P.; Bin, F.; Marshall, L.; Rubenach, M.; Williams, P.; Baker, T., 2004, Modeling the role of sodic alteration in the genesis of iron oxide copper-gold deposits, eastern Mount Isa Block, Australia: Economic Geology, v. 99, p. 1145–1176.

Orrell, S.E., Bickford, M.E., and Lewry, J.F., 1999, Crustal evolution and age of thermotectonic reworking in the western hinterland of Trans-Hudson Orogen, northern Saskatchewan: Precambrian Research, v., 95, p. 187–223.

Oreskes, N., and Einaudi, M.T., 1992, Origin of Hydrothermal Fluids at Olympic Dam: Preliminary Results from Fluid Inclusions and Stable Isotopes: Economic Geology, v. 87, p. 64–90.

Pehrsson, S.J., Berman, R.G., and Davis, W.J., 2013, Paleoproterozoic orogenesis during Nuna aggregation: A case study of reworking of the Rae craton, Woodburn Lake, Nunavut: Precambrian Research, v. 232, p. 167–188.

Peterson, T.D., Van Breeman, O., Sandeman, H., and Cousens, B., 2002, Proterozoic (1.85-1.75 Ga) igneous suites of the Western Churchill Province: granitoid and ultrapotassic magmatism in a reworked Archean hinterland: Precambrian Research, v. 119, p. 73–100.

Peterson, T.D., 2006, Geology of the Dubawnt Lake area, Nunavut-Northwest Territories: Geological Survey of Canada Bulletin 580:51.

Peterson, T.D., Scott, J.M.J., and Jefferson, C. W., 2011, Uranium-rich bostonite-carbonatite dykes in Nunavut: recent observations: Geological Survey of Canada Current Research 2011-11, 12p.

Peterson, T.D., Jefferson, C.W., and Anand, A., 2015a, Geological setting and geochemistry of the ca. 2.6 Ga Snow Island Suite in the central Rae Domain of the Western Churchill Province, Nunavut: Geological Survey of Canada, Open File 7841, 29 p., doi:10.4095/296599.

Peterson, T.D., Scott, J.M.J., and LeCheminant, A.N., 2015b, The Kivalliq Igneous Suite: Anorogenic bimodal magmatism at 1.75Ga in the western Churchill Province, Canada: Precambrian Research, v. 262, p. 101–119.

Polito, P.A., Kyser, K., and Stanley, C., 2009, The Proterozoic, albitite-hosted, Valhalla uranium deposit, Queensland, Australia: a description of the alteration assemblage associated with uranium mineralization in diamond drill hole V39: Miner Deposita, v. 44, p. 11–40.

Potter, E.G., Montreuil, J.-F., Corriveau, L., and Davis, W.J., 2019, The Southern Breccia Metasomatic Uranium System of the Great Bear Magmatic Zone, Canada: Iron Oxide-Copper-Gold (IOCG) and Albitite-Hosted Uranium Linkages, *in*, Eds., Decrée, S., and Robb, L., Ore Deposits: Origin, Exploration, and Exploitation, Geophysical Monograph 242, First Edition.

Putnis, A. 2015, Transient porosity resulting from fluid-mineral interaction and its consequences: Reviews in Mineralogy and Geochemistry, v. 80, p. 1–23.

Putnis, A., and Austrheim, H. 2010, Fluid-induced processes: Metasomatism and metamorphism: Geofluids, v. 10, p. 254–269.

Quirt, D.H., 1989, Host-rock alteration at Eagle Point South: Saskatchewan Research Council, Publication No. R-855-1-E-89, 95 p. plus Appendices.

Quirt, D.H., 2003, Athabasca unconformity-type uranium deposits: One deposit type with many variations. *In*, Cuney, M., ed., Uranium Geochemistry, International Conference Proceedings, Géochime de l'Uranium 2003, Nancy, France, p. 309–312.

Quirt, D.H., Kotzer, T., and Kyser, K., 1991, Tourmaline, phosphate minerals, zircon, and pitchblende in the Athabasca Group: Maw Zone and McArthur River areas, Saskatchewan., *in*, Summary of Investigations 1991, Saskatchewan Geological Survey, Saskatchewan Energy and Mines, Miscellaneous Report 91-4, p. 181–191.

Rainbird, R.H., Hadlari, T., Aspler, L.B., Donaldson, J.A., LeCheminant, A.N., and Peterson, T.D., 2003, Sequence stratigraphy and evolution of the Paleoproterozoic intracontinental Baker Lake and Thelon basins, western Churchill Province, Nunavut, Canada: *Precambrian Research*, v. 125 p. 21–53, doi:10.1016/S0301-9268(03)00076-7.

Rainbird, R.H., and Davis, W.J., 2007, U-Pb detrital zircon geochronology and provenance of the late Paleoproterozoic Dubawnt Supergroup: linking sedimentation with tectonic reworking of the western Churchill Province, Canada: Geological Society of America Bulletin, v. 119, p. 314–328.

Rainbird, R.H., Davis, W.J., Pehrsson, S.J., Wodicka, N., Rayner, N., and Skulski, T., 2010, Early Paleoproterozoic supracrustal assemblages of the Rae domain, Nunavut, Canada: intracratonic basin development during supercontinent break-up and assembly: Precambrian Research, v. 181, p. 167–186. doi:10.1016/j.precamres.2010.06.005.

Ramaekers, P., 2004, Development, stratigraphy and summary diagenetic history of the Athabasca Basin, early Proterozoic of Alberta and its relation to uranium potential: Alberta Geological Survey Special Report, v. 62, p. 85.

Reid, A., Smith, R.N., Baker, T., Jagodzinski, E.A., Selby, D., Gregory, C.J., and Skirrow, R.G., 2013, Re-Os dating of molybdenite within hematite breccias from the vulcan Cu-Au prospect, olympic Cu-Au Province, South Australia: Economic Geology, v. 108, p. 883–894.

Regan, S.P., Williams, M.L., Zieman, L., Chiarenzelli, J.R., Jercinovic, M.J., Cousens, B.L., Webber, J.R., and Aspler, L.B., 2022, IN-SIMS zircon U-Pb geochronology from the Snowbird tectonic zone Large igneous Province (STZ LIP), western Churchill Province, Canada: Precambrian Research, v. 377, doi:10.1016/j.precamres.2022.106751.

Richard, A., Cathelineau, M., Boiron, M.-C. Mercadier, J., Banks, D.A., and Cuney, M., 2016, Metal-rich fluid inclusions provide new insights into unconformity-related U deposits (Athabasca Basin and Basement, Canada): Miner Deposita, v. 51, p. 249–270.

Riegler, T., Lescuyer, J-L., Wollenburg, P., Quirt, D., and Beaufort, D., 2014, Alteration related to uranium deposits in the Kiggavik-Andrew Lake Structural Trend, Nunavut, Canada: New insights from petrography and clay mineralogy: The Canadian Mineralogist, v. 52, p. 27–45.

Riegler, T., Beaufort, M-F., Allard, T., Pierson-Wickmann, A-C., and Beaufort, D., 2016, Nanoscale relationships between uranium and carbonaceous material in alteration halos around unconformity-related uranium deposits of the Kiggavik camp, Paleoproterozoic Thelon Basin, Nunavut, Canada: Ore Geology Reviews, v. 79, p. 382–391.

Schlegel, T.U., Wagner, T., Wälle, M., and Heinrich, C.A., 2018, Hematite Breccia-Hosted Iron Oxide Copper-Gold Deposits Require Magmatic Fluid Components Exposed to Atmospheric Oxidation: Evidence from Prominent Hill, Gawler Craton, South Australia: Economic Geology, v. 113, p. 597–644.

Schlegel, T.U., Wagner, T., and Fusswinkel, T., 2020, Fluorite as indicator mineral in iron oxide-copper-gold systems: explaining the IOCG deposit diversity: Chemical Geology, v. 584, doi:10.1016/j.chemgeo.2020.119674.

Scott, J.M.J., Peterson, T.D., and McCurdy, M.W., 2012, U, Th, and REE occurrences within Nueltin granite at Nueltin Lake, Nunavut: recent observations; Geological Survey of Canada, Current Research 2012-1, 11 p., doi: 10.4095/289393.

Scott, J.M.J., Peterson, T.D., Davis, W.J., Jefferson, C.W., and Cousens, B.L., 2015, Petrology and Geochronology of Paleoproterozoic intrusive rocks, Kiggavik uranium camp, Nunavut: Canadian Journal of Earth Sciences, v. 52, p. 494–518.

Shabaga, B.M., Fayek, M., Quirt, D., Jefferson, C.W., and Camacho, A., 2017, Mineralogy, geochronology, and genesis of the Andrew Lake uranium deposit, Thelon Basin, Nunavut, Canada: Canadian Journal of Earth Sciences, v. **54**, p. 850–868.

Shabaga, B.M., Fayek, M., Quirt, D., Jefferson, C.W., and Ledru, P., 2020, Geochemistry and geochronology of the Kiggavik uranium deposit, Nunavut, Canada: Mineralium Deposita, doi:10.1007/s00126-020-01001-8.

Sharpe, R., Fayek, M., Quirt, D., and Jefferson, C., 2015, Geochronology and Genesis of the Bong Uranium Deposit, Thelon Basin, Nunavut, Canada: Economic Geology, v. 110, p. 1759–1777.

Sharpe, R. and Fayek, M., 2016, Mass bias corrections for U-Pb isotopic analysis by secondary ion mass spectrometry: Implications for U-Pb dating of uraninite: Rapid Communications in Mass Spectrometry, v. 30, p. 1601–1611.

Sheahan, C., Fayek, M., Quirt, D., and Jefferson, C.W., 2016, A Combined Ingress-Egress Model for the Kianna Unconformity-Related Uranium Deposit, Shea Creek Project, Athabasca Basin, Canada: Economic Geology, v. 111, p. 225–257.

Skirrow, R.G., Bastrakov, E.N., Barovich, K., Fraser, G.L., Creaser, R.A., Fanning, C.M., Raymond, O.L., and Davidson, G.J., 2007, Timing of iron oxide Cu-Au-(U) hydrothermal activity and Nd isotope constraints on metal sources in the Gawler Craton, South Australia: Economic Geology, v. 102, p. 1441–1470.

Skirrow, R., 2010, “Hematite-group” IOCG ± U ore systems: Tectonic settings, hydrothermal characteristics, and Cu-Au and U mineralizing processes: Geological Association of Canada, Short Course Notes 20, p. 39–58.

Skirrow, R., 2022, Iron oxide copper-gold (IOCG) deposits – A review (part 1): Settings, mineralogy, ore geochemistry and classification: Ore Geology Reviews, v. **140**, doi:10.1016/j.oregeorev.2021.104569.

Sopuck, V.J., de Carle, E.M. and Cooper, B., 1983, The application of lithogeochemistry in the search for unconformity-type uranium deposits, northern Saskatchewan, Canada, *in*, Parslow, G.R., ed., Geochemical Exploration 1982, Special Issue of the Journal of Geochemical Exploration, v. 19, p. 77–99.

Sparkes, G.W., Dunning, G.R., and Langille, A., 2017, The Michelin Deposit: an example of albitite-hosted uranium mineralization within the Central Mineral Belt of Labrador, Current Research Newfoundland and Labrador Department of Natural Resources Geological Survey, Report 17-1, p. 219–238.

Thorkelson, D.J., Mortensen, J.K., Davidson, G.J., Creaser, R.A., Perez, W.A., and Abbott, J.G., 2001, Early Mesoproterozoic intrusive breccias in Yukon, Canada: The role of hydrothermal systems in reconstructions of North America and Australia: Precambrian Research, v. 111, p. 31–55.

Turner, W.A., Heaman, L.M., and Creaser, R.A., 2003, Sm–Nd fluorite dating of Proterozoic low-sulfidation epithermal Au–Ag deposits and U–Pb zircon dating of host rocks at Mallery Lake, Nunavut, Canada: Canadian Journal of Earth Sciences, v. 40, p. 1789–1804.

Verbaas, J., Thorkelson, D.J., Crowley, J., Davis, W.J., Foster, D.A., Gibson, H.D., Marshall, D.D., and Milidragovic, D., 2018, A sedimentary overlap assemblage links Australia to northwestern Laurentia at 1.6 Ga.: Precambrian Research, v. 305, p. 19–39.

Wallis, R.H., Saracoglu, N., Brummer, J.J., and Golightly, J.P., 1985, Geology of the McClean uranium deposits, in, Sibbald, T.I. and Petruk, W., eds., Geology of Uranium Deposits, Canadian Institute of Mining and Metallurgy, Special Volume 32, p. 101–131.

Weyer, H.J., 1992, Die Uranlagerstätte Kiggavik, Nordwestterritorien, Kanada. Genehmigte Dissertation, Rheinisch-Westfälischien Technischen Hochschule, Aachen, Deutchland.

Weyer, H.-J., Friedrich, G., Bechtel, A., and Ballhorn, R.K., 1987, The Lone Gull uranium deposit – new geochemical and petrological data as evidence for the nature of the ore bearing solutions: Metallogenesis of uranium deposits: Proceeding of a technical committee meeting, Vienna, p. 9-12.

Wilde, A., 2013, Towards a model for albitite-type uranium: Minerals, v., 3, p. 36–48.

Wilde, A., Otto, A., Jory, J., MacRae, C., Pownceby, M., Wilson, N., and Torpy, A., 2013, Geology and Mineralogy of Uranium Deposits from Mount Isa, Australia: Implications for Albitite Uranium Deposit Models: Minerals, v. 3, p. 258–283.

Wilson, M.R., and Kyser, T.K., 1987, Stable Isotope Geochemistry of Alteration Associatedwith the

Key Lake Uranium Deposit, Canada: Economic Geology, v. 82, p. 1540–1557.

Xing, Y., Etschmann, B., Liu, W., Mei, Y., Shvarov, Y., Testemale, D.,Tomkins, A., and Brugger, J., 2019, The role of fluorine in hydrothermal mobilization and transportation of Fe, U and REE and the formation of IOCG deposits: Chemical Geology, v, 504, p. 158–176.

Zaleski, E., Davis,W.J., Sandeman, H.A., 2001, Continental extension, mantle magmas and basement/cover relationships, *in*, Fourth International Archaean Symposium, Extended abstracts, Perth, Australia, p. 374–376.

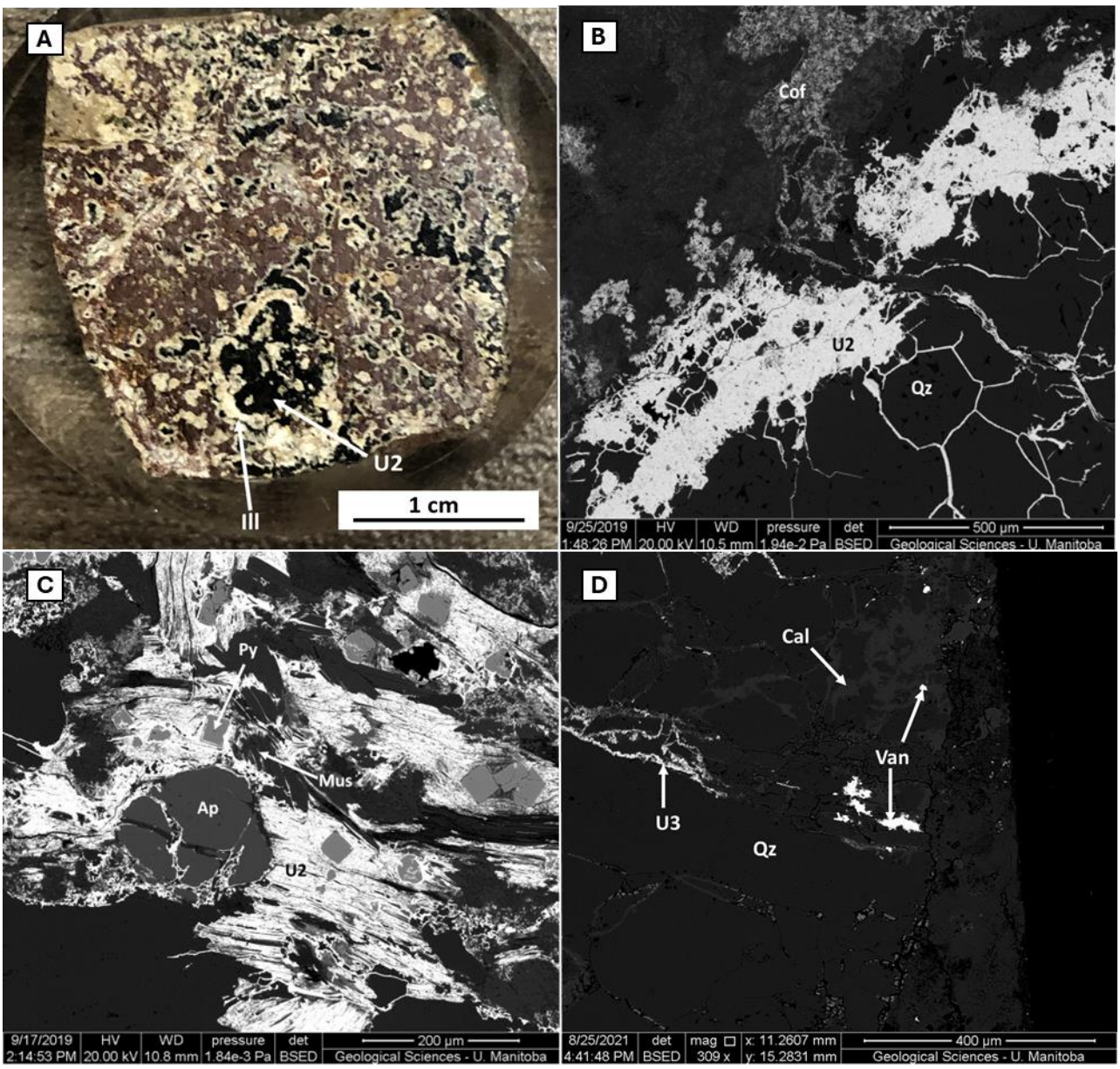

Fig. A1. U2 and U3 textures. A. Distinctive 'Worm-rock' texture with disseminated U2 mantled by a bleached region within illite and brick-red hematized host rock (SW38-590). B. U2 uraninite and coffinite in a quartz vein (SW6-294.7). C. U2 uraninite surrounds pyrite and apatite and replaces muscovite (SW39-952). D. U3 uraninite, vanadinite, and calcite in fractures in a quartz vein (SW6-294.7). Abbreviations: Qz = quartz, Cal = calcite, cof = coffinite, Mus = muscovite, Ill = illite, Ap = apatite, Py = pyrite, Van = vanadinite.

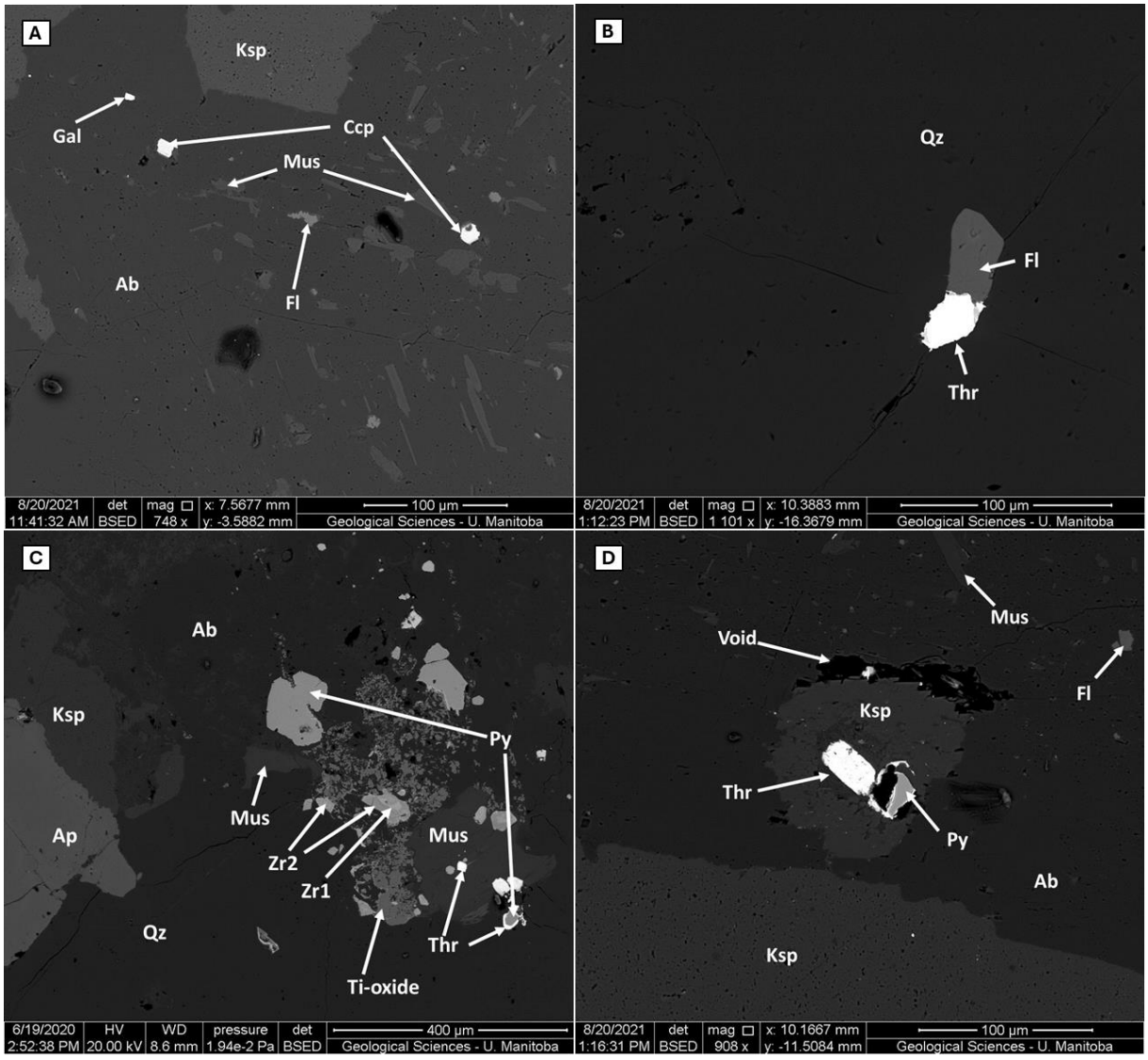

Fig. A2. Backscattered electron images of albitized granitic rocks. A. Muscovite, fluorite, and sulfides infilling dissolution pits in albite (KN04-126) B. Uranothorite and fluorite infilling a dissolution pit in quartz (KN04-126). C. Pyrite partially rimmed by uranothorite, with associated muscovite, Ti-oxides, and zircon (KN02-245.6). D. Uranothorite partially rimming pyrite and surrounded by K-feldspar (KN04-126). Abbreviations: Qz = quartz, Ab = albite, Ksp = K-feldspar, Mus = muscovite, Py = pyrite, Ccp = chalcopyrite, Gal = galena, Zr1 = zoned magmatic zircon, Zr2 = unzoned, Ca-Al-Fe-bearing hydrothermal zircon, Thr = (urano)thorite, Fl = fluorite, Void = open cavity/pore space.

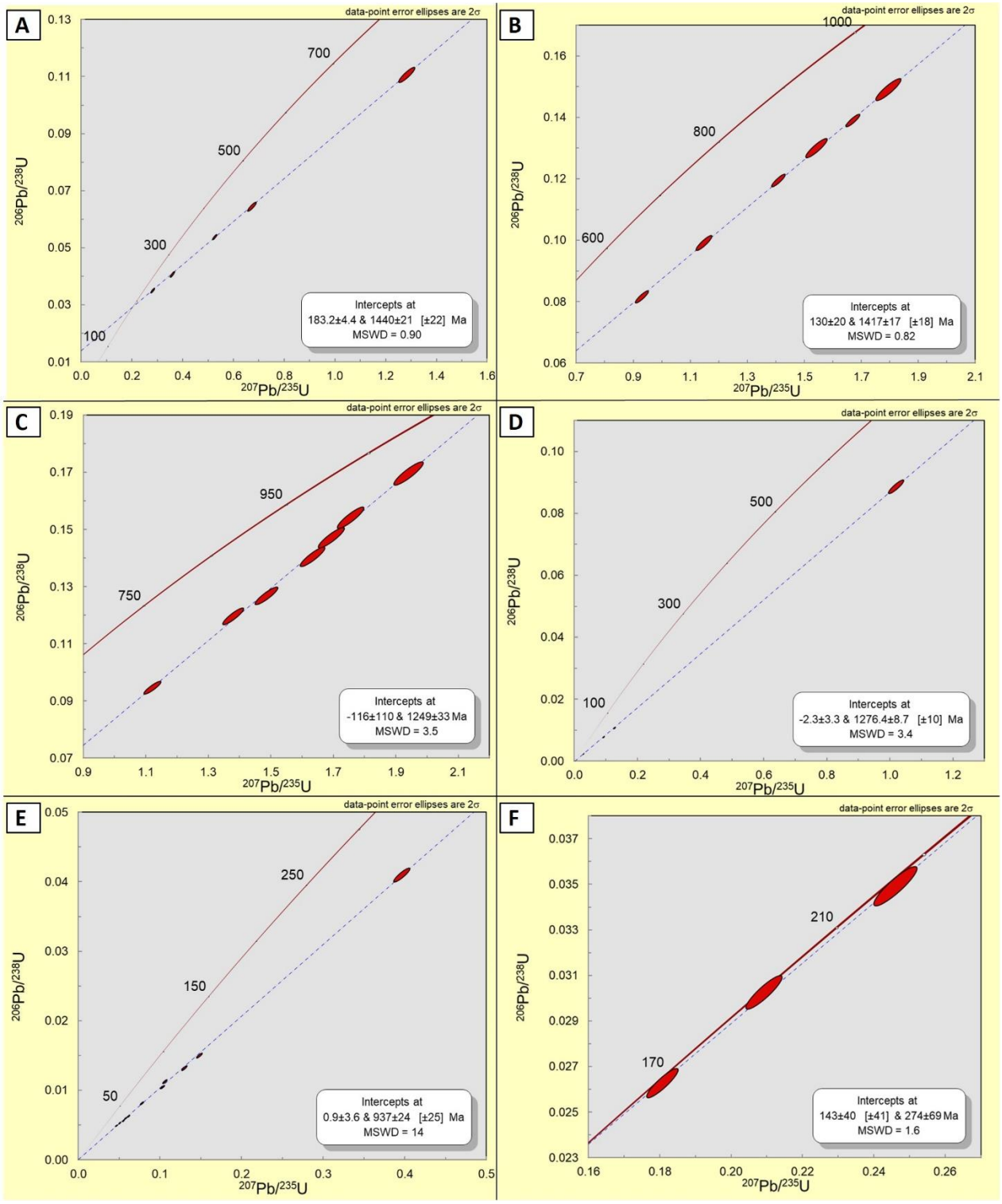
A
data-point error ellipses are 2σ
700
500
300
100
Intercepts at
183.2±4.4 & 1440±21 [±22] Ma
MSWD = 0.90
B
data-point error ellipses are 2σ
1000
800
600
Intercepts at
130±20 & 1417±17 [±18] Ma
MSWD = 0.82
C
data-point error ellipses are 2σ
950
750
Intercepts at
-116±110 & 1249±33 Ma
MSWD = 3.5
D
data-point error ellipses are 2σ
500
300
100
Intercepts at
-2.3±3.3 & 1276.4±8.7 [±10] Ma
MSWD = 3.4
E
data-point error ellipses are 2σ
250
150
50
Intercepts at
0.9±3.6 & 937±24 [±25] Ma
MSWD = 14
F
data-point error ellipses are 2σ
210
170
Intercepts at
143±40 [±41] & 274±69 Ma
MSWD = 1.6
206Pb/238U
207Pb/235U

Fig. A3. U-Pb Concordia plots of SIMS data from uraninite and brannerite. A. U1b brannerite from the End Deposit. B. Altered U1b, c, and U2 uraninite in the End deposit. C. U2 altered uraninite from the Kiggavik Main Zone. D. Altered U1c and U2 uraninite from the End Deposit. E. 'Worm-rock' texture U2 uraninite from the Andrew Lake Deposit. F. Disseminated brannerite from the End Deposit.

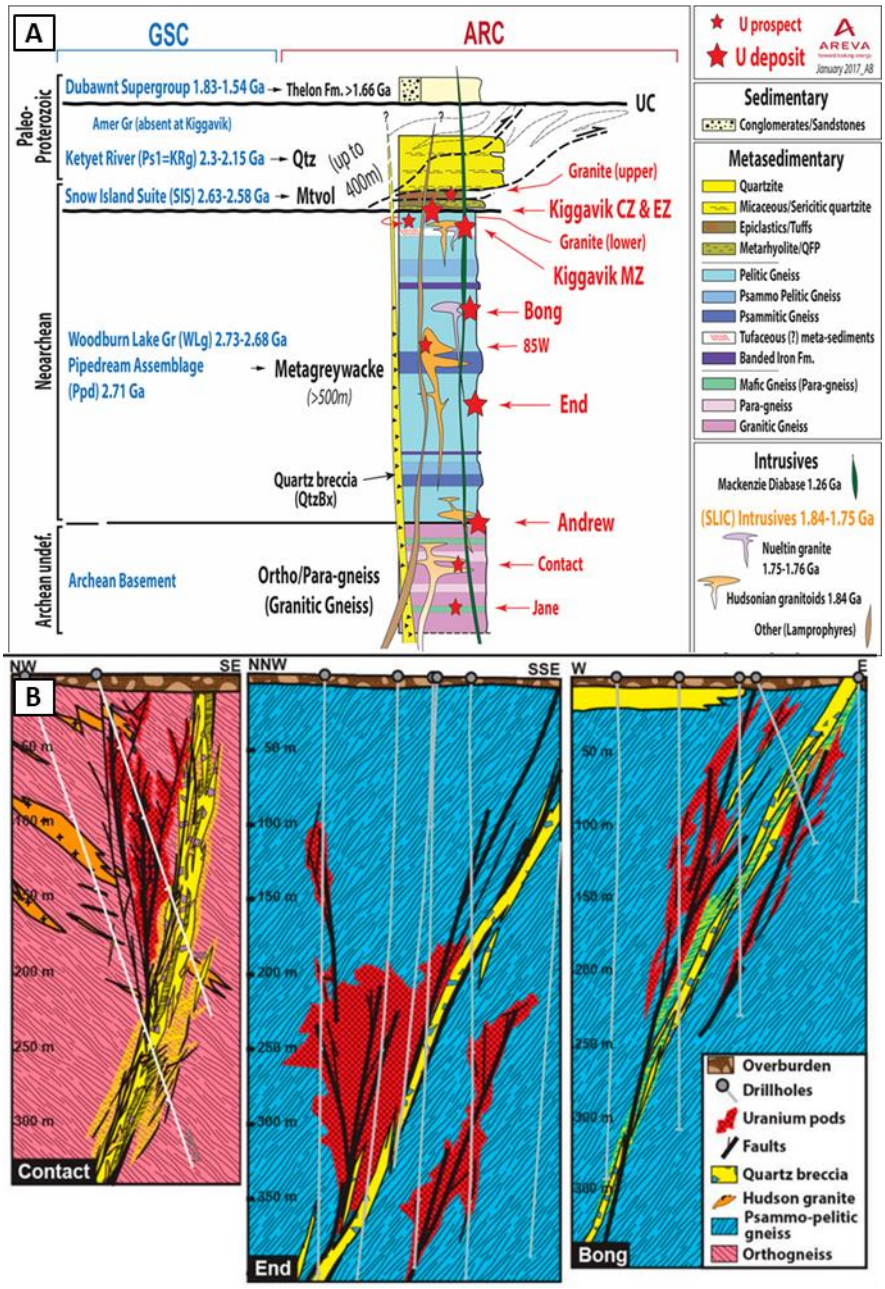

Fig. A4. Schematic diagram for, and cross-sections of, U deposits and prospects in the Kiggavik region. A. Schematic diagram illustrating spatial associations between U mineralization, lithostratigraphy, and intrusions (Modified after Grare, 2016). B. Cross-sections illustrating close spatial associations of faults, the QB, and U mineralization in Kiggavik area deposits and prospects, From Grare et al. (2020).

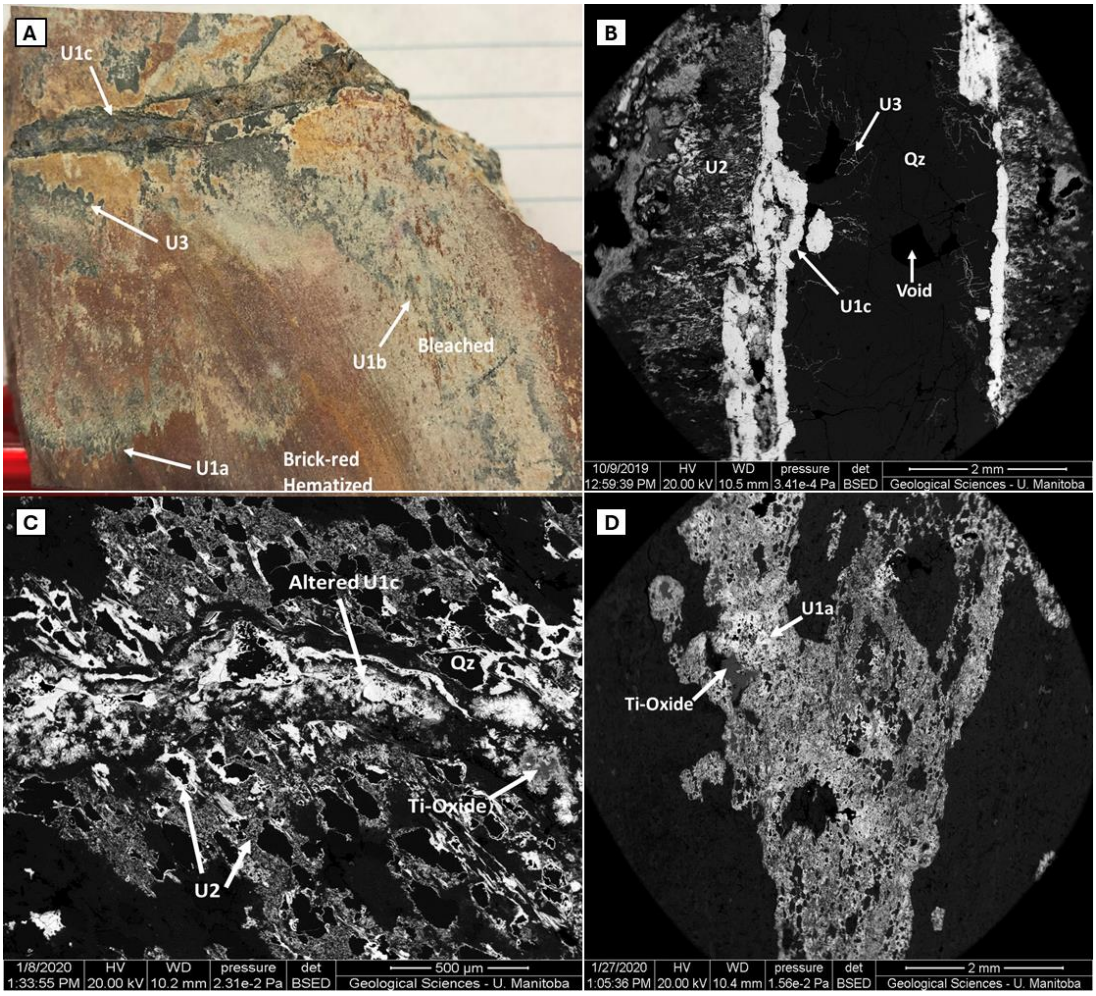

Fig. A5. Textural relationships between U1a, b, and c. A. Core sample END-11-02-327.8 with U1a, U1b, and U1c, and associated bleaching cross-cutting brick-red hematization. U3 is present on the redox boundary of orange hematite-goethite alteration which has developed in close proximity to a vuggy U1c quartz vein. B. BSE image of U1c stringers in a quartz vein, with U2 in the host rock adjacent to the vein and U3 along interstices between quartz crystals (End-11-02-327.8). C. Strongly-altered U1c stringer associated with Ti-oxides in a quartz-carbonate vein (End-09-04-272.9). D. U1a associated with Ti-oxides (Bong-50-292). Abrreviations: Qz = quartz, Void = open cavity/pore space.

Appendix Table A1. Summary of previously reported ages from the Kiggavik region.

Reference	Type	Deposit	Technique	Mineral	Age
Weyer (1992)	Intrusion	Lone Gull granite (Kiggavik Main/Centre)	K-Ar	Biotite	1848 ± 33 Ma
Scott, et al. (2015)	Intrusion	Granite Grid monzogranite (Hudson)	U-Pb	Zircon	1840 ± 11 Ma
Scott, et al. (2015)	Intrusion	Schultz Lake Intrusive Complex (Hudson-Martell)	U-Pb	Zircon	1839.7 ± 9.3 Ma
Scott, et al. (2015)	Intrusion	Bong syenite, Martell (Hudson) portion	U-Pb	Zircon	1837.8 ± 7.7 Ma
Scott, et al. (2015)	Intrusion	Lone Gull granite, Hudson portion	U-Pb	Zircon	1836 ± 22 Ma
Scott, et al. (2015)	Intrusion	Monzogranite sill, Kiggavik (Hudson)	U-Pb	Zircon	1830 ± 16 Ma
Scott, et al. (2015)	Intrusion	Lone Gull granite, Hudson portion	U-Pb	Zircon	1820 ± 12 Ma
Scott, et al. (2015)	Intrusion	Syenite dyke, Kiggavik (Hudson-Martell)	U-Pb	Zircon	1817.5 ± 7.8 Ma
Weyer (1992)	Intrusion	Lone Gull granite (Kiggavik Main/Centre)	K-Ar	Muscovite	1804 ± 32 Ma
Shabaga, et al. (2017)	Host Rock	Andrew Lake (metasedimentary rocks)	Ar-Ar	Muscovite	1782 ± 18 Ma
Scott, et al. (2015)	Intrusion	Lone Gull granite, Nueltin portion	U-Pb	Titanite	1759 ± 44 Ma
Scott, et al. (2015)	Intrusion	Lone Gull granite, Nueltin portion	U-Pb	Zircon	1759 ± 20 Ma
Scott, et al. (2015)	Intrusion	Bong syenite, Nueltin portion	U-Pb	Titanite	1758.5 ± 44 Ma
Davis, et al. (2011)	Cement	Thelon Fluorapatite cement	U-Pb	Apatite	1667 ± 7 Ma
Miller (1981); in Fuchs, et al. (1986)	Alteration	Various Lone Gull	K-Ar (whole rock)	N/A	1648 Ma (No errors reported)
Ashcroft (2020)	Host Rock	End (Metasedimentary Rocks)	Ar-Ar	Muscovite	1603 ± 4 Ma
Shabaga, et al. (2017)	Host Rock	Andrew Lake (Metasedimentary Rocks)	Ar-Ar	Muscovite	1599 ± 20 Ma
Fayek, et al. (2019)	Alteration	Kiggavik (Main)	Pb-Pb	Galena	1589 ± 39 Ma
Miller (1981); in Fuchs, et al. (1986)	Alteration	Various Lone Gull	K-Ar (whole rock)	N/A	1563 Ma (no errors reported)
Chamberlain, et al. (2010)	Volcanic	Kuungmi ultrapotassic Lavas	U-Pb	Baddeleyite	1540 ± 30 Ma
Sharpe, et al. (2015)	Mineralization	Bong	U-Pb	Uraninite	1520 ± 79 Ma
Ashcroft (2020)	Alteration	End	Ar-Ar	Illite	1476 ± 26 Ma

Fayek, et al. (2019)	Alteration	Kiggavik (Main)	Pb-Pb	Galena	1461 ± 16 Ma
Ashcroft (2020)	Mineralization	End	U-Pb	Uraninite	1459 ± 55 Ma
Farkas (1984)	Alteration	Various Lone Gull	Pb-Pb	Galena	1418 Ma (no errors reported)
Farkas (1984)	Mineralization	Various Lone Gull	U-Pb	Uraninite	1403 ± 10 Ma
Miller (1981); in Fuchs, et al. (1986)	Alteration	Various Lone Gull	K-Ar (whole rock)	N/A	1358 Ma (no errors reported)
Shabaga, et al. (2017)	Alteration	Andrew Lake	Ar-Ar	Illite	1330 ± 36 Ma
Ashcroft (2020)	Alteration	End	Ar-Ar	Illite	1308 ± 13 Ma
Chi, et al. (2017)	Mineralization	End	U-Pb	Uraninite	1295 ± 12 Ma
Riegler (2013)	Mineralization	End	U-Pb	Uraninite	1293 ± 6 Ma
Weyer (1992)	Alteration	Lone Gull granite (Kiggavik Main/Centre)	K-Ar	Illite	1291 ± 23 Ma
Weyer (1992)	Alteration	Lone Gull granite (Kiggavik Main/Centre)	K-Ar	Illite	1287 ± 18 Ma
Shabaga, et al. (2020)	Mineralization	Kiggavik (Main)	U-Pb	Uraninite	1284 ± 53 Ma
Ashcroft (2020)	Mineralization	End	U-Pb	Uraninite	1280 ± 32 Ma
Grare, et al. (2020)	Mineralization	End	U-Pb	Uraninite	1277 ± 10 Ma
Fahrig (1987); LeCheminant and Heaman (1989)	Intrusion	Mackenzie diabase dykes	U-Pb	Baddeleyite and Zircon	1267 ± 2 Ma
Grare, et al. (2020)	Mineralization	End	U-Pb	Uraninite	1257 ± 58 Ma
Weyer (1992)	Alteration	Lone Gull granite (Kiggavik Main/Centre)	K-Ar	Illite	1229 ± 18 Ma
Riegler (2013)	Mineralization	End	U-Pb	Uraninite	1187 ± 19 Ma
Grare, et al. (2020)	Mineralization	End	U-Pb	Uraninite	1175 ± 23 Ma
Weyer (1992)	Alteration	Lone Gull granite (Kiggavik Main/Centre)	K-Ar	Illite	1166 ± 18 Ma
Weyer (1992)	Intrusion	Lone Gull granite (Kiggavik Main/Centre)	K-Ar	Hornblende	1155 ± 19 Ma
Riegler (2013)	Alteration	Bong	Ar-Ar	Illite	1124 ± 9 Ma*
Sharpe, et al. (2015)	Mineralization	Bong	U-Pb	Uraninite	1114 ± 8 Ma
Grare, et al. (2020)	Mineralization	85W	U-Pb	Uraninite	1073 ± 5 Ma
Miller (1981); in Fuchs, et al. (1986)	Alteration	Various Lone Gull	K-Ar (whole rock)	N/A	1073 Ma (no errors reported)
Shabaga, et al. (2017)	Mineralization	Andrew Lake	U-Pb	Uraninite	1031 ± 23 Ma
Farkas (1984)	Mineralization	Various Lone Gull	U-Pb	Uraninite	1000 ± 10 Ma
Sharpe, et al. (2015)	Mineralization	Bong	U-Pb	Uraninite	982 ± 19 Ma
Shabaga, et al. (2017)	Alteration	Andrew Lake	Ar-Ar	Illite	941 ± 31 Ma
Weyer (1992)	Alteration	Lone Gull granite (Kiggavik Main/Centre)	K-Ar	Illite	930.4 ± 18.4 Ma; 930.0 ± 19.9 Ma; 912.8 ± 16.7 Ma
Shabaga, et al. (2017)	Mineralization	Andrew Lake	U-Pb	Uraninite	577 ± 37 Ma

Grare, et al. (2020)	Mineralization	Andrew Lake	U-Pb	Uraninite	547 ± 13 Ma
Shabaga, et al. (2017)	Mineralization	Andrew Lake	U-Pb	Uraninite	532 ± 35 Ma; 513 ± 47 Ma; 489 ± 16 Ma
Grare, et al. (2020)	Mineralization	Andrew Lake	U-Pb	Uraninite	347 ± 58 Ma; 344 ± 19 Ma
Shabaga, et al. (2020)	Mineralization	Kiggavik (Main)	U-Pb	Uraninite	284 ± 19 Ma
Shabaga, et al. (2017)	Mineralization	Andrew Lake	U-Pb	Uraninite	<1 Ma

* only plateau age from Riegler (2014) where >50% ^{39}Ar released

Appendix table A2. Chemical compositions of Zr-Th-U silicates in Kiggavik Deposit granitic rocks. All values reported in wt % and measured via EMPA.

Sample ID	Depth (m)	Mineral	UO_2	ThO_2	SiO_2	ZrO_2	HfO_2	CaO	TiO_2	FeO	Al_2O_3	P_2O_5	SO_2	PbO	Na_2O	MgO	K_2O	MnO	Cl	Total
KN-02	245.6	Zr1	0.02	0	31.73	66.36	1.37	0.12	0.15	0.11	0.05	0	0.02	0.09	-	-	-	-	-	100.02
KN-04	106	Zr1	0	0.18	31.48	64.53	1.19	0.04	0	2.06	0.01	-	-	0.07	0	0.02	0.01	0.01	0	99.6
KN-04	106	Zr1	0	0.24	27.77	63.03	1.73	0.79	0.01	1.61	0.64	-	-	0	0	0.06	0	0	0.05	95.93
MZ-10-01	119.3	Zr1	0	0.11	31.87	64.61	1.71	0.25	0.05	0.1	0.12	-	-	0	0	0.01	0.04	0.04	0	98.91
MZ-10-01	130	Zr1	0.31	0.11	28.48	60.07	1.47	0.93	0.08	0.87	0.5	0	0.01	0.19	-	-	-	-	-	93
MZ-10-01	130	Zr1	0.37	0	30.46	63.74	2.11	0.07	0	0.03	0	0	0.02	0.08	-	-	-	-	-	96.89
MZ-10-01	130	Zr1	0.17	0.21	29.23	63.41	1.67	0.48	0	0.87	0.35	0	0.02	0.12	-	-	-	-	-	96.51
MZ-10-01	190	Zr1	0.53	0.32	26.17	57.04	1.66	1.67	0.58	1.43	0.75	0	0.06	0.05	-	-	-	-	-	90.25
MZ-10-01	205	Zr1	0	0.54	31.17	62.96	1.53	0.21	0.18	0.2	0.11	-	-	0.08	0.03	0.02	0.04	0.08	0.05	97.19
MZ-10-01	205	Zr1	0	0	30.4	60.46	1.85	0.33	0.49	0.54	0.17	-	-	0.07	0.09	0.05	0.03	0.09	0.03	94.61
MZ-10-01	237	Zr1	0.04	0.23	30.74	60.78	1.35	0.44	0.06	0.35	0.27	-	-	0.09	0	0.04	0.01	0.03	0.04	94.46
MZ-10-01	237	Zr1	0	0.03	32.17	66.68	1.2	0.03	0	0.47	0	-	-	0	0	0	0.01	0.01	0	100.6
MZ-10-01	237	Zr1	0	0.01	32.13	65.7	1.7	0.01	0.01	0.1	0.02	-	-	0.03	0	0.02	0.01	0.02	0	99.76
MZ-10-01	237	Zr1	0.09	0	29.31	60.29	1.9	1.06	0.03	1.18	0.79	-	-	0.06	0.06	0.19	0.03	0.18	0.1	95.29
MZ-10-01	248.8	Zr1	0.19	0.96	27.9	62.59	1.63	1.68	0.11	0.29	0.26	0	0.02	0	-	-	-	-	-	95.64
MZ-10-01	248.8	Zr1	0.59	0.23	26.69	55.06	1.67	1.92	0.01	1.04	0.81	0	0.04	0	-	-	-	-	-	88.06
KN-02	245.6	Zr2	0.01	0.48	19.98	48.99	4.65	3.17	0.46	0.92	1.56	0.06	0.06	0.02	-	-	-	-	-	80.37
MZ-08-02	193	Zr2	0	4.2	21.71	48.22	2.5	3.2	0.23	1.66	0.92	-	-	0	0.01	0.17	0	0.05	0.17	83.04
MZ-10-01	79.1	Zr2	0.27	3.43	21.7	56.92	1.18	4.23	0.2	0.6	2.01	-	-	0.09	0	0.39	0.04	0	0.18	91.24
MZ-10-01	79.1	Zr2	0.45	3.68	19.04	48.86	1.33	3.97	0.14	0.56	2.03	-	-	0.14	0	0.45	0.02	0.09	0.17	80.92
MZ-10-01	79.1	Zr2	0.16	5.99	16.24	42.65	1.12	3.65	0.19	0.68	1.73	-	-	0	0	0.33	0.11	0.01	0.13	72.98
MZ-10-01	119.3	Zr2	0.66	1.88	20.73	49.35	1.72	3.63	0.41	0.68	1.89	-	-	0	0.01	0.28	0.04	0.24	0.2	81.71
MZ-10-01	119.3	Zr2	0.04	0.49	23.53	55.61	2.14	2.33	0.11	1.23	1.41	-	-	0	0	0.23	0.02	0.19	0	87.31
MZ-10-01	119.3	Zr2	0.58	4.17	21.72	48.77	2.29	3.39	0.36	0.28	2.1	-	-	0	0	0.26	0.06	0.12	0.14	84.24
MZ-10-01	120	Zr2	3	4.16	20	42.38	1.76	3.23	0.04	1.11	1.54	1.11	0.09	0.03	-	-	-	-	-	78.48
MZ-10-01	120	Zr2	1.84	0.93	21.13	42.52	2.31	2.83	0.06	1.67	1.04	0.73	0.01	0.3	-	-	-	-	-	75.36
MZ-10-01	130	Zr2	0.52	0.18	26.71	54.6	4.7	1.48	0.01	1.06	1.1	0	0	0.05	-	-	-	-	-	90.41
MZ-10-01	130	Zr2	0.26	0.91	21.03	51.19	3.3	3.17	0.74	1.09	1.65	0	0.02	0.14	-	-	-	-	-	83.5
MZ-10-01	130	Zr2	0.65	0.49	27.71	56.83	1.74	1.38	0	1.34	0.9	0	0.02	0.04	-	-	-	-	-	91.1

MZ-10-01	130	Zr2	3.12	0.62	23.27	43.53	1.56	2.52	0.04	0.25	2.98	0.07	0	0.06	-	-	-	-	-	78
MZ-10-01	130	Zr2	0.84	0.13	23.31	48.43	5.95	2.64	0.02	0.78	1.98	0	0.04	0.08	-	-	-	-	-	84.22
MZ-10-01	190	Zr2	1.15	0.66	23.32	50.63	1.75	2.32	0.13	1.9	1.7	0	0.01	0.02	-	-	-	-	-	83.59
MZ-10-01	190	Zr2	0.98	0.45	24.73	50.79	2.78	1.94	0.15	3.42	2.82	0	0.07	0	-	-	-	-	-	88.12
MZ-10-01	190	Zr2	0.57	1.46	19.26	46.77	3.61	2.95	0.15	2.21	2.16	0	0.43	0.03	-	-	-	-	-	79.59
MZ-10-01	190	Zr2	0.52	2.18	19.78	48.61	2.28	3.23	0.13	3.15	1.37	0.03	0.15	0	-	-	-	-	-	81.44
MZ-10-01	205	Zr2	0	0.45	28.14	55.95	0.96	1.84	0.19	0.5	0.84	-	-	0.03	0	0.25	0.06	0.15	0.2	89.53
MZ-10-01	205	Zr2	0.39	4.61	20.93	47.46	1.95	2.76	0.25	1.21	1.23	-	-	0	0	0.18	0.01	0.07	0.02	81.06
MZ-10-01	237	Zr2	0.23	0.29	24.55	55.97	2.53	2.42	0.23	0.82	2	-	-	0.02	0	0.21	0.02	0.08	0.11	89.46
MZ-10-01	237	Zr2	0.19	0.48	24.34	51.87	1.91	2.64	0.25	0.91	1.73	-	-	0	0.03	0.25	0.03	0.03	0.26	84.94
MZ-10-01	237	Zr2	3.01	0.79	22.09	49.69	2.22	2.13	0.34	0.9	1.49	-	-	0	0	0.17	0.04	0.06	0.19	83.1
MZ-10-01	248.8	Zr2	0.28	0.14	19.57	50.78	3.46	3.96	0.15	1.07	1.2	0.43	0.08	0.08	-	-	-	-	-	81.2
MZ-10-01	248.8	Zr2	0.19	0.31	21.17	55.66	1.82	4.29	0.04	0.61	1.03	0.24	0.08	0.04	-	-	-	-	-	85.48
MZ-10-01	248.8	Zr2	1.2	4.05	19.38	44.17	3.18	3.26	0.4	2.06	1.25	0.5	0.04	0.12	-	-	-	-	-	79.58
MZ-10-01	248.8	Zr2	1.19	2.49	21.32	52.36	1.1	3.24	0.19	1.56	1.21	0.4	0.02	0.09	-	-	-	-	-	85.16
MZ-10-01	248.8	Zr2	0.86	4.63	19.66	45.32	2.32	3.88	0.18	1.2	1.24	0.49	0.11	0.02	-	-	-	-	-	79.92
KN-02	245.6	Thorite	0.06	53.99	14.71	12.19	0.1	3.1	0.11	0.29	0.34	2.62	0.06	0	-	-	-	-	-	87.59
KN-02	245.6	Thorite	5.02	54.13	14.88	0.65	0.07	1.86	0.12	0.94	2.4	2.88	0.15	0.33	-	-	-	-	-	83.42
KN-02	245.6	Thorite	42.44	13.74	21.44	5.28	0.12	2.84	0.57	0.87	0.56	1.72	0.37	0.11	-	-	-	-	-	90.06
MZ-08-02	193	Thorite	0.68	63.87	15.94	0.88	0.06	2.54	0.12	2.27	0.11	-	-	0	0	0.1	0.08	0	0.02	86.67
MZ-08-02	193	Thorite	0.46	67.12	12.23	1.07	0.07	3.07	0.08	1.53	0.09	-	-	0	1.47	0.11	0.05	0.19	0.21	87.74
MZ-08-02	193	Thorite	1.19	40.99	17.31	23.79	1.35	3.32	0.19	0.08	0.43	-	-	0	0	0.23	0.03	0.02	0.62	89.54
MZ-08-02	193	thorite	0.48	59.7	8.44	1.22	0	4.33	0.11	0.95	0.05	-	-	0.04	0.19	0.26	0.1	0.05	0.33	76.27
MZ-10-01	106.7	Thorite	1.51	35.44	15.98	25.06	0.93	3.74	0.16	0.06	0.77	1.55	0.1	0	-	-	-	-	-	85.32
MZ-10-01	130	Thorite	3.55	59.98	9.02	0.71	0	1.69	0.13	1.41	0.24	1.77	0.12	0.47	-	-	-	-	-	79.09
MZ-10-01	130	Thorite	21.18	47.25	13.5	0.12	0	1.85	0.05	0.09	0.43	0.55	0.08	0.61	-	-	-	-	-	85.72
MZ-10-01	130	Thorite	14.92	50.54	14.62	0.03	0	1.64	0.05	0.09	0.23	1.46	0.16	0.62	-	-	-	-	-	84.38
MZ-10-01	130	Thorite	11.07	22.96	8.43	19.35	1.52	3.93	1.07	0.21	0.37	0.54	0.11	2.8	-	-	-	-	-	72.37
MZ-10-01	130	Thorite	5.14	53.67	12.3	3.65	0.04	1.65	0.1	0.52	0.28	2.33	0.13	0.28	-	-	-	-	-	80.08
MZ-10-01	130	Thorite	4.25	36.45	14.09	19.2	1	3.24	0.65	0.15	0.53	0.88	0.09	0.94	-	-	-	-	-	81.46
MZ-10-01	130	Thorite	8.56	56.06	4.59	1.45	0	4.28	0	0.21	0.15	1.1	0.53	1.1	-	-	-	-	-	78.02
MZ-10-01	130	Thorite	30.92	1.64	15.47	17.5	0.53	3.14	5.98	1.85	1.05	0.29	0.04	0.05	-	-	-	-	-	78.45

MZ-10-01	130	Thorite	19.89	20.52	16.52	14.48	0.53	3.42	1.31	4.32	0.57	0.67	3.89	0	-	-	-	-	-	86.12
MZ-10-01	130	Thorite	0.2	37.99	15.94	19.71	1.05	2.88	0.28	1.21	1.84	0.67	0.33	0	-	-	-	-	-	82.1
MZ-10-01	130	Thorite	0	46.13	15.84	12.71	0.36	3.09	0.6	0.5	2.05	1.39	0.13	0	-	-	-	-	-	82.78
MZ-10-01	130	Thorite	0	57.23	11.03	5.94	0.35	2.96	0.25	1.08	0.34	1.74	0.3	0.51	-	-	-	-	-	81.73
MZ-10-01	190	Thorite	15.84	9.89	16.78	24.92	1.08	3.47	0.59	3.23	3.29	0.55	0.06	0	-	-	-	-	-	79.7
MZ-10-01	190	Thorite	0.19	21.17	16.15	31.57	1.69	3.18	0.26	0.94	0.91	0.44	0.37	0	-	-	-	-	-	76.87
MZ-10-01	190	Thorite	0	62.53	5.55	5.78	0.02	3.98	0.25	0.52	0.25	2.06	0.62	0	-	-	-	-	-	81.55
MZ-10-01	190	Thorite	0	47.94	14.4	11.64	0.24	2.34	0.35	2.9	0.67	1.63	0.25	0.08	-	-	-	-	-	82.44
MZ-10-01	190	Thorite	0.06	51.76	12.42	8.06	0.4	2.19	0.2	4.31	0.87	2.33	1.82	0	-	-	-	-	-	84.42
MZ-10-01	205	Thorite	11.23	51.38	13.47	4.66	0	3.12	0.06	0.42	0.33	-	-	0.37	0.02	0.15	0.15	0.03	0.48	85.85
MZ-10-01	205	Thorite	0.44	55.75	12.95	6.77	0	2.94	0.11	0.11	0.14	-	-	0.33	0.02	0.13	0.07	0.01	0.14	79.89
MZ-10-01	205	Thorite	0.38	59.36	11.13	8.29	0	3.16	0.29	0.73	0.22	-	-	0.09	0.02	0.19	0.06	0.06	0.14	84.14
MZ-10-01	237	Thorite	0.39	59.01	13.91	9.23	0.24	3.45	0.46	1.27	0.3	-	-	0	0	0.16	0.04	0.01	0.24	88.69
MZ-10-01	237	Thorite	0.72	45.85	16.39	21.68	1.5	3.02	1.45	0.21	0.43	-	-	0.02	0	0.26	0.06	0.03	0.54	92.15
MZ-10-01	237	Thorite	0.55	54.44	11.7	9.52	0.57	1.33	0.71	1.23	0.28	-	-	0	0	0.11	0.11	0.57	0.58	81.72
MZ-10-01	237	Thorite	0.57	52.59	11.87	3.48	0	2.97	0.05	0.17	0.19	-	-	0.01	0.23	0.16	0.11	0.02	0.14	72.57
MZ-10-01	237	Thorite	1.64	62.59	13.82	1.47	0	3.14	0.09	0.86	0.25	-	-	0	0	0.12	0.02	0.01	0.19	84.21
MZ-10-01	237	Thorite	0.37	60.54	3.08	0.8	0	2.46	0.08	3.03	0.09	-	-	0.04	0.08	0.14	0.17	0.08	0.35	71.31
MZ-10-01	248.8	Thorite	0.12	46	12.75	16.66	0.73	3.78	0.22	1.81	0.24	3.09	1.19	0	-	-	-	-	-	86.58
MZ-10-01	248.5	Thorite	0	50.71	12.63	15.16	0.74	4.45	0.09	0.26	0.28	3.68	0.07	0	-	-	-	-	-	88.07

Appendix table A3. Whole rock geochemical data from the Kiggavik deposits. Major element oxides and F are reported in wt%, all others are in ppm. *Data from Scott et al. (2015).

Sample	Depth (m)	Lithology	Alteration	SiO_2	Al_2O_3	FeO	MnO	MgO	CaO	Na_2O	K_2O	TiO_2	P_2O_5	F	LOI	Total
KMZ-MG*	0	Monzogranite	Fresh	72	13.66	1.00	0.02	0.66	0.97	3.35	5.69	0.25	0.1	0.16	-	97.70
MZ-10-01	130	Monzogranite	Albitized	73.87	12.59	1.21	0.024	0.38	0.44	2.98	5.82	0.074	0.01	0.12	1.1	98.64
MZ-10-01	230	Monzogranite	Albitized	75.34	12.39	1.65	0.036	0.9	0.29	2.19	5.85	0.071	0.01	0.12	1.47	100.4
MZ-10-01	237.3	Monzogranite	Albitized	72.32	12.98	0.90	0.029	1.35	0.14	0.12	9.01	0.072	0.01	0.03	1.66	98.71
KN-04	126	Monzogranite	Albitized	75.09	12.14	1.46	0.035	0.12	0.55	4.01	4.21	0.072	0.01	0.21	0.74	98.6
MZ-10-01	79.4	Monzogranite	Oxidized	62.76	14.96	4.43	0.023	4.98	1.08	0.05	2.74	0.211	0.06	0.1	6.88	98.66
KN-04	66.5	Monzogranite	Oxidized	71.51	13.65	1.90	0.009	1.18	0.17	0.12	9.06	0.24	0.11	< 0.02	2.01	100.2
KN-04	106.1	Monzogranite	Oxidized	74	13.02	1.48	0.022	0.34	0.36	3.14	5.82	0.145	0.06	0.03	0.71	99.27
MZ-10-01	80.9	Monzogranite	Bleached	71.84	14.3	1.30	0.031	1.42	0.21	0.05	7.85	0.188	0.08	0.07	2.38	99.79
MZ-10-01	90.1	Monzogranite	Bleached	70.44	15.69	0.94	0.014	3.52	0.15	0.04	3.61	0.103	0.04	0.09	5.04	99.68
MZ-10-01	107.2	Monzogranite	Bleached	73.29	13.01	1.20	0.029	0.48	0.09	0.63	9.03	0.094	0.02	0.07	1.79	99.79
LG-86	158.5	Monzogranite	Bleached	63.96	18.52	0.77	0.026	2.65	0.38	0.07	5.48	0.098	0.15	0.14	6.75	98.95
END-09-05	95.08	Granitic dyke	Bleached	74.08	13.68	0.87	0.007	0.7	0.12	0.07	7.26	0.257	0.06	0.02	2.12	99.32
KN-04	12	Epiclastic	Oxidized	60.16	15.2	11.26	0.011	2.34	0.12	0.04	3.49	0.324	0.06	0.04	4.7	98.95
KN-04	12	Epiclastic	Bleached	68.6	14.47	4.04	0.029	3.05	0.14	0.04	2.9	0.332	0.06	0.12	4.89	99
END-10-02A	400	Metasediment	Fresh	64.06	16.99	5.52	0.061	1.92	1.72	2.99	3.65	0.531	0.16	0.04	2.29	100.5
END-11-02	327.8	Metasediment	Oxidized	55.73	17.34	9.01	0.049	2.37	0.34	0.12	4.98	0.663	0.13	0.05	6.95	98.68
END-11-02	327.8	Metasediment	Bleached	66.94	16.2	2.24	0.016	1.24	0.24	0.12	4.7	0.513	0.05	0.04	5.98	98.5
CZ-15-01	82.6	Metasediment	Bleached	45.13	25.98	2.66	0.018	7.81	0.64	0.06	5.76	1.31	0.3	0.16	10.67	100.6
CZ-15-01	82.6	Metasediment	Ferric	46.13	24.65	5.70	0.045	3.61	0.49	0.09	7.18	0.57	0.12	0.17	11.41	100.6

Sample	Depth (m)	Lithology	Alteration	U	Th	Th/U	Pb	Sc	Be	V	Cr	Co	Ni	Cu	Zn	Ga
KMZ-MG*	0	Monzogranite	Fresh	7.3	42.8	5.86	11.8	-	15	-	-	-	-	20.8	14	17.4
MZ-10-01	130	Monzogranite	Albitized	25	25.8	1.03	76	1	8	< 5	< 20	< 1	< 20	< 10	< 30	23
MZ-10-01	230	Monzogranite	Albitized	26.6	26.5	1.00	110	1	10	15	< 20	1	< 20	20	< 30	23
MZ-10-01	237.3	Monzogranite	Albitized	30.6	30.1	0.98	42	2	329	8	< 20	2	< 20	< 10	< 30	22
KN-04	126	Monzogranite	Albitized	21.9	30.9	1.41	115	1	8	7	< 20	1	< 20	10	< 30	27
MZ-10-01	79.4	Monzogranite	Oxidized	72.8	38.8	0.53	849	3	10	179	< 20	4	50	< 10	< 30	20
KN-04	66.5	Monzogranite	Oxidized	4.8	20.2	4.21	28	2	4	13	< 20	3	30	< 10	< 30	17
KN-04	106.1	Monzogranite	Oxidized	13.4	33.4	2.49	68	1	12	10	< 20	1	< 20	< 10	< 30	20

MZ-10-01	80.9	Monzogranite	Bleached	91.1	39.4	0.43	107	2	5	38	< 20	2	< 20	< 10	< 30	21
MZ-10-01	90.1	Monzogranite	Bleached	471	37.2	0.08	168	3	5	43	< 20	3	30	< 10	< 30	26
MZ-10-01	107.2	Monzogranite	Bleached	32.9	28	0.85	117	1	4	9	< 20	4	< 20	20	< 30	22
LG-86	158.5	Monzogranite	Bleached	> 1000	16.8	Na	454	4	7	1625	< 20	2	20	< 10	< 30	26
END-09-05	95.08	Granitic dyke	Bleached	2.29	34	14.85	12	2	2	22	< 20	1	30	< 10	< 30	16
KN-04	12	Epiclastic	Oxidized	4.28	63.3	14.79	14	3	4	29	60	3	30	< 10	< 30	16
KN-04	12	Epiclastic	Bleached	6.76	48.6	7.19	7	4	7	20	40	4	40	< 10	30	20
END-10-02A	400	Metasediment	Fresh	4.05	10.4	2.57	19	11	2	91	50	11	20	20	90	21
END-11-02	327.8	Metasediment	Oxidized	185	1.79	0.01	847	13	4	487	90	8	30	< 10	< 30	20
END-11-02	327.8	Metasediment	Bleached	> 1000	23.1	Na	6330	24	5	545	70	4	< 20	< 10	< 30	18
CZ-15-01	82.6	Metasediment	Bleached	> 1000	19.6	Na	693	26	14	1122	150	22	190	< 10	< 30	27
CZ-15-01	82.6	Metasediment	Ferric	480	28.5	0.06	1790	22	18	1670	80	10	70	30	< 30	25

Sample	**Depth (m)**	**Lithology**	**Alteration**	**Ge**	**As**	**Rb**	**Sr**	**Ba**	**Y**	**Zr**	**Nb**	**Mo**	**Ag**	**In**	**Sn**	**Sb**
KMZ-MG*	0	Monzogranite	Fresh		<0.5	431	342	1214	7.2	188	13	77.3	<0.1	-	2	
MZ-10-01	130	Monzogranite	Albitized	1.4	< 5	428	71	253	2.8	80	7.6	> 100	< 0.5	< 0.1	2	< 0.2
MZ-10-01	230	Monzogranite	Albitized	1.2	< 5	387	56	217	3	78	13.1	60	< 0.5	< 0.1	2	< 0.2
MZ-10-01	237.3	Monzogranite	Albitized	1	< 5	366	46	373	3.3	81	11.8	9	< 0.5	< 0.1	1	< 0.2
KN-04	126	Monzogranite	Albitized	1.7	< 5	516	83	217	3.9	88	12	10	< 0.5	< 0.1	2	< 0.2
MZ-10-01	79.4	Monzogranite	Oxidized	1.1	< 5	73	44	79	2.7	170	10.6	7	< 0.5	< 0.1	3	< 0.2
KN-04	66.5	Monzogranite	Oxidized	0.8	< 5	238	234	1461	29.2	154	9.6	2	< 0.5	< 0.1	2	0.2
KN-04	106.1	Monzogranite	Oxidized	1.1	< 5	429	163	499	3.5	108	7.5	3	< 0.5	< 0.1	1	< 0.2
MZ-10-01	80.9	Monzogranite	Bleached	0.7	< 5	249	64	433	2.3	151	9.1	< 2	< 0.5	< 0.1	2	< 0.2
MZ-10-01	90.1	Monzogranite	Bleached	0.8	< 5	79	24	29	4	115	12.1	< 2	< 0.5	< 0.1	2	< 0.2
MZ-10-01	107.2	Monzogranite	Bleached	0.9	< 5	435	70	427	3.6	85	5.7	25	< 0.5	< 0.1	1	< 0.2
LG-86	158.5	Monzogranite	Bleached	0.9	< 5	132	83	165	11.4	142	18.5	8	< 0.5	< 0.1	3	< 0.2
END-09-05	95.08	Granitic dyke	Bleached	0.7	< 5	199	186	1435	12.8	174	5.7	< 2	< 0.5	0.1	2	< 0.2
KN-04	12	Epiclastic	Oxidized	0.7	6	57	153	66	11.3	211	13.1	< 2	< 0.5	< 0.1	14	0.3
KN-04	12	Epiclastic	Bleached	0.9	< 5	222	111	105	11.3	205	28.1	< 2	< 0.5	< 0.1	10	0.2
END-10-02A	400	Metasediment	Fresh	1.1	< 5	111	318	896	10	147	5.3	2	< 0.5	< 0.1	1	< 0.2
END-11-02	327.8	Metasediment	Oxidized	1.3	< 5	142	53	744	4.1	127	7	< 2	< 0.5	< 0.1	1	< 0.2
END-11-02	327.8	Metasediment	Bleached	1.2	< 5	205	69	904	53.3	129	4.7	7	1.4	< 0.1	1	0.3
CZ-15-01	82.6	Metasediment	Bleached	1.1	6	147	44	275	29.5	216	15.1	4	3.6	< 0.1	4	0.2

CZ-15-01	82.6	Metasediment	Ferric	1.4	11	213	70	874	24.4	279	7	3	7.8	0.1	2	0.2
Sample	**Depth (m)**	**Lithology**	**Alteration**	**La**	**Ce**	**Pr**	**Nd**	**Sm**	**Eu**	**Gd**	**Tb**	**Dy**	**Ho**	**Er**	**Tm**	**Yb**
KMZ-MG*	0	Monzogranite	Fresh	53.6	98	9.24	30.3	3.73	0.75	2.4	0.27	1.26	0.2	0.57	0.1	0.7
MZ-10-01	130	Monzogranite	Albitized	17.6	28.6	2.49	7.32	0.94	0.183	0.53	0.06	0.36	0.07	0.24	0.047	0.35
MZ-10-01	230	Monzogranite	Albitized	19.7	32	2.77	8.13	1.03	0.194	0.54	0.07	0.38	0.08	0.24	0.047	0.39
MZ-10-01	237.3	Monzogranite	Albitized	18.8	30.8	2.52	6.49	0.74	0.141	0.46	0.07	0.45	0.09	0.29	0.057	0.46
KN-04	126	Monzogranite	Albitized	25.8	40.8	3.53	9.85	1.06	0.225	0.62	0.07	0.4	0.09	0.28	0.059	0.58
MZ-10-01	79.4	Monzogranite	Oxidized	3.55	6.12	0.49	1.88	0.37	0.44	0.51	0.09	0.54	0.1	0.3	0.053	0.4
KN-04	66.5	Monzogranite	Oxidized	68.5	123	13.1	44.3	8.19	1.03	5.7	0.84	4.86	0.86	1.95	0.264	1.57
KN-04	106.1	Monzogranite	Oxidized	28.6	48.4	4.44	13.9	2.02	0.403	1.08	0.12	0.6	0.1	0.29	0.046	0.33
MZ-10-01	80.9	Monzogranite	Bleached	2.47	6.16	0.63	2.28	0.36	0.255	0.36	0.07	0.39	0.08	0.23	0.036	0.3
MZ-10-01	90.1	Monzogranite	Bleached	16.4	29.1	1.82	4.39	0.4	0.224	0.46	0.08	0.46	0.1	0.3	0.051	0.38
MZ-10-01	107.2	Monzogranite	Bleached	5.85	10.9	1.05	3.22	0.58	0.176	0.57	0.08	0.45	0.09	0.29	0.048	0.36
LG-86	158.5	Monzogranite	Bleached	30	31.6	1.26	2.84	0.9	0.53	2.68	0.58	3.49	0.53	1.35	0.184	1.11
END-09-05	95.08	Granitic dyke	Bleached	53.7	102	9.53	29.1	4.14	0.994	2.76	0.39	2.34	0.43	1.17	0.161	1.12
KN-04	12	Epiclastic	Oxidized	46.2	77	9.45	36.1	7.36	1.14	3.15	0.36	1.84	0.37	1.17	0.194	1.39
KN-04	12	Epiclastic	Bleached	32.7	55.3	6.69	26.5	5.99	0.916	2.86	0.34	1.82	0.38	1.15	0.193	1.31
END-10-02A	400	Metasediment	Fresh	26.6	53.2	6.18	22.9	3.72	0.953	2.6	0.34	1.91	0.38	1.03	0.143	0.99
END-11-02	327.8	Metasediment	Oxidized	1.75	5.53	0.45	1.99	0.55	0.217	0.88	0.15	0.91	0.16	0.39	0.057	0.36
END-11-02	327.8	Metasediment	Bleached	19.3	49.4	6.74	27.6	10.8	7.11	20.3	4.16	20.6	2.76	5.88	0.681	3.84
CZ-15-01	82.6	Metasediment	Bleached	8.24	14.2	1.85	10.2	6.27	2.58	10.3	1.85	9.22	1.38	3.32	0.451	2.63
CZ-15-01	82.6	Metasediment	Ferric	3.54	150	1.32	6.16	3.14	2.1	6.7	1.3	7.6	1.2	3.26	0.474	2.89

Sample	**Depth (m)**	**Lithology**	**Alteration**	**Lu**	**Cs**	**Zr**	**Hf**	**Ta**	**W**	**Tl**	**Bi**	**Au**
KMZ-MG*	0	Monzogranite	Fresh	0.1	18.4	188	6.4	1	13.2	-	0.2	2
MZ-10-01	130	Monzogranite	Albitized	0.065	8.7	80	4.1	1.31	110	4.82	0.2	< 2
MZ-10-01	230	Monzogranite	Albitized	0.072	6.3	78	4.2	1.71	2.3	4.22	1.9	< 2
MZ-10-01	237.3	Monzogranite	Albitized	0.087	5.1	81	4.9	2.24	0.8	4.38	0.8	< 2
KN-04	126	Monzogranite	Albitized	0.125	11.2	88	6.1	1.63	15.5	5.8	0.8	< 2
MZ-10-01	79.4	Monzogranite	Oxidized	0.068	4.4	170	5.6	1.12	3.3	0.31	0.1	< 2
KN-04	66.5	Monzogranite	Oxidized	0.219	2.7	154	5.1	1.16	15.8	2.48	0.6	< 2
KN-04	106.1	Monzogranite	Oxidized	0.06	10	108	3.9	0.73	1.5	4.36	0.1	< 2
MZ-10-01	80.9	Monzogranite	Bleached	0.053	6.2	151	5.2	1.04	3.3	1.89	0.1	< 2

MZ-10-01	90.1	Monzogranite	Bleached	0.078	2.5	115	7.1	2.17	1.4	0.72	< 0.1	< 2
MZ-10-01	107.2	Monzogranite	Bleached	0.075	11.5	85	3.9	0.76	0.8	4.5	< 0.1	104
LG-86	158.5	Monzogranite	Bleached	0.167	8.4	142	8.8	2.68	5.2	1.21	0.2	10
END-09-05	95.08	Granitic dyke	Bleached	0.168	3.8	174	4.9	0.78	0.8	2.25	0.1	< 2
KN-04	12	Epiclastic	Oxidized	0.239	3.6	211	5.7	0.94	93.5	0.49	0.6	< 2
KN-04	12	Epiclastic	Bleached	0.234	22.8	205	6.2	1.26	33.7	1.29	1.6	< 2
END-10-02A	400	Metasediment	Fresh	0.16	3.9	147	4	0.49	1.8	0.9	0.1	12
END-11-02	327.8	Metasediment	Oxidized	0.059	4.9	127	3.4	0.67	2.2	0.91	0.1	24
END-11-02	327.8	Metasediment	Bleached	0.478	7.1	129	3.9	0.46	7.6	1.72	9.2	888
CZ-15-01	82.6	Metasediment	Bleached	0.342	10	216	7.3	1.45	20.8	1.09	0.6	163
CZ-15-01	82.6	Metasediment	Ferric	0.4	18.8	279	6.4	0.61	23.8	1.4	1.8	71

Appendix Table A4. Corrected U-Pb isotopic ratios used to plot Concordia diagrams for U-minerals and corresponding Pb-Pb ratios. Abbreviations: Urn = uraninite, Bran = brannerite

Sample ID	Depth (m)	Mineral	Style	U-Pb age (Ma)	$^{207}Pb/^{235}U$	$^{206}Pb/^{238}U$	$^{206}Pb/^{204}Pb$	$^{207}Pb/^{204}Pb$
BONG-50	292.2	Urn	U1a	1594	0.04449189	0.00376955	2372.265	213.8346
BONG-50	292.2	Urn	U1a	1594	0.036877065	0.00324347	872.8465	75.29473
BONG-50	292.2	Urn	U1a	1594	0.034731286	0.00305241	810.1225	72.42604
BONG-50	292.2	Urn	U1a	1594	0.042106	0.00362417	831.0375	74.49501
END-09-02	341.2	Urn	U1b	1553	2.571890118	0.2015532	129594.8	11175.28
END-09-04	339.1	Urn	U1c	1553	2.634434674	0.20933414	120957.7	10194.03
END-09-04	339.1	Urn	U1c	1553	2.08109961	0.16993765	83635.86	6923.443
END-09-04	339.1	Urn	U1b	1553	1.939766643	0.16547514	73216.61	6148.597
END-09-04	339.1	Urn	U1c	1553	2.68043668	0.21095796	120237.3	10181.39
END-09-04	339.1	Urn	U1b	1553	1.914376431	0.16082069	104494.6	8831.734
END-09-04	339.1	Urn	U1b	1553	2.2381394	0.18158165	102291.4	8575.712
END-09-04	339.1	Urn	U1c	1553	2.561635387	0.20280026	127714.2	10840.91
END-09-04	339.1	Urn	U1c	1553	2.626544954	0.2075496	86242.61	7339.842
END-09-04	339.1	Urn	U1c	1553	1.969334482	0.16189997	79118.19	6551.371
END-11-02	327.8	Urn	U1c	1553	2.109376284	0.17073774	93631.48	7767.53
END-11-02	327.8	Urn	U1c	1553	2.317913307	0.18706519	32502.28	2774.93
END-11-02	327.8	Urn	U1c	1553	2.478224577	0.19766907	126844.1	10562.64
END-11-02	327.8	Urn	U1c	1553	2.307038954	0.1877933	95318.24	7819.383
END-11-02	327.8	Urn	U1c	1553	1.99813477	0.1607846	88207.68	7202.85
END-11-02	327.8	Urn	U1c	1553	1.982007812	0.16453441	107406	8952.106
END-11-02	327.8	Urn	U1c	1553	1.95691935	0.1608792	89005.14	7448.855
END-11-02	327.8	Urn	U1c	1553	1.926515923	0.1605393	103896.9	8572.285
END-11-02	327.8	Urn	U1c	1553	2.071425905	0.16904174	95210.62	7678.508
END-11-02	327.8	Urn	U1c	1553	1.855609806	0.15635803	78605.64	6390.371
END-11-02	327.8	Urn	U1c	1553	2.168449647	0.17923773	85130.09	6948.574
END-34	1061	Urn	U1c	1553	2.080415961	0.17232441	91170.3	7848.839
END-34	1061	Urn	U1c	1553	2.326647301	0.18326606	60962.47	5261.599
END-34	1061	Urn	U1c	1553	2.025907029	0.17109679	89864.49	7726.066
END-34	1061	Urn	U1c	1553	2.253763067	0.17845083	85791.65	6699.26
END-34	1061	Urn	U1c	1553	2.101230751	0.16661202	87676.33	7508.364
END-34	1061	Urn	U1c	1553	2.651478062	0.20745817	94696.88	8164.594
END-34	1061	Urn	U1b	1553	2.081656649	0.1737536	116658.5	9923.835
END-34	1061	Urn	U1b	1553	2.33475832	0.18558867	113110.4	9623.359
END-34	1061	Urn	U1b	1553	2.431360336	0.19385718	112192.4	9517.046
END-34	1061	Urn	U1b	1553	2.579366744	0.20288997	121233.9	10402.64
END-09-04	339.1	Bran	U1b	1440	0.672627054	0.06453102	15967.28	1207.74
END-09-04	339.1	Bran	U1b	1440	1.283059958	0.11064392	45757.37	3781.393
END-09-02	341.2	Bran	U1b	1440	0.357924107	0.04075531	11368.05	733.1028

END-09-02	341.2	Bran	U1b	1440	0.280942438	0.03510052	10748.5	628.2313
END-09-04	339.1	Urn	U1b	1417	0.928838361	0.08167347	26886.29	2202.532
END-09-04	339.1	Urn	U1c	1417	1.644070721	0.13617905	83388.66	7024.684
END-09-04	339.1	Urn	U1b	1417	1.401440985	0.11786532	55712.14	4679.214
END-09-02	341.2	Urn	U1b	1417	1.54286848	0.13008426	63236.94	5275.111
END-09-02	341.2	Urn	U1b	1417	1.416593558	0.12128821	79450.98	6543.99
END-09-02	341.2	Urn	U1b	1417	1.401440985	0.11786532	87680.18	7296.737
END-09-02	341.2	Urn	U1b	1417	1.14670478	0.09914447	65119.16	5272.309
END-11-02	327.8	Urn	U1c	1417	1.633542797	0.14049876	90495.06	7265.455
END-34	1061	Urn	U1c	1417	1.730295209	0.14070617	51047.01	4391.947
LG86	158.8	Urn	U1c	1276	0.0324362	0.00288867	1702.069	148.0005
LG86	158.8	Urn	U1b	1276	0.023512984	0.00182119	1145.864	119.667
LG86	158.8	Urn	U1b	1276	0.125657171	0.01069958	6150.54	546.6735
LG86	158.8	Urn	U1b	1276	0.091765079	0.0078391	4977.571	443.0045
LG86	158.8	Urn	U1b	1276	1.019380677	0.08866129	2775.703	228.5108
END-11-02	327.8	Urn	U1c	1249	1.694069974	0.14718494	79592.69	6350.767
END-11-02	327.8	Urn	U1c	1249	1.941270541	0.16969633	96846.15	7941.457
END-11-02	327.8	Urn	U1c	1249	1.485525942	0.12681994	61242.72	5032.864
END-11-02	327.8	Urn	U1c	1249	1.75569979	0.15418198	85791.65	6699.26
END-11-02	327.8	Urn	U1c	1249	1.121046036	0.09471247	62548.16	5526.497
END-11-02	327.8	Urn	U1c	1249	1.379040907	0.11969904	68669.55	5469.387
END-11-02	327.8	Urn	U1c	1249	1.633542797	0.14049876	90495.06	7265.455
SW38	590	Urn	U2	937	0.060889339	0.00627786	2783.235	194.5904
SW38	590	Urn	U2	937	0.057607866	0.00603189	3032.253	212.7616
SW38	590	Urn	U2	937	0.046294987	0.0049268	2262.697	157.1554
SW38	590	Urn	U2	937	0.050291385	0.00530599	2886.08	195.6121
SW38	590	Urn	U2	937	0.054964523	0.00563792	1783.157	117.0003
SW38	590	Urn	U2	937	0.077477231	0.00816067	3148.64	216.4886
SW38	590	Urn	U2	937	0.129636127	0.01321391	6056.399	434.8854
SW38	590	Urn	U2	937	0.102486133	0.01048132	4640.769	332.5852
SW38	590	Urn	U2	937	0.396176984	0.04100004	7346.36	510.9085
SW38	590	Urn	U2	937	0.147939725	0.01501504	6062.184	433.6413
SW38	590	Urn	U2	937	0.105510756	0.01125848	3587.578	248.1266
END-09-04	339.1	Bran	U2	274	0.246232747	0.0349285	8145.961	406.9986
END-09-02	341.2	Bran	U2	274	0.180792333	0.02628909	6766.473	342.5861
END-09-02	341.2	Bran	U2	274	0.209361734	0.03026295	7351.247	372.0032

Chapter 3: Glaciation-induced radionuclide release: implications for geological disposal of nuclear waste

Ian Burron[1], Mostafa Fayek[1], and Julie L. Brown[2]

[1] Department of Earth Science, University of Manitoba; Winnipeg, R3T 2N2, Canada.

[2] Canadian Nuclear Safety Commission; 280 Slater Street, Ottawa, Ontario K1P 5S9, Canada

ABSTRACT

Deep geological disposal of used nuclear fuel requires knowledge of how radionuclides behave over ~100ky to 1My timeframes. New data from the Kiggavik uranium deposits, a natural analogue for deep geological disposal of nuclear waste, shows that oxidized subglacial waters may be injected deeply into the subsurface along fracture systems, resulting in limited radionuclide mobilization. Periods of radionuclide mobility correspond to episodes of climate change during glacial periods and occurred over ~36-471 Ka timescales comparable to the evolution of *Homo sapiens*. While oxidized subglacial waters may pose a hazard to geologic disposal, resulting uranium transport is millions of times slower than glacial movements and short-range (<~5 cm). Reduction by pre-existing uranium minerals and titanium oxides and adsorption onto clay minerals are likely to have effectively trapped radionuclides.

INTRODUCTION

Nuclear energy produces vast amounts of carbon-free electricity, but also creates highly radioactive, long-lived nuclear waste in the form of used nuclear fuel (UNF). Long-term containment and isolation of UNF is provided by the deep geological repository (DGR) concept. DGRs are nuclear waste disposal facilities constructed ≥ several 100 m underground and consist of a series of engineered (reinforced canister, bentonite clay sealant and backfill) and natural (host rock) barriers. Safety assessments must evaluate the mobility and potential impacts of radionuclides over ~1 million year (Ma) timeframes which allow for intensely radioactive fission products to decay and overall UNF radioactivity to decrease to levels found in natural uranium (U) deposits (e.g. SKB, 2010; NWMO, 2017). Ensuring the isolation of UNF over timescales of more than three times the age of *Homo sapiens* and 200 times the age of the pyramids presents considerable challenges.

While there are no human-built structures that span this timeframe, natural geologic systems can persist for much longer. Studies of U deposits in which the U ore mineral uraninite (UO_{2-x}) is chemically similar to the UO_2 that makes up the bulk of UNF provide data on UNF's long-term behavior (Janeczek et al., 1996; Ewing, 1999) in a variety of geological settings.

Studies of U deposit DGR analogues such as Oklo, Gabon and Cigar Lake, Canada, indicate that U oxides are likely to remain isolated and contained underground for >1 Ga (Evins et al., 2005; Cramer and Smellie, 1994; Fayek and Brown, 2021). These studies provide analogues for elucidating DGR performance in an ideal setting. This study, in contrast, focuses on non-ideal conditions affecting the Kiggavik U deposits in central Nunavut, Canada, providing insight into processes that may disrupt DGR performance.

Kiggavik comprises a series of U deposits, with the four largest, Kiggavik, Bong, End, and Andrew Lake, being the subject of this study. The bulk of U mineralization is hosted within hydrothermally (hematite-illite) altered metasedimentary rocks of the ~2.7 Ga Woodburn Lake Group. Some U mineralization in the Kiggavik deposit is hosted within hydrothermally altered granitic rocks of the 1.84-1.73 Ga Lone Gull stock. Uranium minerals, mainly uraninite with lesser coffinite ($U(SiO_4)_{1-x}(OH)_{4x}$), local brannerite ($(U,Ca,Ce)(Ti,Fe)_2O_6$), and minor uranothorite ($(U,Th)SiO_4$) within granitic rocks, occur from surface to ~450 m depth (Fig. S1). This setting is comparable to the ~500m depth described in most DGR conceptual designs and provides insight into two possible DGR host rock types (metasedimentary and granitic). The deposits are located within fractured bedrock representative of an eroded, fractured, post-glacial setting.

Studies have revealed a complex history of U mineralization and mobilization spanning >1.5 Ga (Burron et al., 2024; Sharpe et al., 2015; Grare et al., 2018; 2020). Early generations of

U-minerals (U1 and U2), comprising >90% of all U-minerals, have U-Pb dates ranging from 1594 ± 95 to 274 ± 69 Ma (Burron et al., 2024). A generation of late U-minerals associated with distinctive orange goethite (FeO(OH))-bearing ferric alteration (U3; fig. 1) have very low PbO contents indicative of formation or extensive Pb-loss within the last 1 Ma (Burron et al., 2024). This indicates Kiggavik has been impacted by processes, such as the infiltration of snow/glacial melt (Shabaga et al., 2020), which altered and mobilized U minerals. Kiggavik is therefore an analogue for a DGR in which fluids have bypassed multiple safety barriers, which are not present at Kiggavik, and impacted the UNF directly, resulting in partial loss of the containment safety function.

CAUSES AND TIMING OF RADIONUCLIDE MOBILITY

U3 minerals occur along redox fronts developed between oxidized ferric alteration and bleached, illite-rich host rocks, and are almost exclusively observed within ~5 cm of both much older U1/U2 minerals and open fractures or porous veins systems (fig. 1). These fractures and vein systems form conduits allowing fluids to move through otherwise relatively impermeable illite-rich host rocks. Illite is known to be effective at adsorbing and trapping U^{4+} but is much less effective at retarding U mobility when U is oxidized to U^{6+} or forms carbonate complexes (Schindler et al., 2015; Mei et al., 2022). The presence of goethite and calcite on the fracture/vein-facing sides of U3 fronts suggests fluids infiltrating along these conduits enabled U mobility by oxidizing U and/or forming uranyl-carbonate complexes. The infiltration of oxidized fluids along fractures has been identified as a major concern in geologic disposal (Fayek and Brown, 2021; IAEA, 1999).

Plotting the stable isotope data listed in Table S1 Vs compositions of illite crystalized from meteoric fluids reveals that illite associated with U3 in metsedimentary and granitic rocks is

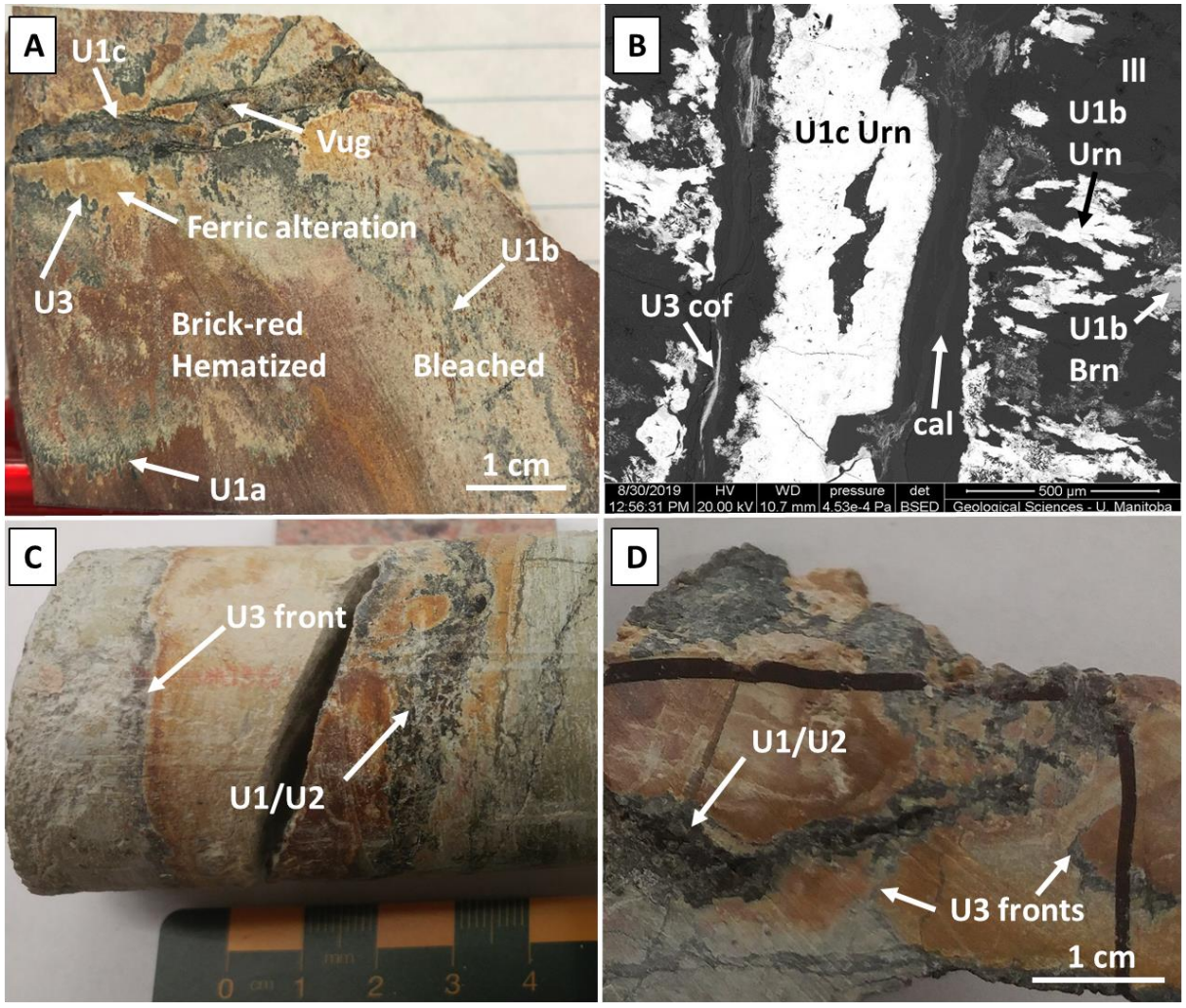

Fig. 1. Textural relationships between U1, U2, and U3 minerals. (A) Orange, goethite-bearing ferric alteration and U3 fronts and fracture fills associated with a vuggy, U1 mineralized vein in sample END-11-02-327.8. Bleaching and brick-red hematization alteration is associated with U1 mineralization, which is subdivided into front-style (U1a), disseminated (U1b), and vein-hosted (U1c). (B) Traces of U3 and associated calcite crosscutting U1b minerals along the margin of a U1c vein in sample END-09-339.1. (C) U3 and orange ferric alteration along an open fracture subparallel to a U1/U2 mineralized vein in sample CZ-15-01-82.6. (D) The same sample cut along the vein to reveal two distinct nested U3 fronts in close proximity to the U1/U2-bearing vein. Abbreviations: Urn = uraninite, brn = brannerite, cof = coffinite, Cal=calcite, Ill = illite.

consistent with isotopic equilibrium with ~60-20° C meteoric fluids (Fig. 2). These temperatures are broadly consistent with the geothermal gradient at ~500 m. These data are similar to isotopic values of illite affected by meteoric fluids in U deposits in the Athabasca Basin, Saskatchewan, Canada (Kotzer and Kyser, 1995; Sheahan et al., 2016). The δ^2H values of illites associated with U3 in the granitic rocks are similar to the –160 ± 36 ‰ value of modern meteoric waters in the Kiggavik region (IAEA/WMO, 2015), whereas δ^2H values for illites in metasedimentary rocks have a wide range and are somewhat higher. This suggests these illites have not been fully isotopically reset because isotopic exchange proceeds extremely slowly at low temperatures (Sheppard and Gilg, 1996).

The δ^{18}O values of these illites are not similar to meteoric waters in the region and this is to be expected. The decoupling of δ^2H from δ^{18}O is common in low-temperature clay-water systems as δ^2H exchanges much faster than δ^{18}O due to a proton-exchange mechanism being viable for H but not O (Sheppard and Gilg, 1996). Low water/rock ratios also favor faster δ^2H exchange as illite contains more O than H whereas water contains more H than O.

These stable isotope data indicate that illite associated with U3 was affected by high-latitude meteoric fluids such as snow or glacial meltwater. This finding is not surprising, as the Kiggavik region has been repeatedly and intensely glaciated throughout the last ~2.6 Ma and is very close to both the interpreted Keewatin ice divide and the limit of marine incursion during the last glacial cycle (McMartin et al., 2020), implying a particularly dynamic glacial influence.

In situ U-Pb Concordia dates of U-minerals in the Kiggavik deposit were previously reported in Burron et al. (2024); however, many of these minerals, including all U3 minerals, did not contain enough Pb to yield a reliable U-Pb Concordia age. These previously undated low-Pb U-minerals yielded ^{235}U/^{207}Pb isochron ages, which are more sensitive for dating low-Pb

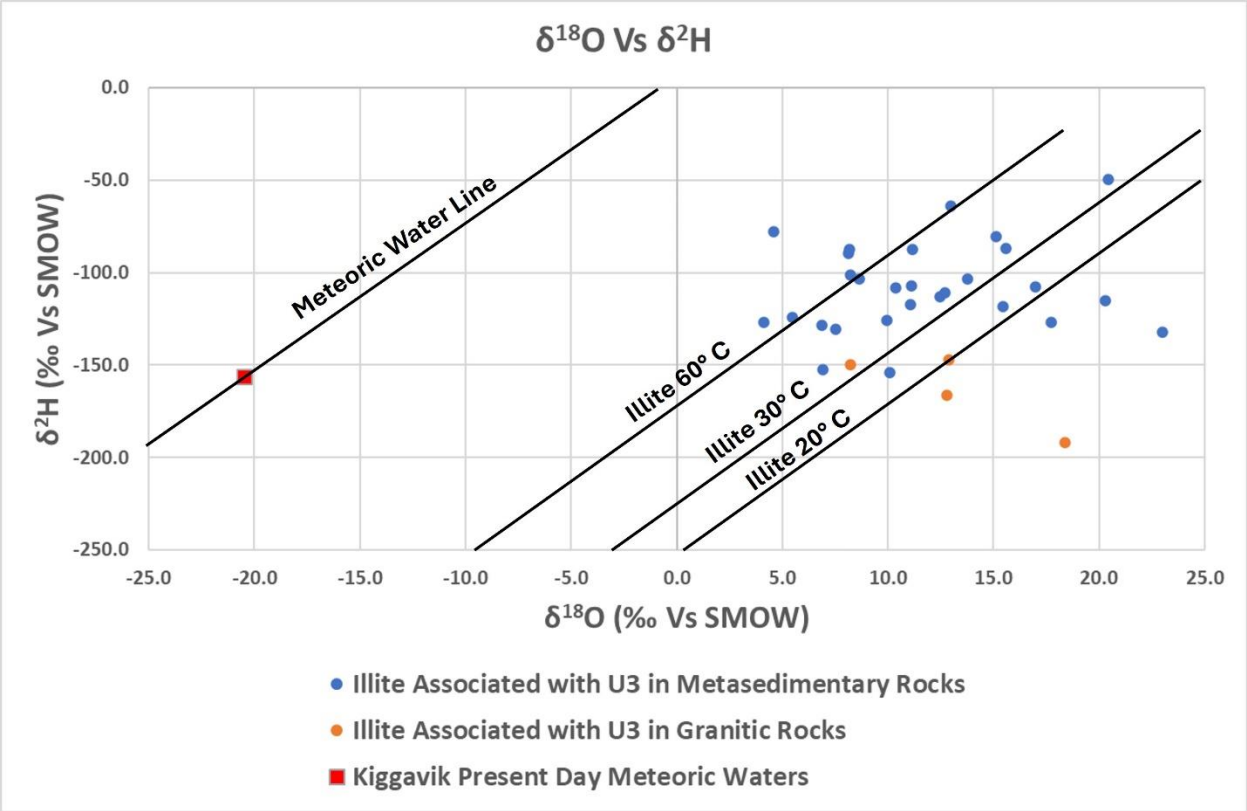

Fig. 2. δ^2H and δ^{18}O compositions of illites associated with U3 minerals. Values are consistent with (re)crystallization from low temperature meteoric waters. δ^2H values are similar to modern meteoric/glacial waters, indicating infiltration of these fluids. Modified from Ziegler and Longstaffe (2000); meteoric water line from Craig (1961).

minerals, ranging from 0.6 – 69.9 Ma (Table S2), with the distribution being strongly skewed to younger ages. These should be considered minimum age constraints only as this method cannot account for Pb-loss.

Decay chain isotopes in 50% of the U-minerals studied by Burron et al. (2024) deviate from expected ratios, indicating isotopic disturbance within the past 1 Ma (Table S3). Uranium-Th disequilibrium dates range from 34 +5.3/-5.2 Ka to 488 +190/-130 Ka. Most of these dates fall into clusters averaging 36.5 ± 1.9 Ka (n=4), 55.7 ± 4.8 Ka (n=3), 153.3 ± 3.7 Ka (n=12), 258.6 ± 11.6 Ka (n=39), and 471.3 ± 6.3 Ka (n=16) (Fig. 3). The ~36 and 56 Ka ages are obtained exclusively from the Kiggavik Deposit granitic rocks, and brannerite was more likely than other U-minerals (74% vs ~50%) to be isotopically disturbed. Decay-chain disturbance has occurred in all studied U deposits, and U-Th dates cannot be readily correlated to mineralogy, mineral textures, or sample depth, suggesting other properties such as proximity to fractures and resulting exposure to infiltrating fluids are the primary influence on disturbance.

Comparing these dates to global climatic records extracted from Antarctic ice cores reveals that all of the U-Th dates fall during glacial periods, with reconstructed Antarctic temperatures ~5-8° C colder than today (Jouzel et al., 2007; Fig. 3). Considering its northerly latitude the Kiggavik area would almost certainly have been covered by icesheets at these times. Most of these dates also coincide with ~1-3° C fluctuations in global temperature.

The 36.5 ± 1.9 Ka U-Th date is the only one within the range of ^{14}C dating. It overlaps with ^{14}C dates of ~35-43.7 Ka obtained from marine shell fragments which indicate significant ice retreat 100's of km NE of Kiggavik during this time (McMartin et al., 2019). The Kiggavik region, however, remained covered by >1 km of ice throughout this time period (Gowan et al., 2021).

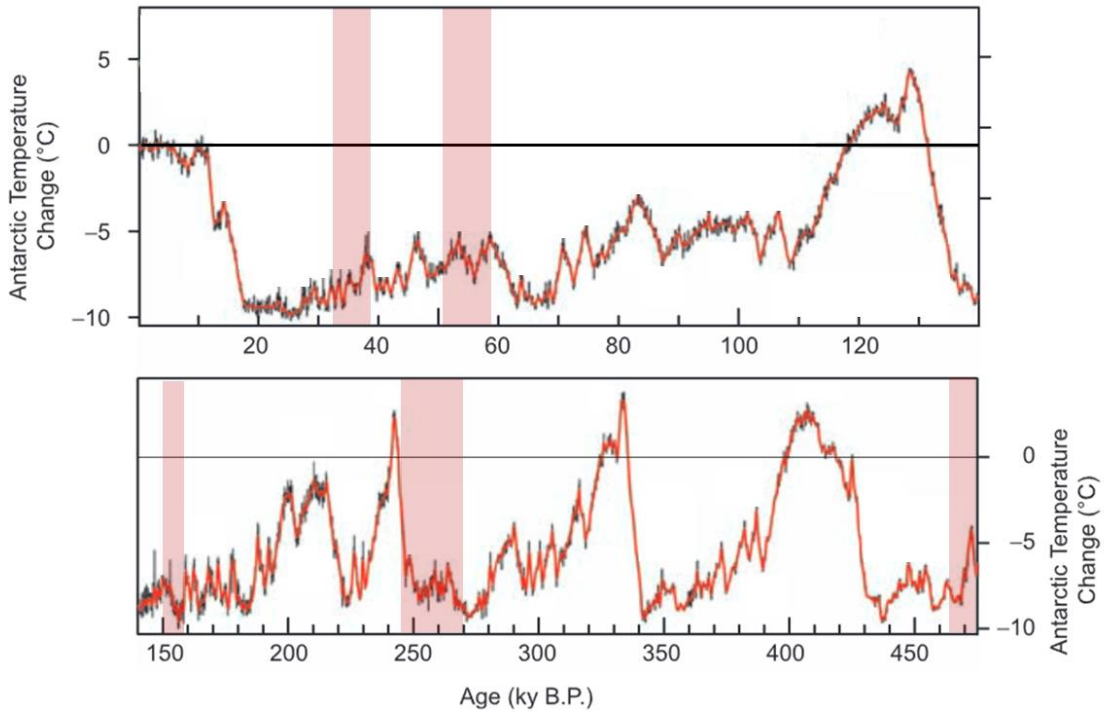

Fig. 3. U-Th disequilibrium dates and associated uncertainties (red boxes) overlayed on reconstructed Antarctic temperatures. Decay-chain disruption events are associated with second-order temperature fluctuations during cold (glacial) stages. Modified from Jouzel et al. (2007).

All of the U-Th dates correlate with glacial stages; conversely, there is no evidence of radionuclide mobility or U decay chain disturbance occurring during interglacial periods. The occurrence of glacial melt or seasonal runoff at the surface does not appear sufficient to cause releases and mobility of radionuclides at depths of 10's-100's of m. Rather, U mobility in the Kiggavik deposits has exclusively occurred beneath an ice sheet.

The weight of the overlying ice sheet is known to pressurize subglacial waters, which can cause them to be injected deeply into permeable rocks (Grasby and Chen, 2005). Regions of injection into the subsurface are typically marked by the absence of eskers (Grasby and Chen, 2005); eskers are not observed in the Kiggavik area (McMartin et al., 2020), suggesting subglacial injection may have driven fluid infiltration.

A layer of impermeable permafrost is generally present in ice-free arctic regions, but may or may not exist beneath icesheets depending on local cold-based vs warm-based ice conditions (Waller, et al., 2012). Freeze/thaw of sub-glacial permafrost due to temperature fluctuations may have played a role in controlling fluid infiltration at Kiggavik.

Taken as a whole, these isotopic data indicate oxidized subglacial waters can periodically be injected >300 m into the subsurface along preexisting conduits, leading to limited degrees of radionuclide mobility in U minerals immediately adjacent to these structures. Rapid climate change appears to trigger these mobility events by perturbing the overlying ice sheets through sea level fluctuations or other processes.

CONTEXT OF RADIONUCLIDE MOBILIZATION

Uranium-Pb dates represent the minimum time since minerals formed or underwent a high degree of crystallization; in a repository context this would represent UNF being

extensively altered, potentially releasing radionuclides including mobile fission products such as ^{129}I, the dominant dose contributor in case studies of Canada's UNF disposal (NWMO, 2017), which are otherwise contained within the UNF matrix. In a DGR this would require penetration of multiple safety barriers that are not present at Kiggavik; Kiggavik is therefore an analogue for a worst-case scenario where these have been breached through unspecified means. Most U1 and U2 minerals yielded ~1594 – 274 Ma U-Pb Concordia ages (Burron et al., 2024), indicating the majority of Kiggavik U-minerals have not experienced such mobilization since before the dinosaurs. Even the most isotopically disturbed minerals yield $^{235}U/^{207}Pb$ isochron minimum ages >0.6 Ma, twice as long as *homo sapiens* have existed.

U-Th data reveal that half of all U-minerals in the Kiggavik deposits have undergone some degree of disturbance to the U decay chain within 500 Ka. These decay products are particularly vulnerable to selective leaching as they are located close to sites of crystal damage caused by the decay of the parent isotope (Faure, 1998). As this leaching occurs without Pb-loss, which would indicate dissolution/recrystallization of the bulk matrix, these U-Th dates imply more limited degrees of radionuclide release. The 36k years since such release last occurred at Kiggavik is ~8 times the age of the pyramids.

Although unobserved longer range radionuclide mobility cannot be ruled out, essentially all U3 minerals occur within ~5 cm of much older U1/U2 U-minerals, which almost certainly represents their source material. Assuming the maximum 5 cm of observed U mobility occurred during the most recent 36 Ka mobilization event, the implied maximum average U transport rate is 0.0014 mm/year; > 7 million times slower than modern glacial flow in the region (Burgess et al., 2005). At this rate U would require 360 million years, ~1200 times the age of the human

species and ~1.5 times the age of the oldest dinosaurs, to travel the 500 m from DGR depth to the surface.

FACTORS LIMITING RADIONUCLIDE MOBILITY

The concentration of U3 minerals along redox fronts indicates that reduction of soluble U^{6+} to insoluble U^{4+} was an important U-trapping mechanism; U3 fronts, however, do not contain substantial amounts of sulfides and Fe^{2+}-bearing minerals such as chlorite and biotite, which are often invoked as U reductants (Jefferson et al., 2007; Yeo and Potter, 2010). Uraninite is by far the most common reduced mineral present in U3 fronts, suggesting that preexisting uraninite may have reduced, precipitated, and trapped dissolved U. In a DGR, this would be equivalent to minerals and engineered materials resisting bulk mobilization of UNF by creating localized redox traps for dissolved radionuclides. U3 is also commonly observed surrounding Ti-oxides, which are known to trap U via catalyzing reduction and/or other mechanisms (Comarmond et al., 2011; Ding et al., 2022). Finally, uraninite and coffinite are ubiquitously intergrown with the illite matrix on ~1 μm scales, suggesting that adsorption onto clay mineral surfaces also played a major role in trapping dissolved U.

Patterns of observed radionuclide mobility between granitic and metasedimentary rocks are largely similar, with the notable exception of the youngest mobility events at 36.5 ± 1.9 Ka, and 55.7 ± 4.8 Ka being observed only within the granites. These rocks also record a much higher degree of isotopic overprinting by subglacial waters, suggesting they were more vulnerable to fluid infiltration.

Although the studied granitic rocks occur at shallower depths (<130 m) than metasedimentary rocks (<350 m), this alone does not explain the observed differences, as there is

no clear relationship between depth and U-mobility or δ^2H values within rock types. It is possible that microporosity within feldspars and partly open dissolution pits within the extensively albite and K-feldspar altered granitic rocks could have increased the permeability of these rocks, encouraging radionuclide mobility.

Our study has developed Kiggavik as a natural analogue for a DGR impacted by intense glaciation, informing safety assessments (i.e. CNSC, 2020) and building confidence in DGR performance over long timescales even in non-ideal settings and circumstances. The available data indicate that resulting radionuclide releases have been small scale and occurred over 10s-100s Ka, within 1Ma DGR timeframes. Kiggavik U-minerals reduced and trapped dissolved U, suggesting analogous reduced UNF components may trap released radionuclides in a DGR. Natural barriers such as clay minerals and Ti-oxides have further restricted radionuclide mobility, validating experimental studies indicating the rate of U redeposition exceeds the rate of U transport in the subsurface (Wronkiewicz and Buck, 1999).

Acknowledgments: EMPA and SIMS analysis was assisted by Panseok Yang and Ryan Sharpe. This study was conducted as part of the Canadian Nuclear Safety Commission's regulatory research on geologic disposal and was partially funded by an NSERC Alliance grant #ALLRP 556702 – 20.

REFERENCES CITED

Burgess, D. O., Sharp, M. J., Mair, D. W. F., Dowdeswell, J. A., Bensam, T. J., 2005, Flow dynamics and iceberg calving rates of Devon Ice Cap, Nunavut, Canada: Journal of Glaciology, v. 51, n. 173, p. 219–229.

Burron, I., Fayek, M., Brown, J., Quirt, D., 2024, Remnants of a 1.55 Ga hybrid between metasomatic iron-alkali-calcic and unconformity-related uranium environments in the Kiggavik region, Nunavut, Canada: Economic Geology, v. 119, no. 8, pp. 1861–1888.

CNSC (Canadian Nuclear Safety Commission), 2020, Waste Management, Volume III: Safety Case for the Disposal of Radioactive Waste, Version 2: CNSC REGDOC-2.11.1.

Comarmond, M. J., Payne, T. E., Harrison, J. J., Thiruvoth, S., Wong, H. K., Aughterson, R. D., Lumpkin, G. R., Muller, K., and Foerstendorf, H., 2011, Uranium sorption on various forms of titanium dioxide - Influence of surface area, surface charge, and impurities: Environmental Science and Technology, v. 45, p. 5536–5542.

Craig, H., 1961, Isotopic variations in meteoric waters: Science, v. 133, p. 1702–1703.

Cramer, J. and Smellie, J., 1994, Final report of the AECL/SKB Cigar Lake analog study: SKB Technical Report 94-04, 226 p.

Ding, B., Liu, H.-X., Qiu, L.-F., Zhang, C., and Xu, D.-R., 2022, Ilmenite alteration and its adsorption and catalytic reduction in U enrichment in sandstone-hosted U deposits from the northern Ordos Basin, north China: Minerals, v. 12, p. 167.

Evins, L. A., Jensen, K. A., and Ewing, R. C., 2005, Uraninite recrystallization and Pb loss in the Oklo and Bangombé natural fission reactors, Gabon: Geochimica et Cosmochimica Acta, v. 69, n. 6, p. 1589 –1606.

Ewing, R.C., Less geology in the geological disposal of nuclear waste, 1999: Science, v. 286, p. 415–416.

Faure, G., 1998, Principles and Applications of Geochemistry: Upper Saddler River, NJ, USA, Prentice Hall, 287 p.

Fayek, M., and Brown, J., 2021, Natural and anthropogenic analogues for high-level nuclear waste disposal repositories: A review: The Canadian Mineralogist, v. 59, p. 287–317.

Gowan, E. J., Zhang, X., Khosravi, S., Rovere, A., Stocchi, P., Hughes, A. L. C., Gyllencreutz, R., Mangerud, J., Svendsen, J.-I., and Lohmann, G., 2021, A new global ice sheet reconstruction for the past 80 000 years: Nature Communications, https://doi.org/10.1038/s41467-021-21469-w.

Grare A., Lacombe, O., Mercadier, J., Benedicto, A., Marie Guilcher, M., Trave, A., Ledru, P., and Robbins, J., 2018, Fault zone evolution and development of a structural and hydrological barrier: the quartz breccia in the Kiggavik area (Nunavut, Canada) and its control on uranium mineralization: Minerals 8, v. 8, n. 318, doi:10.3390/min8080319.

Grare, A., Benedicto, A., Mercadier, J., Lacombe, O., Trave, A., Guilcher, M., Richard, A., Ledru, P., Blain, M., Robbins, J., and Lach, P., 2020, Structural controls and metallogenic model of polyphase uranium mineralization in the Kiggavik area (Nunavut, Canada): Mineralium Deposita, https://doi.org/10.1007/s00126-020-00957-x.

Grasby, S. E., and Chen, Z., 2005, Subglacial recharge into the Western Canada Sedimentary Basin—Impact of Pleistocene glaciation on basin hydrodynamics: GSA Bulletin, v. 117, n. 3/4, p. 500–514.

IAEA (International Atomic Energy Agency), 1999, Use of natural analogues to support radionuclide transport models for deep geological repositories for long lived radioactive wastes: IAEA-TECDOC-1109.

IAEA/WMO, 2015, Global network for isotopes in precipitation: GNIP Database, https://nucleus.iaea.org/wiser (accessed December 2023).

Janeczek, J., Ewing, R.C., Oversby, V.M., Werme, L.O., 1996, Uraninite and UO_2 in spent nuclear fuel: a comparison: Journal of Nuclear Material, v. 238, p. 121–130.

Jefferson, C.W., Thomas, D.J., Gandhi, S.S., Ramaekers, P., Delaney, G., Brisbin, D., Cutts, C., Quirt, D., Portella, P., and Olson, R.A., 2007, Unconformity-associated uranium deposits of the Athabasca Basin, Saskatchewan and Alberta, in Goodfellow, W.D., ed., Mineral Deposits of Canada: A Synthesis of Major Deposit-Types, District Metallogeny, the Evolution of Geological Provinces, and Exploration Methods: Geological Association of Canada, Mineral Deposits Division, Special Publication 5, p. 273–305.

Jouzel, J., et al., 2007, Orbital and millennial Antarctic climate variability over the past 800,000 years: Science, v. 317, p. 793–796.

Kotzer, T.G. and Kyser, T.K., 1995, Petrogenesis of the Proterozoic Athabasca Basin, northern Saskatchewan, Canada, and its relation to diagenesis, hydrothermal uranium mineralization and paleohydrogeology: Chemical Geology, v. 120, p. 45–89.

McMartin, I., Campbell, J.E., and Dredge, L.A., 2019, Middle Wisconsinan marine shells near Repulse Bay, Nunavut, Canada: implications for Marine Isotope Stage 3 ice-free conditions and Laurentide Ice Sheet dynamics in north-west Hudson Bay: Journal of Quaternary Science, v. 34, n. 1, p. 64–75.

McMartin, I., Godbout, P.-M., Campbell, J. E., Tremblay, T. and Behnia, P., 2020, A new map of glaciogenic features and glacial landsystems in central mainland Nunavut, Canada: Boreas, doi:/10.1111/bor.12479. ISSN 0300- 9483.

Mei, H., Aoyagi, N., Saito, T., Kozai, N., Sugiura, Y., and Tachi, Y., 2022, Uranium (VI) sorption on illite under varying carbonate concentrations: Batch experiments, modeling, and cryogenic time-resolved laser fluorescence spectroscopy study: Applied Geochemistry, v. 136, https://doi.org/10.1016/j.apgeochem.2021.105178.

Nuclear Waste Management Organization (NWMO), 2017, Postclosure safety assessment of a used fuel repository in crystalline rock: NWMO Technical Report TR-2017-02, 718 p.

Schindler, M., Legrand, C. A., and Hochella Jr, M. F., 2015, Alteration, adsorption and nucleation processes on clay–water interfaces: Mechanisms for the retention of uranium by altered clay surfaces on the nanometer scale: Geochemica et Cosmochmica Acta, v. 153, p. 15–36.

Shabaga, B.M., Fayek, M., Quirt, D., Jefferson, C.W., and Ledru, P., 2020, Geochemistry and geochronology of the Kiggavik uranium deposit, Nunavut, Canada: Mineralium Deposita, https://doi.org/10.1007/s00126-020-01001-8.

Sharpe, R., Fayek, M., Quirt, D., and Jefferson, C., 2015, Geochronology and genesis of the Bong uranium deposit, Thelon Basin, Nunavut, Canada: Economic Geology, v. 110, p. 1759–1777.

Sheahan, C., Fayek, M., Quirt, D., and Jefferson, C.W., 2016, A Combined Ingress-Egress Model for the Kianna Unconformity-Related Uranium Deposit, Shea Creek Project, Athabasca Basin, Canada: Economic Geology, v. 111, p. 225–257.

Sheppard, S. M. F., and Gilg, H. A., 1996, Stable isotope geochemistry of clay minerals: Clay Minerals, v. 31, p. 1–24.

SKB, 2010, Spent nuclear fuel for disposal in the KBS-3 repository: Swedish Nuclear Fuel and Waste Management Co Technical Report TR-10-13, 91 p.

Waller, R., I., Murton, J. B., and Kristensen, L., 2012, Glacier–permafrost interactions: Processes, products and glaciological implications: Sedimentary Geology, v. 255–256, p. 1–28.

Wronkiewicz, D.J. and Buck, E.C., 1999, Uranium mineralogy and the geologic disposal of spent nuclear fuel, in Burns, P.C. and Finch, R., Eds. Uranium: Mineralogy, Geochemistry, and the Environment: Mineralogical Society of America Proceedings, v. 38, p. 475–497.

Yeo, G. M., and Potter, E. G., 2010, Review of reducing mechanisms potentially involved in the formation of unconformity-type uranium deposits and their relevance to exploration Saskatchewan Geological Survey Summary of Investigations, v. 2, p. 1–13.

Ziegler, K., and Longstaffe, F. J., 2000, Clay mineral authigenesis along a mid-continental scale fluid conduit in Palaeozoic sedimentary rocks from southern Ontario, Canada: Clay Minerals, v. 35, p. 239–260.

Glaciation-induced radionuclide release: implications for geological disposal of nuclear waste: Supplementary material

Ian Burron, Mostafa Fayek, Julie L. Brown

Corresponding author: Ian Burron: ianmburron@gmail.com

MATERIALS AND METHODS

Petrography

This study examined the same >350 drill-core samples and related thin sections studied in Burron et al. (In Press), which were selected from the University of Manitoba's library of core samples and polished thin sections from the Kiggavik region. These samples represent the various types of U mineralization, associated alteration, and unaltered host rocks from the Kiggavik, Bong, End, and Andrew Lake deposits. The mineralogy and textures of sections were characterized by optical and scanning electron microscopy prior to conducting electron probe micro-analysis and secondary ion isotopic analysis.

The chemical composition of minerals was measured at the University of Manitoba via a CAMECA SX100 Universal EPMA equipped with five wavelength-dispersive spectrometers and

a Princeton Gamma-Tech (PGT) energy-dispersive spectrometer. An accelerating voltage of 15 kV was used with a 1 μm electron beam and a beam current of 20 nA. Elemental detection limits for U, Th, Pb, Zr, and Hf, were ~3000, 3000, 2500, 2000, and 2500 ppm, respectively, with detection limits below 1000 ppm for all other elements.

U-Pb and U-Th Geochronology

Uranium, lead, and thorium isotopic ratios in uraninite, coffinite, brannerite, and uranothorite were measured at the University of Manitoba using a CAMECA 7f SIMS instrument via methods similar to those described in Sharpe and Fayek (2016). These isotopic data were gathered in the same analytical session(s) as U-Pb data presented in Burron et al. (In press), and sample preparation and analysis procedures are consequently identical.

Prior to analysis samples were ultrasonically cleaned in stages comprising a dilute soap solution, water, distilled water, and ethanol before being sputter-coated with a ~200Å layer of gold to ensure a conductive surface. Analysis of U minerals was carried out via a ~9 nA, O^- primary beam accelerated at 12.5 kV and focused to a spot size of 15x30 μm by a 750 μm aperture in the primary column. A 150 μm image field and ±25 eV energy bandpass were used with the largest contrast (400 μm) and field (1800 μm) apertures to maximize sensitivity. Flat-topped peaks were produced using a mass resolving power (measured at 10% valley) of 1300. Entrance slits were set to 36.9 μm. Hydride interferences were minimized by using a 50 V offset created by using a sample accelerating voltage of + 7.95 kV with the electrostatic analyzer in the secondary column set to +8.00 kV. The magnetic field was switched in order to measure U, Th, and Pb isotopes, specifically $^{204}Pb^+$, $^{206}Pb^+$, $^{207}Pb^+$, ^{230}Th,$^{235}U^+$, and $^{238}U^+$. Common Pb was detected, with $^{206}Pb/^{204}Pb$ ratios ≥150 for the majority of samples, although some fine-grained,

texturally altered U minerals in a few samples had lower and more variable $^{206}Pb/^{204}Pb$ ratios of ~1000-50.

Uranium-Pb ratios fractionate as a function of Pb content (Fayek et al., 2002; 2022), therefore analyses of unknown samples were calibrated via a calibration curve using the methods and reference materials of Sharpe and Fayek (2016).

Minimum ages of U minerals were calculated from the ^{235}U - ^{207}Pb decay equation:

$$t = \ln(^{207}Pb/^{235}U + 1) / \lambda \quad (1)$$

where t is time in years and λ is the ^{235}U decay constant (9.8485E-10). Unlike U-Pb Concordia methods, the ^{235}U - ^{207}Pb technique does not take Pb-loss into account and therefore yields minimum ages only. The advantage of this technique is that by only using the decay chain of ^{235}U, which has a much shorter half-life than ^{238}U (703.8 Ma vs 4468 Ma) the method can date younger U minerals.

Even more recent formation and/or isotopic resetting of U minerals was investigated via U-Th disequilibrium geochronology. This method measures ratios between ^{238}U and its intermediate daughter isotopes ^{234}U and ^{230}Th to allow dating of U-minerals. If the U decay chain is not disturbed, the ratios between these isotopes will evolve to a state of secular equilibrium, where the decay of each isotope is offset by its production, over a period of ~500 Kyr. Alteration of U-minerals due to fluid infiltration will cause disturbance to the U-decay chain due to the preferential removal of soluble decay products such as ^{234}U, which are vulnerable to removal due to their locations near sites of structural damage caused by the alpha decay of their parent isotopes (Faure, 1998). Measuring this disturbance from secular equilibrium allows dating of U-mineral alteration or formation occurring within ~475 Ka (Ludwig, 1993).

Uranium-Th disequilibrium isochron ages were calculated by using the ISOPLOT software (Ludwig, 1993). A correlation coefficient of 0.9 was used, with uncertainties calculated via the Monte Carlo method and reported at the 1σ level. To make the resulting data more coherent, groups of similar ages were averaged, with the uncertainty of the group defined as two times the mean of the standard deviation of the group.

Oxygen and Hydrogen Stable Isotopes

Stable oxygen and hydrogen isotope ratios of illite and muscovite were measured using the same SIMS instrument as the U-Th-Pb analysis. Samples were prepared using the same methods as U-Th-Pb samples.

Hydrogen isotope ratios of illite and muscovite were measured using a ~50 nA primary O^- beam accelerated at 12.5 Kv. A 750 μm aperture in the primary column was used to focus the beam to a 50 μm spot size. A 50 V sample voltage offset was used with the electrostatic analyzer in the secondary column set to + 10 kV. This offset, together with a mass resolving power of 800 was used to eliminate interferences. Analytical spots were pre-sputtered for 60 s with analysis comprising 50 analytical cycles for a total analysis times of ~6 min.

Oxygen isotope ratios of illite and muscovite were measured with a ~7 nA primary Cs+ ion beam, accelerated at 10.0 kV. A 750 μm aperture in the primary column was used to focus the beam to a 15 μm spot size. Molecular interferences were eliminated via a 300 V sample offset voltage, with the electrostatic analyzer in the secondary column set to −9 kV. A mass resolving power of 350 was used, with entrance slits set to 225 μm. A typical analysis comprised 80 cycles and lasted ~13 min.

An internal muscovite standard from Pied des Monts, Quebec was used for correction of both muscovite and illite data due to their similar matrix compositions. This muscovite has a δ^2H value of – 65 ‰, spot-to-spot reproducibility of better than 2.0‰, and a δ^{18}O value of +10.4 ‰ with spot-to-spot reproducibility of better than 0.9‰. Hydrogen and oxygen isotopic data are reported in δ-notation relative to Vienna Standard Mean Ocean Water (V-SMOW).

Although methods are available for calculating the isotopic composition of fluids in equilibrium with illite, i. e. the H isotopic fractionation equation of Capuano (1992) and the O isotopic fractionation equation of Sheppard and Gilg (1996), these methods require knowing the precise temperature of isotopic exchange. The only independent method of determining this temperature from the available data is the illite chemistry geothermometer of Battaglia (2004). This geothermometer yields temperatures of 261 and 333° C for illite in metasedimentary and granitic rocks, respectively, which almost certainly reflects the temperature of illite formation from hydrothermal fluids early in the deposits history. Such fluids have δ^2H values much too high to be responsible for the measured values (Sheppard, 1986), indicating measured temperatures are a relic of previous hydrothermal processes and cannot be applied to the measured isotopic values. Illite mineral isotopic compositions were instead compared directly to data from illites which crystalized from low temperature meteoric fluids.

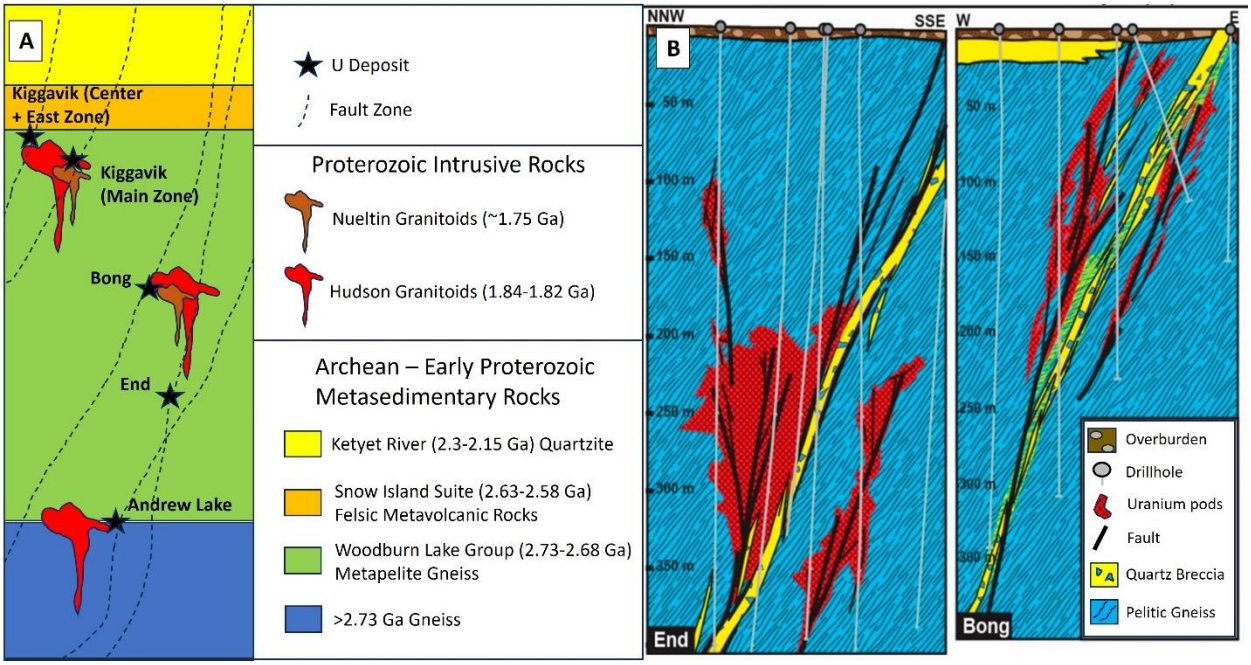

Fig. S1. Simplified geology of the Kiggavik deposits. A. Illustration of the general geology of the host rocks. The host rocks are crystalline, comprising dominantly fine-grained clastic sediments which have been strongly metamorphosed and deformed; these have been intruded by two phases of granitoid rocks, with the younger Nueltin Granitoids intruding into and reworking the older Hudson Granites. The Kiggavik Main Zone is hosted within these granitoids. B. Simplified cross-sections of the End and Bong deposits. Modified from Grare et al. (2018).

Table S1. STABLE O AND H ISOTOPIC DATA FROM ILLITE ASSOCIATED WITH U3 MINERALIZATION IN THE KIGGAVIK DEPOSITS.

Host Rock	Deposit	Sample	Depth (m)	Mineral Values (‰; VSMOW)	
				$\delta^{18}O$	$\delta^{2}H$
Metasedimentary	End	END-09-02	259.7	+15.1	-80.7
Metasedimentary	End	END-09-02	259.7	+11.2	-87.3
Metasedimentary	End	END-09-02	259.7	+8.1	-89.6
Metasedimentary	End	END-09-02	259.7	+12.5	-113.3
Metasedimentary	End	END-09-02	259.7	+10.3	-108.4
Metasedimentary	End	END-09-02	259.7	+12.7	-110.8
Metasedimentary	End	END-09-02	259.7	+8.2	-87.4
Metasedimentary	End	END-09-02	259.7	+15.6	-87.1
Metasedimentary	End	END-09-02	259.7	+6.9	-128.3
Metasedimentary	End	END-09-02	259.7	+5.5	-124.4
Metasedimentary	End	END-09-02	259.7	+8.7	-103.7
Metasedimentary	End	END-09-02	259.7	+23.0	-132.1
Metasedimentary	End	END-09-02	259.7	+10.1	-154.3
Metasedimentary	End	END-09-02	259.7	+11.1	-107.1
Metasedimentary	End	END-09-02	259.7	+20.3	-115.1
Metasedimentary	End	END-09-02	259.7	+17.7	-127.1
Metasedimentary	End	END-09-02	259.7	+15.5	-118.4
Metasedimentary	End	END-09-02	259.7	+4.6	-77.6
Metasedimentary	End	END-09-02	259.7	+17.0	-107.8
Metasedimentary	End	END-09-02	259.7	+4.1	-127.0
Metasedimentary	End	END-09-02	259.7	+10.0	-126.0
Metasedimentary	End	END-09-02	259.7	+7.5	-130.5
Metasedimentary	Kiggavik (CZ)	CZ-15-01	82.6	+13.0	-64.0
Metasedimentary	Kiggavik (CZ)	CZ-15-01	82.6	+11.1	-117.4
Metasedimentary	Kiggavik (CZ)	CZ-15-01	82.6	+8.2	-101.3
Metasedimentary	Kiggavik (CZ)	CZ-15-01	82.6	+20.4	-49.6
Metasedimentary	Kiggavik (CZ)	CZ-15-01	82.6	+13.8	-103.4
Metasedimentary	Kiggavik (CZ)	CZ-15-01	82.6	+6.9	-152.7
Average				**+11.7**	**-108.3**
Std Dev				**4.9**	**24.3**
Granitic	Kiggavik (MZ)	MZ-10-01	120.0	+12.9	-147.0
Granitic	Kiggavik (MZ)	MZ-10-01	120.0	+12.8	-166.6
Granitic	Kiggavik (MZ)	MZ-10-01	120.0	+18.4	-191.7
Granitic	Kiggavik (MZ)	MZ-10-01	120.0	+8.2	-149.6
Average				**+13.1**	**-163.7**

Std Dev	**4.2**	**20.6**

Table S2. CORRECTED U-Pb ISOTOPIC DATA AND CALCULATED 207Pb/235U MINIMUM AGES FOR U-MINERALS FROM THE KIGGAVIK DEPOSITS.

ABBREVIATIONS: Urn = URANINITE, brn = BRANNERITE, cof = COFFINITE.

Host Rock	Deposit	Sample	Depth (m)	Mineral	Corrected $^{207}Pb/^{235}U$	Age (Ma)
Granitic	Kiggavik (MZ)	MZ-10-01	120	Cof	0.000617	0.6
Granitic	Kiggavik (MZ)	MZ-10-01	120	Cof	0.000807	0.8
Granitic	Kiggavik (MZ)	MZ-10-01	120	Cof	0.001034	1.0
Granitic	Kiggavik (MZ)	MZ-10-01	120	Cof	0.001051	1.1
Granitic	Kiggavik (MZ)	MZ-10-01	120	Cof	0.001494	1.5
Metasedimentary	Kiggavik (CZ)	CZ-15-01	82.6	Urn	0.001597	1.6
Granitic	Kiggavik (MZ)	MZ-10-01	120	Cof	0.001954	2.0
Granitic	Kiggavik (MZ)	MZ-10-01	120	Cof	0.002757	2.8
Metasedimentary	Andrew Lake	AND-10-02	163	Urn	0.004908	5.0
Metasedimentary	Andrew Lake	AND-10-02	163	Urn	0.005443	5.5
Metasedimentary	Andrew Lake	AND-10-02	163	Urn	0.005737	5.8
Metasedimentary	Andrew Lake	AND-10-02	163	Urn	0.005799	5.9
Metasedimentary	Andrew Lake	AND-10-02	163	Urn	0.006414	6.5
Metasedimentary	Andrew Lake	SW39	290.2	Urn	0.009580	9.7
Metasedimentary	Kiggavik (CZ)	CZ-15-01	82.6	Urn	0.010219	10.3
Metasedimentary	Andrew Lake	SW39	290.2	Urn	0.010285	10.4
Metasedimentary	Andrew Lake	SW39	290.2	Urn	0.010292	10.4
Metasedimentary	Andrew Lake	SW39	290.2	Urn	0.010429	10.5
Metasedimentary	End	END-09-02	259.7	Urn	0.010605	10.7
Metasedimentary	Andrew Lake	SW39	290.2	Urn	0.010629	10.7
Metasedimentary	Andrew Lake	SW39	290.2	Urn	0.011086	11.2

Metasedimentary	Andrew Lake	SW39	290.2	Urn	0.011300	11.4
Metasedimentary	Kiggavik (CZ)	CZ-15-01	82.6	Urn	0.012405	12.5
Metasedimentary	Kiggavik (CZ)	CZ-15-01	82.6	Urn	0.012513	12.6
Metasedimentary	Kiggavik (CZ)	CZ-15-01	82.6	Urn	0.013247	13.4
Metasedimentary	End	END-09-02	259.7	Urn	0.015600	15.7
Metasedimentary	End	END-09-02	259.7	Urn	0.015724	15.8
Metasedimentary	End	END-09-02	259.7	Urn	0.016398	16.5
Metasedimentary	End	END-09-02	259.7	Urn	0.017655	17.8
Metasedimentary	Andrew Lake	AND-10-02	163	Urn	0.018112	18.2
Metasedimentary	End	END-09-02	259.7	Urn	0.019206	19.3
Metasedimentary	Bong	BONG-50	292.2	Urn	0.019398	19.5
Metasedimentary	End	END-09-02	259.7	Urn	0.019535	19.6
Metasedimentary	Andrew Lake	AND-10-02	163	Urn	0.020708	20.8
Metasedimentary	Bong	BONG-50	292.2	Urn	0.023155	23.2
Metasedimentary	End	END-09-02	259.7	Urn	0.023870	24.0
Metasedimentary	End	END-09-02	259.7	Urn	0.025270	25.3
Metasedimentary	Kiggavik (CZ)	CZ-15-01	82.6	Urn	0.030432	30.4
Metasedimentary	Kiggavik (CZ)	CZ-15-01	82.6	Urn	0.032443	32.4
Metasedimentary	Bong	BONG-50	292.2	Urn	0.034731	34.7
Metasedimentary	Bong	BONG-50	292.2	Urn	0.035641	35.6
Metasedimentary	Bong	BONG-50	292.2	Urn	0.036877	36.8
Metasedimentary	Kiggavik (CZ)	CZ-15-01	82.6	Urn	0.038226	38.1
Metasedimentary	Kiggavik (CZ)	CZ-15-01	82.6	Urn	0.041603	41.4
Metasedimentary	Bong	BONG-50	292.2	Urn	0.042106	41.9
Metasedimentary	Bong	BONG-50	292.2	Urn	0.044492	44.2
Metasedimentary	Bong	BONG-50	292.2	Urn	0.044808	44.5
Metasedimentary	Kiggavik (CZ)	CZ-15-01	82.6	Urn	0.045313	45.0
Metasedimentary	Bong	BONG-50	292.2	Urn	0.051779	51.3

Metasedimentary	Andrew Lake	AND-10-02	163	Urn	0.063937	62.9
Metasedimentary	Kiggavik (CZ)	CZ-15-01	82.6	Urn	0.064603	63.6

Table S3. CORRECTED ISOTOPIC DATA AND CALCULATED U/Th DISEQUILIBRIUM AGES FROM U MINERALS IN THE KIGGAVIK DEPOSITS. ABBREVIATIONS: Urn = URANINITE, brn = BRANNERITE, cof = COFFINITE, Thr = URANOTHORITE.

Host Rock	Deposit	Sample	Depth (m)	Mineral	[Th230/ U238]A	Error 1σ (%)	[U234/ U238]A	Error 1σ (%)	Age (Ka)	Error (+) (Ka)	Error (-) (Ka)
Granitic	Kiggavik (MZ)	MZ-10-01	205	Thr	0.99	NaN	3.60	28.7	34	5.3	5.2
Granitic	Kiggavik (MZ)	LG86	158.8	Urn	0.27	24.1	0.95	3.7	36	8.4	8.6
Granitic	Kiggavik (MZ)	LG86	158.8	Urn	0.31	19.8	1.04	3.4	38	6.7	7.8
Granitic	Kiggavik (MZ)	LG86	158.8	Urn	0.28	21.5	0.95	3.6	38	7.3	7.7
Average									36.5		
2x Std Dev Mean									1.9		
Granitic	Kiggavik (MZ)	MZ-10-01	130	Thr	0.30	NaN	0.81	22.9	51	9.0	8.4
Granitic	Kiggavik (MZ)	LG86	158.8	Urn	0.39	20.4	0.96	3.8	57	13.0	12.0
Granitic	Kiggavik (MZ)	MZ-10-01	205	Thr	0.40	31.6	0.96	17.7	59	12.0	15.0
Average									55.7		
2x Std Dev Mean									4.8		
Metasedimentary	And	SW38	180	Urn	0.83	14.7	1.11	5.8	142	28.0	26.0
Metasedimentary	Kiggivik (CZ)	CZ-15-01	82.6	Urn	0.74	10.8	1.00	4.6	146	20.0	19.0
Metasedimentary	End	END-09-02	259.7	Urn	0.81	11.7	1.08	4.4	146	22.0	21.0
Metasedimentary	Bong	BONG-50	292.2	Urn	0.79	13.1	1.06	5.2	149	27.0	24.0

Metasedimentary	And	SW38	180	Urn	0.73	10.3	0.97	4.3	152	20.0	19.0
Metasedimentary	End	END-09-02	259.7	Urn	0.65	16.1	0.89	7.0	152	33.0	29.0
Granitic	Kiggavik (MZ)	MZ-10-01	120	Cof	0.75	10.8	0.99	4.9	156	22.0	21.0
Metasedimentary	And	SW6	294.7	Urn	0.70	12.1	0.93	5.2	158	26.0	23.0
Granitic	Kiggavik (MZ)	MZ-10-01	130	Thr	0.84	12.8	1.08	7.1	159	24.0	22.0
Granitic	Kiggavik (MZ)	LG86	158.8	Urn	0.78	12.5	1.01	3.5	159	32.0	30.0
Metasedimentary	End	END-09-02	341.2	Bran	0.67	12.5	0.90	5.5	159	26.0	25.0
Granitic	Kiggavik (MZ)	MZ-10-01	130	Thr	0.89	31.6	1.13	11.2	162	79.0	59.0
Average									153.3		
2x Std Dev Mean									3.7		
Metasedimentary	End	END-11-02	327.8	Urn	0.76	9.1	0.93	4.0	195	28.0	27.0
Granitic	Kiggavik (MZ)	LG86	158.8	Urn	0.89	9.4	1.05	3.7	201	33.0	31.0
Granitic	Kiggavik (MZ)	LG86	158.8	Cof	0.83	9.2	0.99	3.7	203	38.0	30.0
Metasedimentary	And	SW38	180	Urn	0.92	9.9	1.06	3.8	211	41.0	35.0
Metasedimentary	End	END-09-02	259.7	Urn	0.92	12.9	1.06	5.1	212	52.0	48.0
Metasedimentary	End	END-09-04	322.3	Urn	0.95	8.1	1.08	3.5	219	32.0	29.0
Metasedimentary	And	SW38	180	Urn	0.82	11.1	0.95	4.6	221	51.0	41.0
Granitic	Kiggavik (MZ)	MZ-10-01	120	Cof	0.93	10.1	1.05	4.3	226	43.0	37.0
Metasedimentary	Kiggavik (MZ)	CZ-15-01	82.6	Urn	1.00	9.6	1.11	4.0	229	45.0	38.0
Metasedimentary	End	END-09-04	339.1	Urn	0.83	9.3	0.96	4.1	230	43.0	37.0
Metasedimentary	End	END-09-04	322.3	Bran	0.86	7.3	0.98	4.2	232	30.0	25.0
Metasedimentary	Bong	Bong-36	410.4	Urn	0.93	6.3	1.04	3.3	232	26.0	23.0
Granitic	Kiggavik (MZ)	LG86	158.8	Cof	0.81	9.1	0.94	3.8	235	49.0	39.0
Metasedimentary	End	END-09-04	339.1	Urn	0.85	10.2	0.97	4.0	236	61.0	45.0

Granitic	Kiggavik (MZ)	LG86	158.8	Urn	0.90	9.2	1.01	3.7	244	56.0	43.0
Metasedimentary	End	END-09-04	339.1	Bran	0.97	9.6	1.07	3.9	246	54.0	45.0
Metasedimentary	And	AND-10-02	163	Urn	0.80	9.6	0.92	4.1	247	61.0	48.0
Metasedimentary	End	END-09-04	322.3	Urn	0.95	7.5	1.05	3.5	248	39.0	33.0
Metasedimentary	End	END-09-02	259.7	Urn	0.99	13.2	1.08	5.1	250	91.0	59.0
Metasedimentary	Bong	Bong-36	410.4	Urn	0.87	6.1	0.98	3.4	251	31.0	27.0
Metasedimentary	Bong	Bong-36	410.4	Urn	0.92	6.5	1.01	3.5	260	37.0	31.0
Metasedimentary	And	SW38	180	Urn	0.98	10.9	1.06	4.2	261	85.0	57.0
Metasedimentary	End	END-09-04	322.3	Urn	0.96	7.4	1.04	3.5	264	49.0	39.0
Metasedimentary	End	END34	312.7	Urn	1.01	7.9	1.09	3.3	266	54.0	42.0
Metasedimentary	End	END-09-02	341.2	Bran	0.86	13.6	0.95	5.7	277	140.0	81.0
Metasedimentary	End	END-09-04	322.3	Urn	0.87	8.1	0.95	4.3	280	57.0	44.0
Metasedimentary	End	END34	312.7	Urn	1.00	7.5	1.06	3.6	283	56.0	43.0
Metasedimentary	End	END34	312.7	Urn	1.00	6.9	1.06	3.1	284	59.0	45.0
Metasedimentary	End	END-11-02	327.8	Urn	1.00	10.7	1.06	3.9	290	130.0	73.0
Metasedimentary	End	END-09-02	341.2	Bran	0.81	13.5	0.90	5.8	294	190.0	90.0
Metasedimentary	End	END-09-04	339.1	Bran	0.83	14.8	0.92	6.4	295	190.0	94.0
Metasedimentary	Kiggavik (CZ)	CZ-15-01	82.6	Urn	1.03	10.0	1.08	3.9	299	100.0	71.0
Metasedimentary	End	END-11-02	327.8	Urn	1.01	10.5	1.06	3.9	301	120.0	72.0
Metasedimentary	And	AND-10-02	163	Urn	0.89	9.5	0.97	4.0	303	130.0	71.0
Granitic	Kiggavik (MZ)	MZ-10-01	120	Cof	1.01	11.7	1.07	4.6	305	160.0	85.0
Metasedimentary	And	AND-10-02	163	Urn	1.01	11.3	1.06	4.4	310	150.0	85.0
Metasedimentary	End	END-11-02	327.8	Urn	1.01	10.2	1.06	3.9	312	130.0	81.0
Metasedimentary	Bong	Bong-36	410.4	Urn	0.92	6.4	0.98	3.4	317	72.0	52.0
Metasedimentary	Bong	BONG-50	292.2	Urn	0.88	10.4	0.95	4.4	318	160.0	85.0
Average									258.6		
2x Std Dev Mean									11.6		

Metasedimentary	And	SW39	290.2	Urn	0.93	11.0	0.93	4.6	451	220.0	150.0
Metasedimentary	End	END-09-02	341.2	Bran	1.01	11.2	0.92	4.2	453	180.0	140.0
Granitic	Kiggavik (MZ)	LG86	158.8	Urn	0.91	9.3	0.93	3.9	455	250.0	150.0
Metasedimentary	End	END-11-02	327.8	Urn	0.96	9.4	0.90	3.9	460	150.0	130.0
Metasedimentary	End	END-11-02	327.8	Urn	1.02	11.0	0.93	4.3	463	190.0	150.0
Metasedimentary	And	SW6	294.7	Urn	0.91	9.4	0.91	3.9	465	200.0	140.0
Metasedimentary	And	SW6	294.7	Urn	0.97	10.7	0.94	3.9	468	240.0	170.0
Metasedimentary	Bong	Bong-36	410.4	Urn	0.99	6.7	0.95	3.5	471	260.0	160.0
Metasedimentary	And	SW39	290.2	Urn	1.01	10.7	0.93	4.4	473	190.0	140.0
Metasedimentary	End	END-09-02	341.2	Urn	0.97	10.5	0.95	4.1	475	260.0	160.0
Metasedimentary	End	END34	312.7	Urn	1.01	11.0	0.95	4.3	480	230.0	160.0
Metasedimentary	End	END-11-02	327.8	Urn	0.99	10.2	0.92	4.2	481	200.0	140.0
Metasedimentary	And	SW6	294.7	Urn	1.01	10.8	0.95	4.2	483	230.0	160.0
Metasedimentary	And	SW6	294.7	Urn	0.99	9.6	0.93	3.9	487	190.0	150.0
Metasedimentary	End	END-11-02	327.8	Urn	0.99	9.8	0.94	4.1	487	200.0	140.0
Metasedimentary	End	END-09-04	322.3	Urn	0.96	7.7	0.91	3.9	488	190.0	130.0
Average									471.3		
2x Std Dev Mean									6.3		
Metasedimentary	End	END-09-02	341.2	Bran	0.64	14.1	0.98	6.1	115	16.0	17.0
Metasedimentary	End	END-09-04	322.3	Urn	0.89	8.6	1.10	4.0	173	20.0	19.0
Metasedimentary	End	END-09-02	259.7	Urn	0.83	18.6	0.87	6.2	338	220.0	130.0
Metasedimentary	End	END34	312.7	Urn	1.02	7.6	1.04	3.5	359	140.0	81.0
Metasedimentary	End	END34	312.7	Urn	1.01	7.2	1.04	3.2	360	140.0	80.0
Metasedimentary	End	END-09-02	259.7	Urn	0.96	18.0	0.91	7.3	387	200.0	150.0
Metasedimentary	And	SW38	180	Urn	0.87	14.8	0.90	6.0	389	220.0	150.0
Metasedimentary	End	END-09-02	341.2	Bran	0.99	15.7	0.92	6.0	412	210.0	170.0
Metasedimentary	And	SW6	294.7	Urn	0.89	11.9	0.87	4.9	419	170.0	130.0
Metasedimentary	End	END-09-02	341.2	Bran	0.96	13.8	0.93	5.6	427	250.0	150.0
Metasedimentary	And	SW38	180	Urn	0.93	12.2	0.91	4.9	431	210.0	140.0

5

REFERENCES CITED

Battaglia, S., 2004, Variations in the chemical composition of illite from five geothermal fields: a possible geothermometer: Clay Minerals, v. 39, p. 501–510.

Capuano, R. M., 1992, The temperature dependence of hydrogen isotope fractionation between clay minerals and water: Evidence from a geopressured system: Geochimica et Cosmochimica Acta, v. 56, p. 2547–2554.

Fayek, M., Kyser, T.K., and Riciputi, L.R., 2002, U and Pb isotope analysis of uranium minerals by ion microprobe and the geochronology of the McArthur River and Sue Zone uranium deposits, Saskatchewan, Canada: The Canadian Mineralogist, v. 40, p. 1553–1569.

Fayek, M., Harrison, T.M., Ewing, R.C., Grove, M., Coath, C.D., 2022, O and Pb isotope analyses of uranium minerals by ion microprobe and U-Pb ages from the Cigar Lake deposit: Chemical Geology v. 185, p. 205–225.

Ludwig, K., 1993, ISOPLOT, excel based program for plotting radiogenic isotopes: USGS Open File Rep 91-445, 42 p.

Sharpe, R. and Fayek, M., 2016, Mass bias corrections for U-Pb isotopic analysis by secondary ion mass spectrometry: Implications for U-Pb dating of uraninite: Rapid Communications in Mass Spectrometry, v. 30, p. 1601–1611.

Sheppard, S. M. F., 1986, Characterization and isotopic variations in natural waters: Reviews in Mineralogy and Geochemistry, v. 16, p. 165–183.

Sheppard, S. M. F., and Gilg, H. A., 1996, Stable isotope geochemistry of clay minerals: Clay Minerals, v. 31, p. 1–24.

Chapter 4: Extreme H isotope fractionation of phyllosilicates from the Kiggavik Uranium deposits

Ian Burron[1*], Mostafa Fayek[1], Julie Brown[2], and Alfredo Camacho[1]

1: Department of Earth Sciences, University of Manitoba, Winnipeg, MB R3T 2N2, Canada

2: Canadian Nuclear Safety Commission, 280 Slater Street, Ottawa, Ontario K1P 5S9, Canada

*: Corresponding author

Abstract

The Kiggavik Uranium (U) Project in Nunavut, Canada hosts U deposits for which both unconformity-related and metasomatic-iron-alkali-calcic genetic models have been proposed. We propose a five-phase genetic model consisting of: (1) albitization; (2) hematization and illitization; (3) bleaching and primary (U1) mineralization; (4) ~1450 Ma to 274 Ma overprinting events linked to distant tectonic and igneous events and: (5) geologically recent (~471 Ka to 36 Ka) overprinting linked to subglacial meteoric fluids.

M2 muscovite formed during albitization of granitic rocks and is Ar-Ar dated to ~1820-1830 Ma, which is consistent with igneous and seismic activity and albitite-hosted U mineralization in the region. M2 muscovite has δ^2H values as high as +128.9 ‰. This high value is unprecedented in terrestrial minerals. M2 is in equilibrium with isotopically heavy ($\delta^{18}O$ and δ^2H values of +10.4 ± 2.1 ‰ and +130.1 ± 30.6 ‰, respectively) fluids proposed to have been produced through multiple cycles of seismically-induced fluid boiling, phase separation, and condensation.

Multiple generations of illite, formed through retrograde metamorphic (Il1) and subsequent hydrothermal (Il2-Il5) processes, are present. Il3 and Il5 are isotopically consistent with precipitation from basinal fluids and with subsequent overprinting by meteoric fluids, while Il4 is isotopically consistent with highly fractionated, boiled fluids. Il3-Il5 illites yield post U1 Ar-Ar dates, reflecting overprinting events.

Highly fractionated fluids are strongly linked to albitization and an early albitite-style U mineralization event. Both highly fractionated and basinal fluids may have been involved in U1

mineralization. Basinal and meteoric fluids are strongly linked to post depositional alteration events.

Keywords:

Stable isotope geochemistry; Uranium deposits; Ar-Ar geochronology; H isotope fractionation; Hydrothermal ore deposits

Abstract

The Kiggavik Uranium (U) Project in Nunavut, Canada hosts U deposits for which both unconformity-related and metasomatic-iron-alkali-calcic genetic models have been proposed. We propose a five-phase genetic model consisting of: (1) albitization; (2) hematization and illitization; (3) bleaching and primary (U1) mineralization; (4) ~1450 Ma to 274 Ma overprinting events linked to distant tectonic and igneous events, and: (5) geologically recent (~471 Ka to 36 Ka) overprinting linked to subglacial meteoric fluids.

M2 muscovite formed during albitization of granitic rocks and is Ar-Ar dated to ~1820-1830 Ma, which is consistent with igneous and seismic activity and albitite-hosted U mineralization in the region. M2 muscovite has δ^2H values as high as +129 ‰. This high value is unprecedented in terrestrial minerals. M2 is in equilibrium with isotopically heavy ($\delta^{18}O$ and δ^2H values of +10.4 ± 2.1 ‰ and +130 ± 31 ‰, respectively) fluids proposed to have been produced through multiple cycles of seismically-induced fluid boiling, phase separation, and condensation.

Multiple generations of illite, formed through retrograde metamorphic (Il1) and subsequent hydrothermal (Il2-Il5) processes, are present. Il3 and Il5 are isotopically consistent with precipitation from basinal fluids and with subsequent overprinting by meteoric fluids, while Il4 is isotopically consistent with highly fractionated, boiled fluids. Il3-Il5 illites yield post U1 Ar-Ar dates, reflecting overprinting events.

Highly fractionated fluids are strongly linked to albitization and an early albitite-style U mineralization event. Both highly fractionated and basinal fluids may have been involved in U1 mineralization. Basinal and meteoric fluids are strongly linked to post-depositional alteration events.

1. Introduction

Phyllosilicates such as muscovite and illite are common in a wide variety of geologic systems, and isotopic studies of these minerals can provide insights into many geological processes (Suzuoki and Epstein, 1976; Capuano, 1992; Sheppard and Gilg, 1996; Fayek and Kyser, 1999; Chacko et al., 2001; Sharp, 2017). The decay of K to Ar allows these minerals to be dated via K-Ar and Ar-Ar geochronology, while the stable isotope composition of the H and O in these minerals can reveal the temperature and sources of fluids involved in their formation (e.g., Sheppard and Gilg, 1996; Fayek and Kyser, 1999; Sharp, 2017; Fulignati, 2020).

Many geologic processes cause fractionation of stable isotopes including phase changes (evaporation and condensation), microbial processes, mineral precipitation, fluid-rock interactions, temperature, and exchange between different phases (Galley et al., 1972; Suzuoki and Epstein, 1976; Horibe and Craig, 1995; Fayek and Kyser, 1999). Phase changes are capable of causing particularly significant isotopic fractionation; high-latitude meteoric fluids, derived from sea water (δ^2H and $\delta^{18}O$ 0 ‰; Vienna Standard Mean Ocean Water (V-SMOW)) through Rayleigh fractionation, have δ^2H and $\delta^{18}O$ values as depleted as –428 ‰ and –55.5 ‰, respectively (NIST, 2022). Conversely, evaporated and condensed hydrothermal waters may have ^2H values as enriched as +30 ‰ (Beaudoin and Chiaradia, 2016).

The widespread occurrence of phyllosilicates, especially illite, associated with hydrothermal uranium (U) deposits makes these methods particularly useful in studying the genesis and evolution of hydrothermal U deposits (Wilson and Kyser, 1987; Kotzer and Kyser 1995; Fayek and Kyser, 1999; Renac et al., 2002; Hunt et al., 2011; Sharpe et al., 2015; Sheahan et al., 2016; Zhang et al., 2019). Stable ^2H and ^{18}O investigations of muscovite, chlorite,

kaolinite, and illite from Unconformity-Related U (URU) deposits helped develop the URU deposit models by identifying multiple pre, syn, and post-mineralization diagenetic-hydrothermal fluid sources as well as late overprinting by meteoric fluids (Wilson and Kyser, 1987; Kotzer and Kyser 1995; Fayek and Kyser, 1999; Alexandre et al., 2005; Sheahan et al., 2016). Ar-Ar geochronology has allowed timing constraints to be placed on mineralization and resetting events that have formed and modified U deposits from the Athabasca and Thelon basins (Renac et al., 2002; Alexandre et al., 2009; Cloutier et al., 2009;2011; Sheahan et al., 2016; Shabaga et al., 2017).

The Kiggavik U deposits, Thelon area, Nunavut, have often been interpreted as basement-hosted URU deposits, similar to those in the Saskatchewan's Athabasca Basin (Fuchs et al., 1986; Riegler et al., 2014; 2016; Chi et al., 2016; Grare et al., 2020; Ashcroft, 2020). Despite similarities in geologic setting between these areas, the Kiggavik deposit's complex fluid history as well as inconsistencies with the URU model such as the presence of epithermal mineral textures and quartz breccias, minerals such as brannerite, hydrothermal zircon and uranothorite, fluorite, and Bi-minerals, and lack of evidence of basinal fluids, suggests that this model may not fully describe these deposits (Flotté, 2009; Sharpe et al., 2015; Chi et al., 2016; Grare et al., 2020; Burron et al., 2024). Burron et al. (2024) recently proposed that the Kiggavik deposits represent a hybrid between a paragenetically early Metasomatic Iron Alkali Calcic (MIAC) system and later overprinting URU system. Several important aspects of this model, including the timing relationships between these systems and source(s) of mineralizing fluids, have not been constrained.

This paper presents Ar-Ar geochronology, and O and H isotopic data from altered and unaltered muscovite and illite associated with the various stages of alteration and U mineralization in the Kiggavik U deposits in order to constrain their timing and genetic relationships, including unusually high H isotopic compositions.

2. Geological Setting

The Kiggavik deposits are located ~2-25 km southeast of the faulted margin of the Paleo-Mesoproterozoic Thelon Basin, a large intracratonic sedimentary basin located in the Rae Domain of the Churchill Province in the northwestern Canadian Shield (Fig. 1). The Thelon Basin, as well as the underlying Baker Lake Basin, is filled by undeformed volcano-sedimentary rocks of the 1845-1540 Ma Dubawnt Supergroup (Rainbird et al., 2003; Peterson, 2006; Chamberlain et al., 2010). The Thelon Basin is capped by the uppermost formations of the Barrensland Sequence; the 1540 ± 30 Ma Kunngmi shoshonitic basalts (Chamberlain et al., 2010) and the Lookout Point Formation dolomite (Gall et al., 1992). The timing, ~1850-1700 Ma, and intracratonic setting of the Thelon Basin is similar to Saskatchewan's Athabasca Basin, which hosts many economically significant URU deposits (Orrell et al., 1999; Ramaekers 2004; Rainbird and Davis, 2007).

The basement underlying the Thelon Basin consists of Archean granitoid gneiss, 2.74-2.68 Ga supracrustal rocks of the Woodburn Lake group (WLg) (Pehrsson et al., 2013), ~2.6 Ga felsic volcanic and related intrusive rocks of the Snow Island Suite (Jefferson et al., 2011; Peterson et al., 2015; Johnstone, 2017), and orthoquartzite of the Paleoproterozoic Keyet River Group (Rainbird et al., 2010). The Pipedream assemblage of the WLg hosts the majority of the mineralization in the Kiggavik area and consists of felsic, intermediate, and ultramafic volcanic

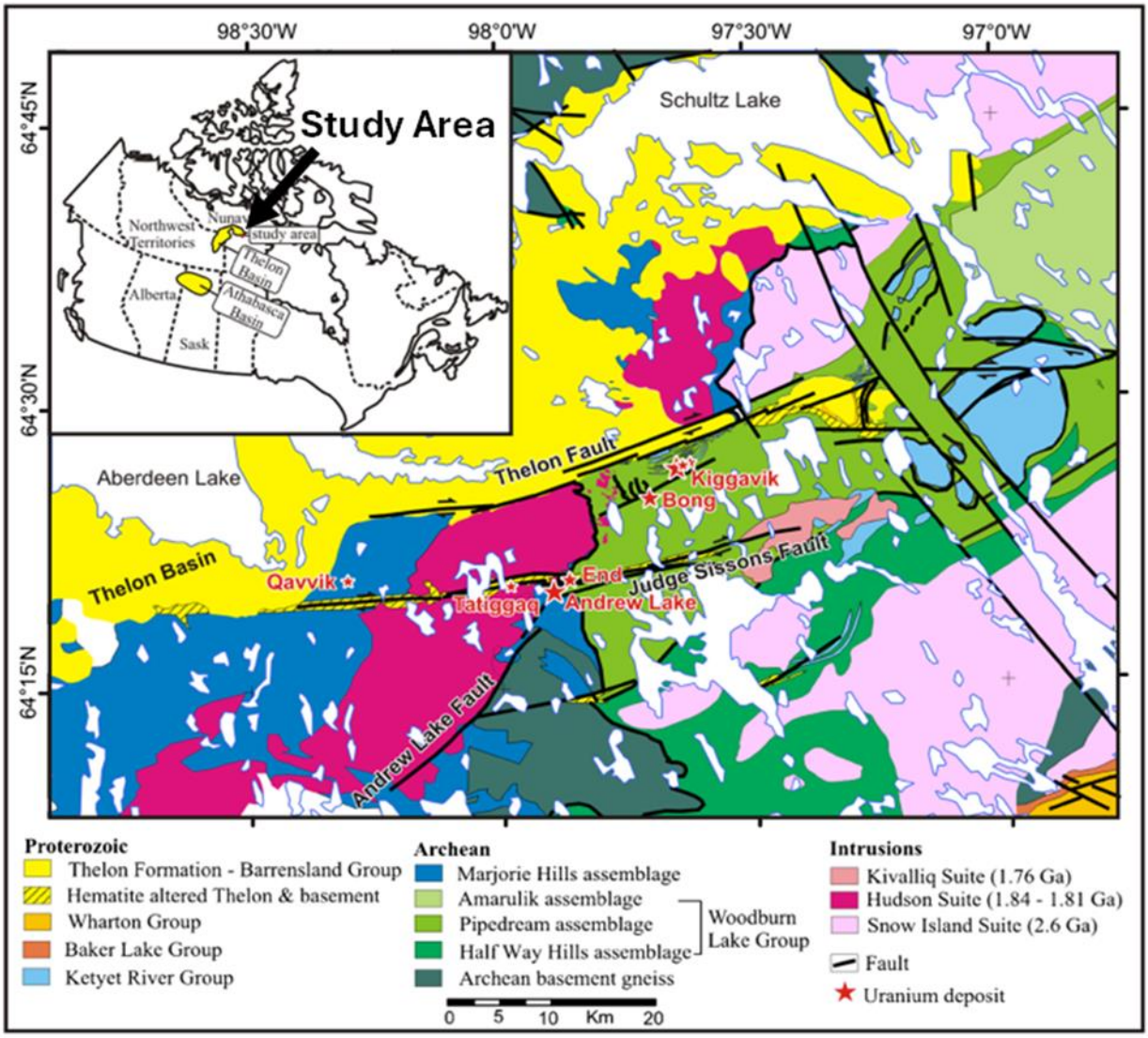

Figure 1. Simplified geological map of the Kiggavik project area. From Chi, *et al.* (2016).

rocks, and subordinate greywacke-mudstone turbidites and iron-formation (Pehrsson et al., 2013). This assemblage is believed to have formed in an intra-continental back-arc to marginal basin setting (Pehrsson et al., 2013). Although volcanic rocks and iron-formations are present, the Pipedream assemblage has generally been described as metagreywacke in previous studies of U mineralization (Shabaga et al., 2017).

These basement lithologies are intruded by the Schultz Lake Intrusive Complex, which is comprised of the 1.84-1.79 Ga Hudson Granites and the 1.76-1.73 Ga Nueltin Granites (Peterson et al., 2002; Peterson, 2006; Scott et al., 2012; Scott et al., 2015). The Hudson Granites comprise late syn-orogenic, medium-grained monzonite, granodiorite, and granite (Peterson et al., 2002; Scott et al., 2015). These rocks were emplaced along pre-syn magmatic structures at mid-crustal levels and are contemporaneous with the ultrapotassic lamprophyres and minettes of the Baker Lake sequence of the Dubawnt Supergroup (Peterson et al., 2002). The Nueltin Granites are K-feldspar megacrystic anorogenic rapakivi-granite (Peterson et al., 2002; Peterson, 2006; Scott et al., 2012). The final episode of igneous activity in the region consists of the 1267 ± 2 Ma intrusion of the Mackenzie diabase dykes (LeCheminant and Heaman, 1989).

The Kiggavik U Project contains an estimated 51 million kg U at an average grade of 0.46% U (AREVA, 2011). Uranium deposits in the region are located at the intersections roughly ESE-WNW and NNE-SSW trending faults, which have been the sites of brittle deformation and intense hydrothermal alteration consisting mainly of clay and hematite alteration and bleaching of host rocks (Fuchs et al., 1986; Sharpe et al., 2015; Grare et al., 2018a; 2020). The studied deposits, Kiggavik, Bong, End, and Andrew Lake, account for the bulk of known U resources in the region, and together with several smaller deposits and prospects form a NE-SW trending

feature informally termed the Kiggavik-Andrew Lake structural trend (Riegler et al., 2014; Sharpe et al., 2015).

Most U mineralization in the Kiggavik region is hosted within metagraywackes of the Woodburn Lake group. Subordinate amounts of mineralization are hosted within the Kiggavik Main Zone and Kiggavik North deposits hosted in the Lone Gull granite. These rocks and the mineralization they host are not as well studied as the clastic metasedimentary rocks. Scott et al. (2015) described the Lone Gull granitic stock as a hybrid between the Hudson and Nueltin granites, with the younger Nueltin magma infiltrating into and altering the older Hudson pluton.

Burron et al. (2024) described the first stage of mineralization as consisting of mineralogically complex albitization (Fig. 2). This albitization consists of porous albite and K-feldspar, quartz, and coarse laths of muscovite, with a diverse suite of trace and accessory minerals comprising biotite, fluorapatite, Ti±(Nb)-oxides, Zr-Th-U silicates, sulfides (pyrite, chalcopyrite, sphalerite, and galena), and monazite (Burron et al., 2024). Lone Gull granitic rocks are more strongly albitized relative to the clastic metasedimentary rocks, with no unalbitized granitic rocks observed; granitic host rocks also include additional minerals which are not observed in the clastic metasedimentary rocks such as fluorite, ilmenite, monazite, REE-(F)-carbonates, molybdenite, scheelite, and native Au as part of the albitized assemblage (Burron et al., 2024). Albitization is associated with a modest enrichment in U hosted mainly in hydrothermal zircon and uranothorite (Burron et al., 2024).

Albitized rocks are observed only in the periphery of the deposits, having been extensively overprinted by texturally destructive hematite-illite alteration (Burron et al., 2024). This hematization consists of small amounts of remnant quartz, Ti-oxides, apatite, and

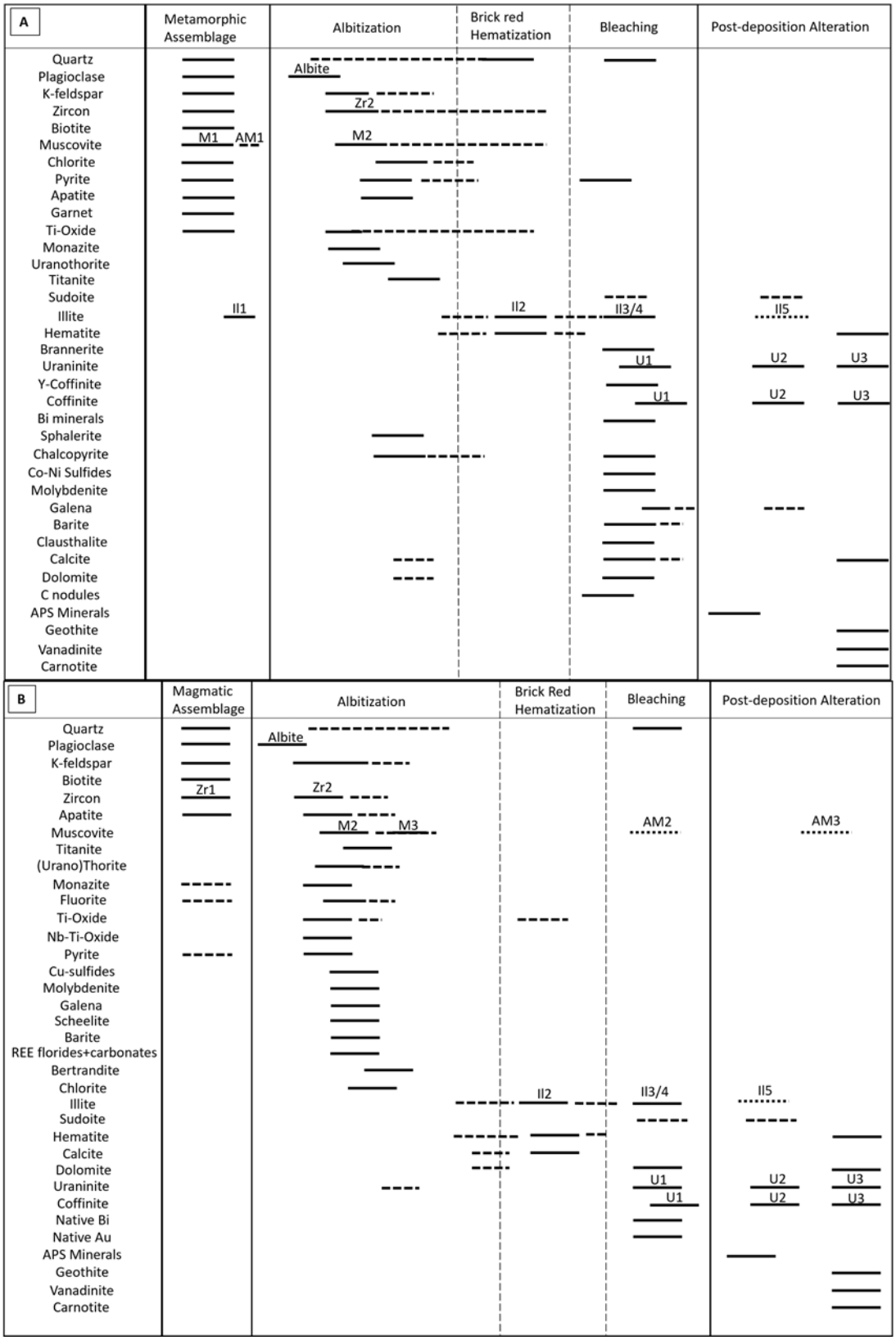
A
Metamorphic Assemblage
Albitization
Brick red Hematization
Bleaching
Post-deposition Alteration
Quartz
Plagioclase
K-feldspar
Zircon
Biotite
Muscovite
Chlorite
Pyrite
Apatite
Garnet
Ti-Oxide
Monazite
Uranothorite
Titanite
Sudoite
Illite
Hematite
Brannerite
Uraninite
Y-Coffinite
Coffinite
Bi minerals
Sphalerite
Chalcopyrite
Co-Ni Sulfides
Molybdenite
Galena
Barite
Clausthalite
Calcite
Dolomite
C nodules
APS Minerals
Geothite
Vanadinite
Carnotite
Albite
Zr2
M1
AM1
M2
II1
II2
II3/4
II5
U1
U2
U3
B
Magmatic Assemblage
Albitization
Brick Red Hematization
Bleaching
Post-deposition Alteration
Quartz
Plagioclase
K-feldspar
Biotite
Zircon
Apatite
Muscovite
Titanite
(Urano)Thorite
Monazite
Fluorite
Ti-Oxide
Nb-Ti-Oxide
Pyrite
Cu-sulfides
Molybdenite
Galena
Scheelite
Barite
REE florides+carbonates
Bertrandite
Chlorite
Illite
Sudoite
Hematite
Calcite
Dolomite
Uraninite
Coffinite
Native Bi
Native Au
APS Minerals
Geothite
Vanadinite
Carnotite
Albite
Zr1
Zr2
M2
M3
AM2
AM3
II2
II3/4
II5
U1
U2
U3

Figure 2. Generalized paragenesis of the Kiggavik deposits. Dashed lines indicate uncertainty in timing, dotted lines indicate overprinting events. A. Metasedimentary and epiclastic host rocks. B. Granitic host rocks. Modified from Burron et al. (2024).

uncommon, heavily altered muscovite laths, within a groundmass of fine grained, massive illite and hematite (Burron et al., 2024). Specular hematite is locally present (Burron et al., 2024). Most hematite is fine-grained (<30 μm), however specular hematite laths may reach several mm in length (Burron et al., 2024).

Hematization is strongly associated with the quartz breccia (QB), <30 m thick sheet-like bodies consisting of clasts of hematized breccia in a matrix comprising multiple stages of quartz and hematite (Grare et al., 2018a). The QB is found in the core of most Kiggavik U deposits and is locally replaced by illite (Grare et al., 2018a; Burron et al., 2024). Although the QB itself is largely barren, it contains traces of hydrothermal zircon and muscovite similar to what is observed in albitized rocks (Burron et al., 2024).

The QB formed by mixing of igneous and meteoric/basinal fluids in an overall epithermal system (Grare et al., 2018a). The QB has not been directly dated, being loosely bracketed between 1.83 Ga Hudson intrusives and the >1.54 Ga deposition of the Thelon Basin (Grare et al., 2018a), although it is often considered to be of Nueltin age (Grare et al., 2018a; b; 2020). This brecciation and hematization bears similarities to brecciation and iron alteration developed in the Southern Breccia U deposits and showings (Burron et al., 2024).

Uranium mineralization is associated with bleaching (hematite removal) of host rocks (Burron et al., 2024). Historic reports describe a relatively simple assemblage of pitchblende (UO_{2-x}), with partial replacement by coffinite ($U(SiO4) \cdot nH_2O$), surrounded by a halo of illite ± hematite ± sudoite alteration (Fuchs et al., 1986); more recent studies, however, have revealed a more complex sequence of mineralization (Sharpe et al., 2015; Shabaga et al., 2017; Grare et al., 2020; Burron et al., 2024). Burron et al. (2024) reported primary U mineralization (U1) as

consisting of three styles: uraninite ± coffinite finely disseminated along interfaces between hematized and bleached rocks (U1a), uraninite ± coffinite ± brannerite (UTi_2O_6) in polymetallic and monometallic epithermal veins (U1b), and disseminated uraninite, coffinite, and brannerite (U1c). Brannerite comprises a significant component of U mineralization in the End Deposit but is not observed in other Kiggavik deposits (Burron et al., 2024). U1a was U-Pb Concordia dated to 1594 ± 95 Ma, while U1b and U1c yielded a more precise Concordia date of 1554 ± 16 Ma (Burron et al., 2024).

This time period is consistent with major episodes of U-mineralization in both albitite-hosted (i.e. the 1551 ± 7 Ma Valhalla deposit (Polito et al., 2009)) and URU (i.e. ~1590 Ma ages reported from several Athabasca Basin deposits (Alexandre et al., 2005; Alexandre et al., 2009; Cloutier et al., 2009)) systems (Burron et al., 2024). The albitization observed at Kiggavik is mineralogically and texturally similar to U-rich albitite-hosted deposits such as Valhalla, Australia (i.e. Polito et al., 2009; Wilde et al., 2013) and the Southern Breccia Zone showings and Sue Dianne deposit, Great Bear Magmatic Zone, Canada (i.e. Montreuil et al., 2015; Corriveau et al., 2016), but not with Athabasca Basin URU systems (Burron et al., 2024). The bleaching associated with U1 is not easily reconciled with either MIAC or URU deposit styles (Burron et al., 2024).

A second stage of mineralization (U2) comprises texturally altered and isotopically reset U minerals with U-Pb dates ranging from 1440 ± 21 to 274 ± 69 Ma (Burron et al., 2024). This is similar to the timing of multiple events affecting Athabasca Basin URU deposits (Burron et al., 2024). A third stage (U3) is associated with distinctive orange goethite-hematite alteration (Burron et al., 2024; 2025). U3 yields U-Th disequilibrium dates ranging from 34 +5.3/-5.2 Ka

to 488 +190/-130 Ka, and is linked to the geologically recent infiltration of subglacial fluids along fracture systems (Burron et al., 2025).

3. Methods

The samples examined in this study are the same as those examined by Burron et al. (2024), and were drawn from the University of Manitoba's library of core samples and polished thin sections from the Kiggavik region. These ~350 samples represent the various stages of alteration and U mineralization, as well as unaltered host rocks from the Kiggavik, Bong, End, and Andrew Lake deposit areas. While many previous studies of the area have focused on mineralization within clastic metasedimentary rocks (i.e. Sharpe, et al., 2015; Ashcroft, 2020), the samples selected for this study also include many mineralized and non-mineralized igneous rocks. The mineralogy and textures of sections were characterized through optical petrography and scanning electron microscopy prior to more advanced instrumental methods.

The chemical compositions of minerals were measured at the Manitoba Isotope Research Facility (MIRF) using a CAMECA SX100 Universal Electron Probe MicroAnalyser (EPMA). This EMPA is equipped with five wavelength-dispersive spectrometers and a Princeton Gamma-Tech (PGT) energy-dispersive spectrometer. A 1 μm electron beam with an accelerating voltage of 15 kV and beam current of 20 nA was used. Elemental detection limits were below 1000 ppm for all elements except for U, Th, Pb, Hf, and Zr, which had detection limits of ~3000, 3000, 2500, 2500, and 2000 ppm, respectively.

Stable O and H isotope ratios in illite, muscovite, and altered muscovite were measured at MIRF using a CAMECA 7f Secondary Ion Mass Spectrometer (SIMS) instrument at the University of Manitoba. Analytical protocols for H and O are similar to those described in Lui et

al. (2010), and Riciputi et al. (1998), respectively. Prior to analysis, samples were cleaned by immersion in an ultrasonic cleaner; first in a dilute soap solution, followed by water, distilled water and finally ethanol. Each stage lasted 10 minutes. Sputter-coating the cleaned samples with a ~200Å-thick layer of gold ensured a conductive surface. Hydrogen isotopes were measured via a ~50 nA primary ion beam of O- accelerated at 12.5 kV. The beam was focused to a 50 μm spot using a 750-μm aperture in the primary column. Interferences were minimized by using a mass resolving power of 800 and setting the sample voltage to 9.95 Kv and the electrostatic analyzer to 10 Kv, creating a 50 V offset. Each analysis comprised 50 six second cycles, with a 60 second pre-sputter. Oxygen isotopes were measured via a ~7 nA primary ion beam of Cs+ accelerated at 10 kV. The beam was focused to a 15 μm spot using a 750-μm aperture in the primary column. Interferences were minimized by using a mass resolving power of 350 and setting the sample voltage to 8.7 Kv and the electrostatic analyzer to 9 Kv, creating a 300 V offset. Each analysis comprised 80 eight second cycles.

An in-house muscovite standard from a pegmatite in Pied des Mont, Quebec, Canada, was used for correction of H and O isotopes in both muscovite and illite samples, due to their similar matrix compositions. This standard has known $\delta^{2}H$ and $\delta^{18}O$ values of –65 ± 1 ‰ and +10.4 ± 0.2 ‰, respectively. Spot-to-spot reproducibility of the standard is better than 3.0 ‰ for H and 1.0 ‰ for O. Both hydrogen and oxygen are reported in the δ-notation relative to Vienna Standard Mean Ocean Water (V-SMOW).

In-situ $^{40}Ar/^{39}Ar$ analytical work was performed at the University of Manitoba following the procedures outlined by Camacho et al. (2020). Samples were irradiated for 30 h in the TRIGA reactor at Oregon State University. Argon-Argon dating was performed at MIRF via a

multi-collector Thermo Fisher Scientific ARGUS VI mass spectrometer linked to a Photon Machines (55 W) Fusions 10.6 CO_2 laser via a stainless steel Thermo Fisher Scientific extraction/purification line. $^{40}Ar/^{39}Ar$ dates were calculated based on the decay constant of Steiger and Jäger (1977).

4.0. Results

4.1. Petrography

4.1.1. Unaltered Clastic Metasedimentary Rocks

Fresh metagraywacke is grey-green, fine-grained, and is strongly foliated. Foliation is defined by elongation of minerals, principally biotite and muscovite, and transposed bedding planes. These clastic metasedimentary rocks are composed of quartz (~60%) and feldspar (~25%), mainly K-feldspar with lesser plagioclase, with ~10-15% metamorphic muscovite (M1) and biotite, and accessory zircon, pyrite, fluorapatite, rutile, and trace garnet. These rocks have undergone retrograde metamorphism, with biotite strongly altered to Fe-Mg chlorite, and feldspars commonly partially to strongly altered to coarse-grained illite (Il1). Quartz and feldspars are sub-rounded to rounded and 0.1-0.5 mm in size. Muscovite and biotite are tabular and 0.1-0.3 mm in size, although laths up to 1 cm long are locally present. Muscovite has commonly undergone variable degrees of alteration; these are termed altered muscovites (AM). M1 is commonly slightly-strongly altered, with recrystallization to finer grain size and variable breakdown to illite along grain margins and cleavage domains (AM1; Fig. 3).

4.1.2. Hematized Clastic Metasedimentary Rocks

Hematized metagraywacke is dominated by massive, fine-grained (<15 μm) illite (Il2), which comprises 70-90% of the rock. Fine grained (<0.1 mm), anhedral hematite is disseminated

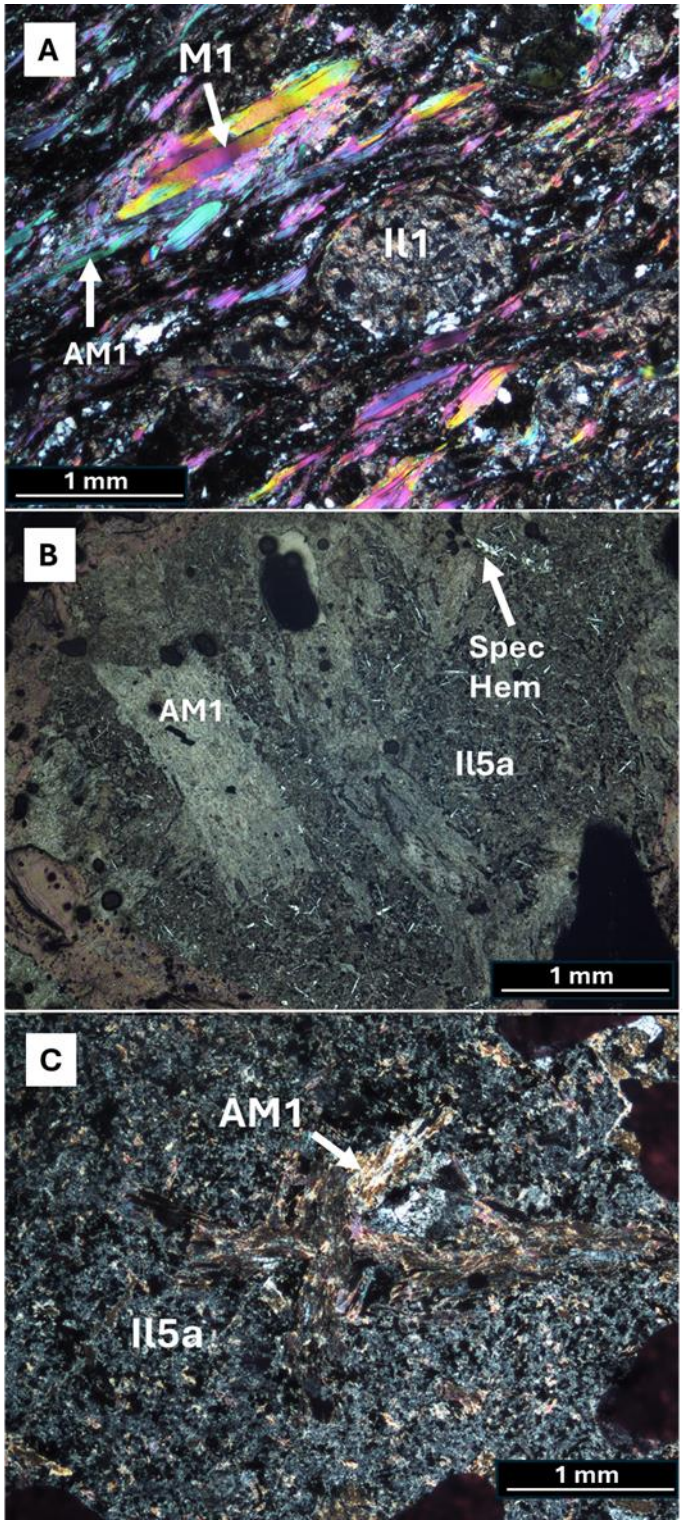
A
M1
Il1
AM1
1 mm
B
Spec
Hem
AM1
Il5a
1 mm
C
AM1
Il5a
1 mm

Figure 3. Textures of muscovite in metasedimentary rocks. A. Cross polarized light image of M1 metamorphic muscovite and lightly altered AM1 muscovite (AND 10-01-274.6). B. Reflected light image of strongly altered AM1 muscovite and Il5a illite with specular hematite laths from the hematized side of a non-mineralized redox interface (END-09-10-32.35). C. Cross polarized light image of strongly altered AM1 muscovite and Il5a illite from the bleached side of a non-mineralized redox interface (END-09-10-32.35). Abbreviations: Spec Hem = Specular hematite.

throughout the illite matrix and comprises 10-15% of hematized clastic metasedimentary rocks. Specular hematite is locally present and forms 0.1-0.3 mm acicular laths with comprise 5-15% of the rock where present. Variable but minor amounts of corroded quartz, strongly illite altered M1 muscovite and chlorite, and remnant Ti-oxides and apatite are commonly present. Altered M1 laths, <1 cm long, are commonly included by hematite and are moderately to strongly broken down to coarse-grained illite (Fig. 3 B,C).

4.1.3. The Quartz Breccia (QB)

The QB is strongly associated with hematization of host rocks (Grare et al., 2018a; Burron et al., 2024). Clasts within the QB are similar to hematized clastic metasedimentary rocks, although specular hematite is somewhat more common in close proximity to the QB. The matrix fill is dominated by quartz with minor amounts of carbonate (calcite with minor dolomite and trace ankerite). Pods of semi-massive sulfides, which have been fractured and partially altered to hematite, are locally present. Trace amounts of hydrothermal textured, Al-Ca-bearing zircon and muscovite were locally observed in association with a late crosscutting specular hematite vein. The QB matrix and clasts are locally weakly-moderately replaced by illite.

4.1.4. Bleached Clastic Metasedimentary Rocks and U Mineralization

Bleached clastic metasedimentary rocks are dominated by massive, fine grained (<15 μm) illite (Il3-Il5; fig. 2). Bleached illite is classified based on its relationship to mineralization and brecciation. Il3 is associated with U mineralization, Il4 forms breccia fill, and Il5 is not associated with U mineralization. Il3 is further subdivided into Il3a, associated with U1a, and Il3b, associated with U1b and U1c. Il5 is subdivided based on host rock: Il5a is present in clastic metasedimentary rocks whereas Il5b is present in granitic rocks.

In addition to illite, bleached rocks commonly contain minor amounts of remnant quartz, Ti-oxides, and apatite, while minor amounts of calcite and sudoite are locally present; calcite is more common, and sudoite is absent, in the End Deposit. Strongly altered laths of muscovite (M1) and chlorite are uncommon. Where U-mineralization is absent bleached rocks are texturally and mineralogically similar to hematized rocks, with the notable exception of the absence of hematite. Bleaching is observed to crosscut and overprint hematization.

Bleaching is locally associated with U-mineralization comprising disseminated uraninite and coffinite along interfaces between hematized and bleached rocks (U1a), disseminated uraninite ± coffinite ± brannerite within the bleached Il3 illite matrix (U1b), and uraninite ± coffinite ± brannerite in polymetallic and monometallic epithermal veins (U1c). Monometallic Ulc veins comprise quartz and U-minerals ± pyrite, while polymetallic U1c veins contain diverse assemblages such as uraninite-molybdenite-chalcopyrite-pyrite-(Ni-Co sulfides), uraninite-galena±barite, and uraninite-coffinite-native Bi. Polymetallic veins are most prevalent in the End Deposit. U-minerals occurring outside of veins are commonly intergrown with Il3 illite on a ~1 μm scale. Where muscovite and chlorite laths are present uraninite commonly partially replaces these phyllosilicates along cleavage domains and may even completely pseudomorph them.

An unusual illite (Il4)-filled breccia crosscutting pervasively hematized host rock was observed in a few samples from the End Deposit (Fig. 4A). Traces of native Bi rimmed by coffinite were observed in one such breccia (Fig. 4B), suggesting a link to U1c mineralization, which also contains Bi minerals surrounded by U minerals (Burron et al., 2024). The Il4 illite breccia matrix, however, proved to be isotopically distinct from other illites (see below).

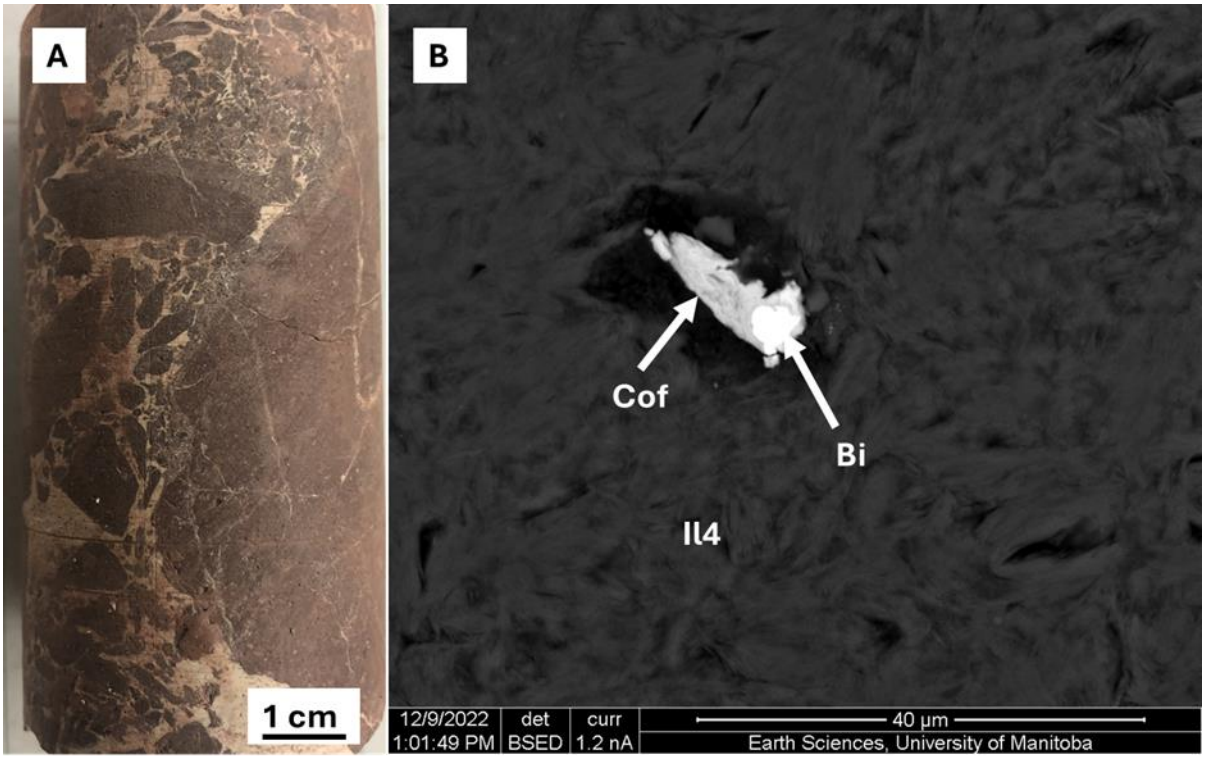

Figure 4. A. Illite breccia crosscutting hematized metasedimentary rocks in drill core (End-09-04-203.65). B. Backscattered electron image of the same sample showing traces of native Bi rimmed in coffinite within the Il4 illite matrix. Abbreviations: Cof = Coffinite, Bi = Native bismuth.

A generation of fractured, texturally altered uraninite and coffinite (U2) comprises a significant proportion (the majority in Bong and Andrew Lake and subequal with U1 in End and Kiggavik) of U-mineralization. These U2 minerals resemble more altered versions of U1, although polymetallic veins are absent. Disseminated U2 uraninite in the Andrew Lake deposit, and locally in the End deposit may exhibit a distinctive 'worm-rock' texture, where uraninite grains are rimmed by a <1 mm halo of bleached zone within an overall hematite-rich Il2 matrix.

The latest generation of U-minerals (U3) is associated with goethite-hematite±calcite alteration, which locally forms halos around fractures and porous, locally U1/U2 mineralized, vein systems. This alteration has a distinctive orange colour. It overprints hematization and bleaching, and weakly remobilizes U1/U2 into U3.

4.1.5. Lone Gull Granitic Rocks

All of the observed granitic rocks have been strongly albitized, with varying degrees of overprinting hematization and bleaching. Albitized granitic rocks consist of albite, K-feldspar, quartz, and muscovite, with accessory zircon, fluorapatite, uranothorite, rutile, pyrite, chalcopyrite, molybendite, galena, biotite, fluorite, Fe-oxides, and Alumino-Phosphate-Sulfate (APS) minerals, and trace amounts of ilmenite, monazite, REE-(F)-carbonates, scheelite, and native Au. All of these minerals, with the exception of the cores of some zircons and larger quartz, feldspar, and biotite grains, are interpreted as the result of replacement of primary igneous minerals. Accessory minerals are strongly concentrated into pockets interpreted as partially infilled dissolution pits. These pits also ubiquitously contain muscovite laths.

Muscovite commonly forms <5 mm sub-euhedral laths within the rock matrix and within dissolution pits (M2), and less commonly forms <2 mm radial aggregates interstitial to quartz,

feldspar, and M2 muscovite (M3; Fig. 5). M3 is commonly in contact with M2 and locally nucleates off M2 laths (Fig. 5) indicating it may have formed through recrystallization/reprecipitation of M2. Feldspars ubiquitously contain <5 μm dissolution pits, which may be infilled by accessory minerals such as sulfides, fluorite, barite, and zircon. Albite is strongly altered to Il5b illite in most samples. K-feldspars are lightly-moderately altered to Il5b. Muscovite is commonly weakly altered to illite, and to a lesser extent chlorite, along cleavage planes and grain margins, while biotite is universally strongly altered to chlorite. M3 is more strongly altered than M2. Uranothorite, and more rarely molybdenite, locally occur along cleavage planes in moderately chlorite-altered muscovite (AM2) laths and chlorite. A single ~15 μm grain of uraninite was observed within a cleavage plane in M2 hosted in an albitized granitic dyke in the End Deposit (Fig 6a).

Granitic rocks have been subject to hematization, bleaching, and late geothite-hematite alteration similar to what is observed in the clastic metasedimentary rocks. Bleaching is locally associated with U1c polymetallic veins and U1b uraninite which locally replaces AM2 laths (Fig. 6b,c). Although still subordinate to illite, sudoite is more common in beached granitic rocks than bleached clastic metasedimentary rocks.

4.1.6. Epiclastic Rocks

Epiclastic rocks, only observed in the Kiggavik Deposit, consist mainly of quartz and lightly to moderately illite-altered muscovite (AM1) with subordinate K-feldspar and plagioclase. Epiclastic rocks are composed of up to 30% rounded, mosaic texture quartz clasts up to 3mm in size. Foliation, defined by elongate AM1 laths, wraps around these clasts. Feldspars have been moderately-strongly altered to Il1 illite. Epiclastic rocks have been subject to

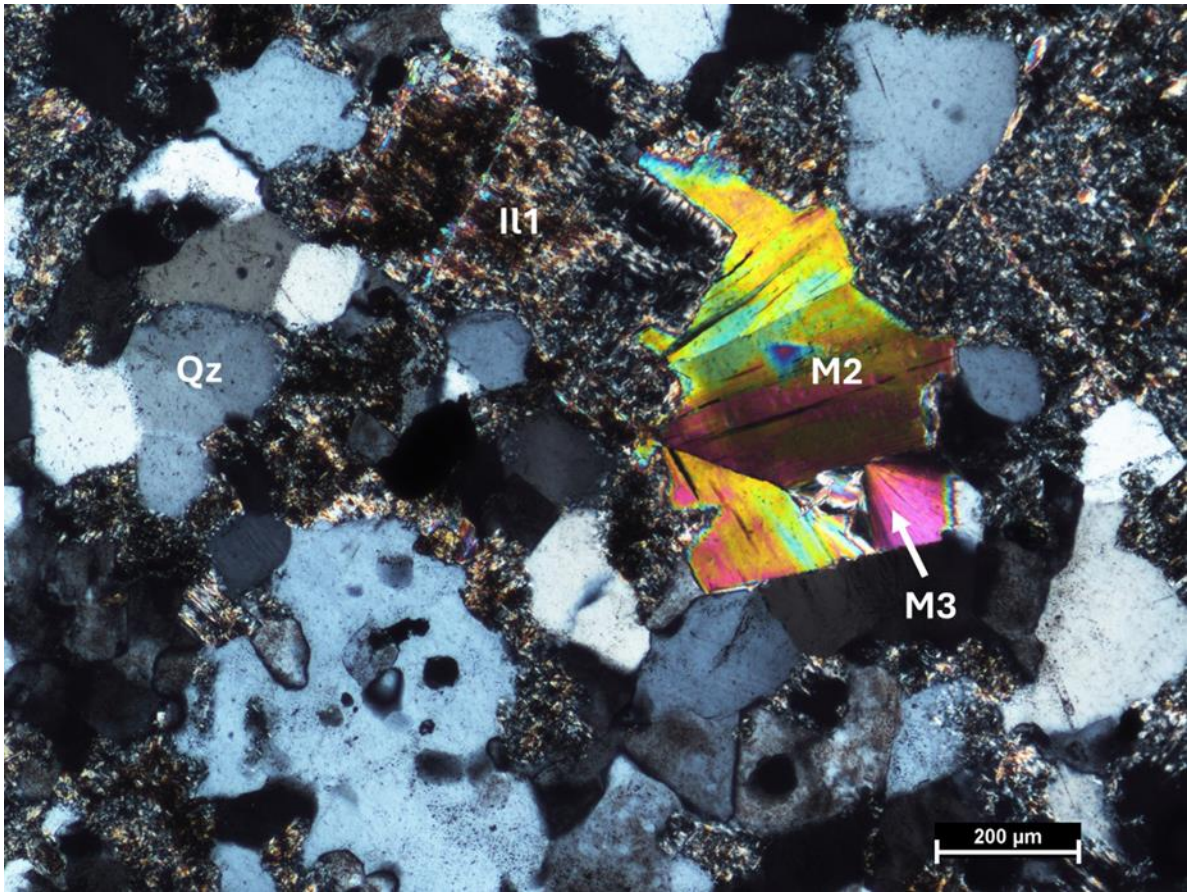

Figure 5. Cross polarized light image of unaltered M2 muscovite laths, finer-grained, locally radial M3 muscovite, and very strongly illite (Il1)-altered K-feldspar (MZ-10-01-106.7). Qz = quartz.

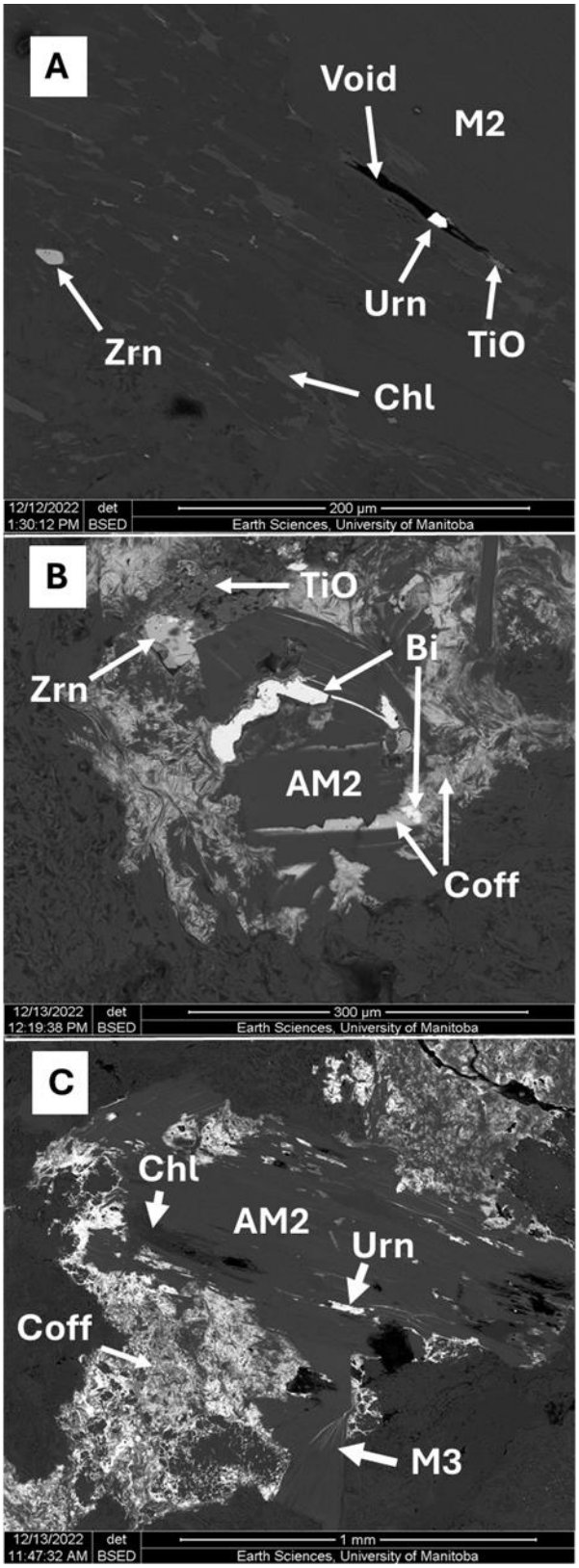
A
Void
M2
Urn
TiO
Zrn
Chl
12/12/2022
1:30:12 PM
det
BSED
200 µm
Earth Sciences, University of Manitoba
B
TiO
Bi
Zrn
AM2
Coff
12/13/2022
12:19:38 PM
det
BSED
300 µm
Earth Sciences, University of Manitoba
C
Chl
AM2
Urn
Coff
M3
12/13/2022
11:47:32 AM
det
BSED
1 mm
Earth Sciences, University of Manitoba

Figure 6. Backscattered electron images of U-mineralized muscovite in granitic rocks. A. Traces of uraninite and Ti-oxides in a large M2 muscovite lath within an albitzed granitic dyke (END-10-02A-129). B. U1 Coffinite and native Bi infiltrating and replacing altered AM2 muscovite along cleavage planes (LG86-158). C. Uraninite and coffinite partially replacing chlorite-altered AM2 muscovite laths and radial M3 muscovite (LG86-158). Abbreviations: Urn = uraninite, Zrn = zircon, TiO = Ti-oxide, Chl = chlorite, void = open pore space, Coff = coffinite, Bi = native bismuth.

hematization and bleaching similar to clastic metasedimentary rocks in the area, however no mineralized epiclastic rocks were observed and the limited number of epiclastic rocks observed prevents more though characterization of alteration to these rocks.

4.2. Ar-Ar Geochronology

Lightly altered M1 muscovite from non-hydrothermally altered clastic metasedimentary rocks yields Ar-Ar ages ranging from 1770.5 ± 10.1 to 1853.9 ± 7.5 Ma (Fig. 7a). These ages cluster between ~1814-1830 Ma. Course-grained M2 laths in albitized Kiggavik granitic rocks, as well as a texturally similar granitic dyke in the End Deposit, yield Ar-Ar ages ranging from 1809.9 ± 7.4 to 1895.2 ± 13.9 Ma (Fig. 7a; Table A1). These ages are strongly clustered between ~1820-1827 Ma. Although the granitic dyke contained a trace amount of uraninite, these rocks are essentially unmineralized.

Ar-Ar ages of AM2 muscovite laths in bleached, U1c mineralized granitic rocks have a wide range of ages from 1591.7 ± 19.8 to 1839.3 ± 20.9 Ma (Fig. 7a). Massive Il3b illite gives Ar-Ar dates ranging from 455.3 ± 5.5 to 1713.6 ± 36.9Ma (fig. 7b,c). Il4 Illite yields Ar-Ar ages ranging from 1469.7 ± 18.4 to 1654.5 ± 46.8 Ma (Fig. 7b,c). While these ages vary significantly, they cluster between ~1493 and 1507 Ma. Il5a Illite yield Ar-Ar ages ranging from 1413.0 ± 12.8to 1517.8 ± 13.8 Ma (Fig. 7b,c). These ages are overwhelmingly concentrated between ~1416-1444 Ma. Illite in hematized and bleached rocks yielded statistically indistinguishable ages.

4.3. Stable Isotopic Composition of Illites and Muscovites

Stable isotope compositions of illites and muscovites are summarized in Table 1. M1 muscovite in clastic metasedimentary rocks has $\delta^{18}O$ and $\delta^{2}H$ values averaging +7.5 ± 1.8 ‰

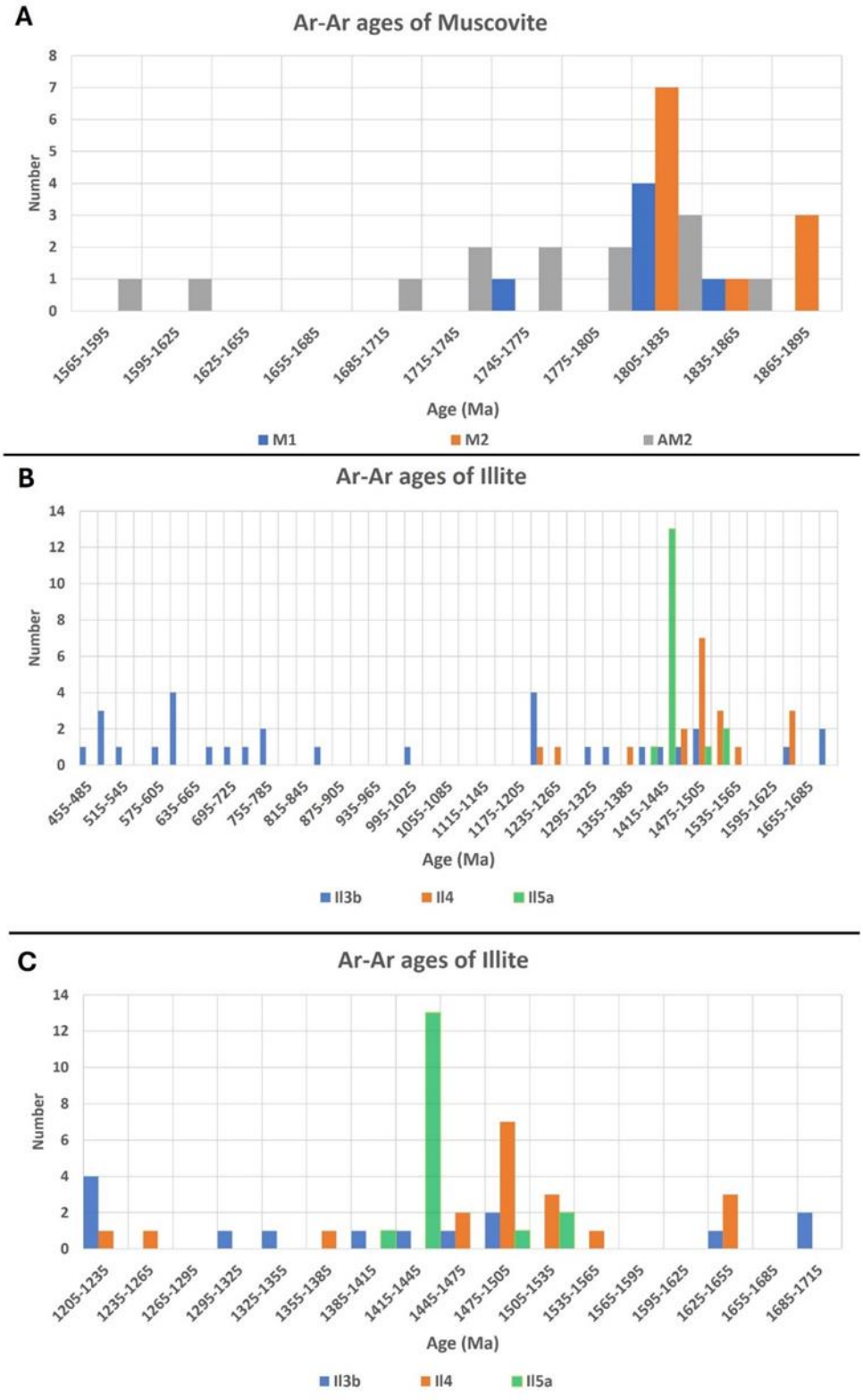
A
Ar-Ar ages of Muscovite
Number
Age (Ma)
1565-1595
1595-1625
1625-1655
1655-1685
1685-1715
1715-1745
1745-1775
1775-1805
1805-1835
1835-1865
1865-1895
M1
M2
AM2
B
Ar-Ar ages of Illite
Number
Age (Ma)
455-485
515-545
575-605
635-665
695-725
755-785
815-845
875-905
935-965
995-1025
1055-1085
1115-1145
1175-1205
1235-1265
1295-1325
1355-1385
1415-1445
1475-1505
1535-1565
1595-1625
1655-1685
Il3b
Il4
Il5a
C
Ar-Ar ages of Illite
Number
Age (Ma)
1205-1235
1235-1265
1265-1295
1295-1325
1325-1355
1355-1385
1385-1415
1415-1445
1445-1475
1475-1505
1505-1535
1535-1565
1565-1595
1595-1625
1625-1655
1655-1685
1685-1715
Il3b
Il4
Il5a

Figure 7. Ar-Ar ages of muscovite and illite in the Kiggavik deposits. A. Ar-Ar ages of muscovites. B. Ar-Ar ages of illite. C. Same as B. zoomed in on the 1205-1715 Ma age range.

Table 1. Stable isotopic composition of phyllosilicate minerals in the Kiggavik Deposits. Abbreviations: Mus = Muscovite, AM = Altered muscovite, Ill = Illite. See text for descriptions of mineral generations.

Drill Hole	Depth (m)	Mineral	Mineral Values		Temperature (°C)	Fluid Values	
			$\delta^{18}O$ (‰; VSMOW)	$\delta^{2}H$ (‰; VSMOW)		$\delta^{18}O$ (‰; VSMOW)	$\delta^{2}H$ (‰; VSMOW)
END-10-02A	400	M1	+10.2	-69.9	400	+7.9	-19.5
END-10-02A	400	M1	+8.9	-90.7	400	+6.5	-40.4
END-10-02A	400	M1	+8.4	-110.6	400	+6.0	-60.3
END-10-02A	400	M1	+9.5	-59.2	400	+7.1	-8.8
EZ-75	321	M1	+4.1	-82.8	400	+1.7	-32.5
EZ-75	321	M1	+5.6	-112.5	400	+3.2	-62.2
RS-11-058	413	M1	+8.4	-64.5	400	+6.1	-14.2
RS-11-058	413	M1	+6.6	-69.1	400	+4.2	-18.8
RS-11-058	413	M1	+6.5	-39.3	400	+4.1	+11.0
Avg		**M1**	**+7.5 ± 1.8**	**-73.8 ± 23.2**	**400**	**+6.4 ± 1.8**	**-44.1 ± 23.2**
MZ-10-01	106.7	M2	+13.3	+127.8	400	+13.3	+149.1
MZ-10-01	106.7	M2	+10.1	+119.2	400	+10.1	+140.4
MZ-10-01	106.7	M2	+9.4	+128.9	400	+9.4	+150.2
MZ-10-01	130	M2	+10.3	+98.2	400	+10.3	+119.5
MZ-10-01	130	M2	+8.6	+112.0	400	+8.6	+133.3
MZ-10-01	90.1	M2	+8.0	+54.8	400	+8.0	+76.0
MZ-10-01	90.1	M2	+13.4	+62.0	400	+13.4	+83.2
Avg		**M2**	**+10.4 ± 2.1**	**+100.4 ± 30.6**	**400**	**+9.3 ± 2.1**	**+130.1 ± 30.6**
MZ-10-01	130	M3	+8.7	-21.0	400	+7.8	+11.7
MZ-10-01	130	M3	+9.6	-3.0	400	+8.7	+29.7
MZ-10-01	90.1	M3	+6.4	+55.2	400	+5.5	+87.9
MZ-10-01	90.1	M3	+8.3	+21.5	400	+7.5	+54.2
MZ-10-01	90.1	M3	+9.5	+5.2	400	+8.7	+37.9
Avg		**M3**	**+8.4 ± 1.3**	**11.6 ± 25.9**	**400**	**+7.2 ± 1.3**	**+43.5 ± 25.9**
EZ-75	290	AM1	+6.9	-52.6	333.4	4.8	-11.6
EZ-75	290	AM1	+7.9	-60.4	333.4	5.8	-19.4

EZ-75	290	AM1	+10.7	-44.2	333.4	8.6	-3.2
Avg		**AM1**	**+8.5 ± 2.0**	**-52.4 ± 8.1**	**333.4**	**+6.4 ± 2.0**	**-11.4 ± 8.1**
LG86	48.3	AM2	+8.9	+112.9	333.4	+6.8	+134.2
LG86	48.3	AM2	+9.6	+42.4	333.4	+7.9	+63.6
Avg		**AM2**	**+9.2 ± 0.5**	**+77.7 ± 49.9**	**333.4**	**+7.1 ± 0.5**	**+118.7 ± 49.9**
MZ-10-01	120	AM3	+6.2	-130.0	333.4	+4.1	-89.0
MZ-10-01	120	AM3	+9.7	-49.1	333.4	+7.6	-8.1
MZ-10-01	120	AM3	+9.2	-80.6	333.4	+7.1	-39.6
Avg		**AM3**	**+8.4 ±1.9**	**-86.6 ± 40.8**	**333.4**	**6.3 ± 1.9**	**-45.6 ± 40.8**
KN-04	15.9	Il1	+18.1	-59.1	333.4	+15.4	-79.1
KN-04	15.9	Il1	+19.1	-31.7	333.4	+16.3	-51.7
KN-04	15.9	Il1	+16.6	-37.6	333.4	+13.9	-57.6
KN-04	15.9	Il1	+14.9	-47.7	333.4	+12.2	-67.7
KN-04	15.9	Il1	+15.5	-117.1	333.4	+12.7	-137.1
Avg		**Il1**	**+16.5 ± 1.8**	**-58.6 ± 34.3**	**333.4**	**+12.3 ± 1.8**	**-78.6 ± 34.3**
Bong-50	292.2	Il3a	+10.1	-44.9	261.0	+5.5	-54.8
Bong-50	292.2	Il3a	+15.6	-52.4	261.0	+11.0	-62.3
Bong-50	292.2	Il3a	+10.4	-13.5	261.0	+5.8	-23.4
Avg		**Il3a**	**+12.0 ± 1.8**	**-36.9 ± 20.6**	**261.0**	**+7.4 ± 1.8**	**-46.8 ± 20.6**
END-09-04	339.1	Il3b	+10.6	-114.3	261.0	+6.0	-124.1
END-09-04	339.1	Il3b	+11.9	-117.3	261.0	+7.3	-127.2
END-09-04	339.1	Il3b	+11.5	-113.2	261.0	+6.9	-123.0
END-09-04	339.1	Il3b	+14.3	-89.9	261.0	+9.7	-99.7
END-09-04	339.1	Il3b	+11.8	-108.0	261.0	+7.1	-117.9
END-09-04	339.1	Il3b	+10.4	-108.0	261.0	+5.8	-117.9
END-09-04	339.1	Il3b	+11.4	-108.0	261.0	+6.8	-117.8
END-09-04	339.1	Il3b	+11.8	-105.5	261.0	+7.2	-115.3
END-11-02	327.8	Il3b	+2.5	-69.3	261.0	-2.2	-79.1
END-11-02	327.8	Il3b	+6.1	-81.9	261.0	+1.5	-91.8
END-11-02	327.8	Il3b	+4.8	-70.7	261.0	+0.2	-80.6
END-11-02	327.8	Il3b	+5.4	-100.5	261.0	+0.8	-110.4

END-34	323.4	Il3b	+11.6	-179.3	261.0	+7.0	-189.1
END-34	323.4	Il3b	+10.8	-157.1	261.0	+6.2	-167.0
END-34	323.4	Il3b	+11.6	-159.9	261.0	+7.0	-169.8
END-34	323.4	Il3b	+11.1	-145.7	261.0	+6.4	-155.6
END-34	323.4	Il3b	+11.7	-145.5	261.0	+7.1	-155.4
Avg		**Il3b**	**+10.0 ± 3.2**	**-116.1 ± 31.6**	**261.0**	**+5.3 ± 3.2**	**-126.0 ± 31.6**
END-09-04	203	Il4	+10.8	+26.2	261.0	+6.1	+16.4
END-09-04	203	Il4	+11.5	+20.3	261.0	+6.9	+10.4
END-09-04	203	Il4	+10.1	+26.0	261.0	+5.4	+16.1
END-09-04	203	Il4	+11.6	+41.9	261.0	+7.0	+32.1
END-09-04	203	Il4	+11.8	+15.3	261.0	+7.2	+5.4
END-09-04	203	Il4	+8.5	+40.6	261.0	+3.8	+30.8
END-09-04	203	Il4	+9.4	+30.1	261.0	+4.7	+20.2
END-09-04	203	Il4	+11.0	+34.7	261.0	+6.4	+24.8
END-09-04	203	Il4	+9.9	+23.1	261.0	+5.3	+13.2
END-09-04	203	Il4	+9.4	+24.0	261.0	+4.8	+14.2
END-09-04	203	Il4	+9.3	+31.2	261.0	+4.6	+21.4
END-09-04	203	Il4	+10.4	+18.5	261.0	+5.8	+8.7
END-09-04	203	Il4	+9.7	+44.1	261.0	+5.1	+34.2
END-09-04	203	Il4	+9.5	+43.1	261.0	+4.9	+33.2
END-09-04	203	Il4	+11.7	+31.0	261.0	+7.0	+21.1
Avg		**Il4**	**+10.3 ± 1.0**	**+30.0 ± 9.3**	**261.0**	**+5.7 ± 1.0**	**+20.1 ± 9.3**
END-09-10	32.35	Il5a	+11.5	-36.4	261.0	+6.9	-46.3
END-09-10	32.35	Il5a	+13.7	-53.4	261.0	+9.1	-63.2
END-09-10	32.35	Il5a	+11.2	-35.8	261.0	+6.6	-45.7
END-09-10	32.35	Il5a	+16.5	-22.6	261.0	+11.9	-32.4
END-09-10	32.35	Il5a	+16.2	-47.4	261.0	+11.6	-57.3
END-09-10	32.35	Il5a	+17.8	-54.0	261.0	+13.2	-63.9
END-09-10	32.35	Il5a	+16.5	-68.9	261.0	+11.9	-78.8
END-09-10	32.35	Il5a	+14.8	-51.0	261.0	+10.2	-60.8
END-09-10	32.35	Il5a	+12.5	-55.9	261.0	+7.8	-65.8

END-09-10	32.35	Il5a	+11.3	-27.9	261.0	+6.7	-37.8
END-09-10	32.35	Il5a	+11.3	-19.9	261.0	+6.7	-29.8
END-09-10	32.35	Il5a	+9.9	-48.3	261.0	+5.3	-58.2
END-09-10	32.35	Il5a	+12.2	-42.3	261.0	+7.6	-52.2
EZ-75	197	Il5a	+10.0	-63.0	261.0	+5.4	-72.8
EZ-75	197	Il5a	+6.5	+4.1	261.0	+1.9	-5.7
EZ-75	197	Il5a	+15.7	-72.5	261.0	+11.1	-82.4
EZ-75	197	Il5a	+8.5	-20.5	261.0	+3.9	-30.4
EZ-75	197	Il5a	+7.6	-21.3	261.0	+3.0	-31.2
EZ-75	197	Il5a	+11.8	-111.9	261.0	+7.2	-121.8
EZ-75	197	Il5a	+12.2	-74.9	261.0	+7.6	-84.7
END-09-02	99.63	Il5a	+12.0	-65.9	261.0	+7.4	-75.7
END-09-02	99.63	Il5a	+11.6	-63.2	261.0	+6.9	-73.1
END-09-02	99.63	Il5a	+10.5	-52.8	261.0	+5.9	-62.6
END-09-02	99.63	Il5a	+13.8	-85.9	261.0	+9.1	-95.7
END-09-02	99.63	Il5a	+15.0	-66.5	261.0	+10.4	-76.4
END-09-02	99.63	Il5a	+12.9	-59.7	261.0	+8.3	-69.6
Avg		Il5a	**+12.4 ± 2.8**	**-50.7 ± 24.4**	**261.0**	**+7.8 ± 2.8**	**-60.5 ± 24.4**
MZ-10-01	106.7	Il5b	+14.3	-68.4	333.4	+11.6	-88.4
MZ-10-01	106.7	Il5b	+6.3	-44.7	333.4	+3.5	-64.7
MZ-10-01	90.1	Il5b	+3.3	-113.5	333.4	+0.6	-133.5
MZ-10-01	90.1	Il5b	+7.5	-131.9	333.4	+4.8	-151.9
MZ-10-01	90.1	Il5b	+8.6	-111.9	333.4	+5.9	-131.9
MZ-10-01	90.1	Il5b	+9.5	-111.4	333.4	+6.8	-131.4
MZ-10-01	90.1	Il5b	+11.7	-122.1	333.4	+9.0	-142.1
MZ-10-01	90.1	Il5b	+9.9	-91.3	333.4	+7.1	-111.3

and –74 ± 23 ‰, respectively. Coarse grained, texturally pristine M2 muscovite laths in Kiggavik granitic rocks have $\delta^{18}O$ and $\delta^{2}H$ values averaging +10.4 ± 2.1 ‰, and +100 ± 12 ‰, respectively. The $\delta^{18}O$ values of finer-grained radial, texturally altered M3 muscovite in Kiggavik granitic rocks average +8.4 ± 1.3 ‰, while $\delta^{2}H$ values average +12 ± 26 ‰.

As no geothermometer is available for muscovite, a temperature must be estimated for formation and/or alteration of muscovite in order to calculate the isotopic composition of the associated fluids. As muscovite generally forms at temperatures greater than 350° C (Vidal et al., 2007) and is interpreted to have formed at lower temperature than the 540-560° C temperature calculated for garnet growth in the Woodburn Lake Group (Pehrsson et al., 2013), we estimated that unaltered muscovite formed at approximately 400° C for purposes of calculating isotopic fractionations. Using the muscovite–water fractionations of Zheng (1993) and Suzuoki and Epstein (1976) for oxygen and hydrogen, respectively, to calculate the $\delta^{18}O$ and $\delta^{2}H$ compositions of the fluid in equilibrium with M1 muscovite in clastic metasedimentary rocks have average $\delta^{18}O$ and $\delta^{2}H$ values of +6.4 ± 1.8 ‰ and –44 ± 23 ‰, respectively (Fig. 8). The average $\delta^{18}O$ of fluids in equilibrium with M2 muscovite laths is +10.2 ± 2.1 ‰, while the average $\delta^{2}H$ value is +130 ± 31 ‰. Fluids in equilibrium with M3 muscovite in Kiggavik granitic rocks have an average $\delta^{18}O$ composition of +7.2 ± 1.3 ‰ and an average $\delta^{2}H$ value of +44 ± 26 ‰.

Coarse-grained illite in epiclastic rocks (Il1) has $\delta^{18}O$ and $\delta^{2}H$ values averaging +16.5 ± 1.8 ‰ and –59 ± 34 ‰, respectively. The $\delta^{18}O$ values of Il3a illite average +12.0 ± 1.8 ‰, and $\delta^{2}H$ values average –37 ± 21 ‰. Il3b illite has $\delta^{18}O$ and $\delta^{2}H$ values averaging +10.0 ± 3.2 ‰ and –116 ± 32 ‰, respectively. Il4 Illite has $\delta^{18}O$ and $\delta^{2}H$ values averaging +10.3 ± 1.0 ‰ and

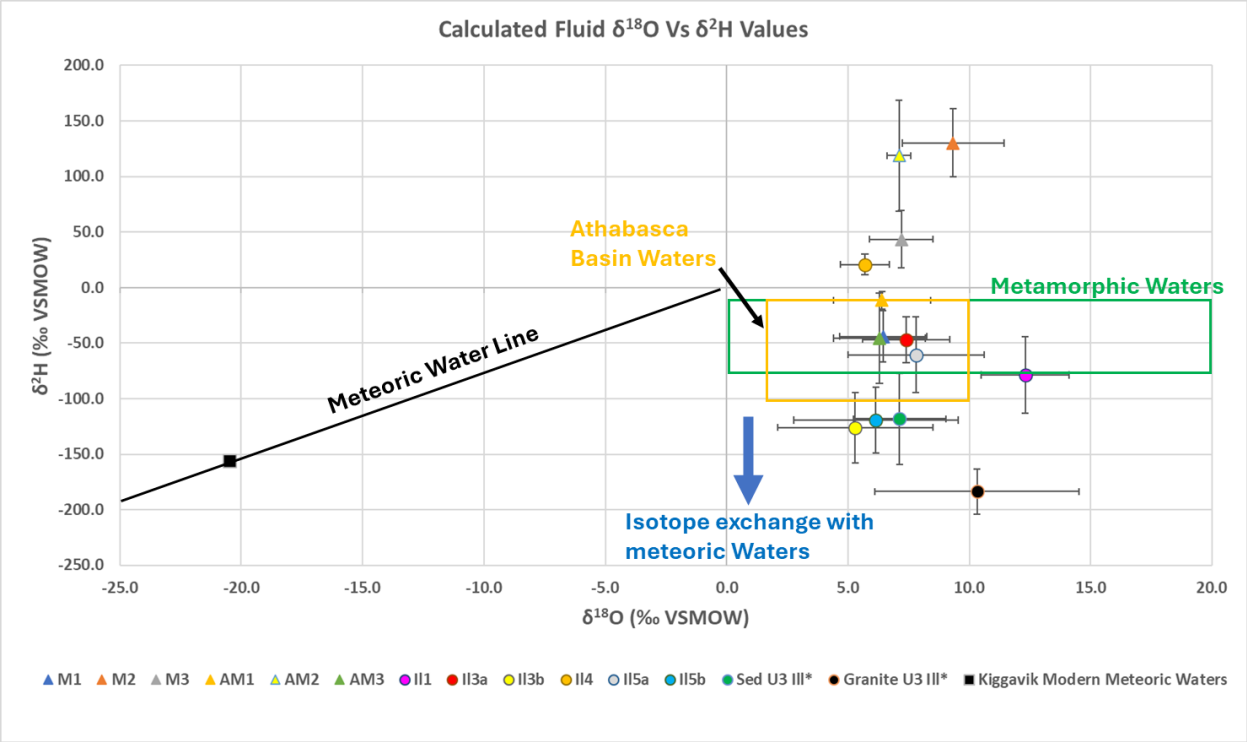

Figure 8. Calculated δ^2H and $\delta^{18}O$ compositions of fluids in equilibrium with phyllosilicate minerals in the Kiggavik Deposits. Meteoric water line from Craig (1961).

+30 ± 9 ‰, respectively. Massive Il5a illite has $\delta^{18}O$ values average +12.4 ± 2.8 ‰, and $\delta^{2}H$ values average –51 ± 24 ‰. No significant differences in isotopic composition were observed between illite in hematized and bleached rocks. Massive illite in Kiggavik granitic rocks (Il5b) has $\delta^{18}O$ values averaging +8.9 ± 3.4 ‰ while $\delta^{2}H$ values average –99 ± 26 ‰.

The $\delta^{18}O$ values of AM1 altered muscovite average +8.5 ± 2.0 ‰ whereas $\delta^{2}H$ values average –52 ± 8 ‰. AM2 altered muscovite has $\delta^{18}O$ and $\delta^{2}H$ values averaging +9.2 ± 0.5 ‰, and +78 ± 50 ‰, respectively. AM3 altered muscovite has $\delta^{18}O$ values averaging +8.4 ± 1.9 ‰, while $\delta^{2}H$ values average –87 ± 41 ‰.

The illite geothermometer of Battaglia (2004) was used to calculate the temperature of illite formation, where:

$$T\ (°C) = 267.95x + 31.50 \quad (1)$$

where $x = K + |Fe–Mg|$ expressed in atoms per formula unit (apfu). Illite and altered muscovite in clastic metasedimentary rocks formed over a range of temperatures, with a main group, observed in all samples and strongly associated with U1 mineralization, averaging 261°C. A secondary group averaging 152°C was observed in a smaller number of more altered samples, some of which were U2/U3 mineralized. These lower temperature illites had lower microprobe totals and exhibited larger deviations from the ideal illite formula relative to the main 261°C group, suggesting they were contaminated by intergrowths of other minerals such as hematite and chlorite. These illites yielding these lower formation temperatures were therefore excluded from isotopic analysis. Illite in granitic and epiclastic rocks formed at a higher temperature, averaging 333.4°C.

Using these temperature estimates, the oxygen isotope illite–water fractionation by Sheppard and Gilg (1996), and the hydrogen isotope illite–water fractionation by Capuano (1992), fluid in equilibrium with Il1has an average $\delta^{18}O$ value of +12.3 ± 1.8 ‰, while $\delta^{2}H$ values are –79 ± 34 ‰. Fluids in equilibrium with Il3a has a calculated average $\delta^{18}O$ composition of +7.4 ± 1.8 ‰, and an average $\delta^{2}H$ value of –47 ± 21 ‰. Fluid in equilibrium with Il3b has average calculated $\delta^{18}O$ and $\delta^{2}H$ values +5.3 ± 3.2 ‰ and –126 ± 32 ‰, respectively. Fluids in equilibrium with Il4 have calculated average $\delta^{18}O$ and $\delta^{2}H$ values of +5.7 ± 1.0 ‰ and +20 ± 9 ‰, respectively. The average $\delta^{18}O$ composition of fluid in equilibrium with Il5a is +7.8 ± 2.8 ‰, while the calculated $\delta^{2}H$ composition of these fluids is –61 ± 24 ‰ (Fig. 8). Fluids in equilibrium with Il5b have calculated average $\delta^{18}O$ and $\delta^{2}H$ values of +6.2 ± 3.4 ‰ and –119 ± 30 ‰, respectively.

The observed alteration of AM1, AM2, and AM3 muscovite is presumably the result of muscovite being broken down by the same fluids which precipitated coeval illite in these rocks. Therefore the temperature of illite precipitation in granitic and epiclastic rocks, 333.4°C, was used for calculating isotopic fractionation for AM1, AM2, and AM3 altered muscovite in granitic and epiclastic rocks. Using this temperature, the average $\delta^{18}O$ value of fluid in equilibrium with AM1 is +6.4 ± 2.0 ‰ whereas the average $\delta^{2}H$ value of this fluid is –11 ± 8 ‰. Fluids in equilibrium with AM2 have average $\delta^{18}O$ values of +7.1 ± 0.5 ‰, while $\delta^{2}H$ values of +119 ± 50 ‰. Fluids in equilibrium with AM3 have average $\delta^{18}O$ values of +6.3 ± 1.9 ‰, while $\delta^{2}H$ values of –46 ± 41 ‰.

5.0 Discussion

5.1. Ar/Ar Geochronology

Approximately 1820-1830 Ma ages commonly obtained from M1 and M2 are somewhat older than the 1782 ± 18 Ma age obtained by Shabaga et al. (2017) for metamorphic muscovite in the Andrew Lake Deposit, but are similar to the U-Pb zircon age of 1806 ± 41 Ma reported by Scott et al. (2015) from the Lone Gull Stock, and to the age of the Hudson granites generally (Peterson et al., 2002; Scott et al., 2015). These ages are also comparable with the 1828 ± 29 Ma age of uraninite within the Lac Cinquante vein-hosted uranium deposit ~200 km south of Kiggavik (Bridge et al., 2013).

Ar-Ar ages obtained from AM2, associated with U1c mineralization, range from 1591.7 ± 19.8 to 1839.3 ± 20.9 Ma. The oldest age is similar to non-mineralized M2 muscovite while the youngest is slightly older than U1 mineralization (Burron et al., 2024), suggesting they formed during albitization and were subsequently partially overprinted and reset during U1 mineralization.

The very large spread of Ar-Ar dates obtained from Il3b illite (~455.3 to 1713.6 Ma) suggests these data represent a mixture between multiple alteration events. While the dates themselves are not considered geologically meaningful, the fact that mineralized areas have apparently been more strongly affected by alteration events than non-mineralized areas is consistent with porous mineralized vein systems having acted as conduits for late, downward-moving fluids (Burron et al, 2025).

The ~1493-1507 Ma ages commonly obtained from Il4 is comparable to the 1476 ± 26 Ma Ar-Ar age obtained from illite associated with mineralization in the End Deposit (Ashcroft,

2020). They are also consistent with the 1520 ± 79 Ma age of uraninite in the Bong Deposit (Sharpe et al., 2015), and 1459 ± 55 Ma uraninite in the End Deposit (Ashcroft, 2020).

The ~1416-1444 Ma ages commonly obtained from Il5a is very similar to ages of 1440 ± 21 and 1417 ± 17 Ma obtained from U2 mineralization (Burron et al., 2024) and is also comparable to the 1476 ± 26 Ma Ar-Ar age of illite in the End Deposit (Ashcroft, 2020). These ~1416-1444 Ma ages are also consistent with the 1434 ± 23 Ma age of fluorite from the Mallory Lake epithermal Au-Ag prospect (Turner 2003), and a 1437 ± 31 Ma age from altered uraninite from the lac Cinquante deposit (Bridge et al., 2013). These ages are also similar to Ar-Ar ages obtained from muscovite (Cloutier et al., 2009) and illite (Alexandre et al., 2009) and U-Pb ages of U-minerals (Fayek et al., 2002) from the Athabasca Basin U deposits.

5.2. Fluid Sources

Fluids in equilibrium with M1 are consistent with either basinal or metamorphic fluids. The fact that the ~1820-1830 Ma age of M1 predates the Thelon Basin, however, suggests a metamorphic origin is much more likely.

To the author's knowledge the δ^2H values of unaltered M2 muscovite in Kiggavik granitic rocks are the highest ever observed in a natural terrestrial mineral, and the fluids they are in equilibrium with have much higher δ^2H than any known geologic fluid. This raises the question of how such fractionated fluids could have formed. A number of geologic processes, such as variations in mineral chemistry, mineral precipitation, exchange with reduced H phases, and phase separation, are capable of causing large (10's-100s ‰) fractionations in hydrogen isotopes (Galley et al., 1972; Suzuoki and Epstein, 1976; Horibe and Craig, 1995; Fayek and Kyser, 1999).

Variations in mineral chemistry, especially Fe content, are known to strongly influence H fractionation factors (Suzuoki and Epstein, 1976). The chemistry of M2 is typical of muscovite, including the lab muscovite RM, in most respects except for an unusually high F content (Table 2). There are no studies on the impact of F contents in muscovite on hydrogen isotope fractionation, however it is deemed unlikely that the presence of ~1.5 wt% more F than typical could solely explain such extreme fractionation. The presence of an unusually high proportion of F relative to OH could, however, potentially make these M2 muscovites more sensitive to other hydrogen isotope fractionation processes by reducing the total amount of H present.

Muscovite, as well as most hydrous minerals, preferentially incorporates ^{1}H (Suzuoki and Epstein, 1976), therefore precipitation of large volumes of hydrous minerals would enrich the residual fluid in ^{2}H (Beaudoin and Chiaradia, 2016). Such a process would create a large amount of paragenetically early hydrous minerals with very low $\delta^{2}H$ values. This is not observed.

Exchange with reduced gases such as H_2S, CH_4, and H_2, could fractionate hydrogen isotopes by 10's-100 ‰ (Galley et al., 1972; Horibe and Craig, 1995). These gases, however, typically account for <1% of fluid volume (Arnórsson, et al., 2007). Producing the magnitude of observed fractionation would therefore require an implausibly large proportion (i.e. an order of magnitude higher than what is normally encountered) of these gases in the precipitating fluid. It is also conceivable that exchange with HF could have caused isotopic fractionation. HF-H_2O fractionation has been suggested to influence the isotopic composition of muscovite in some pegmatites (Taylor et al., 1979); the fractionation between HF and other fluids/minerals, however, has not been well established making testing this scenario impossible with the available data. Furthermore, as the case with exchange with reduced gases, producing the large observed

Table 2. Chemical composition of muscovite and altered muscovite in the Kiggavik Deposits as well as the lab reference material. All data collected via EMPA and reported in wt%. Abbreviations: RM = Reference Material, Mus = Muscovite. See text for descriptions of mineral generations.

Drill Hole	Depth (m)	Mineral	Na_2O	K_2O	CaO	FeO	MgO	MnO	Al_2O_3	SiO_2	TiO_2	PbO	ThO_2	UO_2	Cl	F	Total
RM	-	Mus	0.78	10.32	0	3.01	0.73	0.02	34.10	46.01	0.09	-	-	-	0.00	0.11	95.18
End-09-02A	400	M1	0.45	10.51	0.02	1.87	1.23	0	33.07	46.77	0.53	0	0	0	0	0.11	94.56
End-09-02A	400	M1	0.41	8.64	0.01	2.14	1.62	0	28.64	43.97	0.37	0	0.05	0	0.01	0.19	86.05
End-09-02A	400	M1	0.41	8.74	0	1.48	1.34	0.01	28.54	42.58	0.33	0.02	0.11	0	0	0.12	83.7
End-09-02A	400	M1	0.4	10.76	0	2.11	1.44	0.01	32.62	47.64	0.41	0	0	0	0.01	0.28	95.68
KN-04	106	M2	0.62	9.77	0.19	5.53	3.15	0.08	25.27	45.44	0.56	0.06	0	0	0.06	1.65	92.37
End-09-02A	129	M2	0.24	10.72	0	4.47	1.93	0.05	30.69	45.2	0.62	0.05	0	0	0	0.03	93.99
End-09-02A	129	M2	0.25	10.89	0	4.1	1.91	0.04	30.7	45.8	0.57	0	0.03	0	0.02	0.2	94.51
End-09-02A	129	M2	0.25	10.65	0	4.26	2.01	0.02	30.52	45.62	0.63	0	0.03	0	0.03	0.21	94.23
MZ-10-01	90	M2	0.21	10.19	0.02	3.2	3.19	0.11	24.86	45.13	0.18	0.01	0.02	0	0	1.34	88.43
MZ-10-01	90	M2	0.13	11.04	0.01	4.37	3.63	0.08	24.82	48.71	0.08	0	0	0	0.01	1.46	94.34
MZ-10-01	106	M2	0.13	10.05	0.01	4.41	3.54	0.31	25.61	47.92	0.19	0	0	0	0	2.82	94.98
MZ-10-01	106	M2	0.14	10.71	0.01	4.17	2.42	0.08	28.03	48.6	0.12	0.02	0.05	0	0.02	0.54	94.9
MZ-10-01	90	M3	0.04	7.49	0.21	0.35	5.16	0.04	27.64	49.13	0.02	0.03	0	0	0.08	0.21	90.41
LG-86	48.2	AM2	0.18	9.77	0.02	4.73	3.72	0.31	25.18	46.64	0.36	0	0.1	0	0.01	2.43	93.44
MZ-10-01	120	AM3	0.14	10.76	0.02	5.06	3.25	0.35	26.56	48.09	0.32	0	0	0	0	0.87	95.41
MZ-10-01	120	AM3	0.12	10.01	0.17	2.48	1.76	0.15	30.47	48.86	0.04	0.02	0	0	0.04	0.14	94.25
MZ-10-01	120	AM3	0.07	10.38	0.07	2.24	1.64	0.21	31.32	48.59	0.03	0	0	0	0.01	0.17	94.75

fractionation would likely require an improbably large amount of HF in the system, indicating fractionation due to HF-H_2O/HF-mineral interactions is not a likely explanation for these data.

The most likely explanation for such fractionated fluids is repeated episodes of boiling, phase separation, and condensation. Pressure fluctuations may trigger phase separation in hydrothermal systems, creating highly mobile ^2H enriched vapours (Arnórsson, et al., 2007; Beaudoin and Chiaradia, 2016; Pope et al., 2016; Nuñez-Hernández et al., 2020). Fluids present in fault zones can boil as pressure drops due to the opening of fractures during earthquakes, and resulting vapours may migrate rapidly before condensing as they become trapped in veins and pores when the pressure subsequently returns to higher values (Rossetti et al., 2010; Beaudoin and Chiaradia, 2016). At temperatures above 220° this boiling process will induce a relatively large positive shift in δ^2H values, but only a very small positive shift in $\delta^{18}O$ (Horita et al., 1995; Shmulovich et al., 1999; Nuñez-Hernández et al., 2020). Hydrothermal systems are seismically active areas, frequently experiencing multiple cycles of pressure fluctuations, boiling and condensation (Robert et al., 1995), allowing for large positive shifts in δ^2H to accumulate as the ^2H enriched vapours are repeatedly extracted (Beaudoin and Chiaradia, 2016). Precipitation from such condensed fluids has been invoked to explain fluid δ^2H as high as +30 ‰ (Beaudoin and Chiaradia, 2016).

M2 is commonly concentrated in and around pores (Fig. 9; Burron et al. 2024), which would provide an ideal site for vapours to condense and become trapped. The ~1830-1820 Ma age of M2 is consistent with the Trans-Hudson Orogen, a period of seismic and igneous activity in the Kiggavik region (Peterson et al., 2002; Scott et al., 2015; Grare et al., 2020; Hunter et al., 2021) in which the cycles of boiling and condensation necessary to produce the observed large

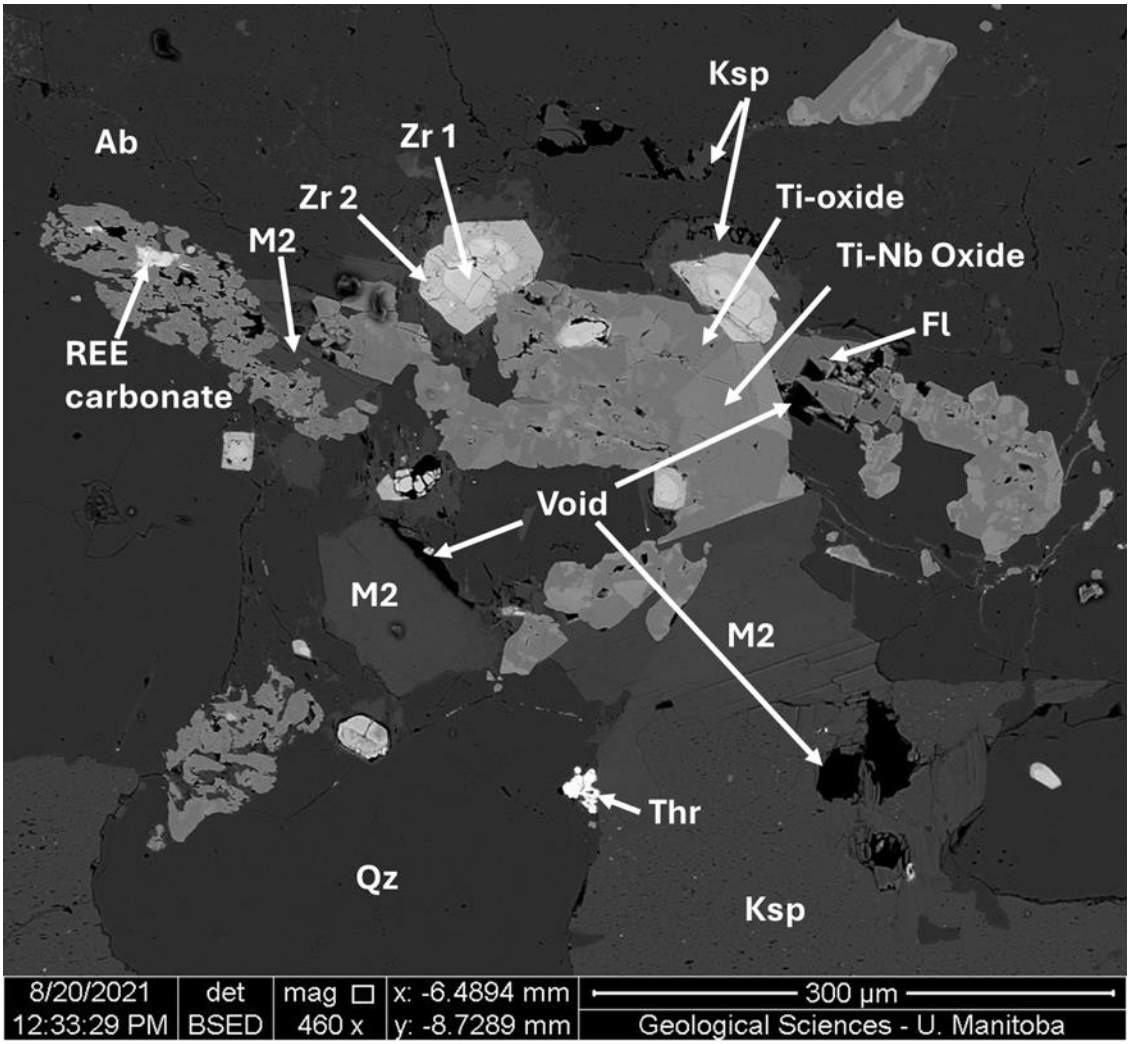

Figure 9. Backscattered electron image of M2 muscovite, together with a wide variety of accessory minerals, which commonly forms in pockets interpreted to have trapped late stage fluids during albitization of granitic rocks (KN04-126). Abbreviations: Qz = quartz, Ab = albite, Ksp = K-feldspar, Zr1 = zoned magmatic zircon, Zr2 = unzoned, Ca-Al-Fe-bearing hydrothermal zircon, Thr = (urano)thorite, Fl = fluorite, Void = open cavity/pore space.

positive shift in δ^2H could have occurred. The massive to comb textures of quartz in fault-parallel extensional veins formed at this time suggest injection of high-pressure fluids following seismic depressurization events (Hunter at al., 2021). The $\delta^{18}O$ composition of this highly fractionated boiled fluid is consistent with derivation from either metamorphic or igneous waters, both of which could have been present in the region at the time of albitization (Grare et al., 2017; Hunter et al., 2021).

The recognition of this mechanism is also of interest to geologic disposal of nuclear waste, as radiation-induced H_2 gas production could also trigger extreme H isotope fractionation (Galley et al., 1972; Smellie and Karlsson, 1996) and this observation establishes a natural mechanism which could explain any extreme fractionation observed at a repository site.

Fluids in equilibrium with M3 have $\delta^{18}O$ and δ^2H values intermediate between those of fluids in equilibrium with M1 and M2, suggesting that M3 may have formed from a mixture of these fluids. Alternatively, it may have precipitated from a late-stage residual of the highly fractionated fluid which had become buffered through fluid-rock interactions, or through isotopically lighter fluids reprecipitating M2.

Stable $\delta^{18}O$ and δ^2H values of fluids in equilibrium with Il1 are consistent with metamorphic fluids; the $\delta^{18}O$ of this fluid, however, is much heavier than the $\delta^{18}O$ of metamorphic fluids precipitating M1 muscovite. This is likely due to buffering through fluid-rock interactions at low water/rock ratios; the breakdown of feldspars replaced by Il1 would have released large amounts of oxygen which likely modified the $\delta^{18}O$ of the fluid which precipitated Il1. This fluid may have had a metamorphic or basinal origin.

Fluids in equilibrium with Il3a and Il5a are isotopically consistent with basinal brines similar to what is observed in Athabasca Basin URU deposits (Kotzer and Kyser, 1995; Alexandre et al., 2005; Cloutier et al., 2009; Ng et al., 2013). These brines are interpreted to be derived from evolved seawater (Kotzer and Kyser, 1995; Alexandre et al., 2005; Ng et al., 2013).

Fluids in equilibrium with Il3b and Il5b have $\delta^{18}O$ values consistent with basinal fluids, but very low $\delta^{2}H$ values interpreted to be the result of overprinting by high latitude meteoric fluids. Such overprinting has previously been reported from metamorphic muscovite (Shabaga et al., 2020) and illite associated with U3 (Burron et al., 2025) in the Kiggavik Deposit. Indeed, the $\delta^{2}H$ of fluids associated with Il3b and Il5b is effectively identical to the $\delta^{2}H$ of fluids associated with U3 illite (Burron et al., 2025). Burron et al. (2025) used the isotopic composition of illite associated with U3, but not the other generations of illite and muscovite studied herein, together with U-Th-Pb geochronology to conclude that U3 formed via sub-glacial meteoric fluids remobilizing U1/U2 minerals over short distances at ~36-471 Ka, with significant implications for geologic disposal of nuclear waste.

Fluids precipitating Il4 likely formed through boiling, phase separation, and condensation, although this occurred at a significantly lower temperature than the boiling and condensation which formed M2 muscovite (261°C vs >400°C). The lower $\delta^{2}H$, relative to M2, of Il4 may reflect these condensed fluids being buffered through interactions with the host rocks surrounding the narrow breccia zone, or it may reflect the lower temperature of Il4 formation. The temperature (261°C) and $\delta^{2}H$ (+20 ± 9 ‰) of fluids precipitating Il4 are similar to those (<280°C and ~-10 to +30 ‰ $\delta^{2}H$, respectively) of seismically boiled, fractionated fluids observed in the Val-d'Or vein field by Beaudoin and Chiaradia (2016).

Intriguingly, fluid inclusion evidence indicates boiling and phase separation occurred during emplacement of the QB (Chi et al., 2017; Grare et al., 2018a) which is understood to postdate albitization (Burron et al., 2024) and predate U mineralization (Chi et al., 2017; Grare et al., 2018a; 2020; Burron et al., 2024). The long-lived fault systems hosting U mineralization at Kiggavik appear to have experienced at least three distinct episodes of boiling and phase separation over a ~300 Ma timespan. Indeed, multiple fluid events of varying origin have been observed throughout the region's ancient and more recent geologic history.

Altered muscovites have isotopic signatures suggesting varying degrees of overprinting. Fluids in equilibrium with AM1 altered muscovite are consistent with metamorphic fluids, suggesting that they have experienced relatively little isotopic resetting. Fluids in equilibrium with AM2 altered muscovite are isotopically similar to fluids associated with M2 muscovite, which is consistent with AM2 being altered from M2 with a low degree of isotopic resetting. Fluids overprinting AM3 altered muscovite associated with U3 in granitic rocks are isotopically consistent with igneous or basinal waters, but their association with U3 in granitic rocks, which is strongly isotopically overprinted (Burron et al., 2025), suggests these may represent M2/M3 overprinted by meteoric fluids.

5.3.0. Genetic Implications

5.3.1. Albitization

The ~1820-1827 Ma age of M2 muscovite, an integral component of albitization, in granitic rocks dates albitization to at or near the time of intrusion of the Hudson granites and large-scale faulting associated with the Trans-Hudson Orogen (Peterson et al., 2002; Scott et al., 2015; Grare et al., 2020; Hunter et al., 2021). Similar ages were obtained from M2 in an albitized

granitic dyke as well as ~1814-1830 Ma M1 in the End Deposit indicating a widespread fluid event in the region at this time.

The age of albitization is effectively identical to the 1828 ± 29 Ma age of U mineralization in the Lac Cinquante uranium deposit, ~200 km south of the Kiggavik deposits (Bridge et al., 2013). Although the Lac Cinquante deposit is distal to Kiggavik deposits, a link between U-mineralization in the two areas has been previously proposed based on the observation of small amounts of polymetallic U mineralization in Kiggavik deposits (Grare et al. 2017; 2020). This mineralization is undated but pre-dates the quartz breccia (Grare et al., 2017; 2020).

The Lac Cinquante deposit has been interpreted as a vein-type U deposit (Bridge et al., 2013) or a Na-metasomatic U deposit (Avery, 2024). Na-metasomatic U deposits are proposed to form as part of MIAC systems (Corriveau et al., 2022a; b; c). Uranium in this deposit occurs in three main forms: 'simple' veins of uraninite associated with pyrite, chalcopyrite, molybdenite, sphalerite, and galena within calcite and albite veins; more complex veins of uraninite associated with brannerite, zircon, fluorapatite, barite, pyrite, chalcopyrite, molybdenite, sphalerite, and galena in calcite and albite veins; and disseminated, fine-grained uraninite with pyrite, chalcopyrite, and hematite throughout the host rock (Avery, 2024). Uranium mineralization was preceded by albitization of host rocks and is related to the emplacement of either the Hudson granites, or, more likely, the Christopher Island minettes (Avery, 2024).

In addition to having similar ages, the albite-rich U-mineralization in the Lac Cinquante deposit bears mineralogical similarities to the albitization observed in the Kiggavik deposits, however it lacks muscovite, which is a major component of albitization in Kiggavik deposits.

This difference may be due to the more mafic character of the host rocks associated with the Lac Cinquante deposit. Mineralization in Lac Cinquante deposit is associated with HFSE mobility, likely indicating the presence of a F-bearing fluid (Avery, 2024), which is similar to the HFSE mobility which occurred during albitization in the Kiggavik deposits (Burron et al., 2024).

The high δ^2H values of M2 muscovite have not been previously described in albitite-hosted or MIAC-U deposits. Indeed, very little δ^2H data are available from these types of deposit. Muscovite in the U-mineralized Wernecke Breccia, Yukon IOCG deposits, however was in equilibrium with waters with δ^2H as high as +27.2 ‰ (Hunt et al., 2011).

The extent of U mineralization developed at this time is a major open question. Polymetallic U mineralization comprising U-oxides, brannerite, uraniferous Ti-phases, and Fe-Cu-Ni sulfides has been observed in multiple Kiggavik deposits and prospects and ascribed to ~1830 Ma based on crosscutting relationships and mineralogical similarity to Lac Cinquante mineralization (Grare et al., 2017; 2018b; 2020). This polymetallic mineralization, however, is mineralogically similar to polymetallic U1c veins, which have been dated to 1553 ± 16 Ma (Burron et al., 2024). Although albitization is associated with a whole-rock enrichment in U and the precipitation of significant amounts of U-bearing uranothorite and zircon (Burron et al., 2024), only traces of U-oxides are observed to be clearly associated with ~1830 Ma albitization in this study. It is highly likely that much of the U precipitated at this stage has been remobilized by subsequent fluid events (Grare et al., 2018b; 2020; Burron et al., 2024; this study).

5.3.2. Main Stage Uranium Mineralization and Resetting Events

Although illite is strongly associated with U mineralization at the Kiggavik deposits (Sharpe et al., 2015; Shabaga et al., 2017; Grare et al., 2020; Burron et al., 2024), the Ar-Ar ages

obtained from illite are not readily correlated to the ages of primary U mineralization. Il3 illite associated with U1 have a wide range of dates that are not considered geologically meaningful. The ~1493-1507 Ma Ar-Ar age of Il4 illite overlaps with the 1520 ± 79 Ma U-Pb age obtained from uraninite in the Bong Deposit (Sharpe et al., 2015); this U-Pb age, however, has a very large uncertainty. Ages of ~1416-1444 Ma commonly obtained from Il4 are broadly similar to ~1400-1475 Ma ages reported from illite and (altered) U mineralization in the region (Farkas, 1984; Aschroft, 2020; Burron et al., 2024) as well as from Athabasca Basin URU deposits (Fayek et al., 2002; Alexandre et al., 2009; Cloutier et al., 2009). These ages post-date 1553 ± 16 Ma U1 mineralization (Burron et al., 2024) and are considered to be the product of a widespread ~1400-1450 Ma isotopic resetting event.

The available stable isotopic evidence suggests two distinct fluids could have been involved in U mineralization: Il3a, Il5a, and Il5b have stable isotope compositions indicating basinal brines, whereas Il4 precipitated from a highly fractionated fluid similar to the one involved in albitization. Both of these fluids could have precipitated U minerals. Highly fractionated fluids are linked to ~1830 Ma albitization and U enrichment (± mineralization) at Kiggavik deposits, while basinal brines are linked to U deposition in the Athabasca Basin (Wilson and Kyser, 1987; Kotzer and Kyser 1995; Fayek and Kyser, 1997; Alexandre et al., 2005; Jefferson et al., 2007; Alexandre et al., 2009; Cloutier et al., 2009; Ng et al., 2013; Martz et al., 2019).

Chi et al. (2017) found fluid inclusion evidence of both high salinity fluids, most likely basinal brines, and low salinity fluids of less certain origin in quartz veins associated with U mineralization. Coexisting vapour-dominated and liquid-dominated fluid inclusions within these

quartz veins indicate phase separation (i.e. boiling and rapid migration of the vapour phase) occurred in this system, possibly as a result of seismic pumping (Chi et al., 2017). This is essentially the same seismically-induced boiling and phase separation process which created fluids precipitating M2 muscovite during albitization and MIAC-U mineralization at ~1830 Ma and Il4 illite at ~1500 Ma. This suggests that the low salinity fluid observed by Chi et al. (2017) may in fact have had a MIAC affinity and could have been U-bearing.

Seismic pumping, combined with heat and/or fluids released by the 1540 ± 30 Ma Kuungmi basalts (Chamberlain et al., 2010), which are temporally linked to U1 mineralization (Burron et al., 2024), could have spurred circulation of an oxidized basinal brine into the basement. While this fluid may have been U-bearing, the fact that the isotopic signature of basinal brines is found primarily in unmineralized areas suggests any U carried by this fluid was sourced from leaching ~1830 Ma albitization and MIAC-U style mineralization. Mixing of this brine with the (potentially U-bearing) fractionated fluid within the fault system and/or seismically induced phase separation events could have triggered U precipitation (Chi et al., 2017).

This phase separation mechanism is more analogous to precipitation mechanisms in epithermal systems than in URU systems (Chi et al., 2017), which would explain the epithermal textures (i.e. comb, crustiform, and euhedral zoned crystals and vuggy porosity) commonly observed in U1c veins (Burron et al., 2024). Fluid mixing, a major component of polymetallic basin-hosted but not necessarily of monometallic basement-hosted URU systems (Fayek and Kyser, 1997; Alexandre et al., 2005; Jefferson et al., 2007), could also explain the polymetallic nature of many U1c veins.

Accessing the relative contribution of specific fluids is complicated by the area's extensive fluid history. Although isotopic evidence for basinal brine is widespread, much of this appears to be the result of post-depositional isotopic resetting at ~1416-1445 Ma. This resetting likely also formed 1440 ± 21 and 1417 ± 17 Ma U2 minerals (Burron et al., 2024).

Il3b illite closely associated with U1b and U1c mineralization has young, scattered Ar-Ar dates, and very low δ^2H values. This is considered to be the result of the naturally permeable vein and fracture networks U mineralization associated with this mineralization (Burron et al., 2024; 2025) acting as a conduit, allowing meteoric waters to infiltrate deeply into the deposits and extensively overprint associated illite (Burron et al., 2025). In some cases, this has resulted in short range remobilization of U, forming U3 (Burron et al., 2025). Il3a, which is not strongly associated with these networks, also yields older, although wide ranging, Ar-Ar dates, suggestive of a variable degree of overprinting.

Il5b has very low δ^2H values, indicating it has been strongly overprinted despite a lack of obvious fracture networks. The observed open porosity within these granitic host rocks may have increased their susceptibility to fluid infiltration. AM3, which is spatially associated with U3 mineralization in granitic rocks also appears to have been isotopically overprinted by meteoric fluids, although the degree of resetting is lesser, most likely due to the larger grain size vs overprinted illite.

5.3.3. Genetic Model

Based on our data, a five-stage genetic model is proposed for the Kiggavik U deposits (Fig. 10):

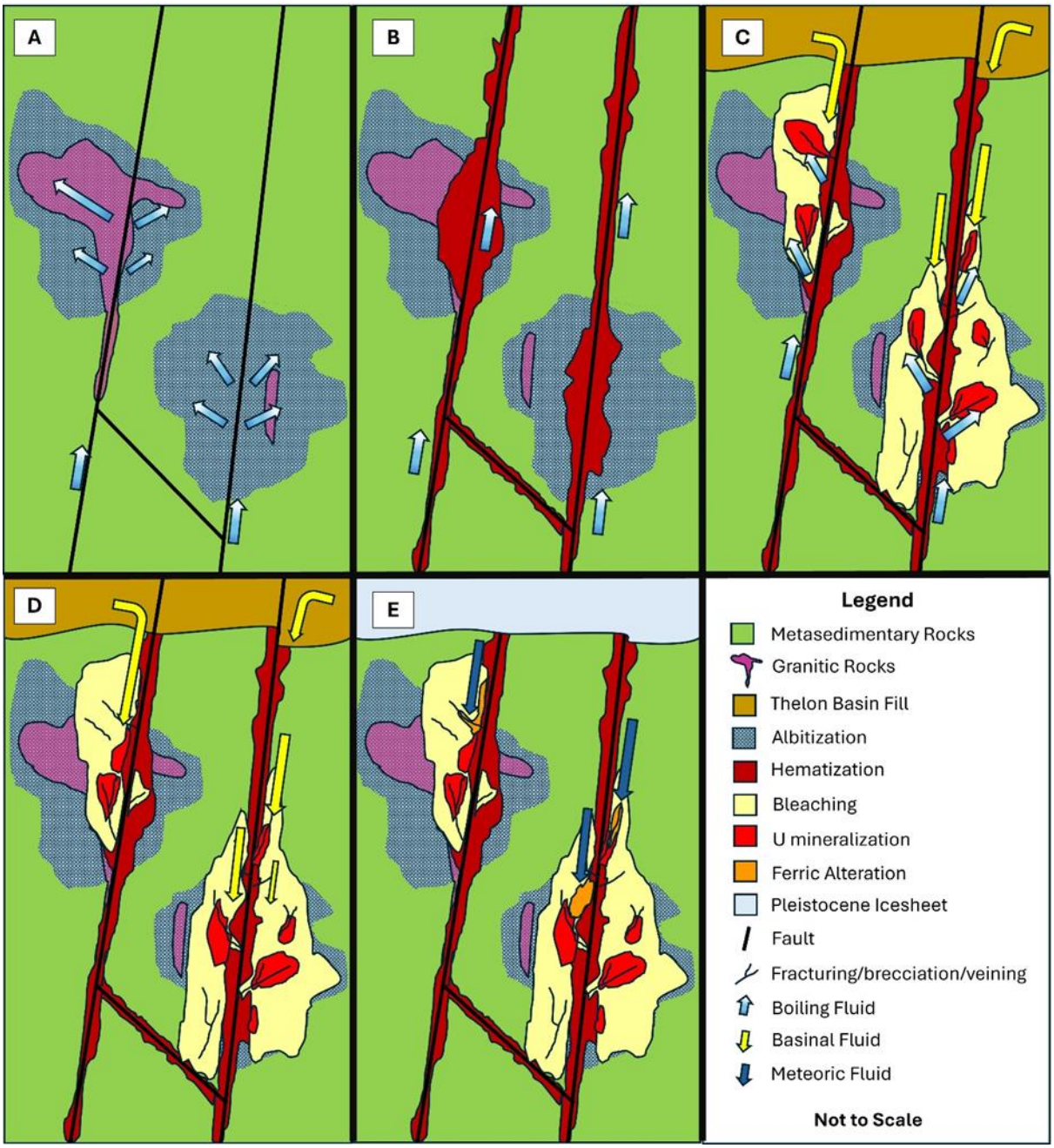
A
B
C
D
E
Legend
Metasedimentary Rocks
Granitic Rocks
Thelon Basin Fill
Albitization
Hematization
Bleaching
U mineralization
Ferric Alteration
Pleistocene Icesheet
Fault
Fracturing/brecciation/veining
Boiling Fluid
Basinal Fluid
Meteoric Fluid
Not to Scale

Figure 10. Genetic model of the Kiggavik deposits. A. Stage 1: ~1830 Ma Albitization and U-enrichment (± U-mineralization) linked to boiling fluids ascending along major faults. B. Stage 2: undated hematization along major faults. C. Stage 3: ~1553 Ma bleaching and U1 mineralization linked to both boiling and basinal fluids. D. Stage 4: ~1450-274 Ma resetting and U remobilization (U2) events linked to basinal fluids and distant tectonic and igneous events. E. Stage 5: ~471 Ka to 36 Ka resetting and minor U remobilization (U3) linked to subglacial meteoric fluids.

The first stage consists of albitization of the host rocks occurring at ~1820-1830 Ma. This albitization shares many attributes of albitite-hosted U deposits developed in MIAC environments (Burron et al., 2024), and the timing is coeval with the Lac Cinquante albitite U deposit (Avery, 2024). Albitization is almost certainly linked to contemporaneous regional igneous activity; either the intrusion of the Hudson phase of the Lone Gull stock, which partially hosts the Kiggavik Deposit, or synchronous ultrapotassic igneous activity, such as the Dubawnt minettes, as has been proposed for the Lac Cinquante deposit albitite U deposit (Avery, 2024). The long-lived regional fault systems which host the Kiggavik deposits have repeatedly acted as conduits for hydrothermal fluids in the region (Grare et al., 2017; 2018a; 2020; Burron et al., 2024).

Large, euhedral M2 muscovite laths in Kiggavik granitic rocks formed during albitization precipitated from highly fractionated fluids which experienced multiple cycles of boiling and condensation, whereas coeval M1 muscovite in clastic metasedimentary formed from metamorphic fluids. Slightly paragenetically later M3 muscovite may have formed from a mixture of these fluids, or (re)precipitation from rock buffered late-stage fluids.

Albitization is associated with a significant enrichment in U (Burron et al., 2024), and the pitchblende and uraniferous titanite present in pre-QB veins and fractures (Grare et al., 2017; 2020) are almost certainly related to albitization. Only remnants of albitization are preserved; it is possible that extensive U-mineralization developed at this time, but also possible that albitization served mainly as ground preparation for subsequent mineralization.

The second stage consists of the emplacement of the QB and associated hematization of host rocks. Phyllosilicates within hematized rocks have been overprinted by later fluid events,

precluding definitive dating of this event. Burron et al. (2024) noted small amounts of muscovite and zircon with hydrothermal textures similar to those associated with albitization within the QB, and suggested that emplacement of the QB may have immediately followed albitization, whereas Grare et al. (2018) ascribed it to a hypothetical hydrothermal system associated with the ~1750 Ma Nueltin granites. The epithermal environment indicated by fluid inclusions (Grare et al., 2018a) indicates a shallow formation depth, which is consistent with the shallow depth of preceding albitization implied by open dissolution pits. This stage is not associated with U enrichment or mineralization, although it may have acted as a U remobilization or secondary ground preparation event (Burron et al., 2024).

The third stage consists of bleaching of host rocks and primary (U1) mineralization. U1 uraninite (Burron et al., 2024) yields an age consistent with the Kuungmi ultrapotassic basalts. The source of U1 mineralizing fluids is, however, not consistent with a simple magmatic source.

Il4 is isotopically consistent with a lower-temperature version of highly fractionated, seismically boiled fluids similar to those involved in albitization. Traces of Bi and U minerals within Il4 suggest a possible link to fluids precipitating polymetallic, locally Bi-bearing, U1c mineralization. The ~1493-1507 Ma Ar-Ar ages of Il4 is younger than the 1553 ± 16 Ma U1 mineralization (Burron et al., 2024) but may not accurately reflect the age of formation due to subsequent overprinting and (partial) resetting. The Kiggavik area may thus have experienced MIAC processes at two distinct time periods, with the first linked to albite-hosted metasomatic U, and the second likely involved in main stage polymetallic U mineralization.

The isotopic composition of Il3a and Il5 is consistent with basinal fluids. The ~1416-1445 Ma Ar-Ar ages of Il5a, however, are much younger than U1 and are similar to the 1440 ±

21 and 1417 ± 17 Ma (Burron et al., 2024) age of some U2 minerals, suggesting the Ar-Ar isotope system of these illites have been isotopically overprinted subsequent to primary mineralization. This could be interpreted to suggest that basinal fluids were involved in U2 but not U1 mineralization; fluid inclusion evidence, however, indicates two distinct fluids, with one experiencing phase separation, associated with U-mineralized veins (Chi et al., 2017). U1 mineralization can thus best be explained by the mixing and boiling of basinal and fractionated, MIAC-linked fluids in a shallow, seismically active environment. This would make Kiggavik a true hybrid between MIAC-U and URU systems, explaining why both models individually struggle to fully explain all of Kiggavik's features.

Stage four consists of multiple overprinting and remobilization events spanning from ~1450 Ma to 274 ± 69 Ma (Sharpe et al., 2015; Chi, et al., 2017; Shabaga et al., 2017; Ashcroft, 2020; Grare et al., 2020; Burron et al., 2024). They are temporally linked to regional igneous and tectonic events (Burron et al., 2024) and are genetically linked to the infiltration of basinal fluids.

Stable isotopes and Ar-Ar ages of illite as well as the occurrence of sudoite, considered to form via the breakdown of ferromagnesian minerals by oxidized basinal brines in Athabasca URU deposits (Ng et al., 2013), in proximity to some U2 minerals (Burron et al., 2024), indicates basinal fluids were involved in major U2 forming alteration events. Such basinal fluids would have been oxidized and likely capable of remobilizing and reconcentrating U deposited during albitization and U1 mineralization. Burron et al. (2025) observed U dissolved by infiltrating oxidized subglacial waters being effectively immobilized and reprecipitated as U3 mineralization by the combination of clay, Ti-oxide, and reduced U and sulfide minerals. If the Kiggavik

deposits were similarly efficient at trapping U during previous U2 basinal fluid circulation events, then these could have served to increase the overall grade of the deposits.

Stage 5 consists of geologically recent isotopic resetting and minor remobilization of U mineralization. This stage forms U3 minerals and associated geothite-bearing ferric alteration. U3 minerals yield U-Th disequilibrium ages of ~471 Ka to 36 Ka, and are linked to the infiltration of subglacial waters during periods of icesheet instability (Burron et al., 2025).

The geologic history of the Kiggavik deposits illustrates the variety of processes which serve to concentrate U in the crust. MIAC processes linked to igneous and seismic events dominated early in the deposit's history, with reconcentration by oxidized basinal and eventually meteoric fluids playing important roles during later stages. The Kiggavik deposits' history of repeated overprinting by fluids may have been essential in enhancing the grade of U mineralization over time.

6.0 Conclusions

M2 Muscovite formed during paragenetically early albitization of granitic rocks in the Kiggavik U deposits is Ar-Ar dated to 1830-1820 Ma, has δ^2H values as high as +129 ‰, and is interpreted to have formed from highly isotopically fractionated fluids produced by multiple cycles of seismically induced boiling, migration, and condensation of fluids. This δ^2H signature is unprecedented, however the timing and mineral assemblage of albitization is consistent with albitite-hosted U deposits developed in a MIAC environment.

Il3a Illite associated with U1a mineralization is isotopically consistent with basinal fluids, while Il4 illite potentially linked to U1c mineralization is isotopically consistent with highly fractionated fluids similar to those involved in albitization. This suggests that both of these fluids

may have been involved in bleaching and primary U1 mineralization; the Ar-Ar ages of these illites are younger than U1 mineralization, however, suggesting they may have been isotopically reset by subsequent alteration events.

Non-mineralized Il5a illite has stable $\delta^{18}O$ and $\delta^{2}H$ values consistent with being in equilibrium with basinal brines, and ages similar to many U2 minerals, indicating that basinal brines contributed to U2 alteration and U remobilization events.

Il3b Illite associated with U1b and U1c mineralization and non-mineralized illite in granitic rocks has very low $\delta^{2}H$ values indicative of overprinting by high-latitude meteoric fluids. Ar-Ar datesF of these illites are widely dispersed and relatively young, indicating high degrees of relatively recent isotopic overprinting due to infiltration of high-latitude meteoric fluids along fracture/vein networks.

While the Ar-Ar date of albitization is consistent with another U-mineralized MIAC environment in the region, the extremely high $\delta^{2}H$ values of M2 muscovite associated with albitization are currently unprecedented. Relatively little $\delta^{2}H$ data from muscovite and illite in MIAC environments is available, and further isotopic studies of these minerals are recommended. If such isotopically fractionated fluids are found to be common in such environments it would provide a useful method for identifying them and provide insights into their formation.

Acknowledgments: This study was conducted as part of the Canadian Nuclear Safety Commission's regulatory research on geologic disposal and was partially funded by an NSERC Alliance grant #ALLRP 556702 – 20. EMPA and SIMS analysis was assisted by Panseok Yang and Ryan Sharpe. We also thank the reviewers, who's feedback greatly improved this manuscript and provided stimulating ideas for further study.

References

Alexandre, P., Kyser, K., Polito, P., and Thomas, D., 2005, Alteration mineralogy and stable isotope geochemistry of paleoproterozoic basement-hosted unconformity-type uranium deposits in the Athabasca Basin, Canada: Economic Geology, v. 100, p. 1547–1563.

Alexandre, P., Kyser, K., Thomas, D., Polito, P., and Marlat, J., 2009, Geochronology of unconformity-related uranium deposits in the Athabasca Basin, Saskatchewan, Canada and their integration in the evolution of the basin: Mineralium Deposita, v. 44, p. 41–59.

Arnórsson, S., Stefánsson, A., and Bjarnason, J. Ö., 2007, Fluid-fluid interactions in geothermal systems: Reviews in Mineralogy and Geochemistry, v. 65, p. 259–312.

AREVA Resources Canada Inc., 2011, Kiggavik Project EIS: Popular Summary; Tier 1, v. 1, p. 51.

Ashcroft, G., 2020, The geochemistry and geochronology of the End Deposit, NE Thelon region, Nunavut, Canada: insight into the Athabasca Basin's closest relative: MSc thesis, Winnipeg, Canada, University of Manitoba, 217 pages.

Avery, G., 2024, The Source of Uranium for the Lac Cinquante Uranium Deposit, Nunavut, Canada: Honours thesis, Halifax, Canada, Saint Mary's University, 154 pages.

Battaglia, S., 2004, Variations in the chemical composition of illite from five geothermal fields: a possible geothermometer: Clay Minerals, v. 39, p. 501–510.

Beaudoin, G., and Chiaradia, M., 2016, Fluid mixing in orogenic gold deposits: Evidence from the H-O-Sr isotope composition of the Val-d'Or vein field (Abitibi, Canada): Chemical Geology, v. 437, p. 7–18.

Bridge, N. J., Banerjee, N. R., Pehrsson, S., Fayek, M., Finnigan, C. S., Ward, J., and Berry, A., 2013, Lac Cinquante Uranium Deposit, Western Churchill Province, Nunavut, Canada: Exploration and Mining Geology, v. 21, p. 27–50.

Burron, I., Fayek, M., Brown, J., and Quirt, D., 2024, Remnants of a 1.55 Ga Hybrid Between Metasomatic Iron-Alkali-Calcic and Unconformity-Related Uranium Environments in the Kiggavik Region, Nunavut, Canada: Economic Geology, v. 119, p. 1861–1888.

Burron, I., Fayek, M., and Brown, J., 2025, Glaciation-induced radionuclide release: implications for geological disposal of nuclear waste: Geology, https://doi-org.uml.idm.oclc.org/10.1130/G53021.1.

Camacho, A., Lee, J.K.W., Zhao, J., Abdu, Y.A., Fayek, M. and Creaser, R.A., 2020, A test of the interlayer ionic porosity model as a measure of argon diffusivity in trioctahedral micas: Geochimica et Cosmochimica Acta, v. 288, p. 341-368.

Capuano, R.M., 1992, The temperature dependence of hydrogen isotope fractionation between clay minerals and water: evidence from a geopressured system: Geochimica et Cosmochimica Acta, v. 56, p. 2547–2554.

Chamberlain, K.R., Schmitt, A.K, Swapp, S.M., Harrison, T.M., Swoboda-Colberg, N., Bleeker, W., Peterson, T.D., Jefferson, C.W., and Khudoley, A.K., 2010, In situ U–Pb SIMS (IN-SIMS) micro-baddeleyite dating of mafic rocks: Method with examples: Precambrian Research, v. 183, p. 379–387.

Chacko, T., Cole, D. R., and Horita, J., 2001, Equilibrium Oxygen, Hydrogen and Carbon Isotope Fractionation Factors Applicable to Geologic Systems: Reviews in Mineralogy and Geochemistry, v. 43, p. 1–81.

Chi, G., Haid, T., Quirt, D., Fayek, M., Blamey, N., and Chu, H., 2016, Petrography, fluid inclusion analysis, and geochronology of the End uranium deposit, Kiggavik, Nunavut, Canada: Mineralium Deposita, v. 52, p. 211–232.

Cloutier, J., Kyser, K., Olivo, G.R., Alexandre, P., and Halaburda, J., 2009, The Millennium uranium deposit, Athabasca Basin, Saskatchewan, Canada: An atypical basement-hosted unconformity-related uranium deposit: Economic Geology, v. 104, p. 815–840.

Cloutier, J., Kyser, K., Olivo, G. R., Brisbin, D., 2011, Geochemical, isotopic, and geochronlologic constraints on the formation of the Eagle Point basement-hosted uranium deposit, Athabasca Basin, Saskatchewan, Canada and recent remobilization of primary uraninite in secondary structures: Mineralium Deposita, v. 46, p. 35–56.

Corriveau, L., Montreuil, J-F., and Potter, E.G., 2016, Alteration Facies Linkages Among Iron Oxide Copper-Gold, Iron Oxide-Apatite, and Affiliated Deposits in the Great Bear Magmatic Zone, Northwest Territories, Canada: Economic Geology, v. 111, p. 2045–2072.

Corriveau, L., Mumin, A.H., and Potter, E.G., 2022a, Mineral systems with iron oxide copper-gold (Ag-Bi-Co-U-REE) and affiliated deposits: introduction and overview, in Corriveau, L., Potter, E.G. and Mumin, A.H., eds., Mineral systems with iron oxide copper-gold (IOCG) and affiliated deposits: Geological Association of Canada, Special Paper 52, p. 1–26.

Corriveau, L., Montreuil, J.-F., Potter, E.G., Blein, O., and De Toni, A.F., 2022b, Mineral systems with IOCG and affiliated deposits: Part 3 - metal pathways and ore deposit model, *In* Corriveau, L., Potter, E.G., and Mumin, A.H., Eds., Mineral Systems with Iron

Oxide-Copper-Gold (IOCG) and Affiliated Deposits, Special Paper 52: Geological Association of Canada, Ottawa, Canada, p. 89–121.

Corriveau, L., Montreuil, J.-F., De Toni, A.F., Potter, E.G., and Percival, J.B., 2022c, Mapping mineral systems with IOCG and affiliated deposits: a facies approach, in Corriveau, L., Potter, E.G. and Mumin, A.H., eds., Mineral systems with iron oxide copper-gold (IOCG) and affiliated deposits: Geological Association of Canada, Special Paper 52, p. 69–111.

Craig, H., 1961, Isotopic variations in meteoric waters: Science, v. 133, p. 1702–1703.

Dazé, A., Lee, J.K.W., and Villeneuve, M., 2003, An intercalibration study of the Fish Canyon sanidine and biotite 40Ar/39Ar standards and some comments on the age of the Fish Canyon Tuff: Chemical Geology, v. 199, p. 111–127.

Farkas, A., 1984, Mineralogy and host rock alteration of the Lone Gull deposit: Urangesellschaft Internal report.

Fayek, M., and Kyser, K., 1999, Stable Isotope Geochemistry of Uranium Deposits, In Burns, P. C. and Finch, R. (eds) Uranium: Mineralogy, Geochemistry, and the Environment, Reviews in Mineralogy, De Gruyter, v. 38 p.181–220.

Fayek, M., Harrison, T.M., Ewing, R.C., Grove, M., Coath, C.D., 2002, O and Pb isotope analyses of uranium minerals by ion microprobe and U-Pb ages from the Cigar Lake deposit: Chemical Geology, v. 185, p. 205–225.

Fuchs H.D., Hilger W, and Prosser E., 1986, Geology and exploration history of the Lone Gull property: Canadian Institute of Mining and Metallurgy Special Publication 33, p. 286–292.

Fulignati, P., 2020, Clay Minerals in Hydrothermal Systems: Minerals, v. 10, n. 919, doi:10.3390/min10100919.

Gall, Q., Peterson, T.D., and Donaldson, J.A., 1992, Early Proterozoic stratigraphy of the Thelon and Baker Lake basins, District of Keewatin: a proposed revision, In, Current Research, Part C, Geological Survey of Canada Paper 92-1C, p. 129–137.

Galley, M. R., Miller, A. I., Atherly, J. F., and Mohn, M., 1972, GS Physical Process- Physical properties, Chalk River, Ontario, Canada, Atomic Energy of Canada Limited, AECL-4255.

Grare, A., Benedicto, A., Lacombe, O., and Travé, A., 2017, Structural controls on uranium mineralization at the Kiggavik Project (NE Thelon area, Canada): SGA Conference, Quebec, August 2017, 4 pages.

Grare, A., Lacombe, O., Mercadier, J., Benedicto, A., Marie Guilcher, M., Trave, A., Ledru, P., and Robbins, J., 2018a, Fault zone evolution and development of a structural and hydrological barrier: the quartz breccia in the Kiggavik area (Nunavut, Canada) and its control on uranium mineralization: Minerals, v. 8, doi:10.3390/min8080319.

Grare, A., Benedicto, A., Lacombe, O., Trave, A., Ledru, P., Blain, M., and Robbins, J., 2018b, The Contact uranium prospect, Kiggavik project, Nunavut (Canada): Tectonic history, structural constraints and timing of mineralization: Ore Geology Reviews, v. 93, p. 141-167.

Grare, A., Benedicto, A., Mercadier, J., Lacombe, O., Trave, A., Guilcher, M., Richard, A., Ledru, P., Blain, M., Robbins, J., and Lach, P., 2020, Structural controls and metallogenic

model of polyphase uranium mineralization in the Kiggavik area (Nunavut, Canada): Mineralium Deposita, doi:10.1007/s00126-020-00957-x.

Horibe Y., and Craig H., 1995, D/H fractionation in the system methane-hydrogen-water: Geochimica et Cosmochimica Acta, v. 59, p. 5209–5217.

Horita, J., Cole, D.R., and Wesolowski, D.J., 1995, The activity-composition relationship of oxygen and hydrogen isotopes in aqueous salt solutions: III. Vapour-liquid water equilibration NaCl solutions to 350 °C: Geochimica et Cosmochimica Acta, v. 59, p. 1139–1151.

Hunt, J. A., Baker, T., Cleverley, J., Davidson, G. J., Fallick, A. E., and Thorkelson, D. J., 2011, Fluid inclusion and stable isotope constraints on the origin of Wernecke Breccia and associated iron oxide – copper – gold mineralization, Yukon: Canadian Journal of Earth Science, v. 48, p. 1425–1445.

Hunter, R.C., Lafrance, B., Heaman, L.M., and Thomas, D., 2021, Long-lived deformation history recorded along the Precambrian Thelon and Judge Sissons faults, northeastern Thelon Basin, Nunavut: Canadian Journal of Earth Sciences, v. 58, p. 433–457.

Jefferson, C. J., Thomas, D., Quirt, D.H., Mwenifumbo, C.J., and Brisbin, D., 2007, Empirical models for unconformity-associated uranium deposits, *in*, Milkereit, B., ed., Proceedings of Exploration 07: Fifth Decennial International Conference on Mineral Exploration, p. 741–769.

Jefferson, C.W., Pehrsson, S., Peterson, T., Chorlton, L., Davis, W., Keating, P. et al., 2011, Northeast Thelon region geoscience framework—new maps and data for uranium in Nunavut: Geological Survey of Canada Open File 6949, 1 sheet, doi:10.4095/288791.

Johnstone, D., 2017, Lithostratigraphic and structural controls of uranium mineralization in the Kiggavik East Zone, Centre Zone, and Main Zone deposits, Thelon Basin, Nunavut: unpublished MSc. Thesis, University of Regina, 193 p.

Jourdan, F., Verati, C., and Fe´raud, G., 2006, Intercalibration of the Hb3gr 40Ar/39Ar dating standard: Chemical Geology, v. 231, p. 77–189.

Kotzer, T.G. and Kyser, T.K., 1995, Petrogenesis of the Proterozoic Athabasca Basin, northern Saskatchewan, Canada, and its relation to diagenesis, hydrothermal uranium mineralization and paleohydrogeology: Chemical Geology, v. 120, p. 45–89.

Kuiper, K.F., Deino, A., Hilgen, F.J., Krijgsman, W., Renne, R., and Wijbrans, J.R., 2008, Synchronizing Rock Clocks of Earth History: Science, v. 320, p. 500–504.

LeCheminant, A.N., and Heaman, L.M., 1989, Mackenzie igneous events, Canada: Middle Proterozoic hotspot magmatism associated with ocean opening: Earth and Planetary Science Letters, v. 96, p. 38–48.

Lui, R., Hull, S., and Fayek, M., 2010, A new approach to measuring D/H ratios with the Cameca IMS-7f: Surface and Interface Analysis, v. 43, p. 458–461.

Martz, P., Mercadier, J., Cathelineau, M., Boiron, M-C., Quirt, D., Doney, A., Olivier Gerbeaud, O., Wally, E.D., and Ledru, P., 2019, Formation of U-rich mineralizing fluids through basinal brine migration within basement-hosted shear zones: A large-scale study of the

fluid chemistry around the unconformity-related Cigar Lake U deposit (Saskatchewan, Canada): Chemical Geology, v. 508, p. 116–143.

Montreuil, J.-F., Corriveau, L., and Potter, E.G., 2015, Formation of albitite-hosted uranium within IOCG systems: the Southern Breccia, Great Bear magmatic zone, Northwest Territories, Canada: Miner Deposita, v. 50, p., 293–325.

Ng, R., Alexandre, P., and Kyser, K., 2013, Mineralogical and Geochemical Evolution of the Unconformity-Related McArthur River Zone 4 Orebody in the Athabasca Basin, Canada: Implications of a Silicified Zone: Economic Geology, v. 108, p. 1657–1689.

National Institute of Standards and Technology (NIST), 2022, Reference Material 8537 SLAP Standard Light Antarctic Precipitation: https://tsapps.nist.gov/srmext/certificates/8537.pdf (acessed January, 2025).

Nuñez-Hernández, S., Pinti, D. L., López-Hernández, A., Orfan Shouakar-Stash, O., Martínez-Cinco, M. A., Ahmad Abuharara, A., Eissa, M. A., Castro, M. C., and Miguel Ramírez-Montes, M., 2020, Phase segregation, boiling, and reinjection at the Los Azufres Geothermal Field, Mexico, monitored by water stable isotopes, chloride, and enthalpy: Journal of Volcanology and Geothermal Research, v., 320, doi /10.1016/j.jvolgeores.2019.1067510377-0273/.

Orrell, S.E., Bickford, M.E., and Lewry, J.F., 1999, Crustal evolution and age of thermotectonic reworking in the western hinterland of Trans-Hudson Orogen, northern Saskatchewan: Precambrian Research, v., 95, p. 187–223.

Pehrsson, S.J., Berman, R.G., and Davis, W.J., 2013, Paleoproterozoic orogenesis during Nuna aggregation: A case study of reworking of the Rae craton, Woodburn Lake, Nunavut: Precambrian Research, v. 232, p. 167–188.

Peterson, T.D., Van Breeman, O., Sandeman, H., and Cousens, B., 2002, Proterozoic (1.85-1.75 Ga) igneous suites of the Western Churchill Province: granitoid and ultrapotassic magmatism in a reworked Archean hinterland: Precambrian Research, v. 119, p. 73–100.

Peterson, T.D., 2006, Geology of the Dubawnt Lake area, Nunavut-Northwest Territories: Geological Survey of Canada Bulletin 580:51.

Peterson, T.D., Jefferson, C.W., and Anand, A., 2015, Geological setting and geochemistry of the ca. 2.6 Ga Snow Island Suite in the central Rae Domain of the Western Churchill Province, Nunavut: Geological Survey of Canada, Open File 7841, 29 p., doi:10.4095/296599.

Polito, P.A., Kyser, K., and Stanley, C., 2009, The Proterozoic, albitite-hosted, Valhalla uranium deposit, Queensland, Australia: a description of the alteration assemblage associated with uranium mineralization in diamond drill hole V39: Miner Deposita, v. 44, p. 11–40.

Pope, E. C., Bird, D. K., Arnórsson, S., Giroud, N., 2016, Hydrogeology of the Krafla geothermal system, northeast Iceland: Geofluids, v. 16, p. 175–197. doi.org/https://doi.org/10.1111/gfl.12142.

Ramaekers, P., 2004, Development, stratigraphy and summary diagenetic history of the Athabasca Basin, early Proterozoic of Alberta and its relation to uranium potential: Alberta Geological Survey Special Report, v. 62, p. 85.

Rainbird, R.H., Hadlari, T., Aspler, L.B., Donaldson, J.A., LeCheminant, A.N., and Peterson, T.D., 2003, Sequence stratigraphy and evolution of the Paleoproterozoic intracontinental Baker Lake and Thelon basins, western Churchill Province, Nunavut, Canada: Precambrian Research, v. 125 p. 21–53, doi:10.1016/S0301-9268(03)00076-7.

Rainbird, R.H., and Davis, W.J., 2007, U-Pb detrital zircon geochronology and provenance of the late Paleoproterozoic Dubawnt Supergroup: linking sedimentation with tectonic reworking of the western Churchill Province, Canada: Geological Society of America Bulletin, v. 119, p. 314–328.

Rainbird, R.H., Davis, W.J., Pehrsson, S.J., Wodicka, N., Rayner, N., and Skulski, T., 2010, Early Paleoproterozoic supracrustal assemblages of the Rae domain, Nunavut, Canada: intracratonic basin development during supercontinent break-up and assembly: Precambrian Research, v. 181, p. 167–186. doi:10.1016/j.precamres.2010.06.005.

Renac, C., Kyser, T.K., Durocher, K., Dreaver, G., and O'Connor, T., 2002, Comparison of diagenetic fluids in the Proterozoic Thelon and Athabasca Basins, Canada: implications for protracted fluid histories in stable intracratonic basins: Canadian Journal of Earth Sciences, v. 39, p. 113–132.

Riciputi, L.R., Paterson, B.A., and Ripperdan R.L., 1998, Measurement of light stable isotope ratios by SIMS: Matrix effects for oxygen, carbon, and sulfur isotopes in minerals: International Journal of Mass Spectrometry, v. 178, p. 81–112.

Riegler, T., Lescuyer, J-L., Wollenburg, P., Quirt, D., and Beaufort, D., 2014, Alteration related to uranium deposits in the Kiggavik-Andrew Lake Structural Trend, Nunavut, Canada: New

insights from petrography and clay mineralogy: The Canadian Mineralogist, v. 52, p. 27–45.

Riegler, T., Beaufort, M-F., Allard, T., Pierson-Wickmann, A-C., and Beaufort, D., 2016, Nanoscale relationships between uranium and carbonaceous material in alteration halos around unconformity-related uranium deposits of the Kiggavik camp, Paleoproterozoic Thelon Basin, Nunavut, Canada: Ore Geology Reviews, v. 79, p. 382–391.

Robert, F., Boullier, A.-M., and Firdaous, K., 1995, Gold-quartz veins in metamorphic terranes and their bearing on the role of fluids in faulting: Journal of Geophysical Research, v. 100, p. 12861–12879.

Rossetti, F., Aldega, L., Tecce, F., Balsamo, F., Billi, A., and Brilli, M., 2010, Fluid flow within the damage zone of the Boccheggiano extensional fault (Larderello–Travale geothermal field, central Italy): structures, alteration and implications for hydrothermal mineralization in extensional setting: Geological Magazine, v. 148, n. 4, p. 558–579.

Scott, J.M.J., Peterson, T.D., and McCurdy, M.W., 2012, U, Th, and REE occurrences within Nueltin granite at Nueltin Lake, Nunavut: recent observations; Geological Survey of Canada, Current Research 2012-1, 11 p., doi: 10.4095/289393.

Scott, J.M.J., Peterson, T.D., Davis, W.J., Jefferson, C.W., and Cousens, B.L., 2015, Petrology and Geochronology of Paleoproterozoic intrusive rocks, Kiggavik uranium camp, Nunavut: Canadian Journal of Earth Sciences, v. 52, p. 494–518.

Shabaga, B.M., Fayek, M., Quirt, D., Jefferson, C.W., and Camacho, A., 2017, Mineralogy, geochronology, and genesis of the Andrew Lake uranium deposit, Thelon Basin, Nunavut, Canada: Canadian Journal of Earth Sciences, v. 54, p. 850–868.

Shabaga, B.M., Fayek, M., Quirt, D., Jefferson, C.W., and Ledru, P., 2020, Geochemistry and geochronology of the Kiggavik uranium deposit, Nunavut, Canada: Mineralium Deposita, doi:10.1007/s00126-020-01001-8.

Sharpe, R., Fayek, M., Quirt, D., and Jefferson, C., 2015, Geochronology and Genesis of the Bong Uranium Deposit, Thelon Basin, Nunavut, Canada: Economic Geology, v. 110, p. 1759–1777.

Sharp, Z. D., 2017, Principles of Stable Isotope Geochemistry, 2nd edition, doi: https://doi.org/10.25844/h9q1-0p82.

Sheahan, K., Fayek, M., Quirt, D., and Jefferson, C. W., 2016, A Combined Ingress-Egress Model for the Kianna Unconformity-Related Uranium Deposit, Shea Creek Project, Athabasca Basin, Canada: Economic Geology, v. 111, p. 225–257.

Sheppard, S. M. F., and Gilg, H. A., 1996, Stable isotope geochemistry of clay minerals: Clay Minerals, v. 31, p. 1–24.

Shmulovich, K. I., Landwehr, D., Simon, K., and Heinrich, W., 1999, Stable isotope fractionation between liquid and vapour in water–salt systems up to 600°C: Chemical Geology, v. 157 p. 343–354.

Smellie, J. and Karllson, F., 1996, A reappraisal of some Cigar Lake issues of importance to performance assessment. SKB Technical Report 96-08.

Steiger, R.H., and Jäger, E. 1977, Subcommission on geochronology: convention on the use of decay constants in geo- and cosmochronology: Earth and Planetary Science Letters, v. 36, p. 359–362.

Suzuoki, T., and Epstein, S., 1976, Hydrogen isotope fractionation between OH-bearing minerals and water: Geochimica et Comochim Acta. v. 40, p. 1229–1240.

Taylor, B. E., Foord, E. E., and Friedrichsen, H., 1979, Stable Isotope and Fluid Inclusion Studies of GEM-Bearing Granitic Pegmatite-Aplite Dikes, San Diego Co., California: Contributions to Mineralogy and Petrology. v. 68, p. 187-205.

Turner, W.A., Heaman, L.M., and Creaser, R.A., 2003, Sm–Nd fluorite dating of Proterozoic low-sulfidation epithermal Au–Ag deposits and U–Pb zircon dating of host rocks at Mallery Lake, Nunavut, Canada: Canadian Journal of Earth Sciences, v. 40, p. 1789–1804.

Vidal, O., Baldeyrou, A., Dubac, B., DeAndrade, V., Jullien, M., and Lanson, B., 2007, Thermodynamics of phyllosilicates and low temperature thermometry: Seminarios de la SEM, v. 3, p. 79–84.

Wilde, A., Otto, A., Jory, J., MacRae, C., Pownceby, M., Wilson, N., and Torpy, A., 2013, Geology and Mineralogy of Uranium Deposits from Mount Isa, Australia: Implications for Albitite Uranium Deposit Models: Minerals, v. 3, p. 258–283.

Wilson, M. R., and Kyser, T. K., 1987, Stable Isotope Geochemistry of Alteration Associated with the Key Lake Uranium Deposit, Canada: Economic Geology, v. 82, p. 1540–1557.

Zhang, C., Cai, Y.-Q., Dong, Q., and Xu, H., 2019, Cretaceous–Neogene basin control on the formation of uranium deposits in South China: evidence from geology, mineralization ages, and H–O isotopes: International Geology Reviews, v. 62, n. 3, p. 263–310.

Zheng, Y.F., 1993, Calculation of oxygen isotope fractionation in hydroxyl-bearing silicates: Earth and Planetary Science Letters, v. 120, p. 247–263.

Table A1. Ar-Ar isotopic data from phyllosilicates in the Kiggavik Deposits. See text for descriptions of mineral generations.

Drill Hole	Depth (m)	Mineral	Age (Ma)	±1σ (Ma)	Cum. $\%^{39}Ar$	$\%^{40}Ar$*	$^{39}Ar/^{40}Ar$	±1σ	$^{36}Ar/^{40}Ar$	±1σ	Ca/K	±1σ	Cl/K	±1σ
END-10-02A	400	M1	1814.4	9.5	13.09	98.82	9.59E-03	7.95E-05	3.99E-05	1.86E-06	-0.97	0.66	0.03	0.03
END-10-02A	400	M1	1770.5	10.1	25.67	94.78	9.56E-03	8.53E-05	1.77E-04	3.05E-06	0.64	0.68	0.00	0.03
END-10-02A	400	M1	1822.4	7.5	42.76	98.29	9.47E-03	6.17E-05	5.78E-05	1.70E-06	-0.89	0.51	-0.02	0.02
END-10-02A	400	M1	1830.3	6.9	61.90	96.84	9.27E-03	5.57E-05	1.07E-04	1.73E-06	0.04	0.44	0.01	0.02
END-10-02A	400	M1	1853.9	7.5	81.82	99.53	9.33E-03	6.03E-05	1.60E-05	1.07E-06	0.88	0.43	-0.01	0.02
END-10-02A	400	M1	1827.3	7.3	100.00	99.54	9.55E-03	6.07E-05	1.54E-05	1.21E-06	-0.57	0.45	-0.02	0.02
MZ-10-01	130	M2	1825.6	10.4	11.78	99.79	9.59E-03	8.71E-05	7.13E-06	1.55E-06	0.14	0.67	0.00	0.03
MZ-10-01	130	M2	1820.1	6.2	31.38	99.57	9.61E-03	5.22E-05	1.46E-05	1.07E-06	-0.22	0.42	0.00	0.02
MZ-10-01	130	M2	1823.2	6.4	51.60	99.87	9.62E-03	5.36E-05	4.50E-06	9.53E-07	0.66	0.43	0.02	0.02
MZ-10-01	130	M2	1809.9	7.4	67.65	99.43	9.69E-03	6.29E-05	1.94E-05	1.34E-06	-1.43	0.44	-0.01	0.02
MZ-10-01	130	M2	1820.5	6.6	86.85	99.23	9.58E-03	5.54E-05	2.62E-05	1.22E-06	-0.53	0.43	0.05	0.02
END-10-02A	129	M2	1819.6	9.3	20.52	99.90	9.61E-03	7.77E-05	3.25E-06	1.42E-06	-0.48	0.62	-0.01	0.03
END-10-02A	129	M2	1844.6	10.4	40.64	99.97	9.41E-03	8.44E-05	1.09E-06	1.41E-06	-0.54	0.65	-0.02	0.03
END-10-02A	129	M2	1827.3	15.5	53.57	99.78	9.54E-03	1.29E-04	7.28E-06	2.24E-06	0.09	1.07	0.05	0.04
END-10-02A	129	M2	1888.1	13.8	69.17	99.92	9.06E-03	1.06E-04	2.73E-06	1.79E-06	0.40	0.93	0.01	0.04
END-10-02A	129	M2	1888.6	11.9	85.43	99.79	9.05E-03	9.20E-05	7.22E-06	1.67E-06	-1.54	0.86	-0.03	0.04
END-10-02A	129	M2	1895.2	13.9	100.00	99.94	9.01E-03	1.06E-04	1.97E-06	1.79E-06	-1.35	0.97	-0.07	0.04
LG86	48.3	AM2	1591.7	19.8	8.06	94.73	1.12E-02	2.09E-04	1.78E-04	5.47E-06	-2.29	1.37	0.02	0.06
LG86	48.3	AM2	1723.0	15.1	18.80	98.83	1.04E-02	1.41E-04	3.97E-05	2.94E-06	1.32	1.07	0.09	0.05
LG86	48.3	AM2	1610.3	12.6	31.48	94.70	1.10E-02	1.30E-04	1.79E-04	3.77E-06	1.30	0.94	-0.15	0.04
LG86	48.3	AM2	1786.0	18.0	41.56	94.32	9.35E-03	1.47E-04	1.92E-04	3.91E-06	0.02	1.16	-0.03	0.05
LG86	48.3	AM2	1711.3	19.0	50.78	97.66	1.03E-02	1.77E-04	7.92E-05	3.54E-06	1.68	1.22	0.02	0.06
LG86	48.3	AM2	1799.5	17.8	60.24	97.65	9.56E-03	1.49E-04	7.94E-05	3.55E-06	0.06	1.26	-0.05	0.06
LG86	48.3	AM2	1750.6	23.4	67.71	94.56	9.67E-03	2.01E-04	1.84E-04	4.83E-06	1.01	1.56	0.04	0.07
LG86	48.3	AM2	1832.6	18.0	77.16	99.43	9.46E-03	1.48E-04	1.94E-05	2.71E-06	-1.62	1.25	-0.15	0.06
LG86	48.3	AM2	1808.5	18.9	15.54	97.29	9.45E-03	1.56E-04	9.17E-05	3.75E-06	0.58	1.71	0.04	0.05
LG86	48.3	AM2	1746.1	17.9	31.27	95.55	9.81E-03	1.56E-04	1.51E-04	4.03E-06	0.66	1.58	-0.03	0.06
LG86	48.3	AM2	1810.8	17.0	46.64	97.96	9.50E-03	1.41E-04	6.89E-05	3.67E-06	1.14	1.62	0.03	0.06

LG86	48.3	AM2	1716.3	18.2	62.55	95.97	1.01E-02	1.66E-04	1.36E-04	4.09E-06	-1.96	1.50	-0.07	0.05
LG86	48.3	AM2	1839.3	20.9	77.95	99.36	9.40E-03	1.70E-04	2.16E-05	3.01E-06	0.38	1.60	0.02	0.05
BONG-50	292	Il3a	1228.9	37.1	13.63	85.80	1.47E-02	6.07E-04	4.80E-04	1.52E-05	-3.15	3.21	-0.06	0.13
BONG-50	292	Il3a	1232.0	33.2	29.84	89.90	1.54E-02	5.68E-04	3.42E-04	1.22E-05	0.35	2.85	-0.15	0.14
BONG-50	292	Il3a	1713.6	36.9	47.07	96.60	1.02E-02	3.39E-04	1.15E-04	6.96E-06	5.23	2.85	0.24	0.12
BONG-50	292	Il3a	1504.4	41.0	62.40	92.52	1.19E-02	4.77E-04	2.53E-04	1.03E-05	7.07	2.93	-0.09	0.12
BONG-50	292	Il3a	1472.4	36.6	78.67	92.82	1.23E-02	4.46E-04	2.43E-04	9.68E-06	-6.73	2.95	-0.10	0.12
BONG-50	292	Il3a	1706.3	31.1	100.00	97.28	1.04E-02	2.90E-04	9.19E-05	6.14E-06	2.53	2.50	0.07	0.09
BONG-50	292	Il3a	1207.3	40.6	8.82	86.19	1.52E-02	6.92E-04	4.67E-04	1.78E-05	-5.60	4.66	0.00	0.17
BONG-50	292	Il3a	1504.5	28.6	23.78	93.46	1.20E-02	3.35E-04	2.21E-04	7.86E-06	-0.54	2.62	0.05	0.10
BONG-50	292	Il3a	1340.4	22.1	41.13	93.50	1.42E-02	3.29E-04	2.20E-04	8.34E-06	0.63	2.35	-0.05	0.08
BONG-50	292	Il3a	1638.4	21.7	59.98	96.98	1.10E-02	2.20E-04	1.02E-04	5.50E-06	0.21	2.04	-0.21	0.07
BONG-50	292	Il3a	1423.2	27.8	73.92	95.04	1.33E-02	3.72E-04	1.68E-04	8.87E-06	-1.23	3.07	-0.06	0.09
BONG-50	292	Il3a	1306.7	28.6	86.90	91.01	1.43E-02	4.37E-04	3.04E-04	1.10E-05	0.69	3.17	-0.02	0.10
BONG-50	292	Il3a	1409.7	28.7	100.00	93.25	1.32E-02	3.84E-04	2.28E-04	9.74E-06	3.42	3.26	0.09	0.10
END-09-04	339	Il3b	351.9	4.6	15.06	59.03	4.61E-02	4.93E-04	1.39E-03	1.84E-05	-1.32	0.72	0.10	0.04
END-09-04	339	Il3b	633.2	5.2	33.62	78.37	3.14E-02	2.81E-04	7.32E-04	1.01E-05	-1.45	0.62	0.00	0.03
END-09-04	339	Il3b	621.9	5.1	51.42	76.14	3.11E-02	2.69E-04	8.07E-04	1.14E-05	0.00	0.67	-0.01	0.03
END-09-04	339	Il3b	575.5	5.9	67.07	75.04	3.36E-02	3.62E-04	8.45E-04	1.23E-05	-0.11	0.78	0.00	0.03
END-09-04	339	Il3b	490.9	5.0	83.96	71.91	3.87E-02	3.90E-04	9.51E-04	1.36E-05	-1.23	0.70	-0.04	0.03
END-09-04	339	Il3b	616.5	5.6	100.00	78.69	3.25E-02	3.08E-04	7.21E-04	1.26E-05	-0.13	0.77	0.08	0.03
END-09-04	339	Il3b	489.2	6.0	24.94	71.35	3.85E-02	4.69E-04	9.69E-04	1.61E-05	0.77	1.34	0.06	0.04
END-09-04	339	Il3b	512.6	6.6	47.58	71.52	3.66E-02	4.66E-04	9.64E-04	1.78E-05	-3.76	1.37	0.00	0.05
END-09-04	339	Il3b	1008.7	8.5	74.78	91.05	2.04E-02	2.20E-04	3.03E-04	6.88E-06	0.67	1.22	-0.01	0.04
END-09-04	339	Il3b	455.3	5.5	100.00	69.94	4.10E-02	4.73E-04	1.02E-03	1.65E-05	3.69	1.19	0.05	0.04
END-09-04	203	Il4	1359.2	30.0	10.55	94.10	1.40E-02	4.39E-04	2.00E-04	8.82E-06	-0.82	2.56	-0.12	0.10
END-09-04	203	Il4	1654.5	46.8	18.14	96.76	1.08E-02	4.65E-04	1.10E-04	9.12E-06	-5.32	3.57	-0.22	0.16
END-09-04	203	Il4	1633.9	30.8	28.97	95.98	1.09E-02	3.12E-04	1.36E-04	6.90E-06	0.42	2.49	0.09	0.10
END-09-04	203	Il4	1650.8	33.2	38.97	95.58	1.07E-02	3.27E-04	1.50E-04	7.44E-06	4.66	2.46	-0.06	0.11
END-09-04	203	Il4	1262.9	34.2	47.75	88.86	1.47E-02	5.50E-04	3.77E-04	1.17E-05	-8.92	3.16	-0.19	0.12
END-09-04	203	Il4	1228.4	44.2	54.86	89.00	1.53E-02	7.54E-04	3.72E-04	1.52E-05	5.32	3.81	0.05	0.15

END-09-04	203	Il4	1504.3	28.5	66.47	99.96	1.29E-02	3.59E-04	1.31E-06	5.58E-06	2.69	2.04	0.25	0.10
END-09-04	203	Il4	1506.0	33.0	76.26	99.43	1.28E-02	4.11E-04	1.93E-05	6.85E-06	-4.15	2.66	0.02	0.11
END-09-04	203	Il4	1499.1	29.5	86.90	99.93	1.29E-02	3.73E-04	2.28E-06	6.52E-06	5.03	2.51	-0.29	0.10
END-09-04	203	Il4	1507.1	23.7	100.00	99.76	1.28E-02	2.96E-04	8.02E-06	5.09E-06	-1.50	2.03	-0.06	0.08
END-09-04	203	Il4	1481.3	19.8	8.38	99.88	1.32E-02	2.56E-04	3.94E-06	5.21E-06	-1.29	2.10	-0.08	0.08
END-09-04	203	Il4	1482.9	18.1	18.77	99.74	1.31E-02	2.33E-04	8.91E-06	4.12E-06	-1.91	1.81	0.08	0.06
END-09-04	203	Il4	1493.5	18.7	29.41	100.01	1.30E-02	2.38E-04	-2.40E-07	4.01E-06	2.48	1.80	0.06	0.06
END-09-04	203	Il4	1545.1	18.0	40.43	99.79	1.23E-02	2.13E-04	7.13E-06	3.71E-06	1.94	1.64	-0.06	0.06
END-09-04	203	Il4	1493.3	13.0	55.09	100.08	1.30E-02	1.67E-04	-2.88E-06	2.93E-06	2.31	1.26	0.01	0.05
END-09-04	203	Il4	1531.4	14.3	68.67	100.01	1.25E-02	1.73E-04	-4.81E-07	3.01E-06	0.98	1.35	0.01	0.05
END-09-04	203	Il4	1469.7	18.4	79.21	99.90	1.33E-02	2.42E-04	3.39E-06	4.13E-06	3.22	1.75	-0.02	0.06
END-09-04	203	Il4	1504.3	15.7	90.57	100.11	1.29E-02	1.98E-04	-3.87E-06	3.82E-06	2.84	1.68	0.09	0.05
END-09-04	203	Il4	1474.1	19.6	100.00	99.67	1.32E-02	2.56E-04	1.10E-05	4.41E-06	-1.84	1.84	0.04	0.07
END-09-10	32.35	Il5a	1427.8	12.3	15.06	100.23	1.39E-02	1.73E-04	-7.74E-06	2.96E-06	1.50	0.98	0.00	0.05
END-09-10	32.35	Il5a	1437.0	9.6	32.40	99.91	1.37E-02	1.33E-04	3.17E-06	2.34E-06	0.30	0.83	-0.01	0.04
END-09-10	32.35	Il5a	1413.0	12.8	46.68	99.86	1.41E-02	1.83E-04	4.84E-06	3.19E-06	-0.27	1.16	0.14	0.04
END-09-10	32.35	Il5a	1416.5	13.3	59.47	100.14	1.41E-02	1.90E-04	-4.69E-06	3.38E-06	1.85	1.23	-0.10	0.05
END-09-10	32.35	Il5a	1422.4	13.2	74.42	99.91	1.40E-02	1.86E-04	3.09E-06	2.85E-06	-1.43	0.96	0.03	0.04
END-09-10	32.35	Il5a	1485.5	14.6	88.40	99.97	1.31E-02	1.88E-04	9.06E-07	2.90E-06	0.28	1.04	-0.04	0.05
END-09-10	32.35	Il5a	1427.5	9.0	10.40	99.97	1.39E-02	1.27E-04	9.45E-07	2.43E-06	0.27	0.76	-0.04	0.03
END-09-10	32.35	Il5a	1443.4	10.6	20.97	99.99	1.37E-02	1.46E-04	2.60E-07	2.15E-06	0.22	0.70	-0.04	0.03
END-09-10	32.35	Il5a	1423.4	7.3	34.32	99.81	1.40E-02	1.03E-04	6.49E-06	1.92E-06	-0.47	0.58	-0.05	0.03
END-09-10	32.35	Il5a	1429.0	9.5	45.03	99.68	1.39E-02	1.33E-04	1.08E-05	2.45E-06	-0.67	0.76	0.01	0.03
END-09-10	32.35	Il5a	1435.2	9.3	56.43	99.84	1.38E-02	1.30E-04	5.41E-06	2.11E-06	-1.33	0.67	-0.03	0.03
END-09-10	32.35	Il5a	1422.4	9.5	67.75	99.82	1.40E-02	1.34E-04	6.03E-06	2.16E-06	-0.19	0.69	0.03	0.03
END-09-10	32.35	Il5a	1444.0	11.9	76.66	100.04	1.37E-02	1.64E-04	-1.22E-06	2.70E-06	-0.36	0.88	-0.03	0.04
END-09-10	32.35	Il5a	1443.1	10.5	86.54	99.97	1.37E-02	1.45E-04	1.14E-06	2.54E-06	-0.38	0.79	-0.01	0.04
END-09-10	32.35	Il5a	1517.8	13.8	94.07	99.88	1.27E-02	1.70E-04	4.05E-06	3.07E-06	1.56	1.03	0.04	0.05
END-09-10	32.35	Il5a	1509.8	18.3	100.00	99.32	1.28E-02	2.27E-04	2.28E-05	3.78E-06	4.19	1.28	0.13	0.06
END-09-10	32.35	Il5a	1426.5	14.9	100.00	99.87	1.39E-02	2.09E-04	4.43E-06	3.79E-06	-2.26	1.33	-0.14	0.06

Chapter 5: The Evolution of Porosity and its Impacts on Radionuclide Mobility in the Kiggavik Analogue

Ian Burron[1], Mostafa Fayek[1], Julie Brown[2], Larry Anovitz[3], and Jan Ilavsky[4]

1: Department of Earth Sciences, University of Manitoba, Winnipeg, MB R3T 2N2, Canada

2: Canadian Nuclear Safety Commission, 280 Slater Street, Ottawa, Ontario K1P 5S9, Canada

3: Chemical Sciences Division, MS 6110, Oak Ridge National Laboratory, Oak Ridge, TN 37830, USA

4: Argonne National Laboratory, 9700 S Cass Avenue, Argonne, IL 60439, USA,

Corresponding author: Ian Burron ianmburron@gmail.com

Abstract

The effects of lithology and alteration on host rock porosity are of crucial importance in understanding the mobility of radionuclides in a deep geologic repository. (Ultra) small angle X-ray scattering measurements of rocks from the Kiggavik uranium (U) deposits, an analogue for a DGR affected by glaciation, indicate unaltered metasedimentary and epiclastic rocks have very low porosity, 0.64 ± 0.09 and 0.44 ± 0.08 %, respectively. Hematization has increased the porosity of metasedimentary rocks by an order of magnitude, while subsequent bleaching has not substantially affected porosity. Albitized granitic rocks have a porosity of 1.11 ± 0.4 %. Hematized granitic rocks have a porosity of 4.54 ± 0.74 % and bleached granitic rocks have a much higher porosity of 12.54 ± 4.42 %. In both metasedimentary and granitic rocks increases in porosity are linked to the replacement of feldspars by illite.

Ferric altered granitic rocks have been affected by geologically recent oxidized subglacial waters, resulting in limited degrees of radionuclide mobility. These rocks have much lower porosity (6.05 ± 2.28) than their bleached protoliths. This reduction in porosity is linked to the precipitation of goethite, calcite, vanadinite, and U-minerals in pore space and fractures. Altered metasedimentary rocks studied as part of the Kiggavik analogue tend to have lower porosity than altered granitic rocks, explaining the lower degree of radionuclide mobility observed in metasedimentary rocks.

While oxidized subglacial fluids are capable of disturbing and mobilizing radionuclides, they also tend to destroy the pathways through which they can be mobilized, ultimately restricting U mobility. This is similar to what has been observed at other analogue sites,

indicating that porosity reduction and radionuclide immobilization via precipitation of secondary minerals are important under a range of conditions relevant to geologic repositories.

Introduction

Nuclear energy produces vast amounts of carbon-free electricity but also produces highly radioactive Used Nuclear Fuel (UNF). Safe management of UNF includes interim storage after withdrawal from the nuclear reactor, and eventually its final disposal (e.g. IAEA, 2020). Experts working on the topic at the international level agree that the safest known way to dispose of UNF is in deep geological repositories (DGR) (NEA, 2020). The Deep Geologic Repository concept ensures the long-term (~1 Ma timeframe) isolation of radioactive waste by entombing UNF deep (generally ≥ 500 m) underground where containment is provided by a system of engineered (typically consisting of a reinforced metallic canister, bentonite clay sealant, and backfill) and natural (host rock) barriers (e.g. IAEA 2020, NEA 2020).

Evaluating the performance of a DGR over such long timescales presents challenges, as results from short term experiments must be extrapolated over timescales that are orders of magnitude longer. The study of uranium deposits, which have existed in the subsurface for millions of years, as natural analogues for UNF in a DGR offers a method for gathering real-world data over repository timescales and beyond. Many deposits are particularly valuable analogues because the U ore mineral uraninite (UO_{2-x}) is chemically similar to the UO_2 that makes up the bulk of UNF (Janeczek et al., 1996; Ewing, 1999), allowing the stability of UNF to be evaluated over Ma-Ga (Cramer and Smellie, 1994; Janeczek and Ewing, 1995; Smellie and Karlsson, 1996; IAEA, 1999; Evins et al., 2005; Fayek and Brown, 2021). The Kiggavik

uranium (U) deposits represent a worst-case scenario where a DGR has been breached by natural geological processes (e.g., surface water infiltration) (Burron et al. 2025).

While faults and fractures provide the main conduits for fluid migration in the subsurface, the porosity of rock formations is a major control on how fluids interact with the bulk rock matrix, which in turn influences processes such as ore deposit formation (Corriveau et al., 2016; 2022b; Potter et al., 2019) and transport of radionuclides in the subsurface (IAEA, 1999; Boers, 2017; Martin et al., 2023). Furthermore, mineral dissolution/precipitation reactions due to fluid infiltration may modify the primary porosity and permeability of a DGR host rock by creating and/or infilling pores and vugs and sealing fractures (Steefel and Lichtner, 1998; Sonnenthal and Spycher, 2001; Simmons and Stuckless, 2010; Fayek and Brown, 2021). The infiltration of oxidized meteoric fluids, which are capable of oxidizing relatively insoluble U^{4+} phases into soluble and mobile U^{6+} phases, has been identified as a major concern in geologic disposal of UNF (IAEA, 1999; Fayek and Brown, 2021; Burron et al., 2025) however the effect of these fluids on host rock porosity is not well understood.

Understanding how the incursion of fluids may affect host rock porosity is of crucial importance to DGR performance assessments (i.e. Martin et al., 2023), as the dissolution of DGR materials and primary host rock minerals and (re)precipitation of secondary minerals can greatly modify the pathways available for fluid and radionuclide mobility (Smellie, 1998; Martin et al., 2016; 2023).

The effects of these fluids on clays and clay-rich rocks are of particular interest. While many DGR concepts envision disposal in crystalline rocks (i.e. SKB, 2010; NWMO, 2017), others would use clay-rich sedimentary rocks such as mudstone and shale (i.e. Claret et al., 2004;

Wendling et al., 2019; Martin et al., 2023); furthermore most geologic disposal plans, for both Low/Intermediate-Level Wastes (L/ILW) and High-Level Wastes (HLW) such as UNF, use bentonite as an important sealing and/or backfill material within engineered barrier system. This is because it possesses favourable properties (such as self-sealing and swelling capacity) and is a widely available and stable natural material (e.g. Brachman 2021, Dixon 2016, IAEA 2013). The dissolution, transportation, and (re)precipitation of U in natural clay-rich materials, however, remains poorly understood (Schindler et al., 2015). While porosity modification to clay-rich rocks stemming from alkaline fluids, derived through interactions between groundwaters and cementitious L/ILW and HLW repository materials, has received some investigation (i.e. Martin et al., 2023) the effects of oxidizing meteoric waters has received less attention.

Small angle scattering techniques such as Small and Ultra Small Angle X-ray Scattering (SAXS/USAXS) and Small/Ultra Small Angle Neutron Scattering (SANS/USANS) are powerful tools for investigating porosity, as they are capable of probing the porosity and pore size distribution of rock samples over pores sizes ranging from ~1 nm to several μm (Radlinski, 2004a; 2006; Anovitz and Cole, 2015).

These techniques have increasingly been employed to study porosity in geological materials such as coal (Radlinski et al., 2004b; Zhoa et al., 2014; Liu et al., 2022), shales and mudstones (Busch et al., 2018; Zhoa et al., 2019; Herz-Thyhsen et al., 2021), and igneous rocks (Bazilevskaya et al., 2013; 2015; Navarre-Sitchler, et al., 2015; Anovitz et al., 2021). These studies have often focused on characterizing the porosity of economically significant formations such as coal beds and unconventional hydrocarbon reservoirs (Radlinski et al., 2004b; Zhoa et al., 2014; Zhoa et al., 2019; Liu et al., 2022; Herz-Thyhsen et al., 2021) and probing how

porosity changes as individual rocks are affected by processes such as hydraulic fracturing (Herz-Thyhsen et al., 2021), and weathering (Bazilevskaya et al., 2013; 2015; Navarre-Sitchler, et al., 2015). Few studies, however, have attempted to use these methods to draw conclusions about how porosity varies between different lithologies and alteration styles or to directly apply such data to the mobility of radionuclides through the subsurface (Busch et al., 2018).

The Kiggavik U deposits are hosted in clay-altered metasedimentary and igneous rocks, and have a complex history of hydrothermal alteration and U mobility (Sharpe et al., 2015; Shabaga et al., 2017; 2020; Grare et al., 2020; Burron et al., 2024; 25; in review), including ~36.5 - 471.3 Ka U mobility related to infiltration of oxidized subglacial waters (Burron et al., 2025). Therefore, these deposits are ideal natural laboratories to study the effects of fluid infiltration on the porosity of both metasedimentary and igneous rocks, and associated U mobility through a clay-rich matrix. Since nearly all repository concepts use bentonite clay, in many cases within crystalline host rocks, this has broad applicability to DGR performance.

Herein, we use SXAS and USAXS to investigate how the porosity, pore size distribution, and Specific Surface Area (SSA) of pores in multiple lithologies and alteration styles have influenced radionuclide mobility in the Kiggavik deposits.

Geological Setting

Regional Geology

The Kiggavik U deposits are located in the Rae Domain of the Churchill Province in the northwestern Canadian Shield (Fig. 1). The deposits occur ~2-25 km southeast of the faulted margin of the large Paleo-Mesoproterozoic Thelon Basin, which together with the underlying Baker Lake Basin, is filled by undeformed volcano-sedimentary rocks of the 1845-1540 Ma

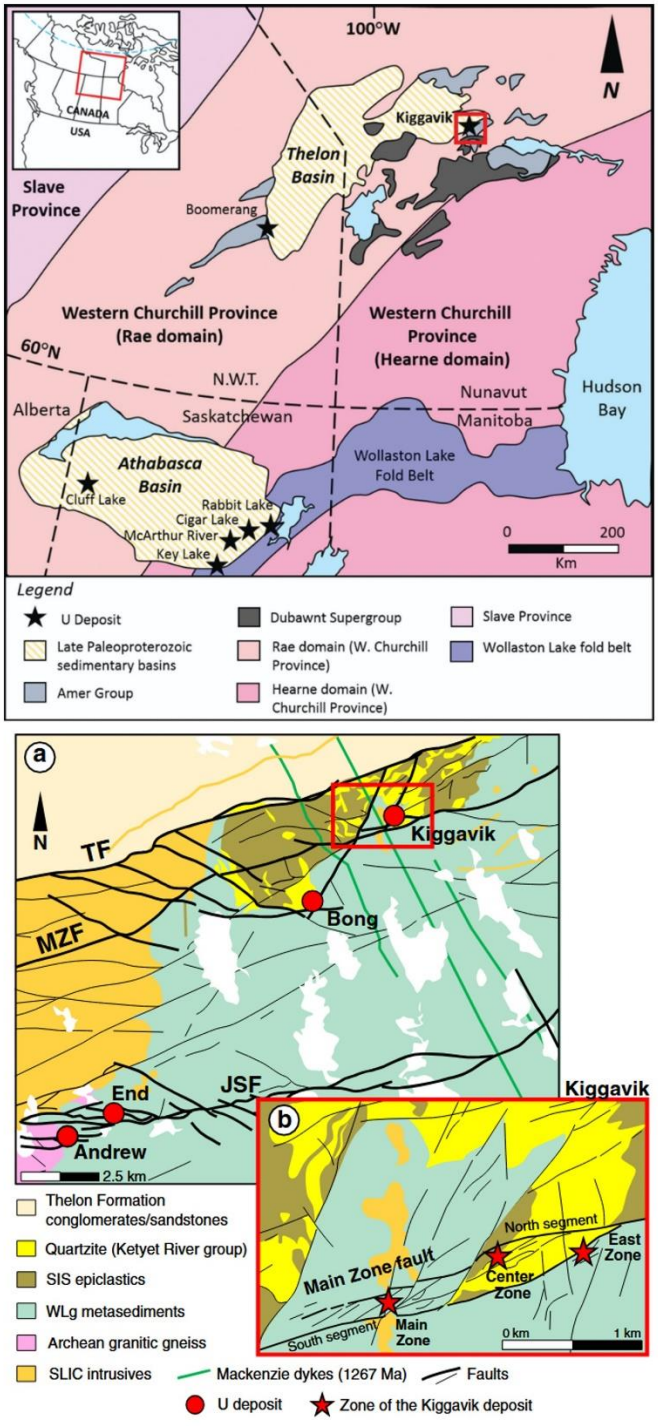

Figure 1. Simplified geologic map of the Kiggavik deposits. Abrreviations: JSF = Judge Sissions fault, MZF = Main Zone fault, SIS = Snow Island suite, SLIC = Schultz Lake intrusive complex, TF = Thelon fault, WLg = Woodburn Lake group. Modified from Shabaga et al. (2017; 2020).

Dubawnt Supergroup (Rainbird et al., 2003; Peterson, 2006; Chamberlain et al., 2010). The Dubawnt Supergroup is divided into three stratigraphic groups: the 1845-1785 Ma Baker Lake, ~1756 Ma Wharton, and <1720 Ma Barrensland sequences (Rainbird et al., 2003). The Baker Lake and Wharton groups fill the older Baker Lake Basin, while the Barrensland sequence comprises the main fill of the Thelon Basin (Hiatt et al., 2010). The Thelon Basin is capped by the uppermost formations of the Barrensland Sequence, the 1540 ± 30 Ma Kunngmi shoshonitic basalts (Chamberlain et al., 2010), and the Lookout Point Formation dolomite (Gall et al., 1992). The Paleo-Mesoproterozoic timing and intracratonic setting of the Thelon Basin is similar to Saskatchewan's Athabasca Basin, which hosts many economically significant U deposits.

Basement lithologies underlying the Thelon Basin comprise unsubdivided Archean granitoid gneiss, 2.74-2.68 Ga supracrustal rocks of the Woodburn Lake group (Pehrsson et al., 2013), ~2.6 Ga felsic volcanic and intrusive rocks of the Snow Island Suite (Jefferson et al., 2011; Peterson et al., 2015; Johnstone, 2017), and orthoquartzite of the Paleoproterozoic Keyet River Group (Rainbird et al., 2010). The majority of the mineralization in the Kiggavik area is hosted in the Pipedream Assemblage of the Woodburn Lake group, which comprises felsic, intermediate, and ultramafic volcanic rocks, subordinate greywacke-mudstone turbidites and iron-formation (Pehrsson et al., 2013).

Basement rocks have been intruded by two major igneous suites: 1.84-1.79 Ga Hudson Granites and the 1.76-1.73 Ga Nueltin Granites, which together comprise the Schultz Lake Intrusive Complex (Peterson et al., 2002; Peterson, 2006; Scott et al., 2012; Scott et al., 2015). The Hudson Granites consist of late syn-orogenic, monzonite, granodiorite, and granite (Peterson et al., 2002; Scott et al., 2015) emplaced along pre-syn magmatic structures at mid-crustal levels.

(Peterson et al., 2002). They are synchronous with the ultrapotassic lamprophyres and minettes of the Baker Lake sequence of the Dubawnt Supergroup (Peterson et al., 2002). The Neultin Granites are anorogenic rapakivi-granite predominately comprised of megacrystic K-feldspar with interstitial quartz, plagioclase, biotite, and minor amphibole and titanite (Peterson et al., 2002; Peterson, 2006; Scott et al., 2012). The Nueltin intrusive rocks are contemporaneous with the equivalent extrusive Pitz Formation rhyolite of the Wharton Group (Scott et al., 2015). The 1267 ± 2 Ma intrusion of the Mackenzie diabase dykes (LeCheminant and Heaman, 1989) marks the last episode of igneous activity in the region.

Deposit Geology

The Kiggavik U Project contains an estimated 51 million kg U at ~0.46% U (AREVA, 2011). These deposits have generally been considered to be basement-hosted unconformity related (URU) deposits similar to those in the Saskatchewan's Athabasca Basin (Fuchs et al., 1986; Riegler et al., 2014; 2016; Chi et al., 2016; Grare et al., 2020; Ashcroft, 2020). More recently, Burron et al. (2024; in review) proposed that the Kiggavik deposits represent a hybrid between a paragenetically early Metasomatic Iron Alkali Calcic (MIAC) system and later overprinting URU system.

Uranium deposits in the region are located at the intersections of faults which trend roughly ESE-WNW and NNE-SSW and have been the sites of brittle deformation and intense hydrothermal alteration of host rocks to mainly clay and hematite (Fuchs et al., 1987; Sharpe et al., 2015; Grare et al., 2018; 2020). Several U deposits and showings, including the Kiggavik, Bong, End, and Andrew Lake deposits, which comprise the majority of the U resource, form a

NE-SW trending feature informally termed the Kiggavik-Andrew Lake structural trend (Riegler et al., 2014; Sharpe et al., 2015).

The bulk of U mineralization in the Kiggavik region is hosted within metagraywackes of the Woodburn Lake group, with minor mineralization in the Lone Gull granite at the Kiggavik Main Zone and Kiggavik North deposits. The Lone Gull granitic stock is interpreted as a hybrid between the Hudson and Nueltin granites, with the younger Nueltin magma infiltrating into and altering the preexisting Hudson pluton (Scott et al., 2015).

Burron et al. (in review) proposed a 5-stage genetic model consisting of 1) albitization 2) hematization 3) bleaching and primary (U1) mineralization 4) Multiple resetting events and U2 mineralization and 5) geologically recent subglacial alteration and U3 mineralization. Albitization consists of porous albite and K-feldspar, quartz, and course laths of muscovite, with a diverse suite of trace and accessory minerals (Burron et al., 2024; in review; Fig. 2). Albitization has been dated by the Ar-Ar method at ~1830 Ma and is linked to extremely isotopically fractionated fluids produced through multiple episodes of boiling and condensation (Burron et al., in review). Albitization has affected both metasedimentary and granitic rocks but is more pervasive and better preserved in granitic rocks (Burron et al., 2024; in review). This albitization is associated with an enrichment in U (Burron et al., 2024), and is temporally linked to other albite-rich metasomatic U deposits in northern Canada (Burron et al., 2024; in review).

Albitized rocks are commonly replaced by a hematized assemblage dominated by illite, hematite, and variable amounts of remnant quartz, apatite, and Ti-oxides (Burron et al., 2024; in review). Rocks affected by hematization do not preserve primary textures (Burron et al., 2024; in review). Hematization is thought to be related to the emplacement of the quartz breccia (QB),

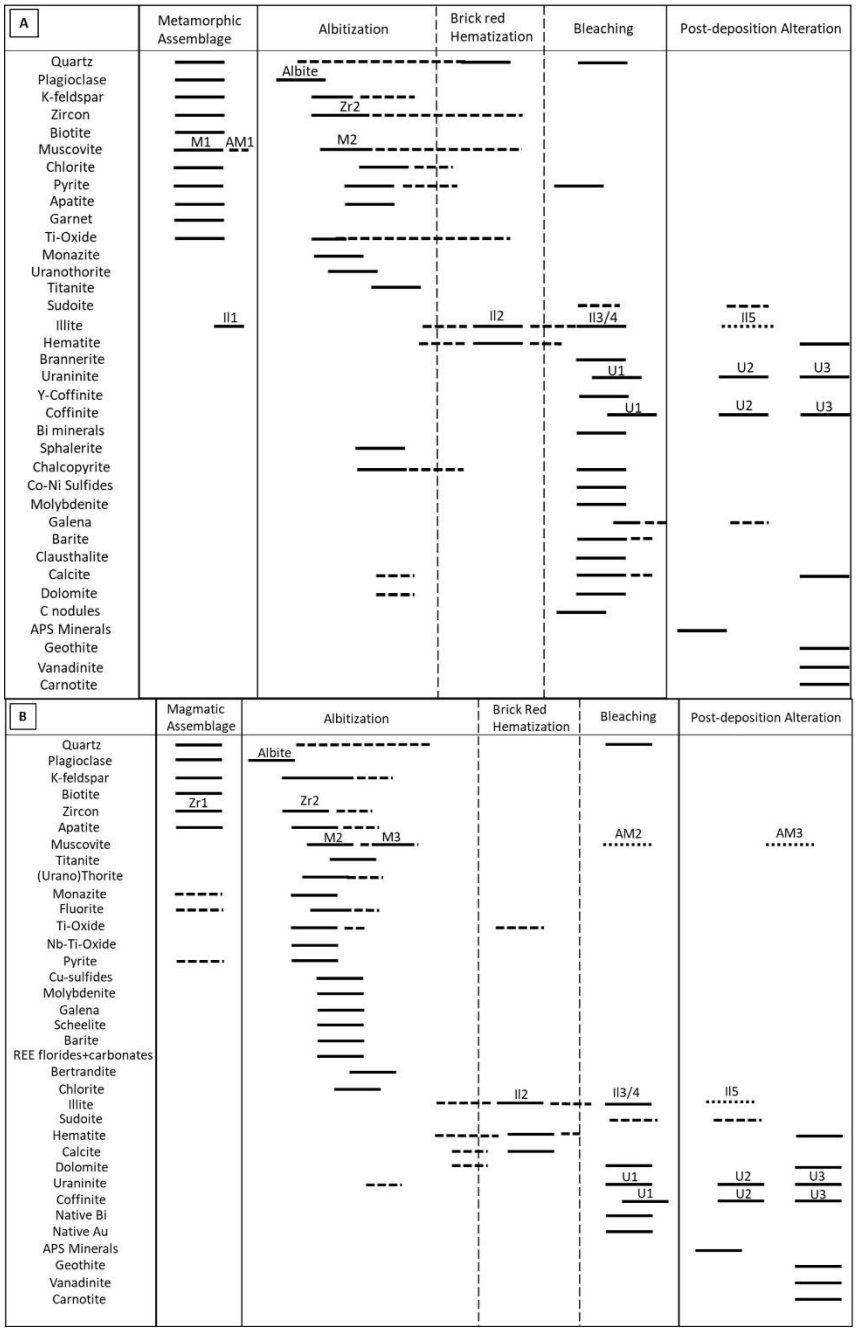

Figure 2. Generalized paragenesis of the Kiggavik deposits. A. Metasedimentary and epiclastic host rocks. B. Granitic host rocks. Dashed lines indicate uncertainty in timing, dotted lines indicate overprinting events. From Burron et al. (2025).

sheet-like bodies up to 30 m in thickness which consist of clasts of hematized breccia in a matrix comprising multiple stages of quartz and hematite (Grare et al., 2018). The QB is found in the core of most Kiggavik U deposits, and is interpreted to have formed from mixing of igneous and meteoric/basinal fluids in an epithermal system (Grare et al., 2018). Although the QB is unmineralized, it is believed to have controlled the flow of U-mineralizing fluids by acting as a barrier to fluid flow (Grare et al., 2018).

Uranium mineralization is associated with bleaching (hematite removal) of host rocks (Burron et al., 2024; in review). Recent studies indicate a complex sequence of mineralization (Sharpe et al., 2015; Shabaga et al., 2017; Grare et al., 2020; Burron et al., 2024), with primary U mineralization (U1) consisting of three styles: fine-grained uraninite ± coffinite disseminated along interfaces between hematized and bleached rocks (U1a), uraninite ± coffinite ± brannerite (UTi_2O_6) in polymetallic and monometallic epithermal veins (U1b), and disseminated uraninite, coffinite, and brannerite (U1c) (Burron et al., 2024). Brannerite and polymetallic veins comprise a significant component of U mineralization in the End Deposit but are rare to absent in other Kiggavik deposits (Burron et al., 2024). U1a is dated to 1594 ± 95 Ma, while U1b and U1c yielded a more precise overlapping date of 1554 ± 16 Ma (Burron et al., 2024). U1 and bleaching is linked to both highly fractionated fluids and basinal brines (Burron et al., in review).

Resetting events precipitated a second generation of U-minerals (U2) at 1440 ± 21, 1417 ± 17 Ma, 1276.4 ± 8.7 Ma, 1249 ± 33 Ma, 937 ± 24 Ma, and 274 ± 69 Ma (Burron et al., 2024). Resetting events are linked to the infiltration of basinal fluids (Burron et al., in review) during periods of igneous and distant tectonic activity (Burron et al., 2024).

The most recent generation of U-minerals (U3) is associated with distinctive orange goethite-bearing ferric alteration (Burron et al., 2014; 2025; in review). U3 is dated to 36.5 ± 1.9, 55.7 ± 4.8, 153.3 ± 3.7, 258.6 ± 11.6, and 471.3 ± 6.3 Ka and is linked to the infiltration of subglacial fluids along fracture systems (Burron et al., 2025). These U3 minerals are found within a few cm of much older U1/U2 minerals, indicating U mobility has been restricted to short distances (Burron et al., 2025).

Methods

Drill core samples representative of unaltered and altered metasedimentary, granitic, and epiclastic rocks from the End, Bong, Andrew Lake, and Kiggavik deposits were selected for (U)SAXS analysis. Restrictions in handling radioactive material ultimately prevented the analysis of U-bearing samples. The mineralogy and textures of these samples were characterized by petrographic microscope and scanning electron microscopy prior to (U)SAXS experiments.

Rock samples were prepared as 150 µm thick polished sections mounted to quartz glass slides. Absolutely calibrated USAXS, SAXS, and WAXS experiments were performed at the 20-IDB beamline of the Advanced Photon Source at Argonne National Laboratory. The combined q range was between ~1 x 10^{-4} and 4.5 $Å^{-1}$. The X-ray energy was 21 keV, with a wavelength of 0.5904 Å. Slit length for USAXS was 0.026113. Sample to detector distance was 1.08 m. Sample transmission ranged from ~80-90%, and a CdTe detector was used. The beamsize was 800 µm.

For each section a series of measurements were taken so as to produce a transect across the sample. This allowed for average porosities of entire samples to be calculated and for abrupt variations in porosity associated with sharp redox/lithology boundaries to be quantified. Blank

quartz glass slides were also measured to allow the background to be determined and subtracted during data reduction.

SAXS and USAXS data were reduced using the Nika (Ilavsky, 2012) and Indra (Ilavsky and Jemian, 2009) programs of the IGOR software, respectively. The SAXS and USAXS datasets were then merged using the Irena package (Ilavsky and Jemian, 2009) to yield a combined SAXS and USAXS scattering curve. Although WAXS data was gathered, many spectra had unusually high background curves and strongly shifted peaks indicative of orientation effects. This is almost certainly due to these samples, many of which contain strongly aligned grains or very large crystals, deviating from the assumed isotropic distributed of crystals upon which WAXS analysis depends. For this reason, these WAXS data were not used and are not considered further.

Although rocks are complex systems generally composed of multiple minerals, contrast in scattering length densities between minerals are generally small compared to contrast between minerals and pores, allowing rocks to be modelled as two-phase systems of pores within a mineral matrix (Radlinski, 2006; Anovitz and Cole, 2015). The two-phase assumption allows the scattering intensity I(q) to be expressed as:

$$I(q) = |\Delta\rho|^2 \int_0^\infty |F(q,r)|^2 V(r)^2 NP(r) dr \qquad (1)$$

where Δρ is the contrast in scattering length density, $|F(q,r)|^2$ corresponds to the form factor, *V(r)* is the particle volume, *N* is the total number of scatterers, and *p(r)* is the probability of occurrence of scatterers of size r. The values of scattering contrast and form factor used for each measured point were selected to be representative of the average composition of the sample at the location in question as observed through optical and electron microscopy. For instance, a spot

comprising 70% acicular (aspect ratio ~10) illite (Δρ = 559.7) and 30% equant quartz (Δρ = 504.2) would be represented as having Δρ = 543.05 and the form factor of a cylinder with an aspect ratio of 7.

Quantitative interpretation of the scattering intensity yields the porosity (ϕ):

$$\int_0^\infty I(Q)Q^2 dQ = 2\pi^2 (\Delta\rho)^2 \phi(1-\phi) \qquad (2)$$

The total porosity, pore volume size distribution, and specific surface area of pores were estimated via the size distribution tool in Irena using the IPG/TNNLS method (Ilavsky and Jemian, 2009) over the measured q range.

Results

Petrography

Unaltered Metasedimentary Rocks Unaltered metasedimentary rocks of the Woodburn Lake Group, traditionally referred to as metagraywacke, are grey-green and fine grained (<0.5 mm). They are strongly foliated, with foliation defined by alignment of elongated minerals and transposed bedding planes. The metasedimentary rocks are composed mainly of 0.1-0.5 mm equant quartz grains (~60%), 0.1-0.3 mm tabular feldspar (mainly K-feldspar with minor plagioclase) (~20%), and 0.1-0.5 mm tabular muscovite and biotite (~20%), with accessory pyrite, zircon, rutile, apatite, and local garnet. Proportions of muscovite versus biotite vary, with some samples dominated by muscovite and others by biotite. Metasedimentary rocks have been affected by retrograde metamorphism, with biotite strongly retrograded to chlorite and feldspars moderately-strongly altered to coarse-grained illite. Muscovite is locally broken down into finer-grained altered muscovite.

Hematized Metasedimentary Rocks Hematized metasedimentary rocks have a distinct brick red color, and are dominated (~55-90%) < 15 μm massive illite. Quartz is extensively corroded and comprises ~10-40% of the rock. Anhedral hematite is disseminated throughout the rock, typically comprising 5-15% of the rock. Hematite is typically ~1-30 μm, but larger subhedral grains and aggregates up to ~100 μm and are locally present. Trace to minor amounts of Ti-oxides and apatite are present, with local chlorite and strongly illite-altered muscovite laths.

Approximately 10% of hematized metasedimentary rock samples contain specular hematite which forms acicular laths up to 0.3 mm in length. Specular hematite is commonly associated with ~0.1-3 mm voids which penetrate the entire thickness of the section. The presence of these voids indicates these samples contain substantial porosity outside of the size range measurable by USAXS, and that these sample may not have a uniform thickness, indicating USAXS measurements cannot provide a meaningful description of the porosity of these samples. For these reasons all samples containing specular hematite were excluded from USAXS experiments.

The Quartz Breccia (QB) The QB is spatially associated with hematization and has often been considered to be genetically related to hematization (Grare et al., 2018a; Burron et al., 2024; in review). Clasts, typically 1-10 cm in size, are comprised of hematized metasedimentary rocks, while the vein fill is comprised of massive quartz with minor amounts of local carbonate and pyrite. Many ~1-5 μm pores and fluid inclusions are present.

Bleached Metasedimentary Rocks Bleached metasedimentary rocks are beige-white, with a mineralogy dominated by massive <15 μm illite and variable amounts of corroded, relict quartz. Trace to minor amounts of apatite and Ti-oxides are commonly present, while minor

amounts of calcite, sudoite, muscovite, and chlorite are locally present. Calcite is more common, and sudoite is absent, in the End Deposit. Bleached rocks are texturally and mineralogically similar to hematized rocks, with the notable exception of the absence of fine-grained hematite. Specular hematite and the associated voids, however, locally survive bleaching and are present in a few samples.

Bleaching is locally associated with primary U mineralization (U1), comprising fine grained uraninite and coffinite disseminated along interfaces between bleached and hematized areas (U1a), uraninite ± coffinite ± brannerite disseminated within the bleached matrix (U1b), and uraninite ± coffinite ± brannerite in polymetallic and monometallic epithermal veins (U1c). These veins contain substantial porosity in the form of microfractures and open vugs.

Uranium minerals are commonly altered to a generation of fractured, anhedral uraninite and coffinite (U2). With the exception of the absence of polymetallic veins these U2 minerals strongly resemble texturally altered versions of U1 minerals.

Ferric Altered Metasedimentary Rocks A small proportion (~5-10%) of bleached metasedimentary rocks have been subject to goethite-bearing ferric alteration, giving these rocks a characteristic orange color (Fig. 3a). This ferric alteration is spatially associated with open fractures and porous, sometimes U-mineralized, vein systems. Goethite and local minor hematite is ubiquitously disseminated throughout the matrix of ferric-altered rocks in the form of <10 μm grains intergrown with illite and larger pore and fracture filling aggregates up to ~200 μm. Calcite, goethite, and rare vanadinite locally fill fractures (Fig. 3b, c).

Disseminated and fracture-filling uraninite and coffinite (U3) are strongly concentrated along boundaries between ferric alteration and bleached rocks. Although U3 is strongly

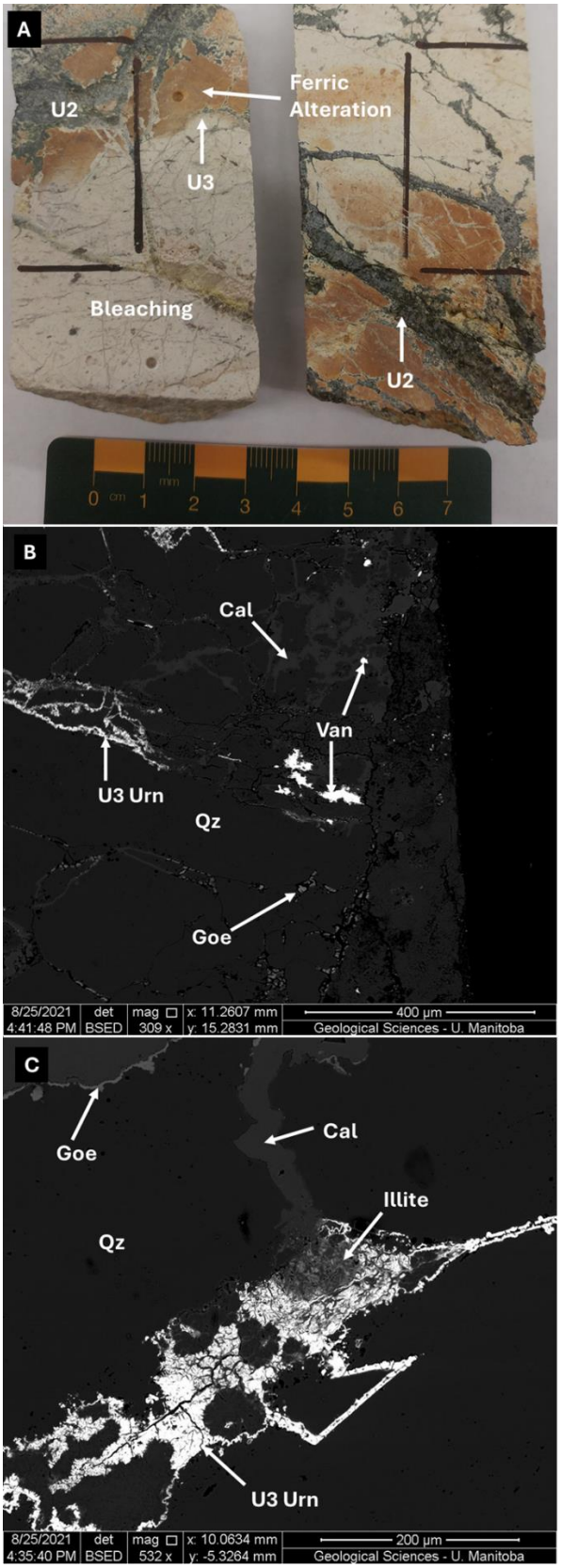
A
U2
Ferric Alteration
U3
Bleaching
U2
B
Cal
Van
U3 Urn
Qz
Goe
8/25/2021 4:41:48 PM
det BSED
mag 309 x
x: 11.2607 mm
y: 15.2831 mm
400 µm
Geological Sciences - U. Manitoba
C
Goe
Cal
Illite
Qz
U3 Urn
8/25/2021 4:35:40 PM
det BSED
mag 532 x
x: 10.0634 mm
y: -5.3264 mm
200 µm
Geological Sciences - U. Manitoba

Figure 3. Textures of ferric alteration and U3 mineralization in metasedimentary rocks. A. Orange ferric alteration and minor U3 mineralization developed in proximity to a U2 vein system (SW6-294.7). Black lines denote where the thin section was cut from. B, C. U3 uraninite and associated vanadinite, calcite, and geothite filling fractures in a U2 mineralized quartz vein (SW6-294.7). B is modified from Burron et al., 2024. Abbreviations: Qz = quartz, Urn = uraninite, Cal = calcite, Goe = goethite, Van = vanadinite.

associated with goethite, these minerals do not occur in equilibrium and are always separated by other minerals or open pore space (Fig. 3c).

Epiclastic Rocks (Meta)epiclastic rocks are only observed in the Kiggavik Deposit. They are fine-grained (<0.5 mm), with a variable mineralogy consisting of ~30-50% quartz, 20-50% plagioclase, 5-10% K-feldspar, 5-10% chlorite, and 0-20% muscovite with accessory apatite and local stringers of blocky pyrite. Epiclastic rocks contain 5-30% <3 mm mosaic texture quartz clasts. Hematized and bleached epiclastic rocks were observed, however they contained specular hematite and very large voids (Fig. 4) and were excluded from further analysis.

Albitized Granitic Rocks All Lone Gull granitic rocks examined are pervasively albitized. Albitized granitic rocks consist of roughly subequal amounts of ~0.2-5 mm albite, K-feldspar, and quartz, with minor muscovite and diverse suite of accessory minerals comprising zircon, fluorapatite, uranothorite, rutile, pyrite, chalcopyrite, molybendite, galena, biotite, fluorite, Fe-oxides, and Alumino-Phosphate-Sulfate (APS) minerals, and trace local ilmenite, monazite, REE-(F)-carbonates, scheelite, and native Au. With the exception of some zircons and the cores of large quartz, feldspar, and biotite grains all of these minerals are interpreted as the result of hydrothermal replacement of igneous minerals.

Feldspars, and to a lesser extent quartz, within albitized granitic rocks contain many ~1 μm scale pores (Fig. 5a). Larger voids are uncommonly present within pockets interpreted as partially infilled dissolution pits. Muscovite and accessory minerals tend to be concentrated into these pockets.

Hematized Granitic Rocks Granitic rocks have been subject to varying degrees of hematization, which overprints albitization. One sample, KN04-106, has been subject to only

incipient degrees of hematization, with very minor breakdown of albite to illite intergrown with trace amounts of hematite, whereas sample KN04-66.5 is intensely hematized. In KN04-66.5

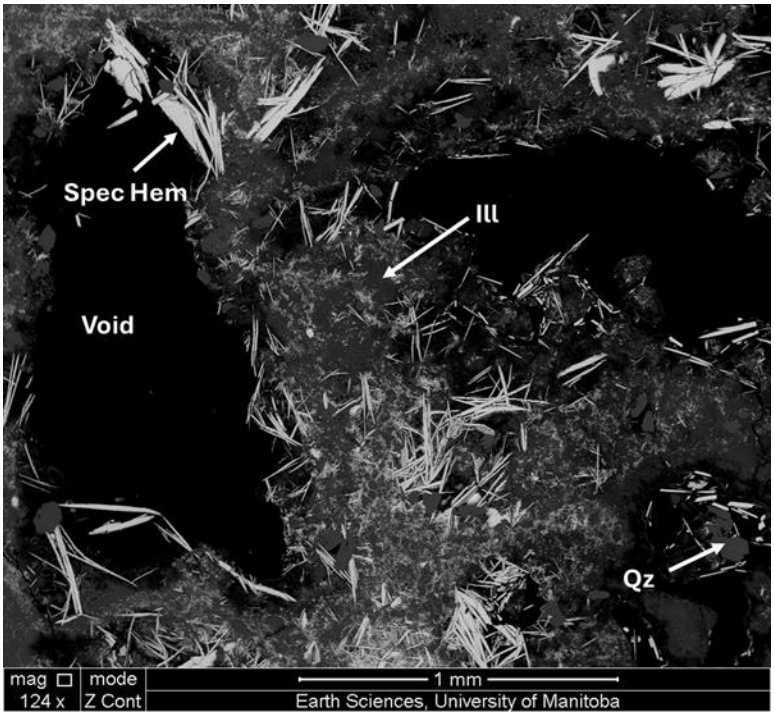

Figure 4. Specular hematite associated with large voids in sample KN04-15. Abbreviations: Spec Hem = specular hematite, Ill = illite, Qz = quartz.

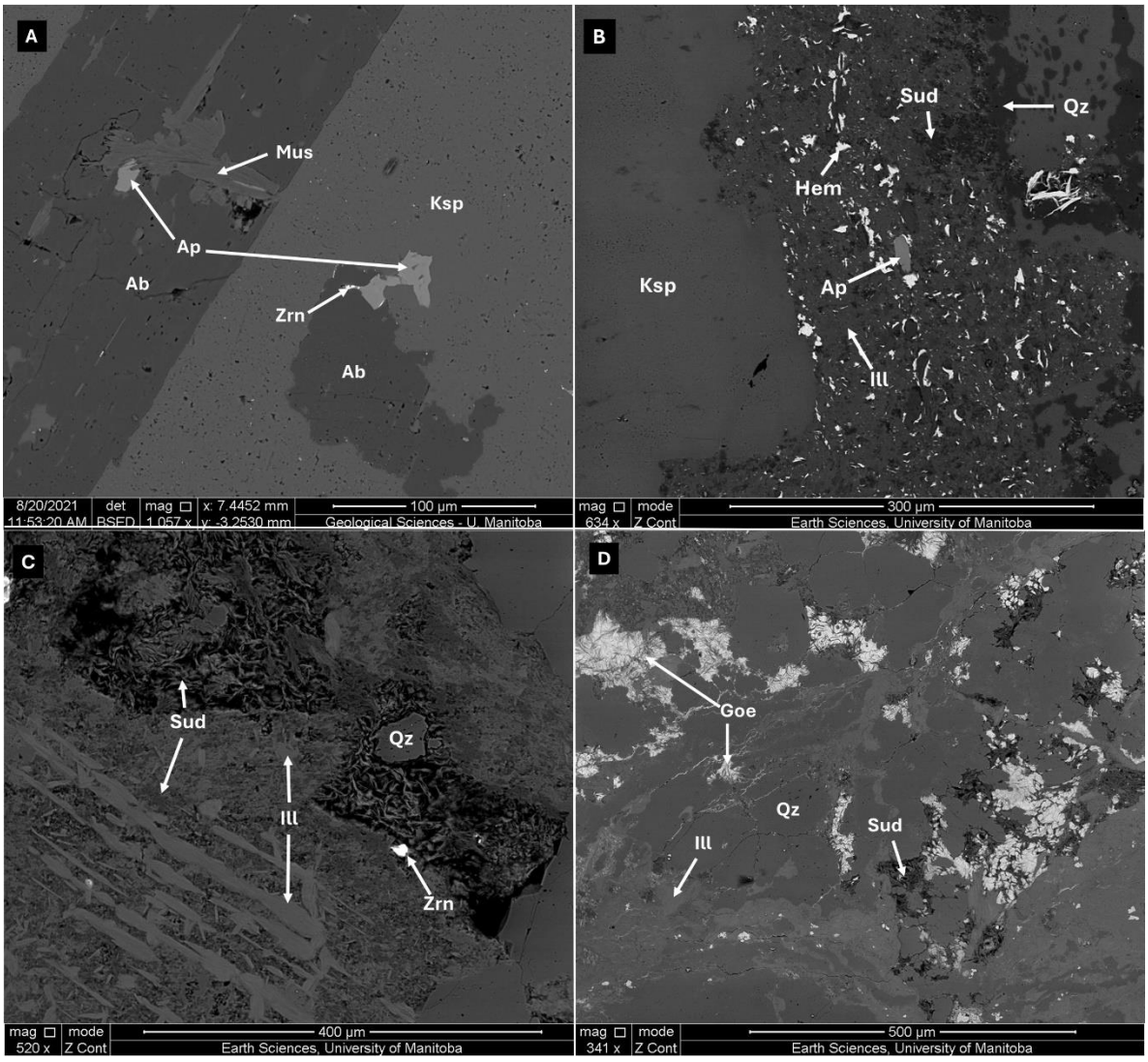

Figure 5. Textures of Kiggavik granitic rocks. A. Albitized granitic rock. Note the many ~µm scale pores within feldspar grains (KN04-126). B. Hematized granitic rock. Albite has been pervasively replaced with illite, sudoite, and hematite, while K-feldspar persists within only minor breakdown to illite (KN04-66.5). C. Bleached granitic rock. K-feldspar has been replaced with a porous intergrown of coarse-grained sudoite and illite (MZ-10-01-90). D. Ferric altered granitic rock. Goethite has precipitated in many of the pores (MZ-10-01-120). Abbreviations: Qz = quartz, Ksp = K-feldspar, Ab = albite, Ap = apatite, Mus = muscovite, Zrn = zircon, Sud = sudoite, Hem = hematite, Ill = illite, Goe = goethite.

essentially all albite has been replaced by illite intergrown with ~1-50 μm grains of hematite; K-feldspar, however, has largely been preserved with only relatively minor breakdown to illite along grain margins (fig. 5b). Zircon, apatite, and Fe-Ti-oxides are the only accessory minerals present in intensely hematized granitic rocks.

Bleached Granitic Rocks Granitic rocks have also been subject to bleaching, which overprints hematization and albitization. Strongly bleached granitic rocks contain no feldspar, with albite replaced by coarse grained illite (locally up to ~100 μm) intergrown with minor amounts of fine grained sudoite, and K-feldspar replaced by sudoite intergrown with lesser amounts of illite (fig. 5c). These sudoite-illite replaced K-feldspar grains contain substantial 1-10 μm scale porosity. Hematite is absent in bleached granitic rocks.

Ferric Altered Granitic Rocks Bleached granitic rocks proximal to fracture/vein networks have been affected by ferric alteration. Ferric alteration affects granitic rocks similarly to metasedimentary rocks, with precipitation of goethite and local illite, calcite, vanadinite, and U3 uraninite and coffinite in pore spaces and fractures (Fig. 5d).

X-ray Scattering Experiments

Porosity and Pore Size Distribution Unaltered metasedimentary rocks in the Kiggavik area have a very low porosity of 0.64 ± 0.09 % (Table 1). The pore size distribution is skewed towards larger diameter pores, with 1-7 μm pores comprising 48.5 ± 9.5 % of pore volume. The porosity of these rocks is remarkably consistent, with effectively no difference in porosity or pore size distribution between samples from the End and Bong deposits, which are separated by more than 15 km.

Table 1. Summary of porosity, pore size distribution, and specific surface area (SSA) of rocks from the Kiggavik deposits. Full data presented in appendix table A1.

	Lithology	Alteration	Porosity (%)	SSA (m2/cm3)	Porosity in 3-10 nm (%)	SSA in 3-10 nm (%)	Porosity in 10-100 nm (%)	SSA in 10-100 nm (%)	Porosity in 100-1000 nm (%)	SSA in 100-1000 nm (%)	Porosity in 1000-7000 nm (%)	SSA in 1000-7000 nm (%)
Range	Metasedimentary	Unaltered	0.53-0.86	0.09-0.46	0.0-4.7	0.1-50.0	10.0-30.9	39.5-73.3	14.5-38.3	5.4-23.3	33.8-73.5	0.5-3.4
Avg (n=18)			0.64 ± 0.09	0.24 ± 0.09	2.5 ± 1.2	31.6 ± 11.9	20.8 ± 5.0	56.6 ± 8.4	27.9 ± 4.9	10.3 ± 4.3	48.5 ± 9.5	1.3 ± 0.7
Range	Metasedimentary	Hematized	3.21-12.25	2.0-6.5	4.0-7.5	33.0-46.2	30.6-35.6	40.6-56.7	22.0-37.6	2.6-8.3	11.5-30.9	0.2-0.6
Avg (n = 48)			6.20 ± 2.02	3.66 ± 0.98	7.5 ± 2.0	44.5 ± 5.8	38.4 ± 5.8	49.8 ± 4.5	31.2 ± 4.1	5.2 ± 1.7	22.9 ± 6.1	0.4 ± 0.1
Range	Metasedimentary	Bleached	2.02-12.26	0.0-5.0	1.3-8.6	5.8-54.2	5.8-32.0	4.5-68.8	4.1-41.2	1.7-12.5	6.1-65.4	0.1-3.0
Avg (n =61)			6.35 ± 2.41	2.49 ± 1.17	4.7 ± 2.1	41.9 ± 6.9	24.7 ± 6.2	49.5 ± 5.1	31.3 ± 5.5	7.9 ± 2.1	39.3 ± 11.7	1.0 ± 0.7
Range	Granitic	Albitized	0.55-2.10	0.13-1.90	0.0-3.9	0.0-73.7	2.6-10.9	15.2-91.4	29.6-65.4	5.8-57.9	24.3-57.8	1.4-14.0
Avg (n = 18)			1.11 ± 0.40	0.37 ± 0.40	0.6 ± 1.3	12.8 ± 22.7	7.9 ± 2.1	46.0 ± 16.9	53.9 ± 8.7	38.0 ± 13.7	37.9 ± 8.9	4.8 ± 2.8

Range	Granitic	Hematized (incipient)	0.79-2.61	0.32-1.7	0.7-5.7	25.0-64.2	4.8-20.6	19.0-53.1	16.1-73.1	4.8-50	15.9-70.1	0.7-1.9
Avg (n = 10)			1.32 ± 0.52	0.82 ± 0.45	2.6 ± 1.5	44.6 ± 13.6	11.3 ± 4.4	32.8 ± 9.1	52.5 ± 20.1	21.9 ± 14.3	33.7 ± 17.7	1.2 ± 0.4
Range	Granitic	Hematized	3.46-6.07	2.3-5.5	7.6-13.9	48.1-59.4	30.5-42.6	37.5-46.4	25.8-38.0	3.4-5.9	12.1-31.8	0.1-0.4
Avg (n = 10)			4.54 ± 0.74	3.41 ± 0.93	10.3 ± 1.8	54.6 ± 3.5	36.2 ± 3.9	41.2 ± 2.9	30.7 ± 3.7	4.2 ± 0.8	22.5 ± 6.3	0.3 ± 0.1
Range	Granitic	Bleached	7.08-22.85	2.8-17	2.6-10.6	25.6-43.5	28.7-53.6	51.8-69.0	20.9-36.9	2.6-10.6	14.6-40.3	0.1-0.7
Avg (n = 10)			12.54 ± 4.42	5.97 ± 4.11	4.7 ± 2.3	32.7 ± 5.2	37.5 ± 7.6	60.3 ± 4.4	27.3 ± 5.5	6.5 ± 2.4	30.5 ± 7.8	0.4 ± 0.2
Range	Granitic	Ferric	1.59-14.33	0.72-4.1	2.5-7.7	32.3-45.6	19.0-41.4	44.3-59.3	25.2-37.3	3.9-11.6	25.6-45.8	0.3-1.4
Avg (n = 26)			6.05 ± 2.28	2.37 ± 0.89	3.6 ± 1.2	37.4 ± 3.7	28.6 ± 5.3	54.4 ± 3.9	31.4 ± 2.5	7.9 ± 1.7	36.5 ± 5.1	0.7 ± 0.3
Range	Epiclastic	Unaltered	0.34-0.59	0.25-0.91	2.0-8.5	20.0-56.0	25.6-28.6	38.5-64.0	27.1-38.2	4.3-12.4	31.0-39.1	0.5-1.2
Avg (n = 8)			0.44 ± 0.08	0.44 ± 0.20	3.7 ± 2.1	32.1 ± 11.6	26.8 ± 0.9	57.6 ± 8.7	34.4 ± 3.5	8.8 ± 2.4	35.2 ± 2.6	0.9 ± 0.2
Range	Quartz Breccia	Quartz vein	0.12-2.05	0.17-1.1	0.0-8.3	0.0-70.5	3.9-27.1	18.9-68.2	19.6-48.8	4.3-38.5	25.3-75.6	0.6-12.3
Avg (n = 21)			1.37 ± 0.48	0.46 ± 0.29	1.5 ± 2.2	23.6 ± 21.2	10.7 ± 6.8	49.8 ± 12.8	35.1 ± 8.1	20.5 ± 9.4	52.3 ± 13.1	6.0 ± 3.9

The porosity of both hematized and bleached metasedimentary rocks are approximately an order of magnitude higher than unaltered metasedimentary protoliths. Although there is a great deal of variation between samples, the average porosity of all data points from hematized metasedimentary rocks (6.2 ± 2.0 %) is almost identical to the average of all data points from bleached metasedimentary rocks (6.4 ± 2.4 %).

The pore size distribution of hematized metasedimentary rocks favors smaller pores than unaltered metasedimentary, with 10-100 nm pores accounting for the largest share of volume (38.4 ± 5.8 %). Bleached metasedimentary rocks have a higher proportion of larger pores, with 1-7 μm pores being the most common (39.3 ± 11.7 %).

The porosity of hydrothermal quartz in the QB (1.37 ± 0.48 %) is significantly higher than unaltered metasedimentary rocks but much lower than hematized or bleached metasedimentary rokcs. The pore size distribution of this hydrothermal quartz is dominated by larger pores, with 52.3 ± 13.1 % of pore volume in the 1-7 μm range.

One transect crosses the margin between hydrothermal quartz of the QB and the surrounding hematized matrix (Fig. 6a). This reveals a sharp increase in porosity on the hematized side of the interface (fig. 6b), indicating that silicification does not penetrate into the surrounding host rock. Two transects cross sharp interfaces between hematized and bleached areas of metasedimentary rocks (Fig. 6a). The bleached side of sample Bong-49-131 has a lower overall porosity (fig. 6c). In sample END-09-10-126 there is a significant increase in porosity within ~3 μm of the hematized/bleached interface, with the bleached side having a much wider range in porosity versus the hematized side (Fig. 6d).

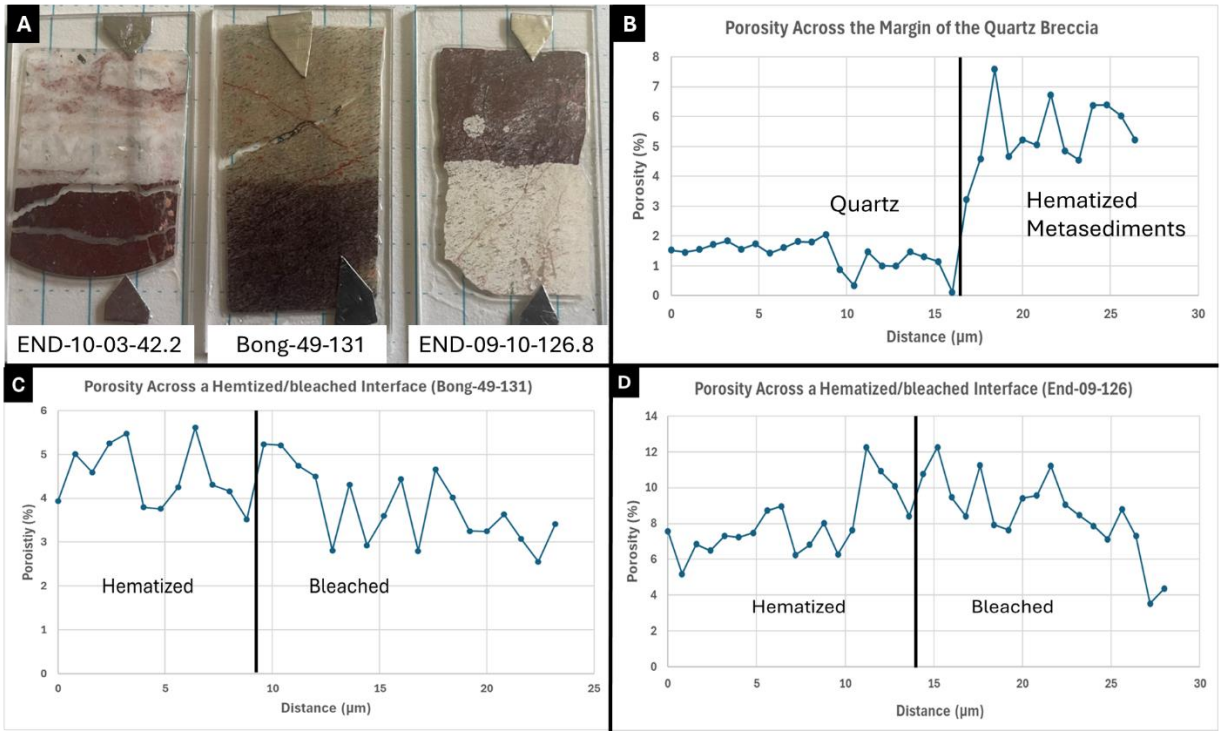

Figure 6. Results of (U)SAXS transects across alteration and lithology boundaries. Location of boundaries are marked by black lines in the porosity plots (B-D). A. Photograph of samples containing sharp alteration/lithology boundaries. Start and end points of transects are marked by the tips of lead tape arrows. The dark line visible in END-10-03-42.2 is the result of damage to the quartz glass slide caused by the X-ray beam. B. A sharp increase in porosity occurs at the margin of hydrothermal quartz of the quartz breccia in sample End-10-03-42. C. Sample Bong-49-131 displays a slight decrease in porosity crossing from the hematized to the bleached side. D. In sample END-09-126 porosity increases within ~3 µm of the interface between hematized and bleached metasedimentary rocks.

Epiclastic rocks have the lowest porosity of all rocks examined (0.44 ± 0.08 %). Pore size distribution is relatively even, with both 0.1-1 and 1-7 μm pores accounting for ~35% of volume.

The porosity of albitized granitic rocks (1.11 ± 0.4 %) is approximately double that of unaltered metasedimentary rocks, and similar to that of hydrothermal quartz of the QB. The pore size distribution of albitized granitic rocks is dominated (>85%) by >100 nm diameter pores, with 100-1000 nm pores comprising 46.0 ± 8.7 % of pore volume.

The porosity of lightly hematized granitic rocks is only slightly higher (1.32 ± 0.52 %) than albitized granitic rocks; pervasively hematized granitic rocks are more porous (4.54 ± 0.74 %). Hematization has shifted pore size distribution towards smaller pores, with 10-100 nm pores comprising the largest share of volume (36.2 ± 3.9 %) in pervasively hematized granitic rocks.

Bleached granitic rocks have by far the highest porosity (12.54 ± 4.42 %) of the rocks investigated. The range of measured porosity is very large (7.08 to 22.85 %). Pore size distribution is similar to that of pervasively hematized granitic rocks, with 10 to 100 nm pores comprising the largest share of volume (37.5 ± 7.6 %).

Ferric altered granitic rocks have approximately half the porosity (6.05 ± 2.28 %) of their bleached protolith. This reduction in porosity is accompanied by a shift towards larger pore sizes, with 1-7 μm pores comprising the largest share of pore volume (36.5 ± 5.1 %).

Specific Surface Area Specific surface area is strongly correlated with porosity ($R^2 = 0.92$) in all samples investigated (Fig. 7). Hematized metasedimentary and granitic rocks have a somewhat higher SSA than would be expected from their porosity, which is associated with the higher proportion (~7.5-10%) of 3-10 nm pores in these rocks. Smaller pores have larger SSA/volume

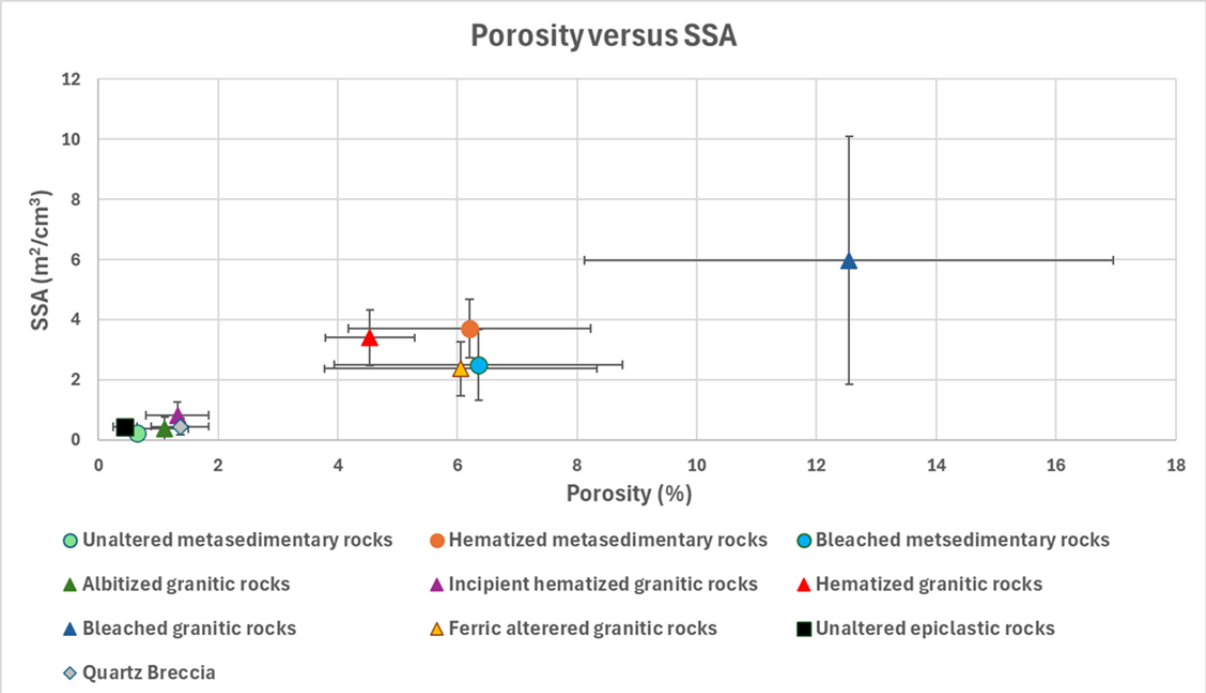

Figure 7. Plot of porosity versus specific surface area (SSA) for rocks from the Kiggavik deposits. Porosity and SSA are highly correlated, with strongly hematized rocks having slightly higher SSA per unit of porosity than non-hematized rocks.

ratios, and consequently most of the SSA is associated with nanoscale pores, even if these comprise only a minor proportion of the pore volume.

Approximately 90% of SSA is associated with <100 nm pores in all metasedimentary and epiclastic rocks, as well as strongly hematized, bleached, and ferric altered granitic rocks. Albitized granitic rocks and hydrothermal quartz in the QB have smaller proportions of nanoscale pores than other rock types, and consequently a higher proportion of SSA, 38.0 ± 13.7 and 20.5 ± 9.4 %, respectively, is associated with 100 nm to 1 μm pores. The distribution of pores sizes and SSA in granitic rocks with only incipient hematization falls in between these groups.

Discussion

Effects of lithology and hydrothermal alteration

Rocks with higher degrees of hydrothermal alteration tend to be more porous; different rock types, however, respond to alteration in different ways. Hematization of metasedimentary rocks increases porosity by approximately an order of magnitude while shifting the pore size distribution towards <100 nm pores. This is interpreted to be the result of the formation of large amounts of fine-grained illite at the expense of larger feldspar grains.

While bleaching has not substantially changed the overall porosity of hematized metasedimentary rocks, it has modified the pore size distribution by creating >1 μm pores and destroying <100 nm pores. The creation of >1 μm pores is likely the result of the dissolution of hematite, which commonly has a grain size of ~1-30 μm. The reason for the destruction of <100 nm pores is less obvious as bleaching is not observed to be systematically associated with the precipitation of new minerals in the samples studied. Bleaching is, however, associated with an

increase in SiO_2 and K_2O throughout bleached samples (Burron et al., 2024) as well as precipitation of quartz and carbonate minerals in veins and surrounding areas in U1 mineralized samples. This suggests that precipitation of small amounts of <100 nm quartz and/or carbonate, which would be very difficult to detect via SEM, could have influenced the measured porosity. A second possibility is that the larger hematite grains hosted nanoscale porosity within them, which was lost when the hematite was destroyed.

Unaltered epiclastic rocks are the least porous rocks examined; bleached and hematized epiclastic rocks, however, contain many ~1 mm scale holes indicating a major increase in porosity. This is associated with the presence of specular hematite, which is also associated with ~1 mm voids in metasedimentary rocks and large vugs in the QB (Burron et al., 2024), suggesting specular hematite may be related to particularly aggressive quartz dissolution.

Hydrothermal alteration has had major effects on the porosity of granitic rocks. Albitized granitic rocks have double the porosity of both typical unaltered granitic rocks (Schild et al., 2001) and unaltered metasedimentary rocks in the area. This is consistent with the observation of numerous ~1 μm pores in these rocks and the fact that albitization tends to create porous, brittle rock masses (Corriveau et al., 2016; 2022b; Potter et al., 2019).

Hematization has further increased the porosity of granitic rocks. Sample KN04-106, which shows only incipient hematization, shows only a slight increase in porosity, while KN04-66.6, which is strongly hematized, has ~410 % higher porosity than its albitized protolith. This is associated with a shift in pore size distribution to smaller pore diameters, particularly in the 10-100 nm range. As in hematized metasedimentary rocks, this shift is attributed to the formation of fine grained illite at the expense of larger feldspar grains.

The fact that hematized granitic rocks have somewhat lower porosity than hematized metasedimentary rocks is likely due to the smaller grain size of metasedimentary rocks favoring more complete illitization. Relict K-feldspar is commonly observed in hematized granitic rocks but not in hematized metasedimentary rocks.

Bleaching of granitic rocks is associated a relatively small shift in pore size distribution towards larger pores but a very significant ~280 % increase in overall porosity. This is the reverse of the effect of bleaching on metasedimentary rocks, where it is associated with a major modification to pore size distribution but not in overall porosity.

The differing mineralogy of the protoliths offers an explanation for this dichotomy. Hematized metasedimentary rocks contain only trace amounts of K-feldspar whereas hematized granitic rocks contain ~40% K-feldspar. In bleached granitic rocks, this K-feldspar has been replaced by a visibly porous intergrowth of illite and chlorite (Fig. 5c), suggesting this illitization of K-feldspar is the likely cause of the dramatic increase in porosity. Hematized metasedimentary rocks, in contrast, lacked feldspar that could be broken down, allowing the bleaching fluids to infiltrate without causing significant modification to mineralogy besides the dissolution of hematite.

Ferric altered granitic rocks have just 48% the porosity of their bleached granitic protoliths. This change is due to the precipitation of goethite within pore space (Fig. 5d). These minerals have a wide range in grain size, with <1 μm grains finely intergrown with illite and larger aggregates and grains infilling larger pores. This is accompanied by a shift in pore size distribution towards larger pores, suggesting smaller pores were preferentially infilled. A suite of

alteration minerals comprising goethite, calcite, vanadinite, and U3 U-minerals, is observed to seal fractures in some metasedimentary rocks (Fig. 3b, c).

The infiltration of low temperature meteoric fluids commonly leads to the formation of Fe (hydr)oxides at the expense of reduced Fe-bearing minerals, such as biotite, causing volume expansion (Bazilevskaya et al., 2013; 2015; Navarre-Sitchler, et al., 2015; Anovitz et al., 2021). While this process leads to fracturing and enhanced weathering in fresh crystalline rocks (Brantley et al., 2014; Bazilevskaya et al., 2015; Anovitz et al., 2021), it appears to have had the opposite effect in the already porous and fractured Kiggavik rocks, where volumetric changes were accommodated by infilling of pore/fracture space.

Implications for U Mineralization

The Kiggavik deposits have been affected by many fluid events spanning ~1.83 Ga (Sharpe et al., 2015; Shabaga et al., 2017; 2020; Grare et al., 2020; Burron et al., 2024; 2025; in review). These events fall into five main stages: 1) albitization, 2) hematization, 3) bleaching and U1 mineralization, 4) Resetting events and U2 mineralization, and 5) ferric alteration and U3 mineralization (Burron et al., in review). The first two stages are associated with an increase in porosity of metasedimentary rocks and the first three are associated with an increase in the porosity of granitic rocks, which likely played a role in subsequent stages.

Albitization creates porous rock masses that are preferential sites for further hydrothermal circulation and potential mineralization (Corriveau et al., 2016; 2022b; Potter et al., 2019), a process which may have facilitated U mineralization at Kiggavik (Burron et al., 2024; 2025). The observation that albitized granitic rocks have a similar porosity, pore size distribution, and SSA to hydrothermal quartz of the QB also supports the interpretation that

essentially all primary in igneous minerals within the granitic rocks have been metasomatically replaced.

Hematization has also increased the porosity of affected rocks. The QB, which is present in the cores of most Kiggavik U deposits and prospects, and may be genetically related to hematization (Grare et al., 2018; 2020; Burron et al., 2024), has been interpreted to influence mineralization by acting as a barrier to the flow of mineralizing fluids (Grare et al., 2018; 2020). The observation that the QB is significantly less porous than the hematized metasedimentary rocks surrounding it lends credence to this theory. Unaltered metasedimentary rocks are even less porous than the QB, suggesting that any fluid entering the basement rocks would have channeled into these porous hematized zones.

The relatively high porosity of these zones was preserved or enhanced by bleaching and later fluid events, which formed U1 at 1553 ± 16 Ma and U2 at 1440 ± 21, 1417 ± 17 Ma, 1276.4 ± 8.7 Ma, 1249 ± 33 Ma, 937 ± 24 Ma, and 274 ± 69 Ma (Burron et al., 2024). These zones of high porosity have proven persistent over > 1 Ga timescales, which doubtlessly contributed to the long history of U mobility and alteration in these deposits. Of all the fluid events affecting Kiggavik over ~1.83 Ga only the geologically recent infiltration of low temperature meteoric fluids has measurably reduced the porosity of the affected rocks.

Implications for radionuclide mobility

Igneous rocks are generally considered to have very low porosities (e.g. Schild et al., 2001). Metasedimentary and metavolcanic rocks in the Kiggavik area, however, have significantly lower porosities than granitic rocks. This is at least partially due to the effects of albitization, which is more pervasive in granitic rocks (Burron et al., 2024). The albitization of

granitic rocks in the Kiggavik deposits is invisible to the naked eye and requires SEM examination to be detected; therefore simple identification of lithology, alteration, and fracture distribution may not be enough to confidently predict the porosity of DGR host rocks.

Albitization of granitic rocks has also been observed at the Forsmark, Sweden, DGR site (Petersson et al., 2012). Surprisingly, investigation of albitized granitic rocks at the Forsmark site did not find a substantially higher porosity compared to unalbitized granitic rocks (Petersson et al., 2012). This may be due to the fact that the immersion method used only measures connected porosity, which is lower than the total porosity measured by USAXS, or due to subsequent metamorphic recrystallization which may have reduced any porosity formed during albitization.

Burron et al. (2025) observed that the ~36-471 Ka infiltration of oxidized subglacial waters has caused multiple widespread episodes of disturbance to Kiggavik U-minerals, mainly via leaching of soluble decay chain isotopes. Isotopic overprinting and isotopic disturbance of U-minerals is more extensive and has occurred more recently in granitic rocks versus metasedimentary rocks (Burron et al., 2025). The much larger porosity of bleached granitic rocks versus bleached metasedimentary rocks provides an obvious explanation for this. Although the complex history of hydrothermal alteration affecting these rocks is broadly similar in both lithologies (Burron et al., 2024; in review), it has affected their porosity differently due to differences in mineralogy and grain size.

Geologically recent fluid infiltration events have caused only limited amounts of short range (~< 5 cm) U mobility, with reduction by U and Ti oxide minerals and adsorption onto clay minerals surfaces likely retarding U mobility (Burron et al., 2025). The ~50% reduction in porosity due to the precipitation of Fe (hydr)oxides, ± calcite, vanadinite, and the U-minerals

themselves associated with this subglacial alteration offers an additional reason for the lack of observed long range U mobility. In some cases these minerals can be clearly observed sealing fractures through which U appears to have been mobilized (Fig. 3b, c; 8).

Goethite is widespread in the pores of ferric altered rocks, whereas other minerals associated with ferric alteration such as calcite, vanadinite, and U3 U-minerals tend to be concentrated into smaller areas such as redox interfaces and fracture systems. These minerals thus play complimentary roles in restricting U-mobility, with goethite sealing pores of all sizes in the matrix while other minerals seal the fractures that provide conduits for rapid fluid infiltration. Goethite is absent in areas within 10-100's of μm of U3 U-minerals, leaving a narrow band of enhanced porosity between the geothite-bearing matrix and U3 (Fig. 8). This suggests that when geothite precipitates before U3 it must be dissolved to clear pore space before U-bearing fluids can more widely infiltrate the matrix. Multiple closely spaced U3 fronts are observed in some samples (Burron et al., 2025); this may be due to the pore-filling effects of ferric alteration progressively reducing the ability of fluids to infiltrate the rock matrix so that subsequent fluid pulses do not penetrate as far.

This situation has significant parallels to the fracture sealing and pore clogging observed in the Maqarin analogue site in Jordan. Pyrometamorphism of bituminous limestones at Maqarin has produced natural cementitious material that interacted with meteoric water to produce hyperalkaline (pH ~12.5-12.9) groundwaters, which are considered to be an excellent analogue for the alkaline plume that would be created by groundwaters interacting with cements used in many low/intermediate level radioactive waste repositories (Linklater et al., 1996; Smellie, 1998; Shoa et al., 2013; Martin et al., 2016; Watson et al., 2016). Biomicrite country rocks at Maqarin

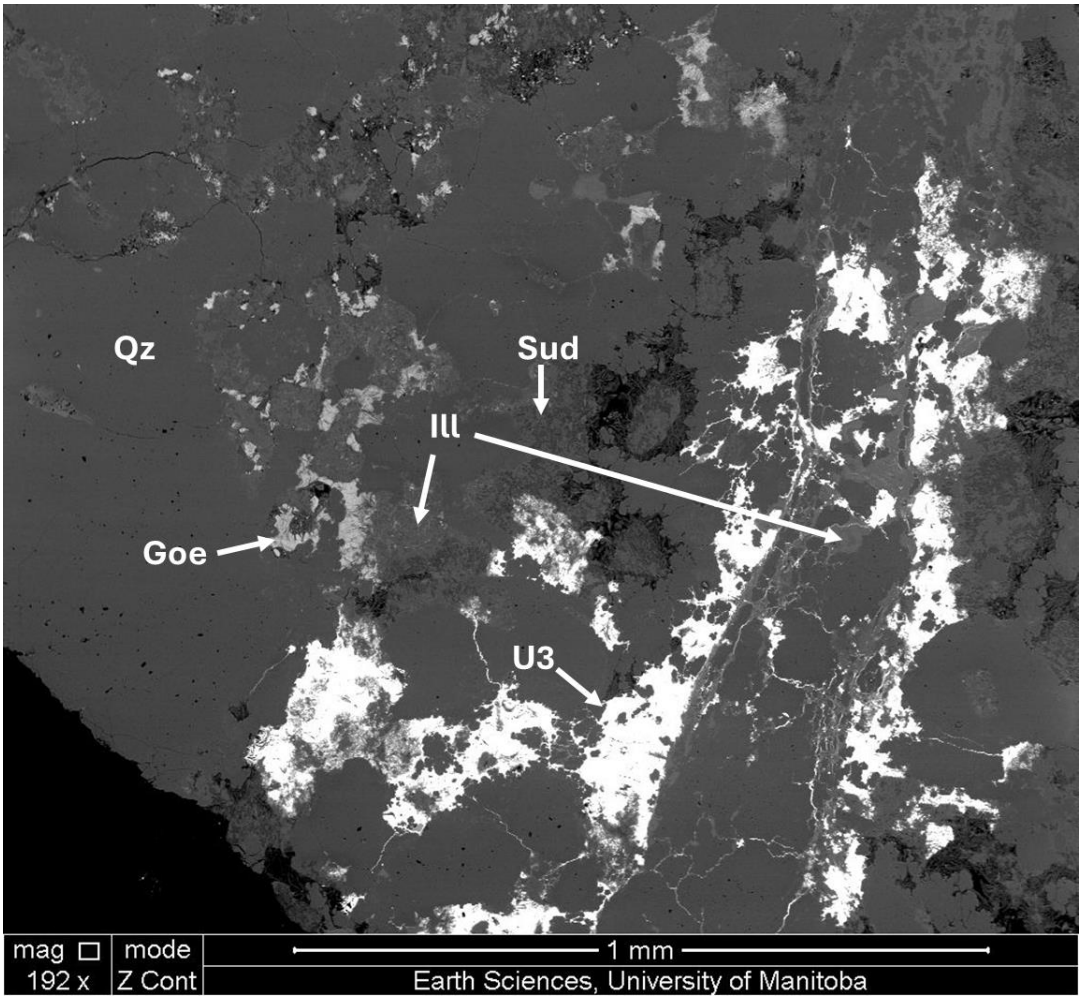

Figure 8. U3 uraninite and illite sealing fractures within a quartz vein. Large amounts of goethite infill pore space throughout the matrix of the sample, but is not present within ~50 µm of U3 (MZ-10-01-120). Abbreviations: Goe = goethite, sud = sudoite, Qz = quartz, Ill = illite.

have a high porosity (~30%) and are extensively fractured (Smellie, 1998; Shoa et al., 2013; Martin et al., 2016; Watson et al., 2016). The infiltration of hyperalkaline waters along these fractures has sealed many of them through the precipitation of Ca-Al-S-OH gels, ettringite ($Ca_6Al_2(SO_4)_3$ $(OH_{12}\cdot 26(H_2O))$, thaumasite ($Ca_3Si(CO_3)(SO_4)(OH)_6\cdot 12(H_2O)$), calcite, and other minerals (Linklater et al., 1996; Smellie, 1998; Shoa et al., 2013; Martin et al., 2016; Watson et al., 2016). Mineral precipitation has also significantly reduced porosity in the host rock matrix near these fractures (Linklater et al., 1996; Smellie, 1998; Shoa et al., 2013; Martin et al., 2016; Watson et al., 2016). Although modelling predicts near total pore-filling near fracture/vein margins (Linklater et al., 1996; Shoa et al., 2013; Watson et al., 2016), the porosity reduction actually observed at Maqarin is closer to ~30-40% (Martin et al., 2016). While this pore clogging is significant, it extends only ~4-30 mm beyond fracture/vein margins (Linklater et al., 1996; Smellie, 1998; Shoa et al., 2013; Martin et al., 2016; Watson et al., 2016).

The large difference in chemistry between infiltrating subglacial waters at Kiggavik and hyperalkaline waters at Maqarin complicates a direct comparison. In addition to the much lower pH (presumably near neutral to slightly alkaline given the precipitation of calcite) of subglacial Kiggavik waters, Kiggavik waters also contained more redox-sensitive elements such as Fe, U, and V, and less alkali elements such as Na and K, compared to Maqarin waters. Fluid-host rock reactions at Maqarin were largely driven by changes in pH (Linklater et al., 1996; Smellie, 1998; Shoa et al., 2013; Martin et al., 2016; Watson et al., 2016), while redox reactions were more important at Kiggavik. Evolution towards lower pH and higher S contents in fluids drove dissolution of early pore-clogging minerals and precipitation of later secondary minerals at Maqarin (Martin et al., 2016; Watson et al., 2016), whereas evolution of fluid from oxidizing

(geothite-precipitating) to reducing (uraninite-precipitating) conditions appear to have driven dissolution-precipitation at Kiggavik.

Nevertheless, it is notable that compared to Maqarin, the porosity reduction observed at Kiggavik extends much further into the host rock, > 50 mm in some samples, and fills a somewhat larger proportion of pore space. The limited penetration of the matrix by Maqarin waters may be the result of fracture armoring rapidly cutting off fluid ingress (Martin et al., 2016). The highly reactive nature of hyperalkaline Maqarin fluids would almost certainly have encouraged rapid mineralization. The presence of preexisting pore waters and very fine (~<100 nm) size of these pores (Martin et al., 2016) may also have contributed to the short range of penetration.

The dissolution of cementitious materials is considered to be a major source of ions which may then precipitate to fill pore space with Ca-Al-S-OH phases in a DGR (Linklater et al., 1996; Smellie, 1998; Shoa et al., 2013; Martin et al., 2016; 2023). The observation of Fe and U minerals playing a similar role at Kiggavik suggests that dissolution of metallic DGR components (i.e. Cu-steel canister) and even the waste form itself could also be relevant to the evolution of overall site porosity if these components came into contact with oxidized waters.

Mineral precipitation and resulting fracture sealing and pore clogging can occur under a wide range of conditions and would be relevant to geologic repositories for both low/intermediate and high level nuclear wastes. Although complete filling of pore space is not observed at either Maqarin (Martin et al., 2016; 2023) or Kiggavik, the observations of Burron et al. (2025) and this study suggest that even moderate degrees of secondary mineral precipitation may have significant impacts on radionuclide mobility. This is consistent with experimental

observations indicating the rate of U redeposition exceeds the rate of U transport in the subsurface, limiting U mobility (Wronkiewicz and Buck, 1999).

Conclusions

Multiple stages of hydrothermal alteration have substantially modified the porosity of both granitic and metasedimentary rocks in the Kiggavik U deposits, with granitic rocks being significantly more affected by these changes. The nature of the effect of hydrothermal alteration on porosity is variable and dependent on the nature of the fluids as well as site specific factors such as the mineralogy, grain size, and preexisting porosity of the host rocks. Most stages of alteration (albitization, hematization, and bleaching) have increased porosity, whereas ferric alteration associated with geologically recent subglacial fluid infiltration and U mobility has reduced the porosity of affected rocks by more than half.

The precipitation of Fe (hydr)oxides, calcite, U-minerals, and vanadinite associated with ferric alteration has infilled porosity and sealed fractures, inhibiting radionuclide mobility. While oxidized subglacial fluids are capable of mobilizing radionuclides such as U, the precipitation of secondary minerals limits the overall scale of this mobility. This behavior is similar to what has been observed at other natural analogue sites, suggesting that such processes are significant under a range of physical and chemical conditions, and that the reprecipitation of radionuclides and other dissolved repository materials may occur over relatively short distances and timescales.

References

Anovitz, L. M., Cheshire, M. C., Hermann, R. P., Gu , X., Sheets, J. M., Brantley, S. L., Cole, D. R., Ilton, E. S., Mildner, D. F. R., Gagnon, C., Allard, L. F., and Littrell, K. C., 2021, Oxidation and associated pore structure modification during experimental alteration of granite. Geochemica et Cosmochemica Acta; **292**, 532–556.

AREVA Resources Canada Inc., 2011, Kiggavik Project EIS: Popular Summary; Tier 1, v. 1: p. 51.

Ashcroft, G., 2020. The geochemistry and geochronology of the End Deposit, NE Thelon region, Nunavut, Canada: insight into the Athabasca Basin's closest relative. MSc thesis, Winnipeg, Canada, University of Manitoba. 217 pages.

Bazilevskaya, E. A., Lebedeva, M., Pavich, M., Rother, G., Parkinson, D., Cole, D. R., Brantley, S. L., 2013, Where fast weathering creates thin regolith and slow weathering creates thick regolith. Earth Surf Process Landforms; **38**, 847–858.

Bazilevskaya, E. A., Rother, G., Mildner, D. F. R., Pavich, M., Cole, D. R., Bhatt, M. P., Jin, L., Steefel, C., and Brantley, S. L., 2015. How oxidation and dissolution in diabase and granite control porosity during weathering. Soil Sci Soc, Am J; **79**, 55–73.

Boers, C., 2017, Investigation of pore evolution in concrete by spin-echo small angle neutron scattering. B.Sc Thesis, Delft University of Technology, NL.

Brantley, S.L., M. Lebedeva, and E. Bazilevskaya. 2014, Relating weathering fronts for acid neutralization and oxidation to pCO 2 and pO 2. In: H.D. Holland and K.K. Turekian, editors, Treatise on geochemistry. 2nd ed. Elsevier, Oxford. p. 327–352.

Burron, I., Fayek, M., Brown, J., Quirt, D., 2024. Remnants of a 1.55 Ga Hybrid Between Metasomatic Iron-Alkali-Calcic and Unconformity-Related Uranium Environments in the Kiggavik Region, Nunavut, Canada. Economic Geology; **119**, 1861–1888.

Burron, I., Fayek, M., and Brown, J., 2025. Glaciation-induced radionuclide release: implications for geological disposal of nuclear waste. Geology; doi: https://IAEA doi.org/10.1130/G53021.1.

Brachman, R. W. I., Rowe, R. K., Baral, A., Hosney, M. S., Su, G., Nguyen, T. S., Brown, J., and Lange, K., 2021, Bentonite swelling characteristics with a hypersaline multi-component pore fluid. Can. Geotech. J.; **58**, 367–376, dx.doi.org/10.1139/cgj-2019-0558.

Busch, A., Kampman, N., Bertier, P., Pipich, V., Feoktystov, A., Rother, G., Harrington, J., Leu, L., Aertens, M., and Jacops, E., 2018, Predicting effective diffusion coefficients in mudrocks using a fractal model and small-angle neutron scattering measurements. Water Resources Research; **54**, 7076–7091. https://doi.org/10.1029/2018WR02342.

Chamberlain, K.R., Schmitt, A.K, Swapp, S.M., Harrison, T.M., Swoboda-Colberg, N., Bleeker, W., Peterson, T.D., Jefferson, C.W., and Khudoley, A.K., 2010, In situ U–Pb SIMS (IN-SIMS) micro-baddeleyite dating of mafic rocks: Method with examples. Precambrian Research; **183**, 379–387.

Chi, G., Haid, T., Quirt, D., Fayek, M., Blamey, N., and Chu, H., 2016, Petrography, fluid inclusion analysis, and geochronology of the End uranium deposit, Kiggavik, Nunavut, Canada. Mineralium Deposita; **52**, 211–232.

Corriveau, L., Montreuil, J-F., and Potter, E.G., 2016, Alteration Facies Linkages Among Iron Oxide Copper-Gold, Iron Oxide-Apatite, and Affiliated Deposits in the Great Bear Magmatic Zone, Northwest Territories, Canada. Economic Geology; **111**, 2045–2072.

Corriveau, L., Montreuil, J.-F., Potter, E.G., Blein, O., and De Toni, A.F., 2022b, Mineral systems with IOCG and affiliated deposits: Part 3 - metal pathways and ore deposit model, *In* Corriveau, L., Potter, E.G., and Mumin, A.H., Eds., Mineral Systems with Iron Oxide-Copper-Gold (IOCG) and Affiliated Deposits, Special Paper 52: Geological Association of Canada, Ottawa, Canada, p. 89–121.

Cramer, J. and Smellie, J., 1994, Final report of the AECL/SKB Cigar Lake analog study: SKB Technical Report 94-04, 226 p.

Dixon, D. A., Man, A., Stone, J., Rimal, S., Siemens, G., Abootalebi, P., and Birch, K., 2016, Backfilling and sealing materials for a deep geological repository. In Proceedings of the 3rd Canadian Conference on Nuclear Waste Management, Decommissioning and Environmental Restoration, Ottawa, ON, Canada, 11–14 September 2016.

Evins, L. A., Jensen, K. A., and Ewing, R. C., 2005, Uraninite recrystallization and Pb loss in the Oklo and Bangombé natural fission reactors, Gabon. Geochimica et Cosmochimica Acta; **69**, 6, 1589 –1606.

Fayek, M., and Brown, J., 2021, Natural and anthropogenic analogues for high-level nuclear waste disposal repositories: A review. The Canadian Mineralogist; **59**, 287–317.

Herz-Thyshen, R. J., Miller, Q. R. S., Rother, G., Kazuba, J. P., Ashley, T. C., Littrell, K. C., 2021, Nanoscale Interfacial Smoothing and Dissolution during Unconventional Reservoir

Stimulation: Implications for Hydrocarbon Mobilization and Transport. ACS Applied Materials and Interfaces; **13**, 15811–15819.

Hiatt, E.E., Kyser, T.K., and Dalrymple, R.W., 2003, Relationships among sedimentology, stratigraphy and diagenesis in the Proterozoic Thelon basin, Nunavut, Canada: Implications for paleo-aquifers and sedimentary-hosted mineral deposits. Journal of Geochemical Exploration; **80**, 221–240.

Fuchs H.D., Hilger W, and Prosser E., 1986, Geology and exploration history of the Lone Gull property. Canadian Institute of Mining and Metallurgy Special Publication; **33**, 286–292.

Gall, Q., Peterson, T.D., and Donaldson, J.A., 1992, Early Proterozoic stratigraphy of the Thelon and Baker Lake basins, District of Keewatin: a proposed revision, In, Current Research, Part C, Geological Survey of Canada Paper 92-1C, p. 129–137.

Grare, A., Lacombe, O., Mercadier, J., Benedicto, A., Marie Guilcher, M., Trave, A., Ledru, P., and Robbins, J., 2018a, Fault zone evolution and development of a structural and hydrological barrier: the quartz breccia in the Kiggavik area (Nunavut, Canada) and its control on uranium mineralization. Minerals; **8**, doi:10.3390/min8080319.

Grare, A., Benedicto, A., Mercadier, J., Lacombe, O., Trave, A., Guilcher, M., Richard, A., Ledru, P., Blain, M., Robbins, J., and Lach, P., 2020, Structural controls and metallogenic model of polyphase uranium mineralization in the Kiggavik area (Nunavut, Canada). Mineralium Deposita, doi:10.1007/s00126-020-00957-x.

IAEA (International Atomic Energy Agency), 1999, Use of natural analogues to support radionuclide transport models for deep geological repositories for long lived radioactive wastes: IAEA-TECDOC-1109.

IAEA. 2013. Characterization of swelling clays as components of the engineered barriers system for geological repositories. International Atomic Energy Agency, IAEA-TECDOC-1718.

IAEA, 2020, Design Principals and Approaches for Radioactive Waste Repositories: IAEA Nuclear Energy Series No. NW-T-1.27, 89 pages.

Ilavsky, J., 2012, Nika: software for two-dimensional data reduction. J. Appl. Crystallogr.; **45**, 2, 324–328, https://doi.org/10.1107/S0021889812004037.

Ilavsky, J., and Jemian, P. R., 2009, Irena: tool suite for modeling and analysis of small-angle scattering. J. Appl. Crystallogr.; **42**, 2, 347–353, https://doi.org/10.1107/S0021889809002222.

Janeczek, J., and Ewing, R. W., 1995, Mechanisms of lead release from uraninite in the natural fission reactors in Gabon. Geochimica et Cosmochimica Acta; **59**, 10, 1917–1931.

Jefferson, C.W., Pehrsson, S., Peterson, T., Chorlton, L., Davis, W., Keating, P. et al., 2011, Northeast Thelon region geoscience framework—new maps and data for uranium in Nunavut: Geological Survey of Canada Open File 6949, 1 sheet, doi:10.4095/288791.

Johnstone, D., 2017, Lithostratigraphic and structural controls of uranium mineralization in the Kiggavik East Zone, Centre Zone, and Main Zone deposits, Thelon Basin, Nunavut: unpublished MSc. Thesis, University of Regina, 193 p.

LeCheminant, A.N., and Heaman, L.M., 1989, Mackenzie igneous events, Canada: Middle Proterozoic hotspot magmatism associated with ocean opening. Earth and Planetary Science Letters; **96**, 38–48.

Linklater, C. M., Albinsson, Y., Alexander, W. R., Casas, I., McKinley, I. G., Sellin, P., 1996, A natural analogue of high-pH cement pore waters from the Maqarin area of northern Jordan: Comparison of predicted and observed trace-element chemistry of uranium and selenium. Journal of Contaminant Hydrology; **21**, 59–69.

Liu, K.-Q., Jin, Z.-J., Lian-Bo Zeng, L.-B., Sun, M.-D., Liu, B., Jang, H. W., Safaei-Farouji, M., Shokouhimer, M., and Ostadhassan, M., 2022, Microstructural analysis of organic matter in shale by SAXS and WAXS methods, Petroleum Science, 19, 979-989. https://doi.org/10.1016/j.petsci.2022.01.012.

Martin, L. H. J., Leemann, A., Milodowski, A. E., Mäder, U. K., Münch, B., Giroud, N., 2016, A natural cement analogue study to understand the long-term behaviour of cements in nuclear waste repositories: Maqarin (Jordan). Applied Geochemistry; **17**, 20-34.

Martin, L., Kosakowski, G., Papafotiou, A., and Smith, P. A., 2023, Evolution of the Sealing System Porosity and its Impact on Performance. nagra working report NAB 23-21, 127 pages.

Montavon, G., Ribet, S., Hassan Loni, Y., Maia, F., Bailly, C., David, K., Lerouge, C., Madé, B., Robinet, J. C., and Grambow, G., 2022, Uranium retention in a Callovo-Oxfordian clay rock formation: From laboratory-based models to in natura conditions, Chemosphere, 299, https://doi.org/10.1016/j.chemosphere.2022.134307.

Navarre-Sitchler, A., Brantley, S. L., and Rother, G., 2015; How Porosity Increases During Incipient Weathering of Crystalline Silicate Rocks. Reviews in Mineralogy & Geochemistry; **80**, 331–354.

Nuclear Energy Agency (NEA), 2020, Two decades of Safety Case Development: An IGSC 20th Anniversary Brochure, 52 pages.

Nuclear Waste Management Organization (NWMO), 2017, Postclosure safety assessment of a used fuel repository in crystalline rock: NWMO Technical Report TR-2017-02, 718 p.

Pehrsson, S.J., Berman, R.G., and Davis, W.J., 2013, Paleoproterozoic orogenesis during Nuna aggregation: A case study of reworking of the Rae craton, Woodburn Lake, Nunavut. Precambrian Research; **232**, 167–188.

Peterson, T.D., Van Breeman, O., Sandeman, H., and Cousens, B., 2002, Proterozoic (1.85-1.75 Ga) igneous suites of the Western Churchill Province: granitoid and ultrapotassic magmatism in a reworked Archean hinterland. Precambrian Research; **119**, 73–100.

Peterson, T.D., 2006, Geology of the Dubawnt Lake area, Nunavut-Northwest Territories: Geological Survey of Canada Bulletin 580:51.

Peterson, T.D., Jefferson, C.W., and Anand, A., 2015, Geological setting and geochemistry of the ca. 2.6 Ga Snow Island Suite in the central Rae Domain of the Western Churchill Province, Nunavut: Geological Survey of Canada, Open File 7841, 29 p., doi:10.4095/296599.

Petersson, J., Stephens, M. B., Mattsson, H., and Möller, C. 2012, Albitization and quartz dissolution in Paleoproterozoic metagranite, central Sweden — Implications for the disposal of spent nuclear fuel in a deep geological repository. Lithos; **148**, 10–26.

Potter, E.G., Montreuil, J.-F., Corriveau, L., and Davis, W.J., 2019, The Southern Breccia Metasomatic Uranium System of the Great Bear Magmatic Zone, Canada: Iron Oxide-Copper-Gold (IOCG) and Albitite-Hosted Uranium Linkages, *in*, Eds., Decrée, S., and Robb, L., Ore Deposits: Origin, Exploration, and Exploitation, Geophysical Monograph 242, First Edition.

Radlinski, A., Ioannidis, M., Hinde, A., Hainbuchner, M., Baron, M., Rauch, H., and Kline, S., 2004a, Angstrom-to-millimeter characterization of sedimentary rock microstructure. J Colloid Interf Sci; **274**, 607–612.

Radlinski, A. P., Mastalerz, M., Hinde, A. L., Hainbuchner, M., Rauch, H., Baron, M., Lin, J. S., Fan, L., and Thiyagarajan, P., 2004b, Application of SAXS and SANS in evaluation of porosity, pore size distribution and surface area of coal. International Journal of Coal Geology; **59**, 245–271.

Radlinski, A., 2006, Small-Angle Neutron Scattering and the Microstructure of Rocks. Reviews in Mineralogy & Geochemistry; **63**, 363–397.

Rainbird, R.H., Hadlari, T., Aspler, L.B., Donaldson, J.A., LeCheminant, A.N., and Peterson, T.D., 2003, Sequence stratigraphy and evolution of the Paleoproterozoic intracontinental Baker Lake and Thelon basins, western Churchill Province, Nunavut, Canada. Precambrian Research; **125**, 21–53, doi:10.1016/S0301-9268(03)00076-7.

Rainbird, R.H., Davis, W.J., Pehrsson, S.J., Wodicka, N., Rayner, N., and Skulski, T., 2010, Early Paleoproterozoic supracrustal assemblages of the Rae domain, Nunavut, Canada: intracratonic basin development during supercontinent break-up and assembly. Precambrian Research; **181**, 167–186. doi:10.1016/j.precamres.2010.06.005.

Riegler, T., Lescuyer, J-L., Wollenburg, P., Quirt, D., and Beaufort, D., 2014, Alteration related to uranium deposits in the Kiggavik-Andrew Lake Structural Trend, Nunavut, Canada: New insights from petrography and clay mineralogy. The Canadian Mineralogist; **52**, 27–45.

Riegler, T., Beaufort, M-F., Allard, T., Pierson-Wickmann, A-C., and Beaufort, D., 2016, Nanoscale relationships between uranium and carbonaceous material in alteration halos around unconformity-related uranium deposits of the Kiggavik camp, Paleoproterozoic Thelon Basin, Nunavut, Canada. Ore Geology Reviews; **79**, 382–391.

Schild, M., Siegesmund, S., Vollbrecht, A., and Mazurek, M., 2001, Characterization of granite matrix porosity and pore-space geometry by in situ and laboratory methods. Geophys. J. Int.; **146**, 111–125.

Schindler, M., Legrand, C. A., and Hochella Jr., M. F., 2015, Alteration, adsorption and nucleation processes on clay–water interfaces: Mechanisms for the retention of uranium by altered clay surfaces on the nanometer scale. Geochemica et Chosmochemica Acta; **153**, 15–36, http://dx.doi.org/10.1016/j.gca.2014.12.020.

Scott, J.M.J., Peterson, T.D., and McCurdy, M.W., 2012, U, Th, and REE occurrences within Nueltin granite at Nueltin Lake, Nunavut: recent observations; Geological Survey of Canada. Current Research 2012-1, 11 p., doi: 10.4095/289393.

Scott, J.M.J., Peterson, T.D., Davis, W.J., Jefferson, C.W., and Cousens, B.L., 2015, Petrology and Geochronology of Paleoproterozoic intrusive rocks, Kiggavik uranium camp, Nunavut. Canadian Journal of Earth Sciences; **52**, 494–518.

Shabaga, B.M., Fayek, M., Quirt, D., Jefferson, C.W., and Camacho, A., 2017, Mineralogy, geochronology, and genesis of the Andrew Lake uranium deposit, Thelon Basin, Nunavut, Canada. Canadian Journal of Earth Sciences; **54**, 850–868.

Shabaga, B.M., Fayek, M., Quirt, D., Jefferson, C.W., and Ledru, P., 2020, Geochemistry and geochronology of the Kiggavik uranium deposit, Nunavut, Canada. Mineralium Deposita, doi:10.1007/s00126-020-01001-8.

Shoa, H., Kosakowski, G., Berner, U., Kulik, D., A., Mäder, U., Kolditz, O., 2013, Reactive transport modeling of the clogging process at Maqarin natural analogue site. Physics and Chemistry of the Earth; **64**, 21–31.

Sharpe, R., Fayek, M., Quirt, D., and Jefferson, C., 2015, Geochronology and Genesis of the Bong Uranium Deposit, Thelon Basin, Nunavut, Canada. Economic Geology; **110**, 1759–1777.

Simmons, A. M., and Stuckless, J. S., 2010, Analogues to features and processes of a high-level radioactive waste repository proposed for Yucca Mountain, Nevada: U.S. Geological Survey Professional Paper 1779, 195 p.

SKB, 2010, Spent nuclear fuel for disposal in the KBS-3 repository: Swedish Nuclear Fuel and Waste Management Co Technical Report TR-10-13, 91 p.

Smellie, J., and Karlsson, F., 1996, A reappraisal of some Cigar Lake issues of importance to performance assessment, SKB Technical Report 96-08, 101 p.

Smellie, J., 1998, MAQARIN natural analogue study: Phase III; SKB Technical Report TR-98-04, 383 pages.

Sonnenthal, E.L., and Spycher, N., 2001, Drift-scale coupled processes (DST and THC seepage) models: Las Vegas, Nevada, Bechtel SAIC Company, Report MDL-NBS-HS-000001 REV01, variously paginated.

Steefel, C.I. and Lichtner, P. C., 1998, Multicomponent reactive transport in discrete fractures II: Infiltration of hyperalkaline groundwater at Maqarin, Jordan, a natural analogue site. Journal of Hydrology; **209**, 200–224.

Watson, C., Wilson, J., Savage, D., Benbow, S., Norris, S., 2016, Modelling reactions between alkaline fluids and fractured rock: The Maqarin natural analogue. Applied Clay Science; **121-122**, 46–56, http://dx.doi.org/10.1016/j.clay.2015.12.004.

Wronkiewicz, D.J. and Buck, E.C., 1999, Uranium mineralogy and the geologic disposal of spent nuclear fuel. In: Uranium: Mineralogy, Geochemistry, and the Environment, (Burns, P.C. and Finch, R., Eds.). Min Soc Proc; **38**, 475-497.

Zhao, Y., Liu, S., Elsworth, D., Jiang, Y., and Zhu, J., 2014, Pore Structure Characterization of Coal by Synchrotron Small-Angle X-ray Scattering and Transmission Electron Microscopy. Energy and Fuels; **28**, 3704−3711, doi.org/10.1021/ef500487d.

Zhao, Y., Penga, L., Liu, S., Cao, B., Suna, Y., and Hou, B., 2019, Pore structure characterization of shales using synchrotron SAXS and NMR cryoporometry. Marine and Petroleum Geology; **102**, 116–125. https://doi.org/10.1016/j.marpetgeo.2018.12.041.

Table A1. Porosity, pore size distribution, and specific surface area (SSA) of rocks from the Kiggavik deposits.

Sample	Depth (m)	Lithology	Alteration	porosity (%)	SSA (m2/cm3)	Porosity in 3-10 nm (%)	SSA in 3-10 nm (%)	Porosity in 10-100 nm (%)	SSA in 10-100 nm (%)	Porosity in 100-1000 nm (%)	SSA in 100-1000 nm (%)	Porosity in 1000-7000 nm (%)	SSA in 1000-7000 nm (%)
END-10-02A	400	Metasedimentary	Unaltered	0.55	0.18	1.8	26.1	20.0	61.1	32.7	12.2	43.6	1.3
END-10-02A	400	Metasedimentary	Unaltered	0.55	0.16	1.8	25.0	20.0	62.5	32.7	13.8	45.5	1.5
END-10-02A	400	Metasedimentary	Unaltered	0.60	0.18	1.7	29.4	18.3	61.1	26.7	11.1	51.7	1.5
END-10-02A	400	Metasedimentary	Unaltered	0.54	0.20	1.9	31.0	22.2	55.0	29.6	10.0	48.1	1.2
END-10-02A	400	Metasedimentary	Unaltered	0.86	0.38	3.5	50.0	17.6	39.5	24.7	6.8	52.9	1.1
END-10-02A	400	Metasedimentary	Unaltered	0.62	0.31	3.2	41.9	25.8	48.4	29.0	7.7	41.9	0.8
END-10-02A	400	Metasedimentary	Unaltered	0.67	0.27	3.0	36.7	22.4	51.9	25.4	8.1	49.3	0.9
END-10-02A	400	Metasedimentary	Unaltered	0.75	0.30	2.7	40.0	20.3	50.0	27.0	8.3	48.6	1.0
Bong-49	277.5	Metasedimentary	Unaltered	0.70	0.09	0.0	0.1	10.0	73.3	22.9	23.3	67.1	3.4
Bong-49	277.5	Metasedimentary	Unaltered	0.84	0.15	1.2	23.3	10.8	62.0	14.5	10.7	73.5	2.4
Bong-49	277.5	Metasedimentary	Unaltered	0.53	0.20	1.9	26.0	22.6	60.0	30.2	9.5	45.3	1.3
Bong-49	277.5	Metasedimentary	Unaltered	0.60	0.16	1.7	16.9	18.3	68.8	38.3	16.9	41.7	1.6
Bong-49	277.5	Metasedimentary	Unaltered	0.57	0.23	3.5	36.5	21.1	52.2	26.3	7.8	50.9	1.3
Bong-49	277.5	Metasedimentary	Unaltered	0.63	0.18	1.6	23.3	19.0	66.7	25.4	11.1	54.0	1.5
Bong-49	277.5	Metasedimentary	Unaltered	0.57	0.26	3.5	35.8	24.6	53.8	29.8	8.1	42.1	0.9

Bong-49	277.5	Metasedimentary	Unaltered	0.64	0.35	4.7	42.9	25.0	48.6	28.1	6.3	42.2	0.7
Bong-49	277.5	Metasedimentary	Unaltered	0.68	0.46	4.4	45.7	30.9	50.0	29.4	5.4	33.8	0.5
Bong-49	277.5	Metasedimentary	Unaltered	0.64	0.31	3.1	38.7	25.0	54.8	29.7	7.7	40.6	0.7
Range				**0.53-0.86**	**0.09-0.46**	**0.0-4.7**	**0.1-50.0**	**10.0-30.9**	**39.5-73.3**	**14.5-38.3**	**5.4-23.3**	**33.8-73.5**	**0.5-3.4**
Avg (n=18)				**0.64 ± 0.09**	**0.24 ± 0.09**	**2.5 ± 1.2**	**31.6 ± 11.9**	**20.8 ± 5.0**	**56.6 ± 8.4**	**27.9 ± 4.9**	**10.3 ± 4.3**	**48.5 ± 9.5**	**1.3 ± 0.7**
END-10-03	42	Metasedimentary	Hematized	3.21	2.20	6.8	40.9	48.6	54.5	31.5	4.5	13.2	0.2
END-10-03	42	Metasedimentary	Hematized	4.59	3.30	7.8	45.5	47.3	51.5	31.5	4.2	13.5	0.2
END-10-03	42	Metasedimentary	Hematized	7.59	5.10	7.7	45.1	45.6	51.0	32.7	4.5	14.1	0.2
END-10-03	42	Metasedimentary	Hematized	4.66	3.50	8.8	48.6	43.5	45.7	34.0	4.3	13.7	0.2
END-10-03	42	Metasedimentary	Hematized	5.22	4.00	9.3	47.5	44.2	47.5	32.3	3.8	14.3	0.2
END-10-03	42	Metasedimentary	Hematized	5.06	3.40	7.5	44.1	41.7	50.0	33.1	4.4	18.1	0.3
END-10-03	42	Metasedimentary	Hematized	6.73	4.90	8.4	44.9	44.6	51.0	30.3	3.9	16.7	0.2
END-10-03	42	Metasedimentary	Hematized	4.86	3.00	7.1	46.7	39.6	53.3	29.7	4.3	23.6	0.4
END-10-03	42	Metasedimentary	Hematized	4.55	3.20	7.8	43.8	44.7	50.0	31.6	4.4	15.9	0.2
END-10-03	42	Metasedimentary	Hematized	6.38	4.70	8.2	40.4	48.9	53.2	30.8	4.3	12.1	0.2
END-10-03	42	Metasedimentary	Hematized	6.39	5.00	9.4	46.0	48.2	50.0	29.9	3.8	12.5	0.2
END-10-03	42	Metasedimentary	Hematized	6.03	4.80	9.9	47.9	47.8	47.9	30.0	3.8	12.3	0.2
END-10-03	42	Metasedimentary	Hematized	5.22	4.20	9.7	45.2	48.3	45.2	30.5	3.8	11.5	0.2
Bong-49	131	Metasedimentary	Hematized	3.93	2.40	7.7	45.8	39.4	50.0	25.9	4.6	27.2	0.3

Bong-49	131	Metasedimentary	Hematized	5.01	3.50	9.2	51.4	40.3	45.7	25.6	3.7	24.6	0.3
Bong-49	131	Metasedimentary	Hematized	4.59	3.50	10.0	51.4	42.0	45.7	26.0	3.4	21.7	0.2
Bong-49	131	Metasedimentary	Hematized	5.26	3.70	9.2	48.6	41.4	48.6	24.1	3.5	25.3	0.3
Bong-49	131	Metasedimentary	Hematized	5.48	4.60	12.0	54.3	40.3	41.3	22.0	2.6	25.7	0.2
Bong-49	131	Metasedimentary	Hematized	3.79	2.90	10.4	55.2	38.6	41.4	27.4	3.4	23.6	0.3
Bong-49	131	Metasedimentary	Hematized	3.76	2.70	8.8	48.1	42.5	48.1	26.8	3.7	21.5	0.3
Bong-49	131	Metasedimentary	Hematized	4.25	3.20	10.3	56.3	37.8	40.6	25.3	3.4	26.3	0.3
Bong-49	131	Metasedimentary	Hematized	5.62	4.10	10.6	53.7	36.8	41.5	23.4	3.2	29.2	0.3
Bong-49	131	Metasedimentary	Hematized	4.31	3.00	9.5	50.0	38.3	46.7	27.2	4.0	25.0	0.3
Bong-49	131	Metasedimentary	Hematized	4.16	2.80	8.8	50.0	35.3	42.9	27.8	4.3	28.1	0.3
Bong-49	131	Metasedimentary	Hematized	3.52	2.00	7.4	50.0	33.5	45.5	32.9	5.5	26.5	0.4
End-09-10	126	Metasedimentary	Hematized	7.55	3.00	4.0	33.0	31.8	56.7	36.2	8.3	27.9	0.6
End-09-10	126	Metasedimentary	Hematized	5.18	2.40	5.1	38.8	33.4	54.2	37.5	7.5	24.2	0.5
End-09-10	126	Metasedimentary	Hematized	6.85	3.20	5.2	37.5	34.6	56.3	36.4	7.2	23.8	0.5
End-09-10	126	Metasedimentary	Hematized	6.49	2.70	4.6	37.0	31.0	55.6	36.2	8.1	28.0	0.6
End-09-10	126	Metasedimentary	Hematized	7.32	3.30	5.2	39.4	32.2	54.5	35.8	7.3	27.0	0.5
End-09-10	126	Metasedimentary	Hematized	7.23	3.20	4.9	37.5	33.4	56.3	37.3	7.8	24.3	0.5
End-09-10	126	Metasedimentary	Hematized	7.47	3.10	4.6	35.5	30.4	54.8	36.3	8.1	28.7	0.5
End-09-10	126	Metasedimentary	Hematized	8.72	3.60	4.4	33.3	32.7	55.6	37.6	8.3	25.4	0.5

End-09-10	126	Metasedimentary	Hematized	8.96	3.90	4.7	35.9	34.3	56.4	37.5	7.9	23.4	0.5
End-09-10	126	Metasedimentary	Hematized	6.25	3.30	6.7	45.5	31.7	48.5	31.2	5.5	30.4	0.5
End-09-10	126	Metasedimentary	Hematized	6.81	3.30	6.0	42.4	30.9	51.5	32.3	6.1	30.9	0.5
End-09-10	126	Metasedimentary	Hematized	8.02	3.90	6.1	43.6	32.4	51.3	32.0	6.2	29.5	0.5
End-09-10	126	Metasedimentary	Hematized	6.27	3.10	6.0	41.9	33.3	51.6	32.0	6.1	29.6	0.5
End-09-10	126	Metasedimentary	Hematized	7.63	3.80	6.0	39.5	34.3	52.6	32.6	6.1	27.2	0.5
End-09-10	126	Metasedimentary	Hematized	12.25	6.50	7.5	46.2	34.3	49.2	29.6	5.1	28.7	0.4
End-09-10	126	Metasedimentary	Hematized	10.92	5.70	7.1	43.9	34.2	49.1	33.0	5.8	25.7	0.4
End-09-10	126	Metasedimentary	Hematized	10.09	5.60	7.5	44.6	35.6	48.2	33.7	5.5	23.2	0.4
End-09-10	126	Metasedimentary	Hematized	8.42	3.90	5.6	38.5	32.6	51.3	33.2	6.7	28.8	0.5
Range				**3.21-12.25**	**2.0-6.5**	**4.0-7.5**	**33.0-46.2**	**30.6-35.6**	**40.6-56.7**	**22.0-37.6**	**2.6-8.3**	**11.5-30.9**	**0.2-0.6**
Avg (n = 48)				**6.20 ± 2.02**	**3.66 ± 0.98**	**7.5 ± 2.0**	**44.5 ± 5.8**	**38.4 ± 5.8**	**49.8 ± 4.5**	**31.2 ± 4.1**	**5.2 ± 1.7**	**22.9 ± 6.1**	**0.4 ± 0.1**
Bong-49	131	Metasedimentary	Bleached	5.23	2.90	7.5	51.7	30.8	44.8	30.4	5.2	31.3	0.4
Bong-49	131	Metasedimentary	Bleached	5.21	2.90	7.5	51.7	29.6	44.8	28.1	4.8	34.8	0.5
Bong-49	131	Metasedimentary	Bleached	4.75	1.70	4.2	44.1	22.1	45.9	29.9	7.6	43.6	0.9
Bong-49	131	Metasedimentary	Bleached	4.50	2.30	6.7	52.2	28.8	47.8	24.7	4.8	39.8	0.5
Bong-49	131	Metasedimentary	Bleached	2.81	1.50	6.2	46.0	30.4	46.0	30.0	5.6	33.0	0.5
Bong-49	131	Metasedimentary	Bleached	4.32	2.40	7.3	50.0	30.3	45.8	25.9	4.6	36.3	0.5
Bong-49	131	Metasedimentary	Bleached	2.93	1.30	5.6	46.2	27.1	48.5	27.1	6.1	39.8	0.6

Bong-49	131	Metasedimentary	Bleached	3.60	1.50	4.9	43.3	25.4	46.0	26.8	6.2	42.7	0.7
Bong-49	131	Metasedimentary	Bleached	4.44	2.50	7.8	52.0	30.0	44.0	25.9	4.4	36.3	0.5
Bong-49	131	Metasedimentary	Bleached	2.80	1.50	6.6	46.0	30.5	48.0	25.4	4.8	37.1	0.5
Bong-49	131	Metasedimentary	Bleached	4.66	1.90	5.4	48.4	24.5	45.3	34.2	7.9	36.0	0.6
Bong-49	131	Metasedimentary	Bleached	4.02	1.70	4.9	47.6	25.6	45.9	35.8	7.6	33.7	0.6
Bong-49	131	Metasedimentary	Bleached	3.26	1.60	6.0	45.6	29.8	48.1	31.1	6.1	33.0	0.5
Bong-49	131	Metasedimentary	Bleached	3.25	1.50	5.4	42.7	28.3	48.7	27.7	5.8	38.5	0.6
Bong-49	131	Metasedimentary	Bleached	3.63	2.00	7.1	46.5	32.0	48.5	26.6	4.9	34.3	0.5
Bong-49	131	Metasedimentary	Bleached	3.07	1.30	5.0	40.0	29.2	53.1	31.9	7.3	34.2	0.7
Bong-49	131	Metasedimentary	Bleached	2.56	1.20	6.0	44.2	30.1	50.8	31.3	6.3	32.9	0.6
Bong-49	131	Metasedimentary	Bleached	3.42	1.50	5.5	44.0	28.8	51.3	28.8	6.3	37.6	0.6
End-09-10	126	Metasedimentary	Bleached	10.77	4.00	4.2	35.0	29.0	55.0	40.9	9.8	25.9	0.7
End-09-10	126	Metasedimentary	Bleached	12.26	4.80	4.6	35.4	30.3	56.3	38.4	8.5	26.8	0.6
End-09-10	126	Metasedimentary	Bleached	9.47	3.50	4.0	34.3	28.9	54.3	40.5	9.7	26.6	0.7
End-09-10	126	Metasedimentary	Bleached	8.42	3.30	4.3	33.3	29.6	57.6	36.3	8.2	30.0	0.7
End-09-10	126	Metasedimentary	Bleached	11.24	4.20	4.4	40.5	26.2	50.0	41.2	9.3	28.3	0.7
End-09-10	126	Metasedimentary	Bleached	7.93	3.00	4.5	40.0	25.8	50.0	38.5	8.7	31.2	0.8
End-09-10	126	Metasedimentary	Bleached	7.64	3.10	4.8	41.9	26.9	48.4	40.2	8.4	28.0	0.7
End-09-10	126	Metasedimentary	Bleached	9.42	4.40	6.2	43.2	29.5	47.7	38.1	7.3	26.1	0.5

End-09-10	126	Metasedimentary	Bleached	9.56	4.90	7.5	49.0	28.7	42.9	38.2	6.3	25.5	0.5
End-09-10	126	Metasedimentary	Bleached	11.22	4.60	5.7	45.7	25.7	45.7	40.1	8.0	28.6	0.7
End-09-10	126	Metasedimentary	Bleached	9.06	4.30	6.6	46.5	29.4	48.8	38.3	7.0	25.7	0.5
End-09-10	126	Metasedimentary	Bleached	8.47	5.00	8.6	52.0	30.8	42.0	36.6	5.6	24.0	0.4
End-09-10	126	Metasedimentary	Bleached	7.87	4.40	7.9	50.0	30.5	43.2	35.4	5.7	26.1	0.4
End-09-10	126	Metasedimentary	Bleached	7.12	3.60	6.8	47.2	28.6	44.4	35.4	6.4	29.0	0.6
End-09-10	126	Metasedimentary	Bleached	8.78	4.00	6.0	45.0	27.8	47.5	37.0	7.3	29.1	0.6
End-09-10	126	Metasedimentary	Bleached	7.29	3.60	6.5	47.2	27.7	44.4	37.6	6.7	28.4	0.6
End-09-10	126	Metasedimentary	Bleached	3.52	0.93	3.2	37.6	16.8	49.5	26.5	8.8	47.4	1.6
End-09-10	126	Metasedimentary	Bleached	4.37	1.70	4.3	38.2	26.3	50.6	37.1	8.8	32.3	0.8
End-10-03	217	Metasedimentary	Bleached	7.44	3.00	4.1	36.7	30.2	53.3	37.0	8.3	28.6	0.6
End-10-03	217	Metasedimentary	Bleached	6.17	2.00	3.1	42.0	23.1	47.5	36.4	10.0	37.3	0.8
End-10-03	217	Metasedimentary	Bleached	3.78	1.50	4.4	46.7	25.3	46.7	33.8	8.0	36.5	0.7
End-10-03	217	Metasedimentary	Bleached	6.34	3.90	8.2	51.3	31.6	43.6	32.5	4.6	27.4	0.4
End-10-03	217	Metasedimentary	Bleached	8.65	4.80	8.1	54.2	28.5	41.7	27.0	4.4	36.5	0.5
End-10-03	217	Metasedimentary	Bleached	6.09	1.90	3.0	40.5	23.3	51.1	32.5	9.5	41.4	1.0
End-10-03	217	Metasedimentary	Bleached	8.78	2.30	2.4	33.9	22.1	56.5	32.0	10.9	43.7	1.1
End-10-03	217	Metasedimentary	Bleached	7.40	2.60	3.5	35.0	26.7	53.8	30.9	8.1	38.8	0.8
End-10-03	217	Metasedimentary	Bleached	7.35	2.50	3.7	40.0	24.5	48.0	32.6	8.8	39.2	0.8

End-10-03	217	Metasedimentary	Bleached	5.91	2.20	3.8	36.8	27.5	54.5	33.5	8.2	35.6	0.8
And-10-01	279	Metasedimentary	Bleached	8.18	1.70	1.3	25.3	13.7	58.8	25.6	12.4	59.4	2.3
And-10-01	279	Metasedimentary	Bleached	7.41	2.20	2.6	36.4	17.2	54.5	26.7	9.1	53.4	1.6
And-10-01	279	Metasedimentary	Bleached	7.00	2.20	2.0	28.6	22.6	63.6	27.0	9.5	48.2	1.5
And-10-01	279	Metasedimentary	Bleached	6.85	1.90	2.0	34.2	17.4	52.6	27.3	10.0	53.3	1.8
And-10-01	279	Metasedimentary	Bleached	7.19	2.00	2.1	35.0	17.5	55.0	27.1	10.5	53.2	1.8
And-10-01	279	Metasedimentary	Bleached	5.06	1.20	1.9	37.5	14.0	50.8	27.9	12.5	56.3	2.2
And-10-01	279	Metasedimentary	Bleached	6.93	1.80	2.0	36.7	16.1	53.3	22.0	8.9	59.8	2.1
And-10-01	279	Metasedimentary	Bleached	8.47	1.70	1.8	37.1	11.1	50.6	21.7	10.0	65.4	3.0
And-10-01	279	Metasedimentary	Bleached	6.76	1.60	1.3	21.9	17.8	68.8	23.3	10.6	57.6	2.3
And-10-01	279	Metasedimentary	Bleached	4.70	1.70	2.9	41.2	17.6	47.6	25.4	7.1	54.0	1.5
And-10-01	279	Metasedimentary	Bleached	4.12	1.20	2.3	38.3	15.9	52.5	25.1	8.3	57.0	2.0
And-10-01	279	Metasedimentary	Bleached	6.49	1.20	1.3	33.3	10.4	49.2	23.7	12.5	64.7	2.9
And-10-01	279	Metasedimentary	Bleached	4.46	1.20	2.3	40.0	13.6	46.7	27.7	10.8	56.3	1.9
And-10-01	279	Metasedimentary	Bleached	7.32	1.90	2.7	42.6	13.1	44.7	27.9	10.5	56.3	2.1
And-10-01	279	Metasedimentary	Bleached	5.92	1.40	2.2	44.3	11.8	45.0	24.1	10.0	61.9	2.4
Range				**2.02-12.26**	**0.0-5.0**	**1.3-8.6**	**5.8-54.2**	**5.8-32.0**	**4.5-68.8**	**4.1-41.2**	**1.7-12.5**	**6.1-65.4**	**0.1-3.0**
Avg (n =61)				**6.35 ± 2.41**	**2.49 ± 1.17**	**4.7 ± 2.1**	**41.9 ± 6.9**	**24.7 ± 6.2**	**49.5 ± 5.1**	**31.3 ± 5.5**	**7.9 ± 2.1**	**39.3 ± 11.7**	**1.0 ± 0.7**
KN04	126	Granitic	Albitized	0.94	0.31	1.1	32.3	7.5	38.7	52.7	26.5	41.9	4.2
KN04	126	Granitic	Albitized	1.43	0.26	0.0	0.0	6.4	38.1	58.2	57.7	36.2	5.4

KN04	126	Granitic	Albitized	1.16	0.22	0.0	0.2	7.0	54.5	43.5	39.1	49.6	6.8
KN04	126	Granitic	Albitized	0.80	0.21	0.0	0.0	10.1	57.1	50.6	36.7	39.2	4.2
KN04	126	Granitic	Albitized	1.03	0.19	0.0	0.0	5.9	35.3	57.8	57.9	36.3	6.8
KN04	126	Granitic	Albitized	2.10	1.90	3.9	73.7	8.3	17.4	29.6	5.8	57.8	1.4
KN04	126	Granitic	Albitized	0.56	0.13	0.0	0.0	7.1	46.2	58.9	45.4	35.7	5.1
KN04	126	Granitic	Albitized	1.40	0.39	0.0	0.0	10.9	53.8	63.8	43.6	25.4	3.1
KN04	126	Granitic	Albitized	0.78	0.21	0.0	0.0	10.4	57.1	54.5	37.1	35.1	4.3
KN04	126	Granitic	Albitized	1.16	0.27	0.0	6.3	7.0	44.4	62.6	48.1	30.4	4.8
KN04	126	Granitic	Albitized	0.66	0.22	1.5	22.7	9.1	50.0	48.5	24.1	42.4	4.2
KN04	126	Granitic	Albitized	1.80	0.58	0.0	1.9	10.2	91.4	61.6	34.5	28.2	2.8
KN04	126	Granitic	Albitized	1.05	0.62	3.8	66.1	5.8	15.2	53.8	16.1	35.6	1.8
KN04	126	Granitic	Albitized	0.98	0.27	0.0	3.3	9.3	55.6	60.8	40.7	28.9	3.6
KN04	126	Granitic	Albitized	1.08	0.31	0.0	0.0	10.3	51.6	65.4	45.2	24.3	2.9
KN04	126	Granitic	Albitized	1.18	0.15	0.0	0.0	2.6	30.7	48.7	54.0	48.7	14.0
KN04	126	Granitic	Albitized	1.26	0.26	0.0	12.3	6.5	42.3	46.8	38.5	46.0	6.2
KN04	126	Granitic	Albitized	0.55	0.15	0.0	12.0	7.3	48.7	52.7	33.3	40.0	4.9
Range				**0.55-2.10**	**0.13-1.90**	**0.0-3.9**	**0.0-73.7**	**2.6-10.9**	**15.2-91.4**	**29.6-65.4**	**5.8-57.9**	**24.3-57.8**	**1.4-14.0**
Avg (n = 18)				**1.11 ± 0.40**	**0.37 ± 0.40**	**0.6 ± 1.3**	**12.8 ± 22.7**	**7.9 ± 2.1**	**46.0 ± 16.9**	**53.9 ± 8.7**	**38.0 ± 13.7**	**37.9 ± 8.9**	**4.8 ± 2.8**
KN04	106	Granitic	Hematized (incipient)	1.06	0.55	1.9	45.5	10.5	34.5	46.7	18.2	41.0	1.1
KN04	106	Granitic	Hematized (incipient)	1.06	1.20	5.7	64.2	15.2	30.0	25.7	4.8	53.3	0.7
KN04	106	Granitic	Hematized (incipient)	1.98	1.20	2.6	50.0	12.4	36.7	43.3	15.8	41.8	1.4
KN04	106	Granitic	Hematized (incipient)	1.31	1.10	4.7	63.6	11.6	29.1	30.2	7.3	53.5	1.1
KN04	106	Granitic	Hematized (incipient)	1.28	0.68	1.6	35.3	11.1	35.3	71.4	27.9	15.9	1.0
KN04	106	Granitic	Hematized (incipient)	1.36	0.63	2.2	49.2	6.7	19.0	73.1	30.2	17.9	1.2
KN04	106	Granitic	Hematized (incipient)	0.79	0.32	1.3	37.5	9.0	34.4	64.1	29.7	25.6	1.9

KN04	106	Granitic	Hematized (incipient)	1.57	1.30	2.6	31.5	20.6	53.1	51.0	13.1	25.8	0.8
KN04	106	Granitic	Hematized (incipient)	1.47	0.40	0.7	25.0	4.8	23.0	66.9	50.0	28.3	1.9
KN04	106	Granitic	Hematized (incipient)	2.61	1.70	3.1	58.8	10.6	31.8	16.1	5.4	70.1	1.5
Range				**0.79-2.61**	**0.32-1.7**	**0.7-5.7**	**25.0-64.2**	**4.8-20.6**	**19.0-53.1**	**16.1-73.1**	**4.8-50**	**15.9-70.1**	**0.7-1.9**
Avg (n = 10)				**1.32 ± 0.52**	**0.82 ± 0.45**	**2.6 ± 1.5**	**44.6 ± 13.6**	**11.3 ± 4.4**	**32.8 ± 9.1**	**52.5 ± 20.1**	**21.9 ± 14.3**	**33.7 ± 17.7**	**1.2 ± 0.4**
KN04	66.5	Granitic	hematized	5.39	4.40	11.8	56.8	37.3	38.6	27.1	3.4	22.0	0.2
KN04	66.5	Granitic	hematized	4.47	3.20	9.4	53.1	36.8	43.8	27.2	4.1	26.5	0.2
KN04	66.5	Granitic	hematized	4.39	3.60	11.4	55.6	38.6	41.7	28.6	3.6	21.2	0.2
KN04	66.5	Granitic	hematized	6.07	5.50	13.9	56.4	42.6	40.0	31.8	3.5	12.1	0.1
KN04	66.5	Granitic	hematized	4.05	2.80	9.0	50.0	37.3	46.4	32.1	4.6	21.3	0.3
KN04	66.5	Granitic	hematized	4.76	3.20	9.9	59.4	30.5	37.5	30.9	4.4	28.7	0.4
KN04	66.5	Granitic	hematized	4.51	3.00	9.7	56.7	32.7	40.0	25.8	3.7	31.8	0.4
KN04	66.5	Granitic	hematized	4.28	2.70	7.6	48.1	35.9	44.4	38.0	5.9	18.3	0.3
KN04	66.5	Granitic	hematized	3.99	3.40	11.5	52.9	39.9	41.2	33.4	3.8	15.1	0.2
KN04	66.5	Granitic	hematized	3.46	2.30	9.3	56.5	30.8	38.7	32.3	4.8	27.8	0.4
Range				**3.46-6.07**	**2.3-5.5**	**7.6-13.9**	**48.1-59.4**	**30.5-42.6**	**37.5-46.4**	**25.8-38.0**	**3.4-5.9**	**12.1-31.8**	**0.1-0.4**
Avg (n = 10)				**4.54 ± 0.74**	**3.41 ± 0.93**	**10.3 ± 1.8**	**54.6 ± 3.5**	**36.2 ± 3.9**	**41.2 ± 2.9**	**30.7 ± 3.7**	**4.2 ± 0.8**	**22.5 ± 6.3**	**0.3 ± 0.1**
MZ-10-01	90	Granitic	bleached	7.08	3.10	4.6	35.5	31.9	58.1	23.3	5.5	40.3	0.5
MZ-10-01	90	Granitic	bleached	14.57	7.10	4.3	26.8	46.4	69.0	20.9	4.4	28.4	0.3
MZ-10-01	90	Granitic	bleached	10.58	5.50	5.7	34.5	40.1	60.0	23.3	4.4	31.0	0.3
MZ-10-01	90	Granitic	bleached	22.85	17.00	10.6	43.5	53.6	51.8	21.2	2.6	14.6	0.1
MZ-10-01	90	Granitic	bleached	11.58	4.70	4.4	36.2	32.2	57.4	25.7	6.2	37.7	0.5
MZ-10-01	90	Granitic	bleached	11.93	4.40	3.4	29.5	33.3	61.4	31.3	8.2	32.0	0.5

MZ-10-01	90	Granitic	bleached	9.84	3.40	2.6	25.6	33.9	61.8	36.9	10.6	26.6	0.6
MZ-10-01	90	Granitic	bleached	14.99	5.80	4.0	32.8	36.4	60.3	34.1	8.1	25.5	0.4
MZ-10-01	90	Granitic	bleached	13.48	5.90	4.5	32.2	38.9	62.7	27.9	6.3	28.8	0.3
MZ-10-01	90	Granitic	bleached	8.54	2.80	2.8	30.4	28.7	60.7	28.0	8.6	40.3	0.7
Range				**7.08-22.85**	**2.8-17**	**2.6-10.6**	**25.6-43.5**	**28.7-53.6**	**51.8-69.0**	**20.9-36.9**	**2.6-10.6**	**14.6-40.3**	**0.1-0.7**
Avg (n = 10)				**12.54 ± 4.42**	**5.97 ± 4.11**	**4.7 ± 2.3**	**32.7 ± 5.2**	**37.5 ± 7.6**	**60.3 ± 4.4**	**27.3 ± 5.5**	**6.5 ± 2.4**	**30.5 ± 7.8**	**0.4 ± 0.2**
MZ-10-01	120	Granitic	Ferric	3.23	1.40	3.5	35.0	30.7	55.0	27.2	6.4	38.7	0.6
MZ-10-01	120	Granitic	Ferric	8.05	2.80	2.8	34.3	28.2	57.1	28.2	8.2	40.7	0.6
MZ-10-01	120	Granitic	Ferric	6.80	2.90	4.1	37.9	31.7	55.2	29.5	6.9	34.7	0.5
MZ-10-01	120	Granitic	Ferric	6.14	2.60	3.8	36.5	31.6	53.8	29.5	7.3	34.7	0.5
MZ-10-01	120	Granitic	Ferric	4.37	1.40	2.9	42.1	20.1	45.0	32.1	9.3	45.0	1.1
MZ-10-01	120	Granitic	Ferric	5.63	2.00	2.8	36.0	25.8	55.0	33.0	9.0	38.4	0.8
MZ-10-01	120	Granitic	Ferric	1.59	0.72	3.8	36.1	30.1	55.6	30.8	6.4	35.3	0.7
MZ-10-01	120	Granitic	Ferric	5.74	2.50	3.7	35.6	31.1	56.0	31.2	6.8	33.8	0.5
MZ-10-01	120	Granitic	Ferric	6.02	2.40	3.7	36.3	28.8	58.3	30.7	7.5	36.9	0.6
MZ-10-01	120	Granitic	Ferric	6.45	2.20	3.0	35.9	26.5	59.1	31.2	8.6	39.3	0.8
MZ-10-01	120	Granitic	Ferric	6.84	2.20	2.7	32.3	24.5	54.5	32.0	9.1	41.0	0.8
MZ-10-01	120	Granitic	Ferric	5.69	1.80	2.6	35.0	24.2	55.6	31.5	9.4	41.7	0.9
MZ-10-01	120	Granitic	Ferric	7.23	2.70	3.0	32.6	28.9	59.3	33.7	8.5	34.3	0.7

MZ-10-01	120	Granitic	Ferric	3.93	1.40	2.6	35.0	25.4	54.3	34.9	9.3	37.0	0.9
MZ-10-01	120	Granitic	Ferric	5.30	2.10	3.4	34.3	29.5	57.1	32.5	7.6	34.7	0.6
MZ-10-01	120	Granitic	Ferric	2.60	0.79	2.8	45.6	19.0	44.3	32.8	9.5	45.8	1.4
MZ-10-01	120	Granitic	Ferric	5.25	2.40	4.0	38.3	31.6	54.2	33.0	7.1	31.4	0.5
MZ-10-01	120	Granitic	Ferric	5.58	1.70	2.8	39.4	27.3	52.9	32.6	9.4	42.7	1.0
MZ-10-01	120	Granitic	Ferric	6.13	4.10	7.7	43.9	41.4	51.2	25.2	3.9	25.6	0.3
MZ-10-01	120	Granitic	Ferric	7.99	2.80	3.0	33.6	27.5	57.1	34.0	8.9	35.4	0.8
MZ-10-01	120	Granitic	Ferric	6.01	1.90	2.7	34.7	24.2	57.9	34.0	10.0	38.9	0.9
MZ-10-01	120	Granitic	Ferric	6.19	2.90	4.5	37.9	33.7	55.2	30.5	6.6	31.3	0.5
MZ-10-01	120	Granitic	Ferric	6.21	2.50	3.8	37.6	29.2	56.0	30.9	7.2	36.3	0.7
MZ-10-01	120	Granitic	Ferric	6.83	3.60	5.2	38.9	36.2	55.6	29.7	5.3	28.9	0.4
MZ-10-01	120	Granitic	Ferric	7.23	4.10	6.3	43.9	37.4	53.7	29.5	5.1	26.7	0.4
MZ-10-01	120	Granitic	Ferric	14.33	3.70	2.5	43.2	19.8	45.9	37.3	11.6	40.5	1.1
Range				**1.59-14.33**	**0.72-4.1**	**2.5-7.7**	**32.3-45.6**	**19.0-41.4**	**44.3-59.3**	**25.2-37.3**	**3.9-11.6**	**25.6-45.8**	**0.3-1.4**
Avg (n = 26)				**6.05 ± 2.28**	**2.37 ± 0.89**	**3.6 ± 1.2**	**37.4 ± 3.7**	**28.6 ± 5.3**	**54.4 ± 3.9**	**31.4 ± 2.5**	**7.9 ± 1.7**	**36.5 ± 5.1**	**0.7 ± 0.3**
EZ75	321	Epiclastic	Unaltered	0.34	0.25	2.9	20.0	26.5	64.0	38.2	12.4	35.3	1.2
EZ75	321	Epiclastic	Unaltered	0.37	0.31	2.7	24.8	27.0	61.3	35.1	9.7	35.1	1.1
EZ75	321	Epiclastic	Unaltered	0.49	0.43	2.0	27.9	26.5	62.8	34.7	9.5	32.7	1.0
EZ75	321	Epiclastic	Unaltered	0.46	0.46	4.3	37.0	26.1	56.5	32.6	7.4	39.1	0.9
EZ75	321	Epiclastic	Unaltered	0.59	0.91	8.5	56.0	27.1	38.5	27.1	4.3	37.3	0.5
EZ75	321	Epiclastic	Unaltered	0.43	0.46	4.7	39.1	25.6	52.2	34.9	7.4	34.9	0.8
EZ75	321	Epiclastic	Unaltered	0.42	0.37	2.4	26.8	28.6	62.2	38.1	10.0	31.0	0.9

EZ75	321	Epiclastic	Unaltered	0.41	0.33	2.4	25.5	26.8	63.6	34.1	9.7	36.6	1.0
Range				**0.34-0.59**	**0.25-0.91**	**2.0-8.5**	**20.0-56.0**	**25.6-28.6**	**38.5-64.0**	**27.1-38.2**	**4.3-12.4**	**31.0-39.1**	**0.5-1.2**
Avg (n = 8)				**0.44 ± 0.08**	**0.44 ± 0.20**	**3.7 ± 2.1**	**32.1 ± 11.6**	**26.8 ± 0.9**	**57.6 ± 8.7**	**34.4 ± 3.5**	**8.8 ± 2.4**	**35.2 ± 2.6**	**0.9 ± 0.2**
END-10-03	42	Quartz breccia	Quartz vein	1.52	0.29	0.0	3.4	7.3	62.1	28.7	25.9	64.0	9.3
END-10-03	42	Quartz breccia	Quartz vein	1.45	0.22	0.0	1.7	6.3	63.6	23.8	25.5	69.9	12.3
END-10-03	42	Quartz breccia	Quartz vein	1.54	0.31	0.0	2.1	7.9	61.3	28.9	24.5	63.8	9.0
END-10-03	42	Quartz breccia	Quartz vein	1.71	0.29	0.6	23.4	4.2	48.3	19.6	18.3	75.6	11.4
END-10-03	42	Quartz breccia	Quartz vein	1.83	1.10	2.2	31.8	21.1	51.8	40.0	10.9	36.7	1.5
END-10-03	42	Quartz breccia	Quartz vein	1.55	0.85	1.3	22.4	19.6	58.8	42.5	16.5	36.6	1.9
END-10-03	42	Quartz breccia	Quartz vein	1.73	1.10	1.2	17.3	27.1	68.2	45.9	17.3	25.3	1.2
END-10-03	42	Quartz breccia	Quartz vein	1.42	0.29	0.0	0.8	7.9	58.6	40.0	31.0	52.1	8.6
END-10-03	42	Quartz breccia	Quartz vein	1.61	0.62	0.6	13.5	15.2	62.9	41.1	21.0	43.7	3.2
END-10-03	42	Quartz breccia	Quartz vein	1.81	0.35	0.0	4.3	6.7	54.3	42.1	34.3	51.1	8.6
END-10-03	42	Quartz breccia	Quartz vein	1.79	0.39	0.0	0.0	9.1	59.0	46.6	35.9	43.8	6.9
END-10-03	42	Quartz breccia	Quartz vein	2.05	0.39	0.0	0.0	7.0	53.8	48.8	38.5	44.3	8.2
END-10-03	42	Quartz breccia	Quartz vein	0.88	0.43	2.3	41.9	10.3	41.9	34.5	11.6	51.7	3.0
END-10-03	42	Quartz breccia	Quartz vein	0.34	0.23	5.9	52.2	11.8	33.9	32.4	9.6	52.9	2.3
END-10-03	42	Quartz breccia	Quartz vein	1.46	0.95	4.2	70.5	6.9	18.9	31.3	8.8	56.9	2.0
END-10-03	42	Quartz breccia	Quartz vein	1.00	0.38	2.0	50.0	7.1	31.6	30.3	13.2	59.6	4.2

END-10-03	42	Quartz breccia	Quartz vein	0.99	0.44	2.0	45.5	9.2	38.6	41.8	15.2	46.9	3.2
END-10-03	42	Quartz breccia	Quartz vein	1.46	0.25	0.7	24.4	4.2	39.2	31.3	23.6	64.6	11.6
END-10-03	42	Quartz breccia	Quartz vein	1.30	0.24	0.8	27.5	3.9	40.4	28.9	20.4	66.4	10.8
END-10-03	42	Quartz breccia	Quartz vein	1.14	0.27	0.0	11.1	8.0	55.6	32.7	24.1	58.4	6.3
END-10-03	42	Quartz breccia	Quartz vein	0.12	0.17	8.3	51.2	25.0	43.5	25.0	4.3	33.3	0.6
Range				**0.12-2.05**	**0.17-1.1**	**0.0-8.3**	**0.0-70.5**	**3.9-27.1**	**18.9-68.2**	**19.6-48.8**	**4.3-38.5**	**25.3-75.6**	**0.6-12.3**
Avg (n = 21)				**1.37 ± 0.48**	**0.46 ± 0.29**	**1.5 ± 2.2**	**23.6 ± 21.2**	**10.7 ± 6.8**	**49.8 ± 12.8**	**35.1 ± 8.1**	**20.5 ± 9.4**	**52.3 ± 13.1**	**6.0 ± 3.9**

Chapter 6: Summary and Future Work

Nuclear energy is increasingly seen as a vital part of solving the rising need for zero-carbon electricity; realizing this potential, however, requires developing a permanent solution for the disposal of the highly radioactive Used Nuclear Fuel (UNF) produced by nuclear energy. Burial in a Deep Geologic Repository (DGR) is considered the most viable solution for UNF disposal, and Canada is entering the critical phase of repository approval and construction. Studying the geologic history of uranium (U) deposits can provide insights into the long-term performance of geologic repositories which are difficult to obtain by other means. Studies of natural analogues such as Oklo and Cigar Lake have contributed to the development of the DGR concept but leave knowledge gaps pertaining to how radionuclides can become mobile in the subsurface. The potential effects of glaciation are of particular concern for a Canadian DGR.

The Kiggavik U deposits in central Nunavut have a long and complex history of U mobility and have been extensively impacted by glaciation. In this thesis I developed the Kiggavik deposits as a natural analogue for a DGR through the use optical and scanning electron microscopy, U-Th-Pb and Ar-Ar geochronology, stable isotope analysis, and (ultra) small angle X-ray scattering. This approach enables the history of U deposition and mobility, and the factors that have controlled this mobility, to be evaluated. This section summarizes the major findings of these studies, the implications for long term performance of a DGR, and recommendations for future work.

The History of Uranium Mobility in the Kiggavik deposits

The Kiggavik deposits contain ~51 000 tonnes of U at a grade of 0.46% U across four main deposits: Kiggavik, Bong, End, and Andrew Lake (AREVA, 2011). Uranium mineralization

is hosted along fault systems within Archean metasedimentary rocks of the Woodburn Lake group and subordinate Proterozoic granitic rocks of the Lone Gull Suite. These deposits occur just beyond the margin of the Proterozoic Thelon Basin and have generally been considered to be basement-hosted URU deposits similar to those of Saskatchewan's Athabasca Basin based mainly on similarities in overall alteration style and structural setting (Fuchs et al., 1986; Riegler et al., 2014; 2016; Chi et al., 2016; Grare et al., 2020; Ashcroft, 2020). The lack of a preserved unconformity in the area, however, has made establishing a definitive connection to URU processes difficult, and several studies have noted aspects of mineralogy and stable isotope signatures which are not consistent with the typical URU model (Flotté, 2009; Sharpe et al., 2015; Chi et al., 2016; Grare et al., 2020).

The earliest phase of alteration and U deposition in the Kigavik area consists of albitization of host rocks. Albitization comprises pseudomorphic replacement of primary minerals by albite, K-feldspar, quartz, muscovite, apatite, Ti-oxides, zircon, uranothorite, monazite, and a diverse range of other accessory minerals. Albitization is associated with corrosion of zircon, transport of HFSE, and precipitation of hydrothermal zircon and uranothorite in equilibrium with fluorite, suggesting the presence of a F-rich fluid during albitization. This diverse mineralogy, HFSE mobility, and F-rch fluid chemistry is similar to what is observed in some Metasomatic Iron Alkali Calcic (MIAC) deposits, albitite-hosted U deposits in particular (Polito et al., 2009; Alexandre, 2010; Wilde, 2013; Wilde et al., 2013; Montreuil et al., 2016b; Corriveau et al., 2022). Albitization is pervasive in granitic rocks, but is patchy and poorly preserved in metasedimentary rocks, being heavily overprinted by later stages of alteration.

M2 muscovite formed during albitization of granitic rocks is Ar-Ar dated to ~1820-1830 Ma. This time period is consistent with igneous and seismic activity in the region, which has also been linked to the formation of Lac Cinquante albitite-hosted U mineralization in the region (Avery, 2024). M2 muscovite has δ^2H values as high as +128.9‰; this extremely high value is unprecedented in terrestrial minerals. The isotopically heavy ($\delta^{18}O$ and δ^2H values of +10.4 ± 2.1 ‰ and +130.1 ± 30.6 ‰, respectively) fluids which precipitated M2 was produced through multiple cycles of seismically-induced fluid boiling, phase separation, and condensation. M1 muscovite and Il1 illite formed at this time and are isotopically consistent with precipitation form metamorphic fluids, indicating these fluids were also present at this time. (Ultra) small angle X-ray scattering measurements indicate albitized granitic rocks have a porosity of 1.11 ± 0.4 %, which is significantly higher than most crystalline rocks and indicates albitization increased the porosity of affected rocks, setting the stage for further fluid events.

The second stage consists of hematization of host rocks and emplacement of the quartz breccias. Hematization has increased the porosity of metasedimentary rocks from a starting value of 0.64 ± 0.09 % by an order of magnitude, and the porosity of granitic rocks by ~4 times, due to the pervasive replacement of feldspars by Il2 illite.

The third stage consists of bleaching (dehematization), which overprints earlier styles of alteration and is associated with primary (U1) U mineralization. This U1 mineralization comprises uraninite, coffinite, and local brannerite subdivided into three types: (1) front-style (U1a), (2) euhedral disseminated (U1b), and (3) polymetallic and monometallic vein-hosted (U1c). U1a is U-Pb Concordia dated to 1594 ± 95 Ma, while U1b + c are Concordia dated to 1553 ± 16 Ma. This age suggests a link to the 1540 ± 30 Ma Kuungmi Formation shoshonitic

basalts Chamberlain et al. (2010) which cap the Thelon Basin (Hiatt et al., 2003; Chamberlain et al., 2010; Jefferson et al., 2013). Stable O and H isotope analysis of illites associated with bleaching (Il3-Il5) indicates at least two distinct fluids were present during bleaching. Il3 and Il5 precipitated from basinal fluids and were subsequently partially overprinted by meteoric fluids, while Il4 is isotopically consistent with precipitation from highly fractionated, boiled fluids. Il3-Il5 illites yield widely ranging post U1 Ar-Ar dates. This is interpreted to be the result of multiple partial overprinting events.

Bleaching has not substantially affected the porosity of affected metasedimentary rocks but has increased the porosity of bleached granitic rocks by a factor of ~3, to 12.54 ± 4.42 %. The diverging effects of bleaching on porosity is attributed to differences in mineralogy between granitic and metasedimentary host rocks: while all feldspars in finer grained metasedimentary rocks had been replaced during hematization, substantial amounts of feldspar are still present in hematized granitic rocks. These remnant feldspars were replaced by highly porous course grained illite during bleaching of granitic rocks, leaving them with a much higher porosity.

The fourth stage comprises alteration and isotopic resetting events. Some U1 minerals, and all U2 (fractured and texturally-altered U minerals) minerals, record multiple isotopic resetting/U remobilization events at 1440 ± 21, 1417 ± 17 Ma, 1276.4 ± 8.7 Ma, 1249 ± 33 Ma, 937 ± 24 Ma, and 274 ± 69 Ma. These alteration events are isotopically linked to basinal fluids, the infiltration of which was facilitated by the many faults and porous, hydrothermally altered rocks, and may have served to reconcentrate previously deposited U-minerals and increase the overall grade of U mineralization.

Stage 5 consists of paragenetically late U minerals (U3) associated with orange goethite-bearing ferric alteration which have very low lead contents, indicating recent (<1 Ma) formation or isotopic resetting. Uranium-Th disequilibrium geochronology indicates distinct periods of alteration to U3 minerals at 36.5 ± 1.9 Ka, 55.7 ± 4.8 Ka, 153.3 ± 3.7 Ka, 258.6 ± 11.6 Ka, and 471.3 ± 6.3 Ka. The two most recent events are only observed in granitic rocks. ^{235}U isochron geochronology indicates these minerals have not undergone complete recrystallization in >0.6 Ma, indicating these geologically recent events have produced subtler disturbances to U decay chains.

The distribution of ferric alteration and U3 minerals is strongly controlled by open fractures and porous vein systems, suggesting these provided conduits for surface-derived fluids to penetrate to depths of at least ~300 m. Ferric altered granitic rocks have much lower porosity (6.05 ± 2.28) than their bleached protoliths. This reduction in porosity is linked to the precipitation of goethite, calcite, vanadinite, and U-minerals in pore space and fractures.

The geothite-bearing alteration assemblage associated with U3 indicates the presence of an oxidized, low temperature fluid, while the stable δ^2H compositions of illite associated with U3 are extremely low, indicating the presence of high-latitude meteoric fluids such as glacial melt. The extent of isotopic overprinting and U decay chain disturbance is greater in granitic rocks, almost certainly due to the much higher porosity of these rocks. The timing of U3 alteration events during glacial stages indicates that this alteration occurred underneath an icesheet.

The mineralogy, geochronology, and stable isotope composition of albitization and early U mineralization indicates an albitite-hosted/MIAC affinity to the early stages of Kiggavik U

mineralization, raising the prospect of a previously unrecognized MIAC district in central Nunavut. Later stages of mineralization are more strongly linked to basinal fluids, while meteoric fluids are strongly linked to post depositional alteration events. These recent alteration events occurred within the ~1 Ma timeframe for geologic disposal.

Implications for Geologic Disposal

The ultimate objective of this thesis is to gather data on how U becomes mobilized in the subsurface, and what the results of this mobility are, thereby improving our understanding of how UNF in a DGR will behave over the next ~1 Ma. Kiggavik lacks the engineered safety barriers which would be present in a DGR and is situated in an area of deeply fractured, pervasively hydrothermally altered, and intensely glaciated bedrock, and is therefore an analogue for a worst-case scenario of an extremely poorly conceived and engineered DGR. The above studies indicate that glaciation may impact such a DGR and cause some degree of radionuclide mobility if oxidized subglacial fluids are able to come into contact with UNF; a variety of natural processes, however, are capable of greatly restricting the overall degree and impacts of this mobility.

The presence of open fractures may facilitate fluid incursion to depths of at least 300 m, which is comparable to repository depths. The porosity of the host rock matrix plays a secondary, but still significant role in controlling fluid infiltration and U mobility; bleached granitic rocks (porosity = ~12%) have undergone a higher degree of isotopic overprinting and have experienced two U mobility events which are not observed in bleached metasedimentary rocks (porosity = ~6%). The existence of this large difference in porosity is not immediately evident, suggesting that DGR host rocks must be investigated in great detail to confidently predict their performance.

The fact that granitic rocks, which are normally considered to be highly resilient and non-porous in the absence of fractures, have proven to be so vulnerable to alteration suggests that the geologic history of host rocks can be at least as important as their lithology in determining their performance.

The fact that fluid infiltration is restricted to certain timeframes within glacial periods suggests that a triggering event, such as destabilization of the overlying ice sheet, is required; the mere presence of surface waters does not necessarily lead to deep infiltration.

Most Kiggavik U minerals have not undergone extensive recrystallization since before the time of the dinosaurs, and even the most disturbed U-minerals investigated have resisted complete recrystallization for approximately twice as long as *homo sapiens* have existed. This indicates that the overwhelming majority of radionuclides contained within the UNF matrix would have remained largely in situ despite repeated disturbances to DGR integrity within the ~1 Ma assessment timeframe. The U-Th data, however, reveals that half of all U-minerals in the Kiggavik deposits have undergone a lesser degree of disturbance to vulnerable U decay chain isotopes within 500 Ka. This suggests that some mobile radionuclides such as ^{129}I could become mobile within assessment timeframes under the adverse conditions observed at Kiggavik.

The observed distance of U mobility is very small, < 5 cm, indicating an extremely low rate of overall U mobility (<<1 mm/year). This implies that most of the mobilized radionuclides would be unlikely to reach the surface during the assessment timeframe. It should, however, be noted that unobserved longer range radionuclide mobility cannot be ruled out, and that U-minerals smaller than the ~10 μm analytical spot size could not be reliably dated.

Several factors have contributed to restrict the overall mobility of radionuclides in Kiggavik. Minerals such as uraninite, Ti-oxides, and clays are observed to trap dissolved U, presumably through redox processes, indicating that natural minerals and engineered materials within a DGR would resist bulk mobilization of UNF by creating localized redox traps for dissolved radionuclides. Adsorption onto clay surfaces may also trap U, indicating that the clays utilized as sealant in DGR concepts could also serve as sinks for radionuclides released from UNF. While the infiltration of oxidized subglacial fluids may cause radionuclide mobility, it also limits this mobility though the precipitation of minerals such as geothite, calcite, and vanadinite within fractures and pore space. This minerals precipitation visibly fills some of the fractures through which U was mobilized and has reduced the porosity of the matrix by ~50%. The self-sealing nature of interactions between host rocks and infiltrating surface derived fluids has effectively closed many of the pathways available for further radionuclide mobility. Similar self-sealing and pore clogging has been observed at other natural analogue sites with widely differing geology and fluid chemistry, suggesting such processes may be broadly applicable to geologic disposal projects.

Despite Kiggavik's unique vulnerability to disruption, via glacial processes in particular, these U deposits have proven resistant to large scale mobilization of radionuclides. This indicates that natural host rock barriers in a DGR are capable of providing a significant amount of containment for the entombed UNF even under highly detrimental circumstances.

Recommendations for Future Work

While this thesis has successfully developed the Kiggavik U deposits as a natural analogue for a DGR impacted by glaciation, it also provides a foundation for future research. Significant questions include:

1) What is the fate of ^{129}I? This fission fragment is particularly long-lived and mobile in geologic environments, and is the main dose-contributor in long term assessments (NWMO, 2017). The mobility and presumed location near sites of fission-induced crystal damage of ^{129}I suggests it could become mobile even under relatively limited degrees of isotopic disturbance to UNF. This isotope is present in only tiny amounts in natural U deposits, and attempting to trace its mobility poses significant challenges, but would yield major insight into the potential hazard posed by the limited degree of radionuclide mobility observed at Kiggavik.
2) Could looking for disturbances to shorter-lived U decay chain isotopes such as ^{226}Ra yield further insight into U mobility at Kiggavik?
3) What is the mechanism by which Ti-oxides immobilize dissolved U? Titanium oxide minerals have been observed to effectively trap U in U deposits (Ildefonse, et al., 1990); however, although Ti-oxides are believed to catalyze reduction of soluble U^{6+} to insoluble U^{4+} (Comarmond et al., 2011; Ding et al., 2022), the details of how and why this occurs have remained elusive. Understanding these details could open up new ways of immobilizing radionuclides, and potentially suggest enhancements for engineered barriers.
4) Restrictions in the handling of radioactive materials ultimately prevented X-ray scattering experiments from being conducted on U-mineralized samples, and permeability measurements from being conducted on any samples; conducting these

experiments would improve the quality of porosity data, and increase the confidence in and applicability of conclusions relating to porosity.

5) The discovery of MIAC and albitite-hosted U deposit aspects of Kiggavik's genesis suggests the possibility of additional such deposits, and potentially of other affiliated deposits, in the region. The temporal link to the Lac Cinquante U deposit ~200 km away (Bridge et al., 2013), is particularly interesting, as it suggests Hudsonian-age intrusives, which are widespread in the region, could be prospective for critical mineral deposits.
6) Is the extreme H isotope fractionation observed in Kiggavik granitic rocks unique? Relatively little H isotope data has been reported from MIAC systems; if the extremely positive ^{2}H signature, and the boiling and condensation cycles it is interpreted to reflect, are common features it could be a useful technique for identifying and exploring for these systems.

References

Alexandre, P., 2010, Mineralogy and geochemistry of the sodium metasomatism-related uranium occurrence of Aricheng South, Guyana. Miner Deposita; **45**, 351–367.

Ashcroft, G., 2020, The geochemistry and geochronology of the End Deposit, NE Thelon region, Nunavut, Canada: insight into the Athabasca Basin's closest relative: MSc thesis, Winnipeg, Canada, University of Manitoba, 217 pages.

AREVA Resources Canada Inc., 2011, Kiggavik Project EIS: Popular Summary; Tier 1, v. 1, p. 51.

Avery, G., 2024, The Source of Uranium for the Lac Cinquante Uranium Deposit, Nunavut, Canada: Honours thesis, Halifax, Canada, Saint Mary's University, 154 pages.

Bridge, N. J., Banerjee, N. R., Pehrsson, S., Fayek, M., Finnigan, C. S., Ward, J., and Berry, A., 2013, Lac Cinquante Uranium Deposit, Western Churchill Province, Nunavut, Canada. Exploration and Mining Geology; **21**, 27–50.

Chamberlain, K.R., Schmitt, A.K, Swapp, S.M., Harrison, T.M., Swoboda-Colberg, N., Bleeker, W., Peterson, T.D., Jefferson, C.W., and Khudoley, A.K., 2010, In situ U–Pb SIMS (IN-SIMS) micro-baddeleyite dating of mafic rocks: Method with examples: Precambrian Research; **183**, 379–387.

Chi, G., Haid, T., Quirt, D., Fayek, M., Blamey, N., and Chu, H., 2016, Petrography, fluid inclusion analysis, and geochronology of the End uranium deposit, Kiggavik, Nunavut, Canada. Mineralium Deposita; **52**, 211–232.

Comarmond, M. J., Payne, T. E., Harrison, J. J., Thiruvoth, S., Wong, H. K., Aughterson, R. D., Lumpkin, G. R., Muller, K., and Foerstendorf, H., 2011, Uranium sorption on various forms of titanium dioxide - Influence of surface area, surface charge, and impurities. Environmental Science and Technology; **45**, 5536–5542.

Corriveau, L., Montreuil, J.-F., Potter, E. G., Blein, O., and De Toni, A. F., 2022, Mineral systems with IOCG and affiliated deposits: Part 3 - metal pathways and ore deposit model, *In* Corriveau, L., Potter, E.G., and Mumin, A.H., Eds., Mineral Systems with Iron Oxide-Copper-Gold (IOCG) and Affiliated Deposits, Special Paper 52: Geological Association of Canada, Ottawa, Canada, 89–121.

Ding, B., Liu, H.-X., Qiu, L.-F., Zhang, C., and Xu, D.-R., 2022, Ilmenite alteration and its adsorption and catalytic reduction in U enrichment in sandstone-hosted U deposits from the northern Ordos Basin, north China. Minerals; **12**, 167.

Flotté, N., 2009, AREVA Resources Canada Inc. Kiggavik and Sissions project END-Grid Geological Observations and interpretation and 3D modelling in GoCad, 46p.

Fuchs H.D., Hilger W, and Prosser E., 1986, Geology and exploration history of the Lone Gull property: Canadian Institute of Mining and Metallurgy Special Publication 33, p. 286–292.

Grare, A., Benedicto, A., Mercadier, J., Lacombe, O., Trave, A., Guilcher, M., Richard, A., Ledru, P., Blain, M., Robbins, J., and Lach, P., 2020, Structural controls and metallogenic model of polyphase uranium mineralization in the Kiggavik area (Nunavut, Canada). Mineralium Deposita, doi:10.1007/s00126-020-00957-x.

Hiatt, E.E., Palmer, S.E., Kyser, T.K., and O'Connor, T.K., 2010, Basin evolution, diagenesis and uranium mineralization in the Paleoproterozoic Thelon basin, Nunavut, Canada. Basin Research; **22**, 302–323.

Ildefonse, P., Agrinier, P., Muller, J. P., 1990, Crystal-chemistry and isotope geochemistry of alteration associated with the U Nopal I deposit, Chihuahua, Mexico. Chem Geol; **84**, 371–372.

Jefferson, C.W., Peterson, T.D., Tschirhart, V., Davis, W., Scott, J.M.J., Reid, K., Ramaekers, P., Gandhi, S.S., Bleeker, W., Pehrsson, S., Morris, W.A., Fayek, M., Potter, E., Bridge, N., Grunsky, E., Keating, P., Ansdell, K., and Banerjee, N., 2013, LIPs and Proterozoic Uranium (U) deposits of the Canadian Shield: Geological Survey of Canada Open File 7352, 56 p., doi:10.4095/292377.

Montreuil, J.-F., Potter, E. G., Corriveau, L., and Davis, W. J. 2016, Element mobility patterns in magnetite-group IOCG systems: The Fab IOCG system, Northwest Territories, Canada. Ore Geology Reviews; **72**, 562–584.

Nuclear Waste Management Organization (NWMO), 2017, Postclosure safety assessment of a used fuel repository in crystalline rock. NWMO Technical Report TR-2017-02, 718 p.

Polito, P. A., Kyser, K., and Stanley, C., 2009, The Proterozoic, albitite-hosted, Valhalla uranium deposit, Queensland, Australia: a description of the alteration assemblage associated with uranium mineralization in diamond drill hole V39. Miner Deposita; **44**, 11–40.

Riegler, T., Lescuyer, J-L., Wollenburg, P., Quirt, D., and Beaufort, D., 2014, Alteration related to uranium deposits in the Kiggavik-Andrew Lake Structural Trend, Nunavut, Canada: New insights from petrography and clay mineralogy. The Canadian Mineralogist; **52**, 27–45.

Riegler, T., Beaufort, M-F., Allard, T., Pierson-Wickmann, A-C., and Beaufort, D., 2016, Nanoscale relationships between uranium and carbonaceous material in alteration halos around unconformity-related uranium deposits of the Kiggavik camp, Paleoproterozoic Thelon Basin, Nunavut, Canada. Ore Geology Reviews; **79**, 382–391.

Sharpe, R., Fayek, M., Quirt, D., and Jefferson, C., 2015, Geochronology and genesis of the Bong uranium deposit, Thelon Basin, Nunavut, Canada. Economic Geology; **110**, 1759–1777.

Wilde, A., 2013, Towards a model for albitite-type uranium. Minerals; **3**, 36–48.

Wilde, A., Otto, A., Jory, J., MacRae, C., Pownceby, M., Wilson, N., and Torpy, A., 2013, Geology and Mineralogy of Uranium Deposits from Mount Isa, Australia: Implications for Albitite Uranium Deposit Models. Minerals, **3**, 258–283.

Appendix 1: Analytical Methods

Whole Rock Geochemistry

Samples of drill core were analyzed by Actlabs in Ancaster, Ontario. A mild steel mill was used to crush and pulverize samples. A 0.5 g split of pulverized material was analyzed by lithium metaborate/tetraborate fusion, with the resulting bead being rapidly digested in a nitic acid solution. Major and trace elements were determined via inductively coupled plasma-optical emission spectrometry (ICP-OES) and inductively coupled plasma mass spectrometry (ICP-MS) analysis of this solution. Fluorine was measured via KOH fusion analyzed by an ion selective electrode (ISE). Instrumental neutron activation analysis (INAA) was used to analyze gold. Nine standards were used for the complete analysis.

Electron Probe Micro-Analysis

The chemical compositions of minerals were determined using the CAMECA SX100 Universal Electron Probe MicroAnalyser (EMPA) at the University of Manitoba. This instrument is equipped with five wavelength-dispersive spectrometers and a Princeton Gamma-Tech (PGT) energy-dispersive spectrometer. An accelerating voltage of 15 kV was used to produce a 1 μm electron beam with a beam current of 20 nA. Elemental detection limits were below 1000 ppm for all elements except for U, Th, Pb, Zr, and Hf, which had detection limits of ~3000, 3000, 2500, 2000, and 2500 ppm, respectively.

Secondary Ion Mass Spectrometry

The uranium, thorium, and lead isotope ratios in U-bearing minerals and stable O and H composition of muscovite, altered muscovite, and illite were measured using a CAMECA 7f

Secondary Ion Mass Spectrometer (SIMS) instrument at the University of Manitoba (Fig. A1). Prior to analysis, samples were cleaned by immersion in an ultrasonic cleaner in four ten-minute stages: a dilute soap solution was followed by water, distilled water, and finally ethanol. The cleaned samples were sputter-coating with a ~200Å-thick layer of gold in order to establish a conductive surface.

SIMS analysis of uraninite was conducted using methods described in Sharpe and Fayek (2016). A ~9 nA, O^- primary beam was accelerated at 12.5 kV. A 750 μm aperture in the primary column focused the beam to a spot size of 15 x 30 μm. An energy bandpass of ± 25 eV and a 150 μm image field were used in concert with the largest contrast (400 μm) and field (1800 μm) apertures in order to maximize sensitivity. Hydride interferences were minimized by using a sample accelerating voltage of + 7.95 kV, and setting the electrostatic analyzer in the secondary column set to +8.00 kV, thus creating a 50 V offset. Entrance slits were set to 36.9 μm. A mass resolving power (measured at 10% valley) of 1300 was used to produce flat-topped peaks. The magnetic field was switched in order to measure $^{204}Pb^+$, $^{206}Pb^+$, $^{207}Pb^+$, $^{208}Pb^+$ ^{230}Th, $^{235}U^+$, and $^{238}U^+$. Analyses comprised 40 cycles and required ~7 minutes to complete. Common Pb was detected, with $^{206}Pb/^{204}Pb$ ratios ≥150 for the majority of samples used in the study. Fine-grained, texturally altered U minerals, however, in some samples had lower and more variable $^{206}Pb/^{204}Pb$ ratios (~1000-50).

The fractionation of U-Pb ratios varies as a function of PbO (Fayek et al., 2002a; b), which must be accounted for in order to yield reliable U-Pb dates. This was accomplished via a calibration curve using the methodology and reference materials of Sharpe and Fayek (2016). These corrected data points were plotted on Concordia diagrams using the ISOPLOT software

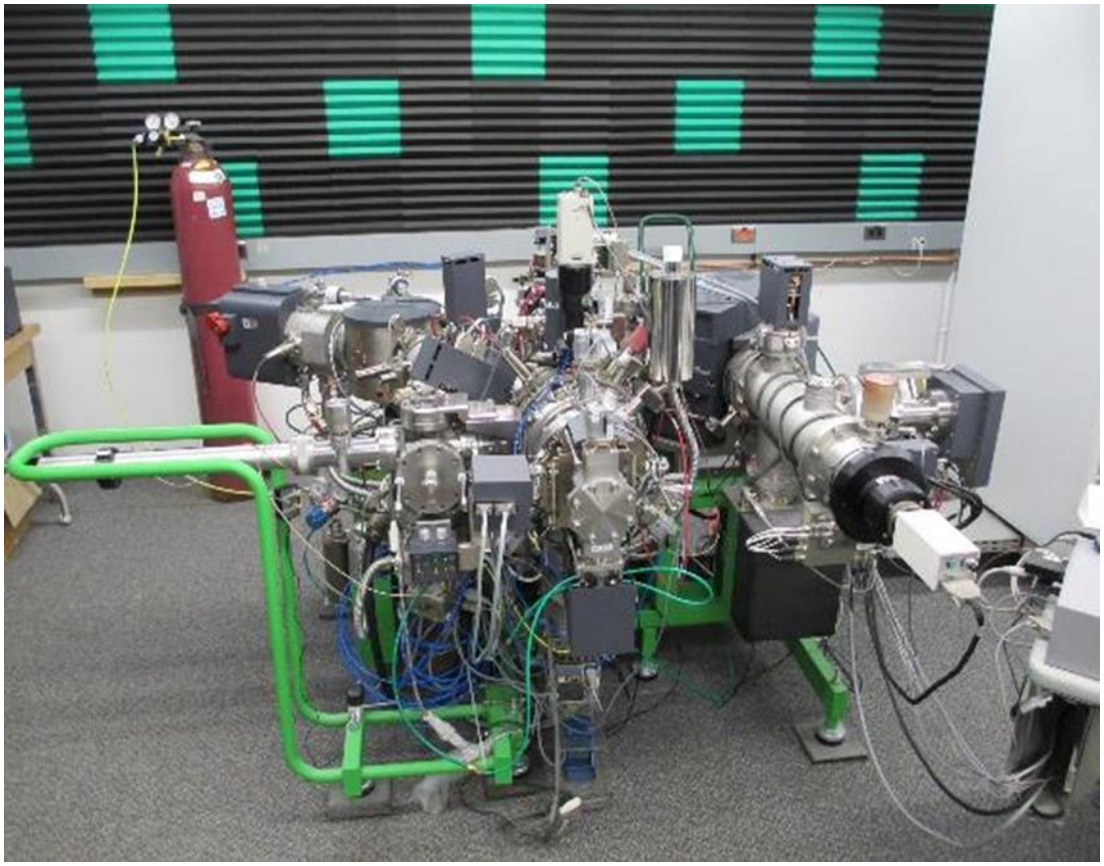

Figure A1. The CAMECA 7f Secondary Ion Mass Spectrometer (SIMS) instrument at the University of Manitoba.

(Ludwig, 1993) to produce U-Pb Concordia ages. Overall errors for U/Pb ratios were ~2%. A correlation coefficient of 0.9 was used, with uncertainties reported at the 1σ level. Where multiple data points yielded overlapping data, these data were grouped and averaged by their $^{206}Pb/^{238}U$ ratios.

Lead isotope ratios were measured in the same analytical session as the U isotope ratios, with $^{206}Pb/^{207}Pb$-$^{206}Pb/^{204}Pb$ isochron ages of U minerals calculated using ISOPLOT software (Ludwig, 1993) and a correlation coefficient of 0.9. Uncertainties are reported at the 1σ level.

Some U-minerals did not contain enough Pb to yield statistically meaningful U-Pb Concordia dates. Minimum ages of these U minerals were calculated from the ^{235}U - ^{207}Pb decay equation:

$$t = \ln(^{207}Pb/^{235}U + 1) / \lambda \quad (1)$$

where t is time in years and λ is the ^{235}U decay constant (9.8485E-10).) This method can date younger, lower Pb, U minerals because it uses only the decay chain of ^{235}U, which has a much shorter half-life than ^{238}U (703.8 Ma vs 4468 Ma). Unlike U-Pb Concordia methods, the ^{235}U - ^{207}Pb technique does not take Pb-loss into account and therefore yields minimum age constraints only.

Uranium-Th disequilibrium geochronology allowed even more recent formation and/or isotopic resetting of U minerals to be investigated. This method measures ratios between ^{238}U and its intermediate daughter isotopes ^{234}U and ^{230}Th. If the U decay chain is not disturbed, the ratios between these isotopes will evolve to a state of secular equilibrium, where the decay of each isotope is offset by its production, over a period of ~500 Kyr. Alteration of U-minerals will disturb the U-decay chain due to the preferential removal of soluble decay products (i.e. ^{234}U)

which are vulnerable to removal due to their locations near sites of structural damage caused by the decay of their parent isotopes (Faure, 1998). Measuring this disturbance from secular equilibrium allows U-mineral alteration or formation occurring within ~475 Ka to be dated (Ludwig, 1993).

Uranium-Th disequilibrium isochron ages were once again calculated using the ISOPLOT software (Ludwig, 1993) with a correlation coefficient of 0.9. Uncertainties were calculated via the Monte Carlo method and reported at the 1σ level. The coherence of the resulting data was increased by averaging groups of similar ages, with the uncertainty of the group defined as two times the mean of the standard deviation of the group.

Stable oxygen and hydrogen isotope ratios of illite and muscovite were measured using the same SIMS instrument as the U-Th-Pb analysis, with samples prepared using the same methods (ultrasonic cleaning, sputter Au coating) as U-Th-Pb samples.

Hydrogen isotope ratios of illite and muscovite were measured using a ~50 nA primary O^- beam accelerated at 12.5 Kv. A 50 µm beam spot size was achieved using a 750 µm aperture in the primary column. A 50 V sample voltage offset, together with a mass resolving power of 800, was once again used to eliminate hydride interferences, with the electrostatic analyzer in the secondary column set to + 10 kV. Total analysis times were ~6 min, with analytical spots pre-sputtered for 60 s with analysis comprising 50 analytical cycles.

Oxygen isotope ratios of illite and muscovite were measured with a ~7 nA primary Cs+ ion beam, accelerated at 10.0 kV. A 750 µm aperture in the primary column focused the beam to a 15 µm spot size. A 300 V sample offset voltage was established by setting the electrostatic analyzer in the secondary column to −9 kV and a mass resolving power of 350 was used to

eliminate molecular interferences. Entrance slits were set to 225 µm. A typical analysis ~13 minute comprised 80 cycles.

An internal muscovite standard from Pied des Monts, Quebec was used for correction of both muscovite and illite data due to their similar matrix compositions. The δ^2H value of this muscovite is − 65‰, with a spot-to-spot reproducibility of better than 2.0‰, and the δ^{18}O value of this muscovite is +10.4‰ with spot-to-spot reproducibility of better than 0.9‰. Hydrogen and oxygen isotopic data are reported in δ-notation relative to Vienna Standard Mean Ocean Water (V-SMOW).

In Situ Ar-Ar Analysis

In-situ ^{40}Ar/^{39}Ar analysis was conducted at the University of Manitoba using the procedures outlined by Camacho et al. (2020). Prior to analysis samples were irradiated for 30 hours in the Cadmium-lined, in-core CLICIT facility of the Oregon State University TRIGA reactor. Standards and unknowns were placed in 2 mm deep wells in 18 mm diameter aluminium disks. Standards were placed so that the lateral neutron flux gradients across the disk could be evaluated.

Samples dated via Ar-Ar analysis were analyzed at MIRF using a multi-collector Thermo Fisher Scientific ARGUS VI mass spectrometer linked to a stainless steel Thermo Fisher Scientific extraction/purification line and a Photon Machines (55 W) Fusions 10.6 CO_2 laser (Fig. A2). Argon isotopes (mass 37 to 40) were measured using Faraday detectors with low noise 1 x 1012 Ω resistors; ^{36}Ar was measured with a compact discrete dynode (CDD) detector.

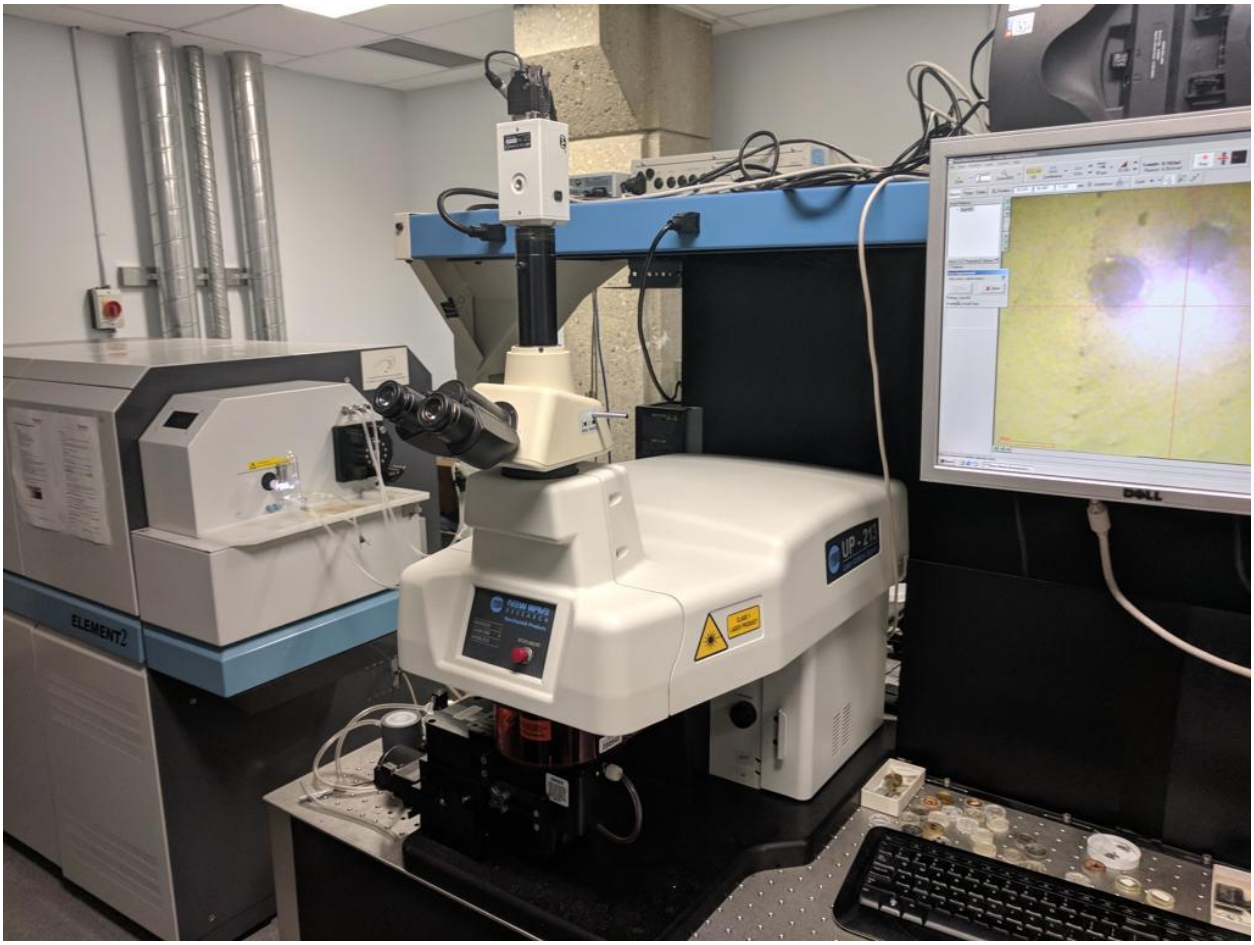

Figure A2. The Thermo Fisher Scientific ARGUS VI mass spectrometer and Photon Machines (55 W) Fusions 10.6 CO_2 laser at the University of Manitoba.

$^{40}Ar/^{39}Ar$ dates were calculated based on the decay constant of Steiger and Jäger (1977). Corrections are made for neutron-induced ^{40}Ar from potassium, ^{39}Ar and ^{36}Ar from calcium, and ^{36}Ar from chlorine (Roddick, 1983; Renne et al.,1998; Renne and Norman, 2001).

(Ultra) Small Angle X-ray Scattering

Rock samples were mounted to quartz glass slides and polished to a thickness of 150 μm. The 20-IDB beamline of the Advanced Photon Source at Argonne National Laboratory was used to perform absolutely calibrated USAXS, SAXS, and WAXS experiments (Fig. A3). X-rays had a wavelength of 0.5904 Å and an energy of 21 keV. The slit length for USAXS was 0.026113, sample to detector distance was 1.08 m, and beamsize was 800 μm. A CdTe detector was used. Sample transmission ranged from ~80-90%. The combined q range of USAXS and SAXS was between ~1 x 10^{-4} and 4.5 $Å^{-1}$.

A line of measurements was taken so as to produce a transect across the sample. This allowed for the average porosity of samples to be calculated while also detecting variations in porosity associated with sharp redox/lithology boundaries. Background was determined by measuring blank quartz glass slides. This background was subtracted during data reduction.

The IGOR software was used for data reduction; the Nika program (Ilavsky, 2012) was used for SAXS data and the Indra program (Ilavsky and Jemian, 2009) was used for USAXS data. A combined SAXS and USAXS scattering curve was produced by merging these datasets with the Irena package (Ilavsky and Jemian, 2009). Although WAXS data as gathered, it was not used.

Rocks are complex systems composed of multiple minerals. X-rays can become scattered off of these interfaces, however this scattering is generally insignificant as contrast in scattering

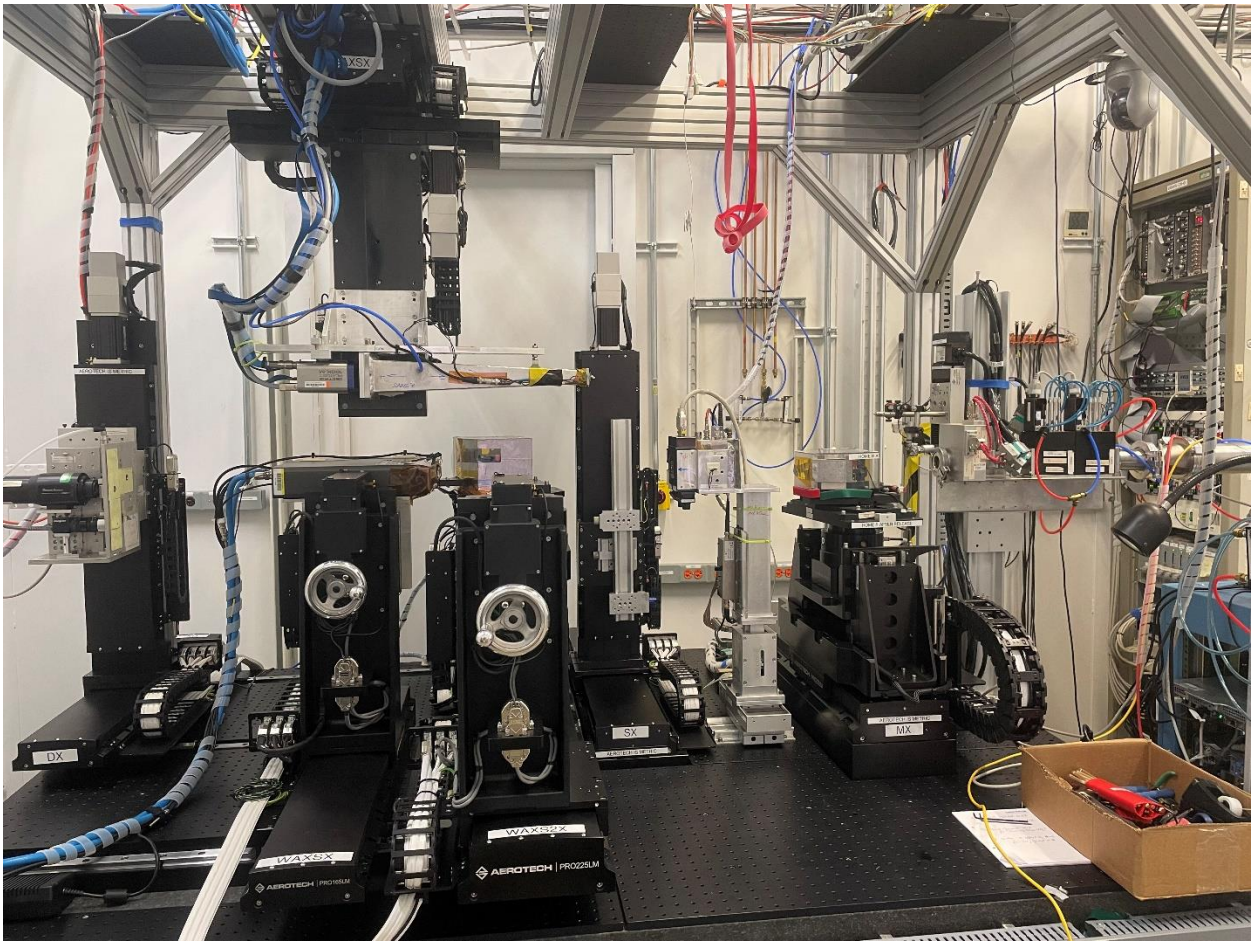

Figure A3. The 20-IDB beamline of the Advanced Photon Source at Argonne National Laboratory.

length densities between minerals are generally small compared to contrast between minerals and pores; this allows rocks to be modelled as two-phase systems of pores within a mineral matrix (Radlinski, 2006; Anovitz and Cole, 2015). Using the two-phase assumption the scattering intensity I(q) is given by:

$$I(q) = \left|\Delta\rho\right|^2 \int_0^\infty \left|F(q,r)\right|^2 V(r)^2\, NP(r) dr \quad (2)$$

where Δρ is the contrast in scattering length density, $\left|F(q,r)\right|^2$ corresponds to the form factor, *V(r)* is the particle volume, *N* is the total number of scatterers, and *p(r)* is the probability of occurrence of scatterers of size r. The values of scattering contrast and form factor used for each measured point were selected to be representative of the average composition of the sample at the location in question. The observations of optical and electron microscopy were used to inform the values selected. For instance, a spot comprising 70% acicular (aspect ratio ~10) illite (Δρ = 559.7) and 30% equant quartz (Δρ = 504.2) would be represented as having an average Δρ = 543.05 and the form factor of a cylinder with an aspect ratio of 7.

Quantitative interpretation of the scattering intensity yields the porosity (ϕ):

$$\int_0^\infty I(Q) Q^2 dQ = 2\pi^2 (\Delta\rho)^2 \phi(1-\phi) \quad (3)$$

The total porosity, pore volume size distribution, and specific surface area of pores were estimated via the size distribution tool in Irena using the IPG/TNNLS method (Ilavsky and Jemian, 2009) over the measured q range.

References

Anovitz, L. M., Cheshire, M. C., Hermann, R. P., Gu , X., Sheets, J. M., Brantley, S. L., Cole, D. R., Ilton, E. S., Mildner, D. F. R., Gagnon, C., Allard, L. F., and Littrell, K. C., 2021, Oxidation and associated pore structure modification during experimental alteration of granite. Geochemica et Cosmochemica Acta, **292**, 532-556.

Camacho, A., Lee, J. K. W., Zhao, J., Abdu, Y.A., Fayek, M. and Creaser, R. A., 2020, A test of the interlayer ionic porosity model as a measure of argon diffusivity in trioctahedral micas. Geochimica et Cosmochimica Acta, **288**, 341-368.

Faure, G., 1998, Principles and Applications of Geochemistry: Upper Saddler River, NJ, USA, Prentice Hall, 287 p.

Ilavsky, J., 2012, Nika: software for two-dimensional data reduction. J. Appl. Crystallogr. **45**, 2, 324–328, https://doi.org/10.1107/S0021889812004037.

Ilavsky, J., and Jemian, P. R., 2009, Irena: tool suite for modeling and analysis of small-angle scattering. J. Appl. Crystallogr. **42**, 2, 347–353, https://doi.org/10.1107/S0021889809002222.

Ludwig, K., 1993, ISOPLOT, excel based program for plotting radiogenic isotopes. USGS Open File Rep 91-445, 42 p.

Radlinski, A., 2006, Small-Angle Neutron Scattering and the Microstructure of Rocks. Reviews in Mineralogy & Geochemistry, **63**, 363-397.

Renne P. R., Swisher C. C., Deino A.L., Karner D. B., Owens T.L., and DePaolo, D. J., 1998. Intercalibration of standards, absolute ages and uncertainties in 40Ar/39Ar dating. Chemical Geology, **145**, 117–152.

Renne, P. R., and Norman, E. B., 2001, Determination of the half-life of 40Ar by mass spectrometry. Physical Review C, **63** (047302), doi-org.uml.idm.oclc.org/10.1103/PhysRevC.63.047302.

Roddick, J. C., 1983, High precision intercalibration of ^{40}Ar-^{39}Ar standards. Geochimica et Cosmochimica Acta, **47**, 887–898.

Sharpe, R. and Fayek, M., 2016, Mass bias corrections for U-Pb isotopic analysis by secondary ion mass spectrometry: Implications for U-Pb dating of uraninite. Rapid Communications in Mass Spectrometry, **30**, 1601–1611.

Steiger, R. H., and Jäger, E. 1977, Subcommission on geochronology: convention on the use of decay constants in geo- and cosmochronology. Earth and Planetary Science Letters, **36**, 359–362.